GPS BASED ATTITUDE DETERMINATION

FINAL TECHNICAL REPORT

to the Naval Research Laboratory

NRL Scientific Officer - Bernard Kaufman

Principal Investigator - Penina Axelrad

Colorado Center for Astrodynamics Research
University of Colorado, CB 431
Boulder, CO 80309

December 4, 1995

Award: N00014-93-1-G030, Account: 153-7545

DEPARTMENT OF THE NAVY
OFFICE OF NAVAL RESEARCH
SEATTLE REGIONAL OFFICE
1107 NE 45TH STREET, SUITE 350
SEATTLE WA 98105-4631

IN REPLY REFER TO:

4330
ONR 247
11 Jul 97

From: Director, Office of Naval Research, Seattle Regional Office, 1107 NE 45th St., Suite 350, Seattle, WA 98105
To: Defense Technical Center, Attn: P. Mawby, 8725 John J. Kingman Rd., Suite 0944, Ft. Belvoir, VA 22060-6218

Subj: RETURNED GRANTEE/CONTRACTOR TECHNICAL REPORTS

1. This confirms our conversations of 27 Feb 97 and 11 Jul 97. Enclosed are a number of technical reports which were returned to our agency for lack of clear distribution availability statement. This confirms that all reports are unclassified and are "APPROVED FOR PUBLIC RELEASE" with no restrictions.

2. Please contact me if you require additional information. My e-mail is *silverr@onr.navy.mil* and my phone is (206) 625-3196.

ROBERT J. SILVERMAN

To: Regional Director
Team Leader
ACO

This technical report was sent to me by DTIC because it does not include the DD-1498 form with the proper disclosure/distribution statement.

Please obtain this form with proper instructions and return it and the technical report directly to DTIC.

Also implement procedures with the contractor to correct this problem.

Thank You,

Jim Carbonara

Jim Carbonara,
Director, Field Operations

REPORT DOCUMENTATION PAGE

OMB No 0704-0188

1. AGENCY USE ONLY (Leave blank)	2. REPORT DATE	3. REPORT TYPE AND DATES COVERED
	04 Dec 1995	Final Technical Report 9/93 - 8/95

4. TITLE AND SUBTITLE

GPS Based Spacecraft Attitude Determination

5. FUNDING NUMBERS

G-N00014-93-1-G030

PR - 81-0333-93

6. AUTHOR(S)

P. Axelrad

7. PERFORMING ORGANIZATION NAME(S) AND ADDRESS(ES)

University of Colorado
Colorado Center for Astrodynamics Research
Campus Box 431
Boulder, CO 80309-0431

8. PERFORMING ORGANIZATION REPORT NUMBER

9. SPONSORING MONITORING AGENCY NAME(S) AND ADDRESS(ES)

Department of the Navy
Naval Research Laboratory
4555 Overlook Ave S.W.
Washington, D.C. 20375-5326

10. SPONSORING MONITORING AGENCY REPORT NUMBER

11. SUPPLEMENTARY NOTES

12a. DISTRIBUTION AVAILABILITY STATEMENT

12b. DISTRIBUTION CODE

13. ABSTRACT (Maximum 200 words)

This final technical report describes the research performed by the Colorado Center for Astrodynamics Research for the Naval Research Laboratory (NRL) on GPS Based Attitude Determination for spacecraft over the period 01 September 1993 - 31 August 1995. The overall project encompasses various methods for using GPS to determine the attitude of a spacecraft in near Earth orbit. The specific topics covered are - 1) attitude estimation for a gravity gradient stabilized satellite using point solution and Kalman Filtering techniques; 2) identification and mitigation of multipath in GPS carrier phase data; and 3) frequency and time domain techniques for attitude estimation of a spinning satellite. This report represents a compilation of four semiannual technical reports provided to NRL over the course of the project.

14. SUBJECT TERMS	15. NUMBER OF PAGES
GPS Attitude Determination	240
	16. PRICE CODE

17. SECURITY CLASSIFICATION OF REPORT	18. SECURITY CLASSIFICATION OF THIS PAGE	19. SECURITY CLASSIFICATION OF ABSTRACT	20. LIMITATION OF ABSTRACT
UNCLASSIFIED	UNCLASSIFIED	UNCLASSIFIED	UL

ABSTRACT

This final technical report describes the research performed by the Colorado Center for Astrodynamics Research for the Naval Research Laboratory (NRL) on GPS Based Attitude Determination for spacecraft over the period 01 September 1993 - 31 August 1995. The overall project encompasses various methods for using GPS to determine the attitude of a spacecraft in near Earth orbit. The specific topics covered are - 1) attitude estimation for a gravity gradient stabilized satellite using point solution and Kalman Filtering techniques; 2) identification and mitigation of multipath in GPS carrier phase data; and 3) frequency and time domain techniques for attitude estimation of a spinning satellite. This report represents a compilation of four semiannual technical reports provided to NRL over the course of the project.

GPS BASED ATTITUDE DETERMINATION

FY'93-94 Technical Report I

to the Naval Research Laboratory

NRL Scientific Officer -	Bernard Kaufman
Principal Investigator -	Penina Axelrad
Co-Investigator -	Peter F. MacDoran
Graduate Students	Charles P. Behre
	Christopher J. Comp
	Lisa M. Ward

Colorado Center for Astrodynamics Research
University of Colorado, CB 431
Boulder, CO 80309

May 16, 1994

Award: N00014-93-1-G030, Account: 153-7545

ABSTRACT

This report describes the research performed by the Colorado Center for Astrodynamics Research during the first half of FY'93-94 on spacecraft attitude determination using GPS. The specific topics currently under investigation are Kalman filtering approaches for Earth pointing and three axis stabilized vehicles, multipath mitigation in GPS phase observations, and modal estimation techniques for attitude determination on spinning satellites.

In the area of Kalman filtering approaches for attitude determination, a boot-strapping algorithm for successive enhancement of GPS attitude determination accuracy was developed. It comprises three steps - an initial batch solution estimate, a Kalman filter baseline estimate, and a high accuracy attitude estimate. The full technique has been tested using simulated data. The two attitude determination steps have also been successfully used to process GPS data collected on-board the RADCAL satellite. The accuracy of this solution is expected to be better than 0.2 deg, 1-σ in each axis.

Multipath is generally thought to be the largest error source for GPS based attitude determination. To address this problem, an algorithm was developed which uses receiver signal-to-noise ratio (SNR) to produce a multipath correction profile for differential phase observations. The algorithm has been successfully applied to actual GPS data collected in a controlled static experiment. Errors in the best case were reduced from a maximum of 6 mm to 2 mm.

A research effort has also been initiated on attitude determination of spinning satellites using modal estimation techniques. This set of approaches may provide an alternative to Kalman filtering in situations where the vehicle dynamics, and consequently, the GPS observations, are dominated by sinusoidal oscillations of various frequencies. A preliminary simulation has been designed and used to investigate these frequency domain techniques.

TABLE OF CONTENTS

LIST OF FIGURES

LIST OF TABLES

1. Overview

This report describes the research performed by the Colorado Center for Astrodynamics Research during the first half of FY'93-94 on spacecraft attitude determination using GPS. This is a continuation of work sponsored by the Naval Research Laboratory during FY'92-93, described in detail in the technical report by Axelrad, Chesley, and Ward [1993].

The overall project encompasses various methods for using GPS to determine the attitude of a spacecraft in near Earth orbit. The specific topics currently under investigation are Kalman filtering approaches for Earth pointing and three axis stabilized vehicles, multipath mitigation in GPS phase observations, and modal estimation techniques for spinning satellites.

Significant advances were made during this six month period.. The highlights are as follows:

- Developed a boot-strapping algorithm for successive enhancement of GPS attitude determination accuracy.
- Successfully generated attitude solutions for the RADCAL spacecraft using data collected on-orbit.
- Developed an algorithm which uses receiver signal-to-noise ratio (SNR) to produce a multipath correction profile for differential phase observations, and successfully applied it to an experimental data set.
- Began an investigation into the application of modal estimation techniques to attitude determination of spinning satellites.

Section 2 covers the bootstrapping attitude determination algorithms and presents results from both simulated and actual on-orbit data. The bootstrapping procedure comprises three steps - 1) initial batch attitude estimate, 2) Kalman filter antenna baseline estimate, and 3) Kalman filter attitude estimate. All three steps have been successfully applied to simulated data. Steps 1 and 3 have also been successfully applied to a data set collected on-orbit from the RADCAL spacecraft. Section 2 concludes with a discussion of future plans for applying the baseline estimation technique to the RADCAL data and for improving the robustness of the algorithms.

Section 3 describes analytical and experimental work performed to characterize and mitigate multipath errors in differential phase measurements. Our previous work and the work of others indicates that multipath is likely to be the largest source of error in GPS attitude determination. We have developed a technique to create a profile of the induced phase error due to multipath, based on the reported signal to noise ratio from each antenna. The technique was successfully applied to a data set in which an electronically generated multipath signal was deliberately injected into the GPS antennas. Section 3 provides a discussion of the technique , the experiment, and plans for continued research in this area.

Section 4 describes preliminary research on attitude determination of spinning satellites using modal estimation techniques. This set of approaches may provide an alternative to Kalman filtering in situations where the vehicle dynamics, and consequently, the GPS observations, are dominated by sinusoidal oscillations of various frequencies. A preliminary

simulation has been designed and used to investigate these frequency domain techniques. The procedures are divided into two parts. First, the dominant frequencies are identified via an FFT or Auto-Regressive (AR) method. Given the frequency estimates and a model of the vehicle motion, the attitude parameters are identified. Thus far the effects of external torques or nutation damping have not been considered. A comparison is made between various methods in terms of accuracy, time required to generate a solution, and computational load.

Appendix A provides an errata sheet for last year's technical report [*Axelrad, et al.*, 1993].

2. GPS Based Spacecraft Attitude and Antenna Location Estimation

Lisa M. Ward

2.0 Introduction

If GPS based attitude determination is to meet the expectations of spacecraft designers and operators, it must be made both accurate and robust. This implies that the receiver processing algorithm should be able to start up with a minimal amount of information and provide an accurate solution in a timely fashion. Furthermore, it must have a means for validating results in real time. Cohen [1992] and others have provided excellent suggestions and algorithms which deal with various levels of a priori knowledge and dynamic uncertainty. What we have done is to combine many of these ideas into a bootstrapping algorithm which starts with very little a priori information about the vehicle, and in several steps, works its way to a highly accurate and reliable solution. We have also developed a simulation to aid in our testing and verification of these algorithms. This section of the report focuses on additions and improvements to the bootstrapping process and simulation. Much of the information presented here draws on the paper by Axelrad and Ward [1994].

2.1 GPS Attitude Determination Basics

To establish definitions and notation we review the basic theory of GPS attitude determination. The principal observable for GPS attitude determination is the difference in carrier phase between a master and slave antenna. The phase difference, $\Delta\varphi$, is related to the range difference, Δr, (both expressed in cycles) as follows,

$$\Delta\varphi = \Delta r - k + \beta + \nu \tag{2.1}$$

where k is the integer number of carrier cycles in the differential range, β is the line bias and ν is the random measurement noise. Geometrically, the range difference is just the projection of the baseline vector, $\mathbf{b}$ (directed from the master antenna to the slave antenna), onto the user-to-GPS line of sight vector, $\mathbf{e}$, which gives

$$\Delta r = \mathbf{b} \cdot \mathbf{e} \tag{2.2}$$

or more specifically,

$$\Delta r = (\mathbf{b}^B)^T \, {}^B\mathbf{C}^L \, \mathbf{e}^L. \tag{2.3}$$

In this notation ${}^B\mathbf{C}^L$ is the transformation matrix from the orbit local reference frame, L, to the body fixed reference frame, B. The superscripts on the vectors denote the reference frame in which the vector is expressed.

2.2 RADCAL Data

The Air Force RADCAL satellite demonstrates the operation of attitude determination using GPS [*Cohen, et al.*, 1993]. A Trimble Quadrex receiver collects the differential carrier phase data. Glenn Lightsey of Stanford University provided us with a sample of the raw data collected in August 1993 during one of the first days of the mission. Since then, with the recommendation of William Feess and Robert Smith of Aerospace Corporation, we now have access to the TECNET where recently collected GPS receiver data and navigation solutions are posted and can be downloaded to a local computer. The receiver data appears in binary packet form. We then use a C program called "qs" to parse the packets and recover the phase data. The navigation solutions have been corrected for selective availability by ARL. With the help of Dave Starr at JPL, we also gained access to the JPL GPS navigation solutions. These solutions are on the sideshow.jpl.nasa.gov computer and are available via anonymous ftp. Both the RADCAL and GPS positions are converted from Earth Centered Earth Fixed to Earth Centered Inertial coordinates, interpolated to the measurement epochs, and then used to form the line of sight vectors. Testing these bootstrapping algorithms on the actual RADCAL data has been indispensable to our effort.

2.3 Simulation

In addition to the actual RADCAL data, we also use data generated from a simulation which models a spacecraft using GPS for attitude determination. Although a few enhancements have been made, the simulation remains largely unchanged from previous reports. As before, the attitude dynamics of the user satellite are based on a gravity gradient satellite (either with or without a gyrostat) while the orbit dynamics are based on a two-body orbit with oblate Earth perturbations. The position and velocity of the GPS satellites are calculated analytically using a simpler model which includes only two-body effects. These dynamical equations as well as the equations describing the construction of observed GPS measurements can be found in the September 1993 Final Report to NRL [*Axelrad, et al.*, 1993].

One change that has been implemented is an improvement in the GPS satellite visibility calculation. GPS satellite signals may be blocked by the Earth or by parts of the user satellite itself. Previously, only one visibility cone, with the boresight along the spacecraft's zenith vector, was specified for the entire spacecraft. Although this approach accounted for Earth blockage, it did not account for variation due to the motion of the user satellite. Furthermore, antenna placement on the spacecraft was not considered at all. A more realistic model is to construct a separate visibility cone is for each antenna. Each cone is specified by the boresight direction and half-angle. An Earth blockage cone centered on the spacecraft nadir vector is specified as well. As shown in Figure 2.1, a GPS satellite is visible if its line of sight vector falls inside the antenna visibility cone and outside the Earth blockage cone.

Another addition made to the simulation is the ability to select a different master antenna for each GPS satellite based on signal strength considerations. Here we consider signal strength to be proportional to the cosine of the angle between the GPS line-of-sight vector

and the antenna boresight vector. The master is set to the antenna with the strongest signal.

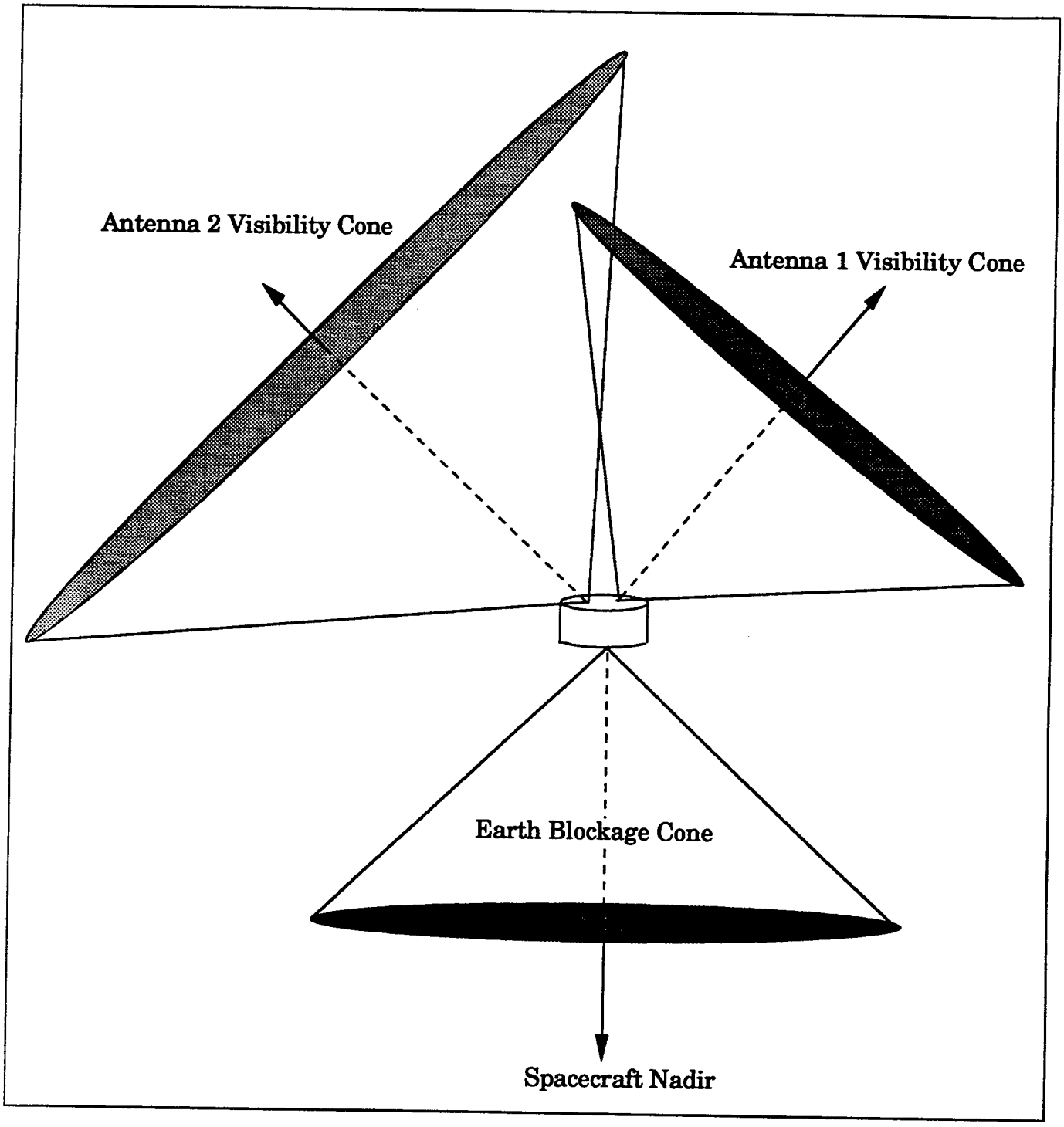

Figure 2.1. GPS Satellite Visibility

The spacecraft modeled in the simulation is based on the RADCAL satellite. The parameters used can be found in Table 2.1. The yaw, roll, and pitch generated from this scenario are shown in Figure 2.2.

Table 2.1. Simulation Parameters

User Orbital Elements
semimajor axis: 7193 km
eccentricity: 0.01
inclination: 90.0 degrees

Moments of Inertia
$I_1 = 5.813$ kg m^2 (radial)
$I_2 = 26.40$ kg m^2
$I3 = 26.40$ kg m^2

Baseline Configuration
- 4 antennas mounted on zenith face
- antennas canted outward 17.5 degrees
- visibility cone half-angle 85 degrees

Baseline Vectors (m)
$\mathbf{b}_1 =$ [0.0 -0.313 0.313]
$\mathbf{b}_2 =$ [0.0 0.0 0.626]
$\mathbf{b}_3 =$ [0.0 0.313 0.313]

Earth Blockage Cone Half-Angle
64.2 degrees measured from nadir

Line Biases
$\beta_1 = 0.2$ cycles
$\beta_2 = 0.5$ cycles
$\beta_3 = 0.8$ cycles

Range Difference Measurement Errors
standard deviation: 5 mm
inverse time constant: 100/sec

Initial Attitude
yaw: 20 degrees
roll: 10 degrees
pitch: -10 degrees

Initial Inertial Angular Velocity
$\omega_1 = 4.45$ deg/min
$\omega_2 = 0.0$
$\omega_3 = 3.44$ deg/min (~orbit rate)

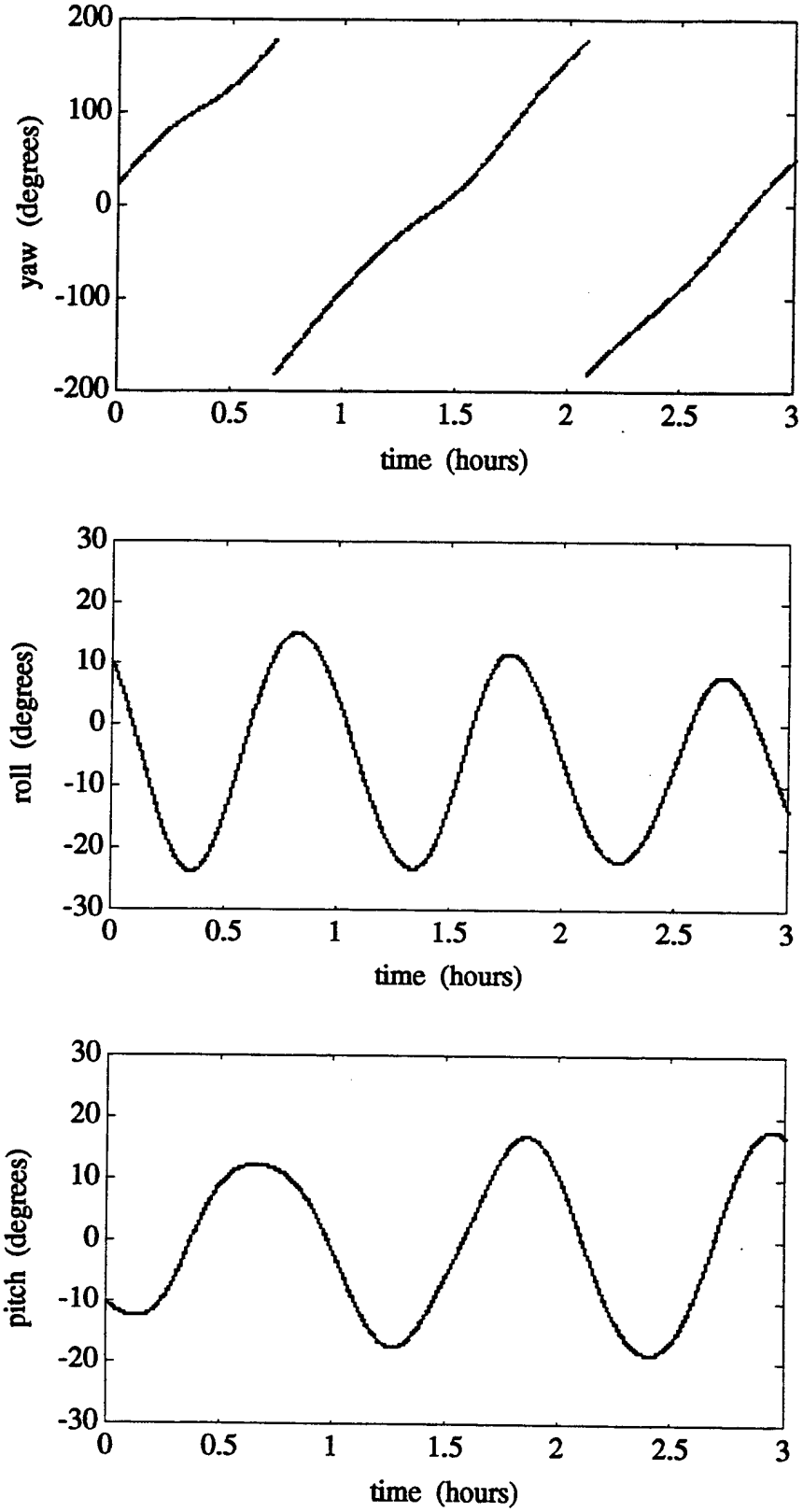

Figure 2.2. Simulated Yaw, Roll, and Pitch

2.4 Bootstrapping Overview

Two key elements are needed to start the bootstrapping process. The first is an approximate attitude (to about 20 degrees for a 1 meter baseline). There are many clever ways of determining an approximate vehicle attitude based on vehicle design and/or GPS satellite visibility. For example, the RADCAL satellite is gravity gradient stabilized with a long boom, thus a good starting assumption is that it is aligned along the radius vector with pitch and roll both zero. If antennas are mounted on different faces of the spacecraft or facing in substantially different directions, received GPS satellite signal strength could be used to determine a likely orientation. This method is not likely to be feasible for many Earth pointing satellites because all the antennas will probably be placed on the anti-nadir side of the vehicle.

The other key element is knowledge of the antenna locations in the spacecraft body frame (to about 2 centimeters for a 1 meter baseline). Cohen [1992] developed a self-survey algorithm to provide baseline and bias estimates to an accuracy of several millimeters. Unfortunately, it is often not possible or convenient to run such a survey on a fully integrated spacecraft as is the case with RADCAL. In this situation we must rely on a mechanical drawing of the spacecraft which should provide the location of antennas to within several centimeters. This drawing also defines the spacecraft "body" frame based on some sensors of interest.

Once a rough estimate of vehicle attitude and antenna locations is obtained we can begin the bootstrapping process. The first stage of the bootstrapping algorithm is an initial attitude estimator which resolves integer ambiguities and improves the attitude estimate to within 5 degrees. These estimates are adequate to resolve the expected phase to within about 1/4 wavelength and thus permit us to compute the correct integers directly. The second stage is a baseline estimator which improves the knowledge of the relative coordinates of the antennas to within 5 millimeters. The final stage is an extended Kalman filter which incorporates knowledge of vehicle dynamics to provide the best estimate of vehicle attitude in real-time. Figure 2.3 shows a diagram of the data flow through the bootstrapping algorithms.

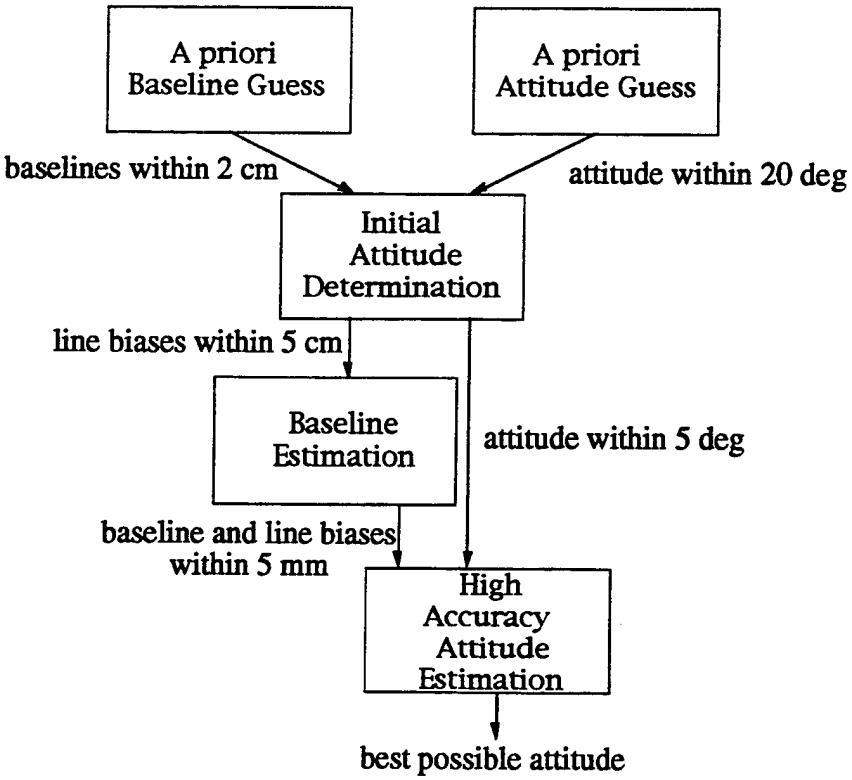

Figure 2.3. Bootstrapping Data Flow

2.5 Initial Attitude Determination Algorithm

Since the receiver only measures the fractional part of the phase difference, the range difference remains ambiguous until the integer part is resolved. This can be done directly if the attitude, angular velocity, and line biases are known to an equivalent uncertainty of 1/4 of a wavelength. This algorithm is based on the method described by Cohen and Parkinson [1992b] to estimate the initial attitude, angular velocity, and integer ambiguities for a spacecraft. Here we use a batch process rather than the sequential filter presented in Axelrad and Ward [1994].

The vehicle is assumed to rotate with a constant angular velocity, so that the attitude matrix can be represented as

$$ {}^{B}\mathbf{C}^{L} = \mathbf{C}(\omega t)\mathbf{C}(\mathbf{q}_0) \tag{2.4} $$

where the quaternion $\mathbf{q}_0$ represents the attitude of the vehicle with respect to the local frame at some initial time, and ω is the constant angular velocity vector of the vehicle with respect to the local frame. With an a priori initial attitude and angular velocity, $\bar{\mathbf{q}}_0$ and $\bar{\omega}$, respectively, we can estimate ${}^{B}\mathbf{C}^{L}$ using the following equation,

$$ {}^{B}\hat{\mathbf{C}}^{L} = \delta\hat{\mathbf{C}}\ {}^{B}\bar{\mathbf{C}}^{L} \equiv (\mathbf{I} + \Theta^{\times})\ \mathbf{C}(\bar{\omega}t)\mathbf{C}(\bar{\mathbf{q}}_0). \tag{2.5} $$

The vector $\bar{\theta}$ represents small rotations about the initial estimate of the body axes and is given by

$$\bar{\theta} = \begin{bmatrix} \delta\theta_1 \\ \delta\theta_2 \\ \delta\theta_3 \end{bmatrix} + \begin{bmatrix} \delta\omega_1 \\ \delta\omega_2 \\ \delta\omega_3 \end{bmatrix} t, \tag{2.6}$$

and $\Theta^{\times}$ is the cross product matrix associated with the components of $\bar{\theta}$. This formulation leads to the following phase measurement model for baseline i and satellite j,

$$\begin{aligned} \Delta\varphi_{ij} &= (\mathbf{b}_i^B)^{\mathrm{T}} \left({}^{B}\mathrm{C}^{L}\, \mathbf{e}_j^L \right) - \kappa_{ij} \\ \Delta\varphi_{ij} &= (\mathbf{b}_i^B)^{\mathrm{T}} \left(\mathbf{I} + \Theta^{\times} \right) {}^{B}\overline{\mathrm{C}}^{L}\, \mathbf{e}_j^L - \kappa_{ij} \end{aligned} \tag{2.7}$$

where κ_{ij} is the integer, k_{ij}, minus the line bias, β_j (i.e. κ_{ij} is a floating point number). If the correction state vector, $\mathbf{x}$, is defined as

$$\mathbf{x} = \left[\delta\theta_1 \quad \delta\theta_2 \quad \delta\theta_3 \mid \delta\omega_1 \quad \delta\omega_2 \quad \delta\omega_3 \mid \kappa_{11} \quad \cdots \quad \kappa_{mn} \right]^{\mathrm{T}}, \tag{2.8}$$

then the measurement gradient, $\mathbf{H}_{ij} = \partial(\Delta\varphi_{ij})/\partial\mathbf{x}$, for a single measurement is given by

$$\mathbf{H}_{ij} = \left[\left({}^{B}\overline{\mathrm{C}}^{L}\, \mathbf{e}_j^L \right)^{\mathrm{T}} \mathrm{B}_i^{\times} \;\middle|\; \left({}^{B}\overline{\mathrm{C}}^{L}\, \mathbf{e}_j^L \right)^{\mathrm{T}} \mathrm{B}_i^{\times} t \;\middle|\; 0 \;\cdots\; 0 \;\; -1 \;\; 0 \;\cdots\; 0 \right] \tag{2.9}$$

where $\mathbf{B}_i^{\times}$ is the cross product matrix associated with the components of the vector $\mathbf{b}_i^B$. The measurement gradient vectors are then concatenated into an m by n matrix, $\mathbf{H}$, where m is the number of measurements and n is the number of states. The measurement residual is computed by subtracting the predicted phase difference,

$$\Delta\hat{\varphi}_{ij} = (\mathbf{b}_i^B)^{\mathrm{T}} \left({}^{B}\overline{\mathrm{C}}^{L}\, \mathbf{e}_j^L \right), \tag{2.10}$$

from the observed phase, $\Delta\varphi_{ij}$. The residuals are then combined into a m-vector, $\mathbf{z}$, to give

$$\mathbf{z} = \begin{bmatrix} \vdots \\ \Delta\varphi_{ijt} - \Delta\hat{\varphi}_{ijt} \\ \vdots \end{bmatrix}. \tag{2.11}$$

Now, to find the best estimate of the corrections solve the system of equations $\mathbf{Hx} = \mathbf{z}$ for $\mathbf{x}$. The small angle corrections are converted to a correction quaternion as follows,

$$\begin{aligned}
\delta q_1 &= \delta\theta_1/2 \\
\delta q_2 &= \delta\theta_2/2 \\
\delta q_3 &= \delta\theta_3/2 \\
\delta q_4 &= \sqrt{1-\delta q_1^2-\delta q_2^2-\delta q_3^2}
\end{aligned} \tag{2.12}$$

which is in turn used to update the a priori estimate of $\mathbf{q}_0$ according to the quaternion composition rule,

$$\hat{\mathbf{q}}_0 = \delta\mathbf{q} \otimes \overline{\mathbf{q}}_0. \tag{2.13}$$

The angular velocity is updated in the traditional manner,

$$\hat{\omega} = \delta\omega + \overline{\omega}. \tag{2.14}$$

This batch process is iterated until the corrections become sufficiently small.

Since the fractional part of each κ_{ij} represents the constant differential line bias between the two antennas, we would like to be able to estimate the line bias associated with the a baseline i by averaging over all satellites $j = 1,\ldots,l$, where l is the number of GPS satellites. If the master antenna varies from satellite to satellite, however, the baseline configuration will vary as well. In this situation, one antenna is chosen to be the *pseudo-master* for all satellites, and the ambiguities are converted to refer this pseudo-master. For example, if the master for a particular satellite is antenna 2, and the pseudo-master is antenna 0 (with antennas numbered 0, 1, 2, 3), then the ambiguities are converted as follows,

$$\begin{aligned}
\kappa_{0\to1} &= \kappa_{2\to1} - \kappa_{2\to0} \\
\kappa_{0\to2} &= \quad 0 \quad - \kappa_{2\to0} \\
\kappa_{0\to3} &= \kappa_{2\to3} - \kappa_{2\to0}
\end{aligned} \tag{2.15}$$

where $i \to j$ denotes the baseline from master i to slave j. Now the fractional portions of each ambiguity can be averaged to estimate the line biases for a particular baseline configuration. Proximity of the fractional portions is used as an integrity check of the algorithm.

This algorithm assumes that each κ_{ij} is constant; thus, an interval of data should be chosen where there are at least 3 visible satellites that do not change master or loose lock. Furthermore, the time span of the data should be short enough so that the angular velocity is approximately constant but long enough to obtain adequate information to resolve the ambiguities.

2.6 Initial Attitude Determination Results

For the simulated data we set the a priori attitude of the vehicle to be aligned with the local level. That is nadir pointing with zero azimuth angle. The a priori angular velocity of the body with respect to the local frame was set to zero. The a priori guess of each baseline

vector differs about 2 centimeters in length from the true baseline. These assumptions seem to be reasonable based on what we know about the RADCAL satellite. The algorithm was run over a 10 minute span of data and converged after 15 iterations. Table 2.2 shows the results of this simulation run. Each estimated angle is within 4 degrees of the true angle.

Table 2.2. Initial Attitude Determination Results - Simulated Data

	A priori	True	Estimated	Error
Euler Angles (degrees)				
yaw	0	20.0	22.87	2.87
roll	0	10.0	6.35	-3.65
pitch	0	-10.0	-8.42	1.58
Angular Velocity ${}^{B}\omega^{L}$ (deg/min)				
ω_1	0	4.45	4.34	-0.11
ω_2	0	0.00	-1.49	-1.49
ω_3	0	3.44	4.42	0.98
Line Bias (cycles)				
β_1	0	0.2	0.143	-0.057
β_2	0	0.5	0.472	-0.028
β_3	0	0.8	0.815	0.015

This algorithm was used to process actual RADCAL data. The baseline vectors were fixed to the values reported in Lightsey et al. [1994] which are based on the vehicle mechanical drawings. The data set was dated 20 March 1994 (Day 079). On the first attempt the a priori attitude was aligned with the local level with zero angular velocity, but the algorithm did not converge. Next the yaw was set to 180 degrees. This time the algorithm converged in 20 iterations. See Table 2.3 for the results.

Table 2.3. Initial Attitude Determination Results - RADCAL Data

Euler Angles (degrees)		
	A priori	Estimated
yaw	180	146.2
roll	0	-15.4
pitch	0	24.3

Angular Velocity (deg/min)		
	A priori	Estimated
ω_1	0	6.73
ω_2	0	1.19
ω_3	0	0.78

Line Biases (cycles)		
	A priori	Estimated
β_1	0	0.839
β_2	0	0.232
β_3	0	0.103

In testing this algorithm we discovered that with some initial conditions it would converge to the wrong answer. Incorrect solutions can be distinguished from the correct one by checking the line biases. If the individual line biases for each baseline are not close to one another, then the solution is deemed incorrect. If a particular set of initial conditions does not produce a consistent answer, we choose another set and try the algorithm again. For a gravity gradient satellite like RADCAL the roll and pitch are constrained, but we have no a priori knowledge of the initial yaw angle. We found if we try various yaw angles at increments of even 40 degrees, the algorithm would converge to a consistent answer on one of these trials.

2.7 Baseline Estimation Algorithm

To properly estimate the attitude of a spacecraft, the body reference frame (B) must be clearly defined and each of the antenna baselines must be accurately known in this frame. For a 1 meter baseline length we estimate that the baseline coordinates must be determined to better than 5 mm to produce high accuracy attitude results.

The B frame may be defined by vehicle geometry, principal axes, or perhaps based on the sensitive axes of payload instruments. If the GPS antennas are not carefully surveyed prior to launch, one must make some assumptions about the relation of the body frame to the antenna array. The method developed here is to initially estimate the baseline vectors in the local reference frame, then specify the body frame based on two of the baselines, and calculate the best estimate of each baseline in this body fixed frame.

The phase difference measurement model shown in Equation (2.7) is modified to represent this new perspective as follows,

$$\begin{aligned} \Delta\varphi_{ij} &= \left(\mathbf{e}_j^L\right)^{\mathrm{T}} \mathbf{b}_i^L + \beta_i - k_{ij} \\ \Delta\varphi_{ij} &= \left(\mathbf{e}_j^L\right)^{\mathrm{T}} \left(\hat{\mathbf{b}}_i^L + \delta\mathbf{b}_i^L\right) + \left(\hat{\beta}_i + \delta\beta_i\right) - \hat{k}_{ij} \end{aligned} \tag{2.16}$$

where the starting estimates of the β's are provided by the initial attitude estimation process. The starting estimates of the baselines in the local frame are derived from the mechanical drawings and the attitude estimate from the initial stage as follows,

$$\hat{\mathbf{b}}_i^L(t_0) = {}^L\hat{\mathrm{C}}^B(t_0)\, \hat{\mathbf{b}}_i^B. \tag{2.17}$$

A sequential filter is used to solve for the line biases and the three components of each baseline in local coordinates. The state vector then is

$$\mathbf{x} = \left[(\delta\mathbf{b}_1^L)^{\mathrm{T}} \quad (\delta\mathbf{b}_2^L)^{\mathrm{T}} \quad (\delta\mathbf{b}_3^L)^{\mathrm{T}} \mid \delta\beta_1 \quad \delta\beta_2 \quad \delta\beta_3\right]^{\mathrm{T}}. \tag{2.18}$$

The filter presented in Axelrad and Ward [1994] assumed no dynamics between measurement epochs. This approach did not use all of the available information and was very sensitive to measurement outages. To address this problem and improve the filter's performance, the following dynamic model was added

$$\left(\frac{d\mathbf{b}^L}{dt}\right)_I = \omega_I^L \times \mathbf{b}^L. \tag{2.19}$$

where ω_I is the inertial angular velocity of the body. Since **b** is known in the local frame, ω_I is also expressed in local coordinates. We assume ω_I is a constant and set it to the value obtained in the initial attitude determination stage.

Consider a measurement on baseline i observing satellite j. The elements of the measurement gradient matrix for baseline i are just the elements of the line of sight vector $\mathbf{e}_j^L$. The element corresponding to the line bias, β_i is 1. All other elements are zero. For example, if baseline 1 observes satellite j, then

$$\mathbf{H}_{1j} = \left[\mathbf{e}_j^T \quad \bar{\mathbf{0}}^T \quad \bar{\mathbf{0}}^T \mid 1 \quad 0 \quad 0\right]. \tag{2.20}$$

After the baselines have been estimated in the local frame, we define the body reference frame by setting the $\mathbf{j}_B$ vector equal to a unit vector in the direction of the $\mathbf{b}_1$ vector. The $\mathbf{i}_B$ vector is set equal to a unit vector in the direction of $\mathbf{b}_1 \times \mathbf{b}_2$ which is nominally along the radial vector for gravity gradient satellites. And finally, the $\mathbf{k}_B$ vector completes the orthogonal triad. In summary,

$$\hat{\mathbf{j}}_B^L \equiv \frac{\hat{\mathbf{b}}_1^L}{\left|\hat{\mathbf{b}}_1^L\right|}, \qquad \hat{\mathbf{i}}_B^L \equiv \frac{\hat{\mathbf{b}}_1^L \times \hat{\mathbf{b}}_2^L}{\left|\hat{\mathbf{b}}_1^L \times \hat{\mathbf{b}}_2^L\right|}, \qquad \hat{\mathbf{k}}_B^L \equiv \hat{\mathbf{i}}_B^L \times \hat{\mathbf{j}}_B^L. \tag{2.21}$$

Defining the body frame in this way makes use of the information that the baselines are fixed relative to one another. This particular definition was chosen because it was convenient to use with the satellite under study, but it is not the only way to define the body frame. In a different situation another definition based on the position of the GPS relative to spacecraft instruments may be more useful.

Now the estimate of the local to body transformation matrix is given by

$${}^B\hat{\mathbf{C}}^L = \begin{bmatrix} \left(\hat{\mathbf{i}}_B^L\right)^T \\ \left(\hat{\mathbf{j}}_B^L\right)^T \\ \left(\hat{\mathbf{k}}_B^L\right)^T \end{bmatrix}. \tag{2.22}$$

${}^B\hat{\mathbf{C}}^L$ is computed at each measurement epoch, and the estimated local baselines are transformed to the body frame. Since the baseline vectors in the body frame should remain constant, their coordinates can be averaged over time to obtain the best estimate.

Currently, the baseline estimation algorithm does not handle a roving master, but this work is in progress. Another improvement we are working on is to estimate the angular velocity in the filter along with the baselines and line biases. Although we have tested this algorithm with simulated data, we do not yet have results from the RADCAL data.

2.8 Baseline Estimation Results

Since baselines 1 and 2 are used to define the rotation matrix from body to local coordinates, we look at the results for baseline 3 as an indication of how well the algorithm works. Figure 4 shows the local baseline filter errors for baseline 3. After transforming the local

baselines to body frame coordinates and averaging, the baselines are determined within 0.5 millimeters. The results for a typical run can be found in Table 2.4. Some baseline coordinates are necessarily exact due to the definition of the body frame and have been omitted from the table.

Table 2.4. Baseline Filter Results - Simulated Data

	A priori	True	Estimated	Error
Baselines (cm)				
$b1_y$	-30.30	-31.30	-31.32	-0.02
$b1_z$	33.30	31.30	31.32	0.02
$b2_y$	1.00	0.00	0.00	0.00
$b2_z$	61.00	62.60	62.60	0.00
$b3_x$	0.00	0.00	0.01	0.01
$b3_y$	32.40	31.30	31.31	0.01
$b3_z$	32.30	31.30	31.28	-0.02
Line Biases (cm)				
b_1	3.00	5.00	5.01	0.01
b_2	12.00	10.00	10.02	0.02
b_3	16.00	15.00	15.04	0.04

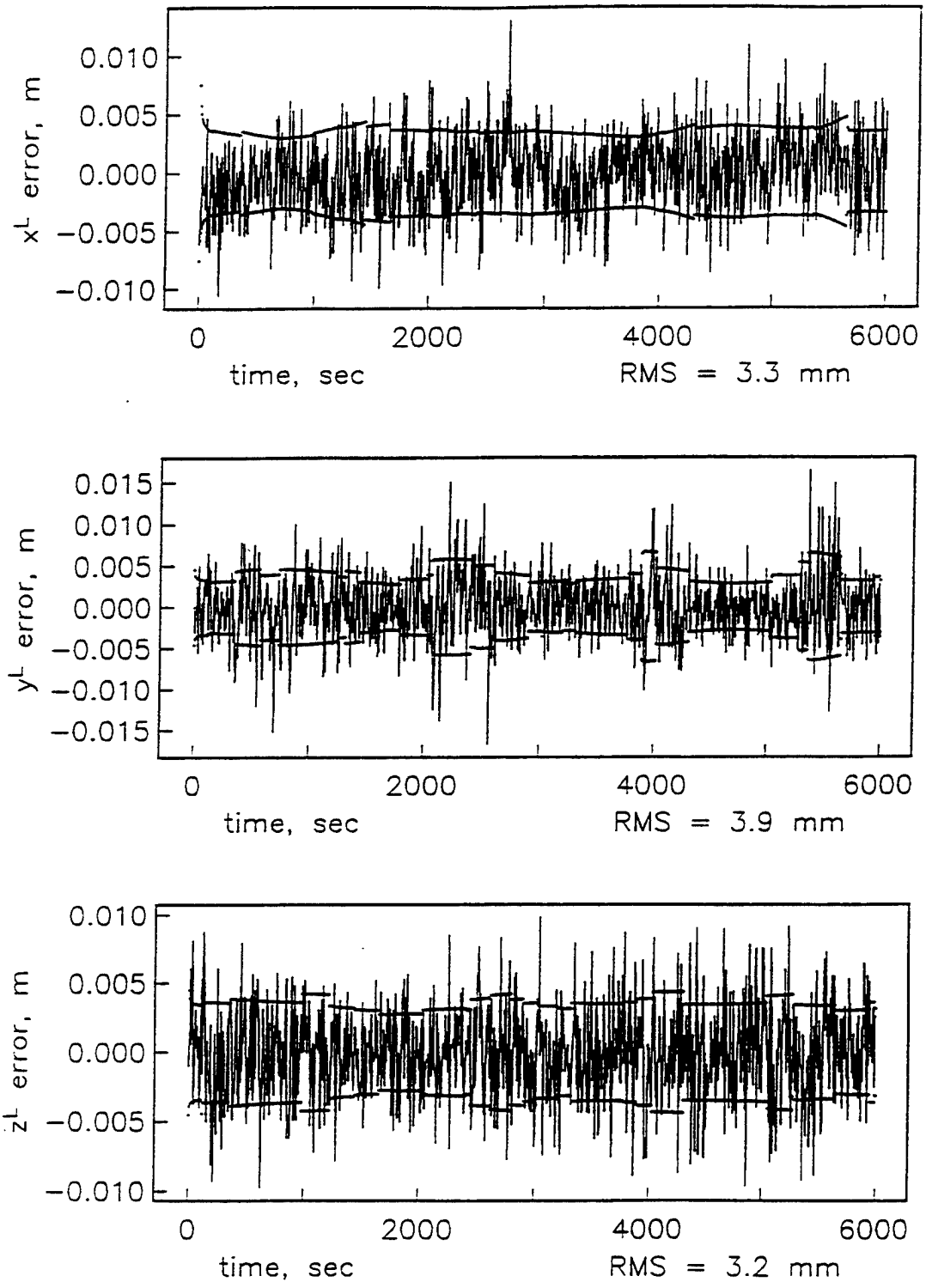

Figure 2.4. Local Baseline 3 Estimation Errors - Simulated Data

2.9 High Accuracy Attitude Estimation Algorithm

With accurate knowledge of the baseline vectors, line biases, and integers we can now proceed to the task of attitude estimation. An extended Kalman filter based on Lefferts, et al. [1982] is used to estimate the local to body quaternion, inertial angular velocity of the body, and line biases. Although much of this algorithm remains unchanged, we have made a change in calculating the dynamics matrix, **F**, due to an error discovered in the previous implementation [*Axelrad et al.*, 1993]. q_4 was used directly in the computation of **F**, even though q_4 was not in the state vector. Formulating the dynamics matrix in this way caused the filter to become unstable when q_4 was close to zero. However, we found that writing **F** in terms of the correction, $\delta\mathbf{q}$, took care of this problem. Thus, if the state vector is given as

$$\mathbf{x} = \left[\delta q_1 \quad \delta q_2 \quad \delta q_3 \mid \delta\omega_{I1} \quad \delta\omega_{I2} \quad \delta\omega_{I3} \mid \delta\beta_1 \quad \delta\beta_2 \quad \delta\beta_3\right]^{\mathrm{T}} \tag{2.23}$$

then the dynamics matrix, **F**, is given as

$$\mathbf{F} = \left[\begin{array}{c|c|c} \dfrac{\partial(\delta\dot{\bar{q}})}{\partial(\delta\bar{q})} & \dfrac{\partial(\delta\dot{\bar{q}})}{\partial(\delta\omega_I)} & \mathbf{0} \\ \hline \dfrac{\partial(\delta\dot{\omega}_I)}{\partial(\delta\bar{q})} & \dfrac{\partial(\delta\dot{\omega}_I)}{\partial(\delta\omega_I)} & \mathbf{0} \\ \hline \mathbf{0} & \mathbf{0} & \mathbf{0} \end{array}\right]. \tag{2.24}$$

Before proceeding with the derivation of **F**, we note the following properties:

1. The quaternion inverse is given by $\mathbf{q}^{-1} = \left[-q_1 \quad -q_2 \quad -q_3 \quad q_4\right]^{\mathrm{T}}$.
2. The distribution of the inverse is given by: $(\mathbf{p}\otimes\mathbf{q})^{-1} = \mathbf{q}^{-1}\otimes\mathbf{p}^{-1}$.
3. If $\underline{\omega} \equiv \left[\omega_1 \quad \omega_2 \quad \omega_3 \quad 0\right]^{\mathrm{T}}$, then the quaternion equation of motion is $\dot{\mathbf{q}} = \frac{1}{2}\underline{\omega}\otimes\mathbf{q}$.
4. Combining properties 2 and 3 leads to $\dot{\mathbf{q}}^{-1} = -\frac{1}{2}\mathbf{q}^{-1}\otimes\underline{\omega}$.

Now, Lefferts, et at. [1982] defines the correction quaternion and angular velocity as

$$\delta\mathbf{q} = \mathbf{q}\otimes\hat{\mathbf{q}}^{-1} \tag{2.25}$$

and $$\delta\omega = \omega - \hat{\omega}$$

where $\mathbf{q}$ and ω are the true values and $\hat{\mathbf{q}}$ and $\hat{\omega}$ are the estimated values. It follows that

$$\begin{aligned} \delta\dot{\mathbf{q}} &= \dot{\mathbf{q}}\otimes\hat{\mathbf{q}}^{-1} + \mathbf{q}\otimes\dot{\hat{\mathbf{q}}}^{-1} \\ \delta\dot{\mathbf{q}} &= \tfrac{1}{2}\underline{\omega}\otimes\mathbf{q}\otimes\hat{\mathbf{q}}^{-1} - \tfrac{1}{2}\mathbf{q}\otimes\hat{\mathbf{q}}^{-1}\otimes\underline{\hat{\omega}} \\ \delta\dot{\mathbf{q}} &= \tfrac{1}{2}(\underline{\omega}\otimes\delta\mathbf{q} - \delta\mathbf{q}\otimes\underline{\hat{\omega}}) \end{aligned} \tag{2.26}$$

We can rewrite the above equation as

$$\delta\dot{\mathbf{q}} = \tfrac{1}{2}(\hat{\underline{\omega}} \otimes \delta\mathbf{q} - \delta\mathbf{q} \otimes \hat{\underline{\omega}} + \delta\underline{\omega} \otimes \delta\mathbf{q}) \tag{2.27}$$

Neglecting second order terms

$$\delta\underline{\omega} \otimes \delta\mathbf{q} = \delta\underline{\omega} + 0(|\delta\omega|\ |\delta\bar{q}|) \tag{2.28}$$

and

$$\tfrac{1}{2}(\hat{\underline{\omega}} \otimes \delta\mathbf{q} - \delta\mathbf{q} \otimes \hat{\underline{\omega}}) = \delta\bar{q} \times \omega = \omega^{\times}\delta\bar{q} \tag{2.29}$$

where $\delta\bar{q}$ denotes $[\delta q_1 \quad \delta q_2 \quad \delta q_3]^{\mathrm{T}}$ and $\omega^{\times}$ denotes the cross product matrix associated with the elements of ω. Thus, substituting Equation 2.28 and 2.29 into Equation 2.27 gives

$$\delta\dot{\bar{q}} = \hat{\omega}^{\times}\delta\bar{q} + \tfrac{1}{2}\delta\omega \tag{2.30}$$

for the kinematic equations of motion. If the above quaternion represents the local to body transformation, then ω must represent the angular velocity of the body with respect to the local frame. Generally, we know the inertial angular velocity of the body frame in body coordinates, ω_I^B, and the inertial angular velocity of the local frame in local coordinates, ω_L^L. Then $\hat{\omega}$ is calculated by

$$\hat{\omega}^B = \omega_I^B - \mathbf{C}(\hat{\mathbf{q}})\omega_L^L. \tag{2.31}$$

Now the partials for the dynamics matrix are

$$\begin{aligned} \frac{\partial(\delta\dot{\bar{q}})}{\partial(\delta\bar{q})} &= \hat{\omega}^{\times} \\ \frac{\partial(\delta\dot{\bar{q}})}{\partial(\delta\omega_I)} &= \tfrac{1}{2}\mathbf{1} \end{aligned} \tag{2.32}$$

where 1 is a 3 by 3 identity matrix.

The linearized dynamic equations of motion for $\delta\omega_I$ can be written as follows,

$$\begin{aligned} \delta\dot{\omega}_{I1} &= \left(K_1\omega_3 - \frac{h}{I_1}\right)\delta\omega_{I2} + K_1\omega_2\delta\omega_{I3} + \left(\frac{\partial N_1}{\partial\delta\bar{q}}\right)^{\mathrm{T}}\delta\bar{q}/I_1 \\ \delta\dot{\omega}_{I2} &= \left(K_2\omega_3 + \frac{h}{I_2}\right)\delta\omega_{I1} + K_2\omega_1\delta\omega_{I3} + \left(\frac{\partial N_2}{\partial\delta\bar{q}}\right)^{\mathrm{T}}\delta\bar{q}/I_2 \\ \delta\dot{\omega}_{I3} &= K_3\omega_{I2}\delta\omega_{I1} + K_3\omega_{I1}\delta\omega_{I2} + \left(\frac{\partial N_3}{\partial\delta\bar{q}}\right)^{\mathrm{T}}\delta\bar{q}/I_3 \end{aligned} \tag{2.33}$$

where **N** is the gravity gradient torque, h is the angular momentum of the gyrostat wheel, (h = 0 for RADCAL), **I** is the inertia tensor expressed in body coordinates as follows,

$$\mathbf{I}=\begin{bmatrix} I_1 & 0 & 0 \\ 0 & I_2 & 0 \\ 0 & 0 & I_3 \end{bmatrix}, \tag{2.34}$$

and $$K_1=\frac{I_2-I_3}{I_1} \qquad K_2=\frac{I_3-I_1}{I_2} \qquad K_3=\frac{I_1-I_2}{I_3}. \tag{2.35}$$

N is not dependent on $\delta\omega_I$, so taking the partials of Equation 2.33 with respect to $\delta\omega_I$ gives

$$\frac{\partial(\delta\dot{\omega}_I)}{\partial(\delta\omega_I)}=\begin{bmatrix} 0 & K_1\omega_{I3}-h/I_1 & K_1\omega_{I2} \\ K_2\omega_{I2}+h/I_2 & 0 & K_2\omega_{I1} \\ K_3\omega_{I2} & K_3\omega_{I1} & 0 \end{bmatrix}. \tag{2.36}$$

Now the gravity gradient torque, **N**, is given by

$$\mathbf{N}=3\Omega^2[\ {}^B\hat{\mathbf{C}}^L\ \mathbf{r}^L\times\mathbf{I}\ {}^B\hat{\mathbf{C}}^L\ \mathbf{r}^L\ ] \tag{2.37}$$

where $\mathbf{r}^L$ is the satellite's radial direction vector and Ω is the orbit rate of the satellite. Expanding the transformation matrix

$${}^B\hat{\mathbf{C}}^L=(1+2\delta\bar{q}^{\times})\ {}^B\mathbf{C}_0^L \tag{2.38}$$

and setting

$${}^B\mathbf{C}_0^L\ \mathbf{r}^L=\mathbf{r}_0^B=\mathbf{r} \tag{2.39}$$

we can now write

$$\begin{aligned}\mathbf{N}&=3\Omega^2[(1+2\delta\bar{q}^{\times})\mathbf{r}\times\mathbf{I}(1+2\delta\bar{q}^{\times})\mathbf{r}] \\ \mathbf{N}&=3\Omega^2[(\mathbf{r}\times\mathbf{I}\mathbf{r}+\mathbf{r}\times2\mathbf{I}\delta\bar{q}^{\times}\mathbf{r}+2\delta\bar{q}^{\times}\mathbf{r}\times\mathbf{I}\mathbf{r}+O(\delta\bar{q}^2)]\end{aligned} \tag{2.40}$$

After some algebraic manipulation and neglecting second order terms, the gravity gradient torque becomes

$$\mathbf{N}=3\Omega^2\{\mathbf{r}\times\mathbf{I}\mathbf{r}+2[\mathbf{r}^{\times}\mathbf{I}\mathbf{r}^{\times}-(\mathbf{I}\mathbf{r})^{\times}\mathbf{r}^{\times}]\delta\bar{q}\}. \tag{2.41}$$

Substituting into Equation 2.33 and taking the partial with respect to the correction quaternion gives

$$\frac{\partial(\delta\omega_I)}{\partial(\delta\bar{q})}=6\Omega^2[\mathbf{r}^{\times}\mathbf{I}\mathbf{r}^{\times}-(\mathbf{I}\mathbf{r})^{\times}\mathbf{r}^{\times}]\mathbf{I}^{-1}. \tag{2.42}$$

Expanding the above equation into its matrix elements gives

$$\frac{\partial(\delta\dot{\omega}_I)}{\partial(\delta\bar{q})} = 6\Omega^2 \begin{bmatrix} K_1(r_2^2 - r_3^2) & -K_1 r_1 r_2 & K_1 r_1 r_3 \\ K_2 r_1 r_2 & K_2(r_3^2 - r_1^2) & -K_2 r_2 r_3 \\ -K_3 r_1 r_3 & K_3 r_2 r_3 & K_3(r_1^2 - r_2^2) \end{bmatrix}. \quad (2.43)$$

Equations 2.32, 2.36, and 2.43 are all of the elements needed to describe the dynamics matrix and in turn derive the state transition matrix.

Another addition to the high accuracy attitude estimation algorithm is the ability to handle a roving master. As in the initial attitude determination stage (Equation 2.15), the line biases are modified so they all refer to the same *pseudo-master*.

2.10 High Accuracy Attitude Estimation Results

First, the simulated data was used to demonstrate the high accuracy attitude estimation algorithm. The initial quaternion was supplied by the initial attitude determination algorithm. The baselines and line biases were supplied by baseline estimation algorithm. Since a lot of the ground work has already been done, the filter works without difficulty estimating the attitude to within 0.2 degrees. Figure 2.5 shows the attitude filter errors for the quaternion states along with their covariance bounds. The magnitude of the errors for q_1 vary with a once per orbit frequency. This is probably due to changes in visibility geometry as the satellite orbits. The root-mean-square (RMS) of the errors in each state are summarized in Table 2.5 where the quaternion errors have been converted to yaw, roll, and pitch errors.

Table 2.5. RMS of Attitude Estimation Errors - Simulated Data

RMS					
Euler Angles (deg)		Ang. Velocity deg/min		Line Biases (cycles)	
yaw	0.19	ω_1	0.221	β_1	$2.1\text{x}10^{-3}$
roll	0.18	ω_2	0.107	β_2	$2.7\text{x}10^{-3}$
pitch	0.17	ω_3	0.110	β_3	$2.7\text{x}10^{-3}$

The RADCAL data downloaded from the TECNET was also processed with this algorithm. Figure 2.6 shows the estimated attitude for RADCAL on 20 March 1994. These results are qualitatively similar to those reported in Lightsey, et al. [1994] for a different data set. Furthermore, the attitude motion shown here agrees with the motion produced by the simulation. Unfortunately, there is not external "truth" reference for the RADCAL attitude. The 1-σ uncertainties reported by the Kalman filter are less than 0.2 deg for yaw, pitch, and roll angles. The 1-σ uncertainty in each of the angular velocities is less than 0.3 deg/min.

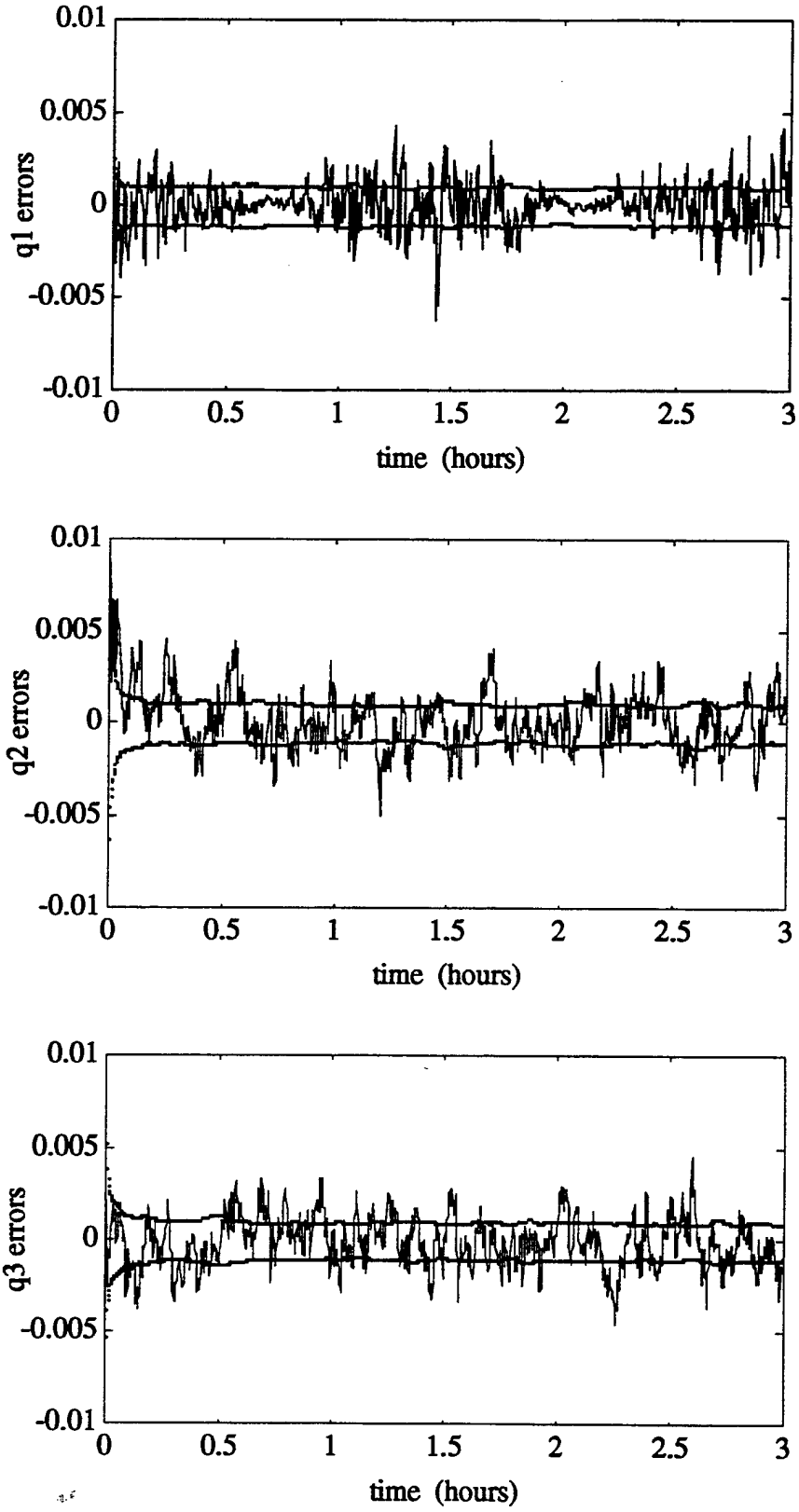

Figure 2.5. High Accuracy Attitude Filter Errors - Simulated Data

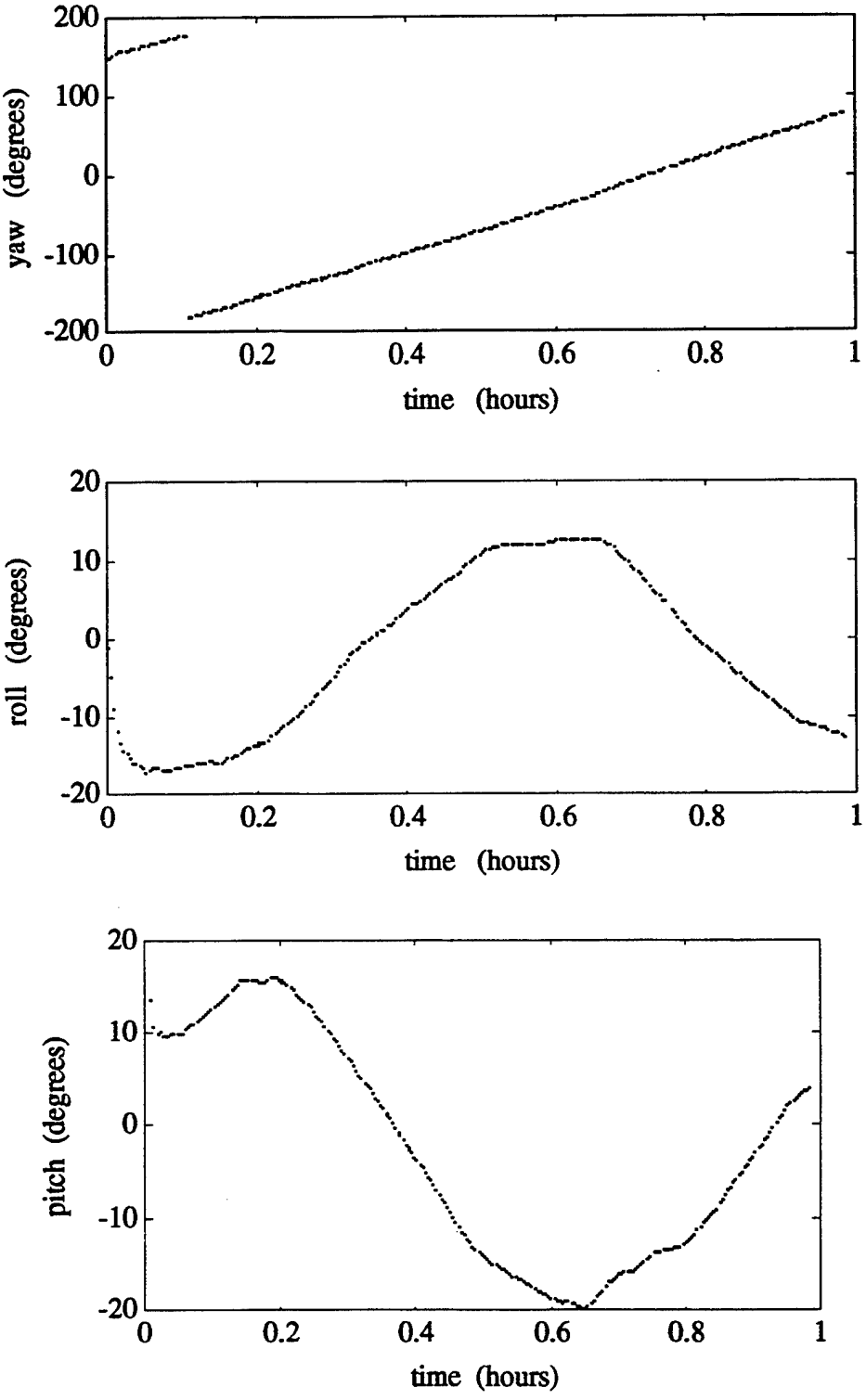

Figure 2.6. High Accuracy Attitude Filter Results - RADCAL Data

2.11 Future Work

Now that we have finally been able to process actual data from RADCAL with success, the next step is to verify our results with another interval of data. Many lessons have been learned in getting to this point which should make further testing go more smoothly. Eventually, we hope to process actual data from another satellite as well.

Currently, the initial attitude determination algorithm needs some manual intervention. Only measurements collected from specific GPS satellite/master pairs are used. The raw data must be examined to choose an appropriate span of data and the corresponding satellite/master pairs. The data must also be checked for cycles slips. We plan to automate this data selection process. In addition, a rigorous method of selecting initial conditions and testing for convergence to a consistent solution is also needed. Furthermore, studying the optimal number of GPS satellites to process would be very useful here. More satellites provides more observations but also introduce more states to estimate.

The next step for the baseline estimation filter is to add the capability to handle data from a roving master. Developing a more generic description of the body frame is also a goal. The approach used thus far requires data to be available from certain baselines. Due to shadowing or vehicle maneuvers, this baseline may not always be available.

In this work, we ran the baseline and attitude estimators in two separate passes. For real time applications we plan to investigate running the two in parallel to determine how best to provide baseline updates to the attitude filter. Two important issues are of course filter stability and computational load. We will also continue to investigate the robustness of both estimators to individual measurement outages, complete satellite outages, and total blockage of one or more antennas.

3. Multipath Mitigation

Christopher J. Comp

3.0 Introduction

The objective of this project was to improve the accuracy of GPS attitude determination by reducing multipath error. In an ideal situation, present attitude determination systems have achieved the state where carrier phase multipath and receiver noise remain as the major sources of error.

Multipath is the corruption of the direct GPS signal by one or more signals reflected from the local surroundings. In the case of carrier phase multipath, the receiver phase locked loop (PLL) tracks the composite signal which comprises a direct component, one or more reflected components, and receiver induced noise. As the GPS satellite moves across the antenna field of view, or as the antenna moves with respect to the reflectors, the phases of the multipath signals change relative to the direct. This is generally depicted with a phasor diagram such as that in Figure 3.1 for a single multipath signal. The axes correspond to the in-phase (I) and quadrature (Q) signal components.

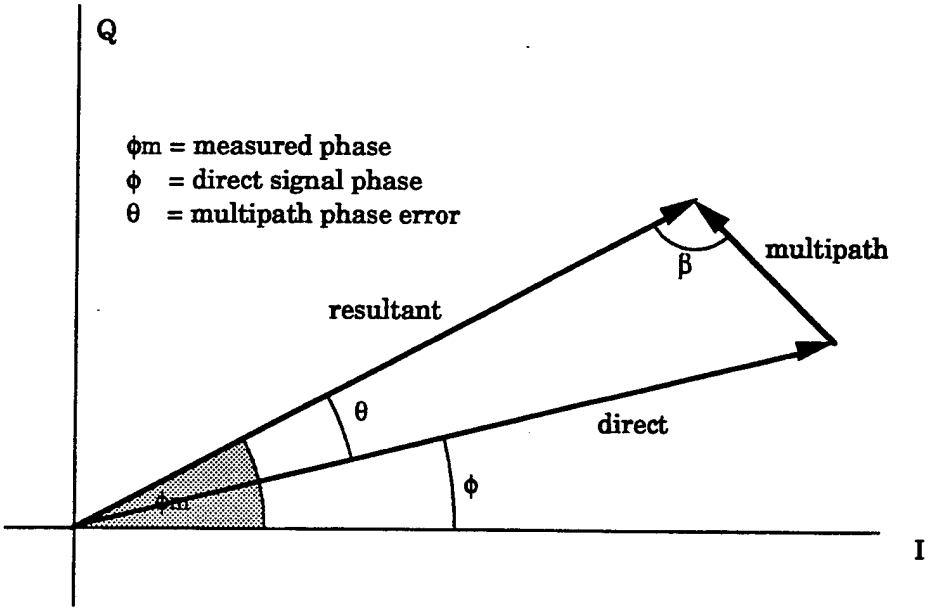

Figure 3.1. Phasor diagram depicting the relationship between the resultant, direct, and multipath signals.

The receiver PLL tracks the vector sum of the direct and multipath signals producing a phase measurement of ϕ_m. The angle θ represents the difference between this measurement and the true phase of the direct signal, ϕ. In the absence of PLL tracking errors, θ is due entirely to multipath.

The amplitudes of the direct, multipath, and resultant signals, are represented by the lengths of the phasors in Figure 3.1. The amplitude of the resultant signal is reported by a

GPS receiver in the form of a signal to noise ratio (SNR) which is an indication of the magnitude of the recovered carrier signal at each antenna.

Any motion due to the GPS satellites, the receiving antenna, or the source of the multipath signal, causes a change in the angle between the direct and multipath phasors. This in turn causes oscillations in both the measured phase and in the amplitude of the resultant signal. If the amplitudes of both the direct and multipath components are constant over the period of interest, the changes in amplitude of the resultant phasor give an indication of the multipath error angle, θ. The variations of the resultant amplitude are manifested as a sinusoidal characteristic in the SNR, similar to its phase counterpart.

3.1 Methodology

Multipath error reduction can be approached in two ways: rejection and correction. Because multipath signals often approach the antenna at low elevation angles, a narrow beam antenna will reject the incoming multipath. GPS multipath has been discussed extensively in the literature [c.f. *Braasch*, 1994; *Braasch and van Graas*, 1992; *Cohen and Parkinson*, 1991; *Counselman and Gourevitch*, 1981; *Georgiadou and Kleusberg*, 1988; *Greenspan et al.*, 1982, *Sennot and Pietraszewski*, 1987; *van Nee*, 1992, 1994].

Several schemes have been suggested for carrier multipath correction. Georgiadou and Kleusberg [1988] developed a model for the error that depended on the satellite elevation, and reflectivity and proximity of the reflector. Cohen and Parkinson [1991] created a spatial map of corrections to be applied based on satellite elevation and azimuth and the local surroundings. In this case the corrections were computed by fitting spherical harmonics to approximately 12 hours of phase data. We investigate a new approach. If the multipath is identifiable in the received SNR, a correction may be derived. The techniques shall be described in detail in the following two subsections.

3.1.1 Multipath Rejection with Narrow Beam Antennas

Typical GPS attitude determination systems employ the standard microstrip patch type of antenna. While this antenna has a wide and uniform gain pattern for good satellite visibility, it is more susceptible to multipath than a narrow beamwidth antenna. If a narrow beamwidth antenna has its boresight pointed toward the satellite, it will attenuate reflections that approach at low elevation angles. The narrow beamwidth gain pattern tends to reject the multipath, however the degree of rejection needs to be quantified.

It is desired to test the multipath rejection performance of wide and narrow beamwidth antennas. This can be done by comparing the amount of multipath present in the differential phase and SNR measurements. The multipath should be fully observable in the data collected with the wide beam antennas. The data collected with the narrow beam antennas should show some multipath but at reduced strength. This is because the low elevation multipath approaches the antenna from a direction near the edge or outside its beamwidth.

An antenna has a gain pattern dictating how an incoming signal is amplified or attenuated depending on its direction of incidence. The shape of the gain pattern depends on the type of the antenna, i.e. microstrip patch or helical, and on the relative dimensions of the antenna. The gain pattern is usually described by a gain map in elevation and azimuth, where the gain at any point is normalized with respect to the maximum gain along the antenna boresight. Ignoring azimuthal variations, the gain pattern is usually viewed as a cross section of the upper hemisphere of the antenna, thereby showing gain versus elevation above the horizontal plane. The antenna beamwidth is defined as the angular width between the half power points (-3 dB), and serves as a gauge on the extent of the field of view.

The two types of antennas used in the experiments were a wide beam microstrip patch antenna, and a narrow beam helical antenna placed within a parabolic bowl (called the helibowl). The antennas were tested in the anechoic chamber located in the microwave transmission laboratory at the University of Colorado. The tests were conducted February 18, 1994. The antenna was mounted on a platform at one end of the chamber facing horizontally towards the opposite side. An RF source transmitting a -10 dBW power sine wave at the GPS L1 frequency was located at the other end of the chamber. The platform was slaved from -90 deg to +90 deg in 6 deg increments relative to the RF source. At the 6 deg points, the power received through the antenna was measured. The resulting cross section of the antenna gain patterns are shown in Figure 3.2. From the gain patterns the beamwidths were estimated as 102 deg and 66 deg for the patch and helibowl antennas, respectively. The dip in the center of the patch gain pattern is a result of a groundplane, a square aluminum sheet mounted to the base of the antenna.

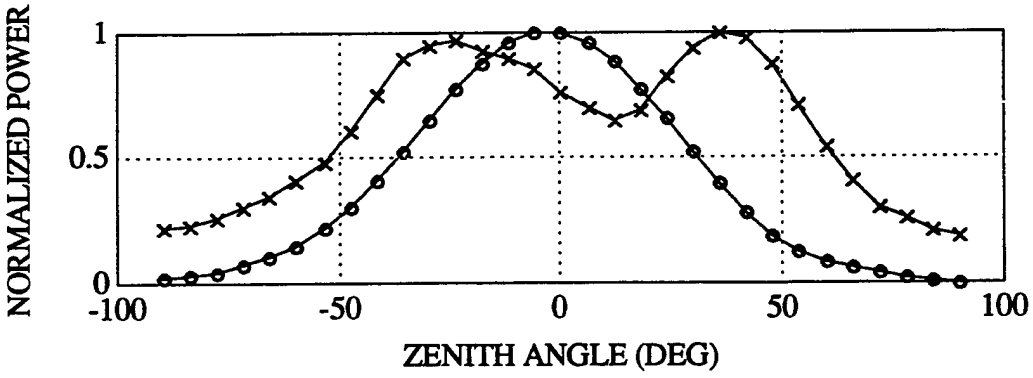

Figure 3.2 Antenna Gain Patterns.

"x" -wide beam (patch) and "o" narrow (helibowl) beam antennas.

3.1.2 Multipath Correction Using the SNR

The multipath induced amplitude variations of the resultant carrier can be observed in the SNR. We have developed an algorithm to use the SNR data to create a profile of the multipath induced differential phase errors. The two antennas that comprise a differential baseline possess unique SNR histories. The SNR multipath fluctuations beat against one

another to form the multipath signature in the differential phase data. The SNR data had large trends removed prior to analysis to account for satellite motion. A satellite elevation time series was derived from the GPS almanac. Using the antenna gain pattern, the elevation angles were mapped into normalized signal power, and converted to SNR amplitude. The measured resultant SNR is equal to the sum of the direct and multipath contributions:

$$SNR_{resultant} = SNR_{direct} + SNR_{multipath} \tag{3.1}$$

Without multipath, the receiver would observe the direct signal moving through the antenna gain pattern. Hence, subtracting the SNR trend computed with the satellite elevation and gain pattern corresponds to removal of the direct portion of the SNR. What remains is the SNR multipath.

The maxima and minima of the multipath fluctuations in the SNR correspond to the direct and multipath phasors pointing in the same direction or opposite directions, respectively. Referring back to Figure 3.1, θ is the angle between the direct and resultant phasors, and β is the angle between the multipath and resultant phasors. A peak in the SNR multipath signifies a maximum resultant amplitude, which occurs when $\theta = \beta = 0$ deg. Conversely, a valley in the SNR multipath signifies a minimum resultant amplitude, which occurs when $\theta = 0$ deg, $\beta = 180$ deg.

The quantity β is a function of the frequency and offset of the cyclic SNR multipath, represented by the formula:

$$\beta(t_i) = \omega\, t_i + \phi \tag{3.2}$$

where ω is the frequency of the multipath observed in the SNR, ϕ is the offset, and t_i is the measurement time. Assuming several multipath frequencies exist, the predominant frequencies are identified by spectral analysis of the SNR data. This is presently done graphically with the Lomb periodogram. The Lomb algorithm is discussed in Press, et al. [1992].

The amplitude and offset of the SNR multipath constituents are estimated by least squares. Modeling each constituent as a sinusoid, the normal equation is:

$$\begin{bmatrix} \cos(\omega_1 t_i) & -\sin(\omega_1 t_i) & \cdots & \cos(\omega_n t_i) & -\sin(\omega_n t_i) \\ \vdots & \vdots & \vdots & \vdots & \vdots \end{bmatrix} \begin{bmatrix} A_1 \cos\phi_1 \\ A_1 \sin\phi_1 \\ \vdots \\ A_n \cos\phi_n \\ A_n \sin\phi_n \end{bmatrix} = \begin{bmatrix} SNR(t_i) \\ \vdots \end{bmatrix} \tag{3.3}$$

where n is the number of multipath constituents. Both the matrix containing sinusoidal arguments and the SNR data vector are accumulated in columnar fashion for the time of interest.

The multipath phase error θ can be constructed from the phasor geometry. Applying the law of sines to the phasor geometry leads to an expression for the angle between the direct and resultant phasors. The multipath error present in the carrier phase measurement at antenna j, for the constituent k, and the time t_i, after some manipulation, is given as:

$$\theta_{jk}(t_i) = \arctan\left[\frac{\sin(\beta_{jk}(t_i))}{\frac{R_j(t_i)}{mp_{jk}} + \cos(\beta_{jk}(t_i))}\right] \tag{3.4}$$

where R_j is the resultant phasor amplitude at antenna j for time t_i, and mp_{jk} is the constant multipath phasor amplitude at antenna j for multipath constituent k. The resultant amplitude R_j is simply the SNR value at antenna j for each measurement time. The multipath amplitude mp_{jk} is the value A from the least squares solution of Equation 3.2. The composite multipath error at antenna j is a linear combination of the constituent errors:

$$\theta_j(t_i) = \sum_{k=1}^{n} \theta_{jk}(t_i) \tag{3.5}$$

The θ_j sequence is essentially a profile of the phase multipath derived from the SNR data. This estimate may be subtracted from the phase data to correct for the multipath. The direction of rotation of the multipath phasor determines the sign of the amplitude of the multipath error. The spectral estimation procedure leaves the sign of the SNR multipath frequency ambiguous. All signs are initially assumed positive and the multipath error is computed. The multipath constituents are then fit to the differential phase data using least squares to solve for the proper sign. The normal equation for this procedure is provided below:

$$\begin{bmatrix} \theta_{11}(t_i) & \cdots & \theta_{1n}(t_i) & \theta_{21}(t_i) & \cdots & \theta_{21}(t_i) \\ \vdots & & \vdots & \vdots & & \vdots \end{bmatrix} \begin{bmatrix} s_{11} \\ \vdots \\ s_{1n} \\ s_{21} \\ \vdots \\ s_{2n} \end{bmatrix} = \begin{bmatrix} dphs(t_i) \\ \vdots \end{bmatrix} \tag{3.6}$$

The s_{1i}, and s_{2i}'s are determined as real numbers which should be close to ± 1. The values are set to ± 1 and used to scale the appropriate multipath profile. The multipath profiles may be differenced between two antennas corresponding to a differential phase measurement. For example, to compute the multipath in the differential phase between the master and number 2 slave antennas for time t_i, the correct value would be $(\theta_{master} - \theta_2)(t_i)$.

3.2 March 1994 Experiments

3.2.1 Description

The motivation for this set of experiments was to test the multipath rejection and correction techniques described in Section 3.1.2 for a static platform. The experiments were conducted March 1-6, 1994. The location was a remote site 10 miles North of Boulder that was nearly void of naturally occurring multipath. The object of the tests was to create the simplest multipath interference possible - a single multipath ray of relatively constant magnitude. This case would provide the best opportunity for successful application of the proposed multipath mitigation techniques.

Preliminary experiments in December of 1993 provided qualitative insight on what kind of multipath rejecting performance to expect from the narrow beam helibowl antennas. The experience brought forth the following improvements for the March 1994 experiments:

- Intentional multipath injection
- Consistent antenna types and orientations
- Diurnal repeatability testing with control
- Record SNR data

The Trimble TANS Vector receiver was used in conjunction with two Trimble patch antennas and two helibowl antennas. This provided both a patch and a helibowl differential baseline. The antennas were mounted on a rigid support structure and were kept oriented in the same direction with respect to each other. The receiver was controlled with a GRiD computer.

Differential phase and SNR data were collected at an average interval of 1.5 seconds. Due to receiver hardware and computer communication problems at the time, the data logging rate was not constant. This did not pose a problem in the analysis however, and has since been corrected. Deliberate multipath injection was accomplished by two methods: known placement of reflectors, and electronic retransmission of the GPS signal. In both cases the distance to the multipath source was in the neighborhood of two meters, which is equivalent to what is expected on a spacecraft.

In the first scenario, aluminum foil reflectors were placed at known distances and orientations from the Vector antenna array. The placement was planned so that the GPS signal transmitted from a known elevation and azimuth would reflect towards the array. The antenna array was directed towards a low satellite. Two reflectors were located symmetrically on either side of the array at a distance of 2.1 meters in the direction of the satellite, and canted outwards at an angle of 45 deg.

The electronic multipath injection, on the other hand, was performed using a satellite near zenith. As the satellite passed overhead, a high gain helical antenna would collect the GPS signal simultaneously with the Vector array. The signal was sent through 50 feet of RG-214 cable, and retransmitted through another helical antenna towards the array. The retransmitting antenna was placed 1.7 meters horizontally and 2.1 meters vertically from the array, causing the multipath to approach at an elevation angle of 60 deg. This angle was chosen because it lies on the fringe of the helibowl beamwidth. The signal power balance was

accounted for by considering the gain of the helical collection and retransmitting antennas, power loss from the cable, and free space loss from the retransmitting antenna to the array. The received power of the multipath signal relative to the direct could be adjusted with a variable step RF attenuator. The multipath relative power was set to -10 dB, a typical value due to the reflectivities associated with a spacecraft environment.

Table 3.1 Multipath Injection Power Budget

Component	Gain/Loss (dB)
Helical Receive Antenna	+17
Low Noise Amplifier	+30
50 ft RG-214 Cable	-6
Variable Attenuator	-14
Helical Retransmit Antenna	+7
Free Space Loss @2.4 m	-44
Net Multipath Power	-10

The antennas comprising the patch and helibowl baselines were consistent in gain pattern throughout the experiment. The antennas were tested in the anechoic chamber to check consistency of gain patterns. The antennas were fixed to the support structure such that their orientations were kept the same throughout the experiment. In the differential mode, this compensated for small azimuthal variations in gain patterns and antenna phase center motion. Each test was conducted for a minimum of three consecutive days to achieve diurnal repeatability. Due to the geometry dependence of multipath, the same error is observed and shifted forward 4 minutes per day. In addition to the three days, a set of data with no intentional multipath was collected as a control. The multipath correction algorithm was implemented in MATLAB. The Lomb algorithm was coded in C, and the output ported into MATLAB. The analysis programs were executed on a Sparc Station 2.

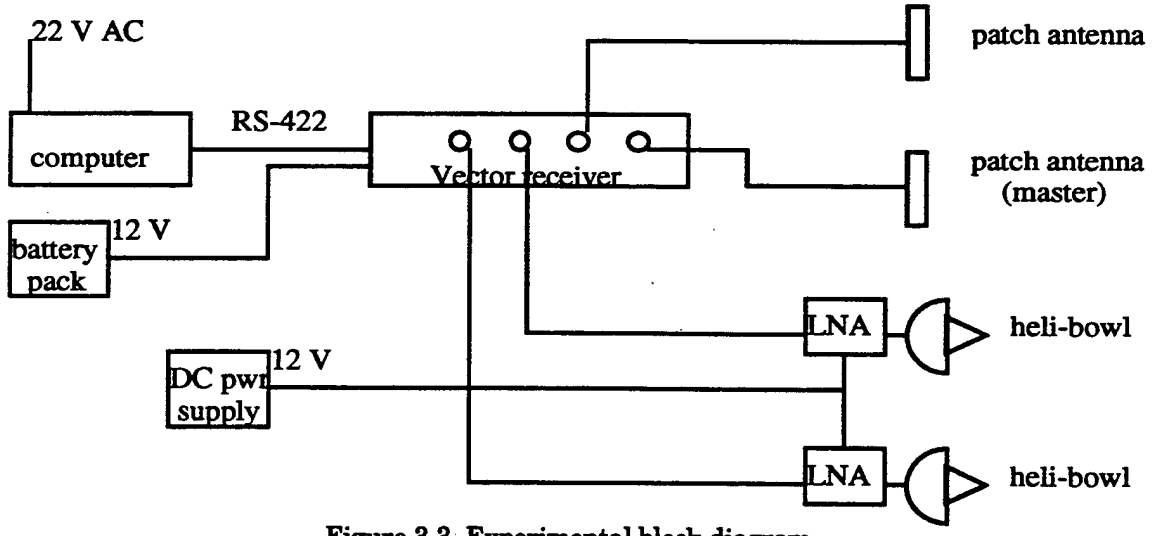

Figure 3.3 Experimental block diagram.

3.2.2 Procedure

An experimental setup block diagram is provided in Figure 3.3. The patch antennas were connected to the master and number 2 slave ports. The helibowl antennas were connected to the number 1 and 3 slave ports. The helibowl antennas required low noise amplifiers to boost the signal to appropriate levels. Figure 3.4 shows the electronic multipath injection apparatus as it occurred in the field. At the far right is the high gain collection antenna. The retransmitting antenna is fixed to the table tripod at center. The receiver and antenna array is at the left. Figure 3.5 shows the reflective multipath injection apparatus. The idea was to imitate a spacecraft environment.

The experimental procedure listed below was executed each day of the test:

1. Antenna array statically positioned and pointing towards 85 deg elevation and 350 deg azimuth. Intentional multipath was electronically injected. Tracked PRN 29 for a duration of 90 minutes.
2. Antenna array statically positioned and pointing towards 30 deg elevation and 240 deg azimuth. No intentional multipath as a control. Tracked PRN 27 for a duration of 60 minutes.
3. Antenna array statically positioned and pointing towards 30 deg elevation and 270 deg azimuth. Intentional multipath was injected with reflectors. Tracked PRN 02 for a duration of 60 minutes.

The data processing procedure:

1. Load time-tagged differential phase and SNR data into MATLAB.
2. Remove satellite motion effects from differential phase and SNR data using Equation 3.1.
3. Select a differential baseline and time window.
4. Export SNR data for execution of Lomb periodogram. Import the product of the Lomb program which contain frequency and power information.
5. Plot the SNR multipath spectrum and input frequencies of predominant constituents.
6. Compute the SNR multipath amplitudes and offsets for the antennas and multipath constituents using the least squares solution to Equation 3.3.
7. Compute the β time series using Equation 3.2 for the antennas and multipath constituents..
8. Compute the θ time series using Equation 3.4 for the antennas and multipath constituents..
9. Determine the correct sign of the constituent frequencies using Equation 3.6.
10. Assemble the differential phase multipath profile using Equation 3.5 at each antenna and then difference.
11. Subtract the profile from the differential phase data.
12. Plot the results.

Figure 3.4. Photograph of electronic multipath injection apparatus.

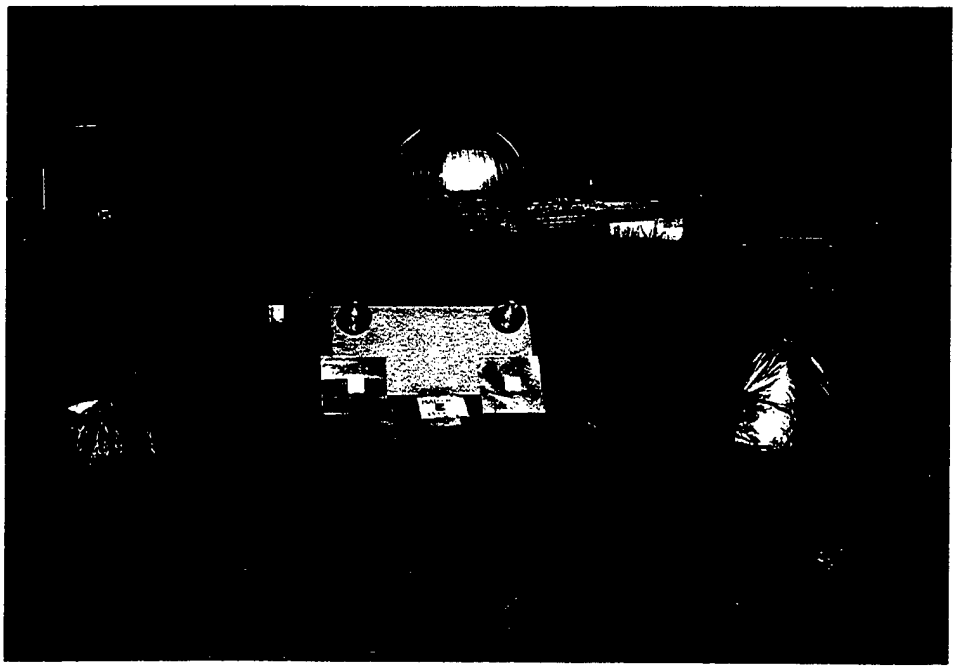

Figure 3.5. Photograph of reflective multipath injection apparatus.

3.2.3 Results

The differential phase and SNR data are shown in Figure 3.6 and Figure 3.7, respectively. This data was collected in the presence of deliberate electronic multipath on March 6. Recall that the satellite motion has been removed from the data as detailed in Section 3.1.2. The figures display the patch differential baseline data at the top, and the helibowl at the bottom. The horizontal axes are the time of day in units of hours. The vertical axes are the differential phase in units of millimeters for Figure 3.6, and the SNR in units of Trimble amplitude measurement units (AMU) for Figure 3.7. The AMU is the amplitude of the recovered carrier within the channel bandwidth. It is not measured in dB as is the commonly reported C/N_0 (in dB-Hz).

The differential phase multipath excursions in the patch baseline peaked at 6 millimeters. Those for the helibowl baseline peaked at 4 millimeters. The SNR multipath effects for the patch antennas peaked around 16 AMUs. Those for the helibowl antennas peaked around 8 AMUs. The narrow beam helibowls appeared to attenuate the multipath.

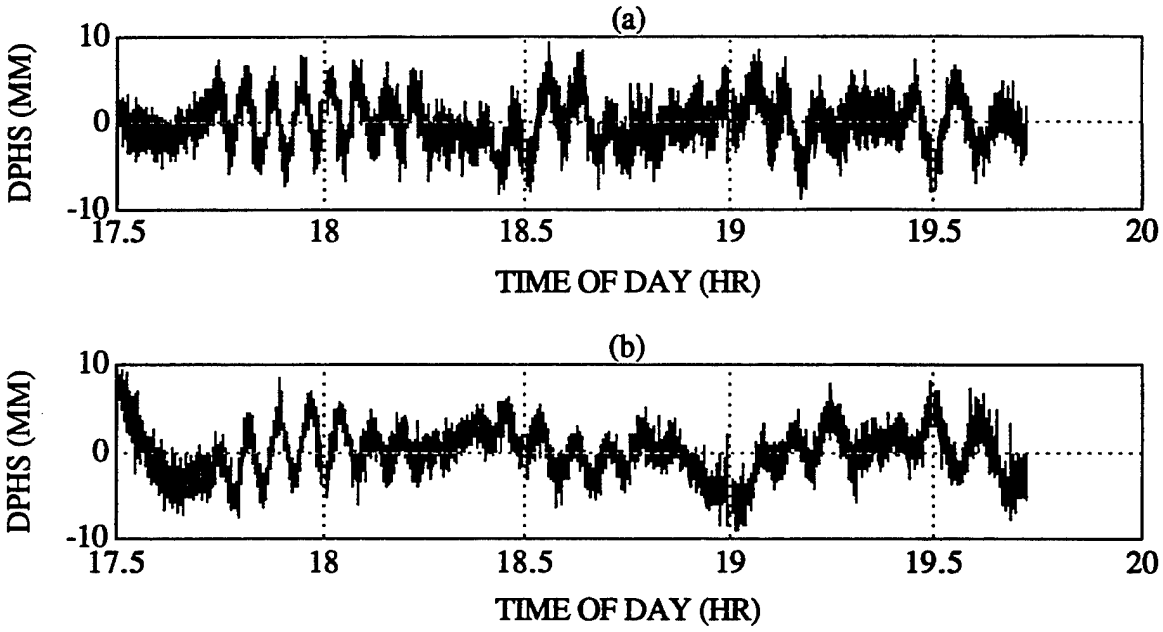

Figure 3.6. Differential phase data for patch (a) and helibowl (b) baselines. The data was collected March 6, 1994, during electronic multipath injection.

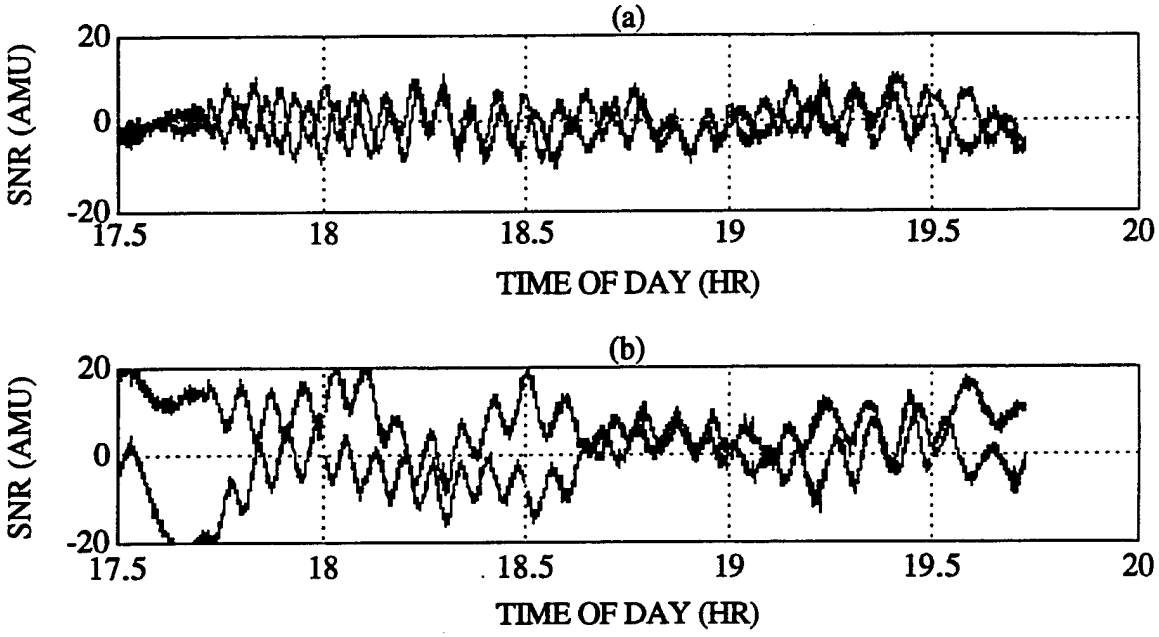

Figure 3.7. SNR data for patch (a) and helibowl (b) baselines.
The data was collected March 6, 1994, during electronic multipath injection.

Figure 3.8 illustrates differential phase data, accompanied by the SNR derived multipath profile. The data was taken using the patch antennas with deliberate electronic multipath on March 6. The horizontal axis is the time of day in units of hours, the vertical axis is the differential phase in units of millimeters. The multipath estimated with the SNR data, which is represented by the smooth line, closely tracks the differential phase multipath. This was the best result we achieved.

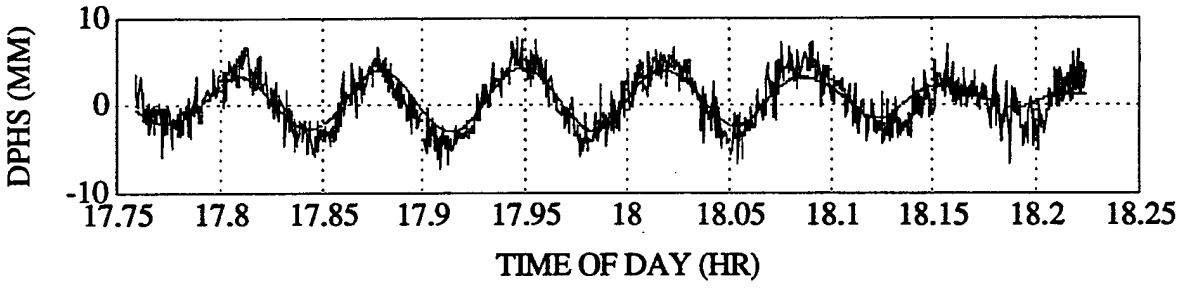

Figure 3.8. Differential phase data and multipath profile.
The data was collected March 6, 1994, during electronic multipath injection.

Figures 3.9 through 3.12 contain the multipath correction results. Again, these are for the patch baseline with electronic multipath on March 6. The horizontal axes are the time of day in units of hours, the vertical axes are the differential phases in units of millimeters. Each figure contains the differential phase in the top plot, and the differential phase after subtracting the SNR derived multipath in the bottom plot. Each figure represents a 30

minute section of data. Figures 3.9 through 3.12 collectively comprise the entire data set, except for several minutes at the beginning and end. Figure 3.9 exhibits the near elimination of multipath. The 6 millimeter excursions in the differential phase data have been reduced to 2 millimeters. The standard deviation was changed from 3.1 to 1.8 millimeters.

Less dramatic results are shown in Figures 3.10, 3.11, and 3.12. The average reduction of the differential phase multipath was 50%. The average compression of the standard deviations was 25%. The multipath corrections for the helibowl baseline followed the same trend.

The deliberate multipath injection by electronic means was very successful for the day of March 6. However, on the other days the multipath injection was only sporadic. We believe that this is due to a misalignment of the high gain antenna. For this reason, the results from the March 6 data have been presented exclusively. Processing of data segments from the other days containing multipath signatures produced results similar to those shown here.

We have not yet attempted to use SNR based multipath profiling on the data collected using the aluminum foil reflectors. An example of the differential phase and SNR data is shown in Figures 3.13 and 3.14. Notice that the noise level in both observables is much higher than the control or electronic multipath induction cases. We expect that this is due to the fluttering of the aluminum foil in the wind. This scenario is probably not applicable to the spacecraft environment but may have implications for ground based antennas. Therefore, we elected to postpone the evaluation of this data.

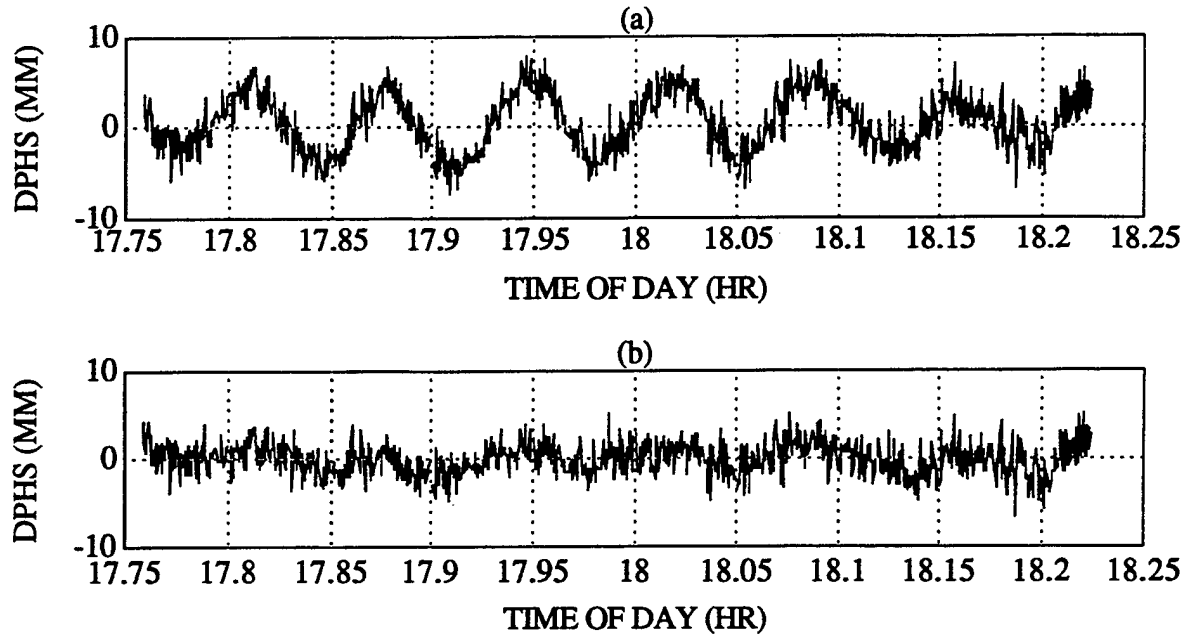

Figure 3.9. March 6, 1994 / Segment 1- Differential phase data
(a) no correction σ=3.1 mm, (b) with multipath correction σ=1.8 mm

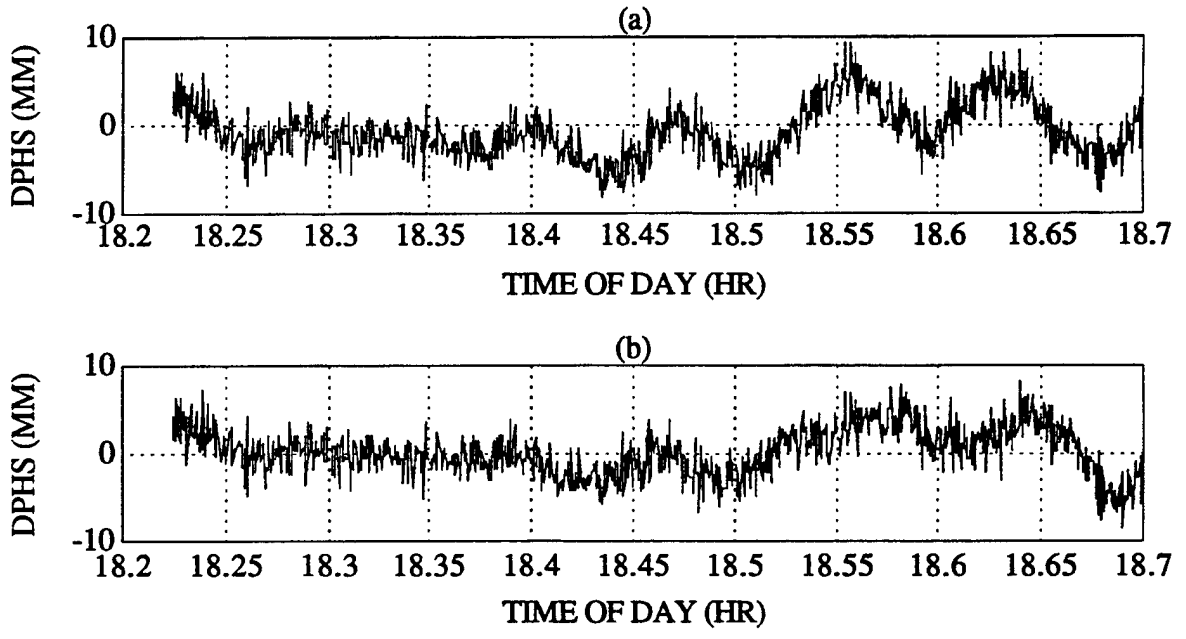

Figure 3.10. March 6, 1994 / Segment 2- Differential phase data
(a) no correction σ=3.1 mm, (b) with multipath correction σ=2.6 mm

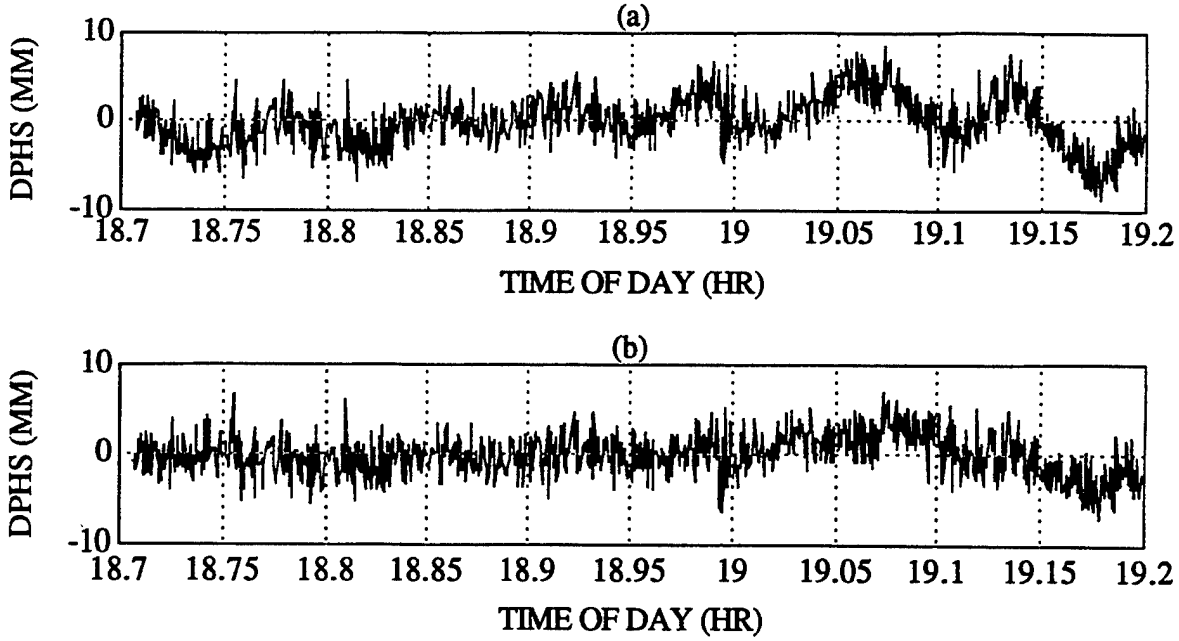

Figure 3.11. March 6, 1994 / Segment 3- Differential phase data
(a) no correction σ=2.8 mm, (b) with multipath correction σ=2.2 mm

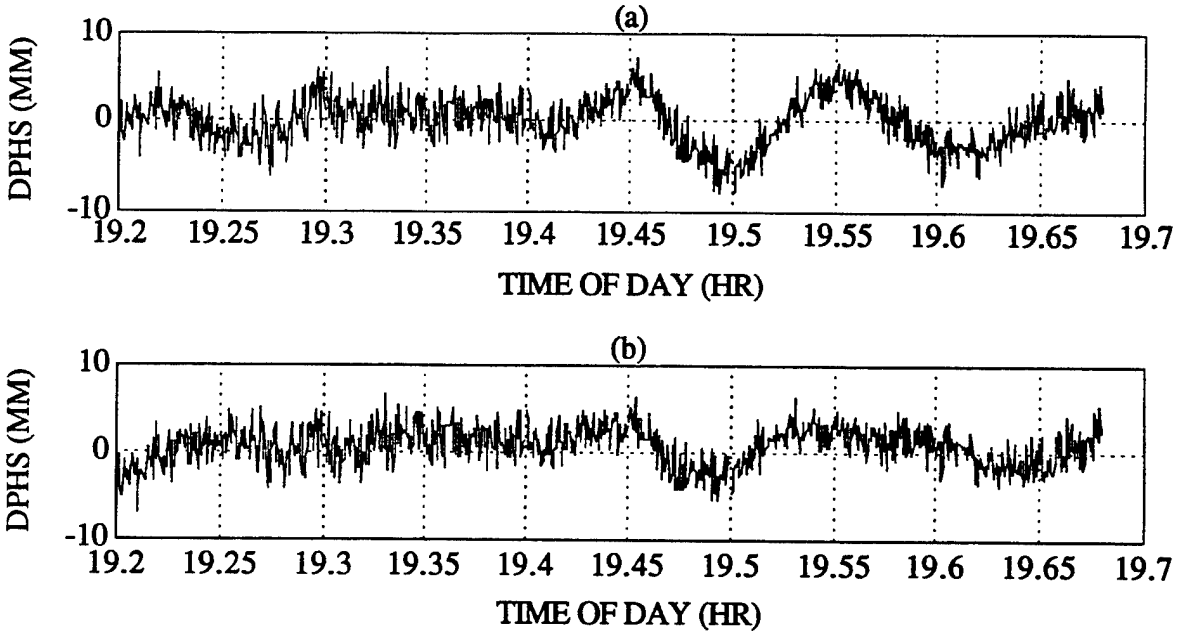

Figure 3.12. March 6, 1994 / Segment 4- Differential phase data
(a) no correction σ=2.7 mm, (b) with multipath correction σ=2.1 mm

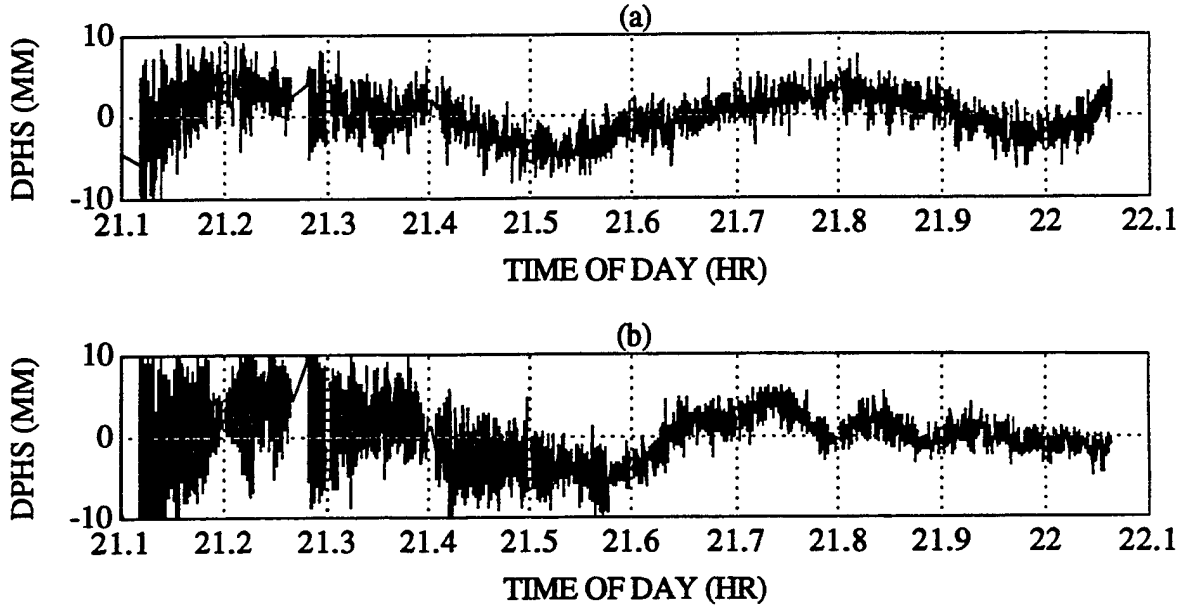

Figure 3.13. Differential phase data for patch (a) and helibowl (b) baselines. The data was collected March 4, 1994, during reflective multipath injection.

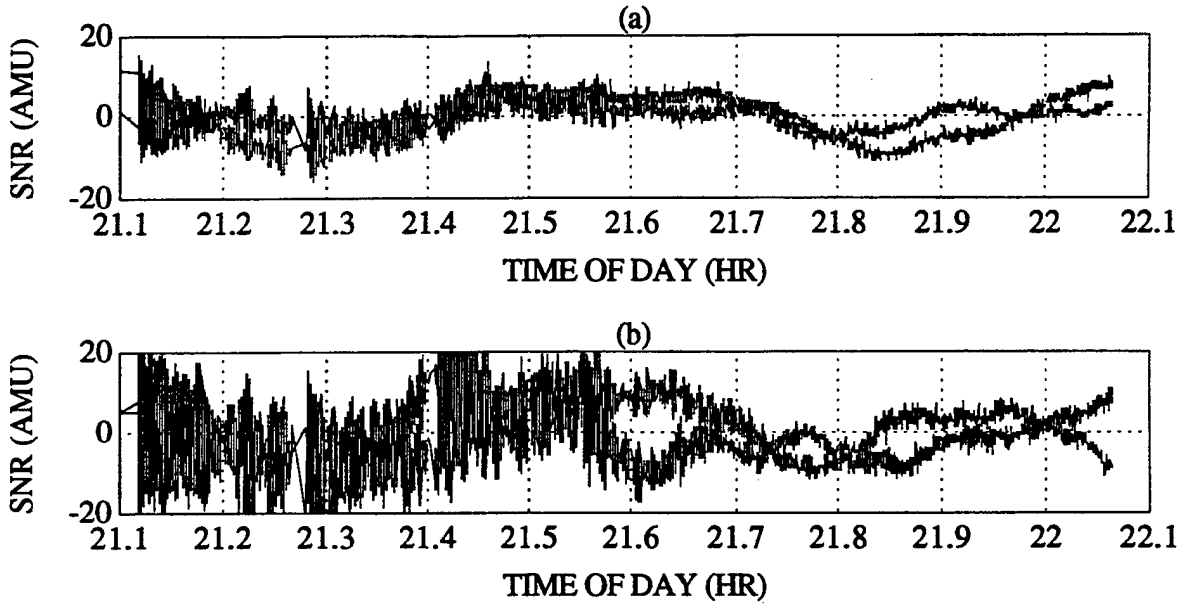

Figure 3.14. SNR data for patch (a) and helibowl (b) antennas. The data was collected March 4, 1994, during reflective multipath injection.

3.3 Discussion of Results

The narrow beam helibowl antenna multipath rejection capability was marginal. This is evidenced by the differential phase data and SNR data in Figures 3.3 and 3.4. Considering both observables, the multipath peaks in the helibowl baseline were less than those in the patch baseline. The multipath was still dominant compared to the noise levels of the data.

The multipath most visible in both the phase and SNR data was the fast constituent which had a period of roughly 300 seconds. This component can be attributed to the electronic multipath inducer based on the separation between the high gain antenna and the Vector antenna array. There was also a slow variation in both data types which had a period of approximately 1600 seconds. Based on considerations of the antenna separations, we concluded that this was produced by the reflective surfaces of the helibowl antennas.

The multipath profiling technique was successful. The multipath corrections for this experiment were computed using two constituents at each antenna, requiring a four element least squares solution to solve for the amplitudes and offsets. The post-multipath-correction differential phases approach the level of receiver noise. There still remains residual multipath, but the magnitudes are generally within the 2 millimeter receiver noise. The correction attempts to remove the severe multipath peaks down to this level by subtracting off a smooth multipath contour. This eliminates or reduces the slow period errors in the differential phase. High frequency receiver errors are not affected.

The effectiveness of the multipath correction is largely dependent on the spectral estimation. It was observed that FFT methods do not provide sufficient resolution at the low multipath frequencies. The current implementation using the Lomb periodogram is satisfactory, but requires user interaction to identify the frequencies of the multipath constituents. An automated routine would be preferred.

The differential phase and SNR data was segmented to enhance the spectral and least squares estimation techniques. The multipath frequencies and amplitudes slowly change over long periods of time. The multipath parameters appear stationary when the data is broken up into 30 minute sections.

The quality of the multipath correction also depends on the antenna gain pattern, because it is used to remove variations in the SNR due to changes in the direct signal magnitude. Most of the residual multipath effects could be eliminated with a more precise map of the antenna gain. Any errors in the residual SNR directly affect the estimates of the phase corrections. The multipath correction results for the helibowl baseline were not shown because the gain patterns for these hand-made antennas were found to have substantial variations azimuthally as well as between the two antennas. They could be used if a detailed pattern were generated in both elevation and azimuth.

The inconsistent multipath injection was attributed to the equipment set up. Since we were dealing with narrow beam antennas, the multipath injection was sensitive to placement of the apparatus. The signal from the GPS satellite passing overhead did not penetrate the

center of the high gain collection antenna gain pattern, except on March 6. In so doing, the multipath signals on the other days were attenuated. This is supported by the fact that the daily routine required the assembly and disassembly of the multipath injection apparatus. The experiment also took place on unevenly surfaced terrain. There was no practical method of placing the equipment in exactly the same position and orientation every day.

3.4 Conclusions

Based on the static test results, the multipath correction technique was successful in reducing differential carrier phase multipath to the levels of receiver noise. The results clearly warrant further investigation. In the form of research, we will soon be conducting another experiment focused on gathering additional experimental data. The Trimble patch antennas will be used, which will give multiple baselines in different directions using the same antenna type. The electronic multipath injection equipment will be assembled and kept stationary for the days of testing. This shall ensure several sets of consistent multipath data. The reflective multipath injection will also be performed. This time a 1/8th inch aluminum plate will be used as a reflective source. It was decided that the aluminum foil flapping in the wind was the source of the noise for the previous experiment. We would also like to test the algorithm with a different type of receiver, for example an Allen Osborne Turborogue or Novatel GPSCard.

The multipath correction algorithm will be adapted to operation in a near real-time mode. At present, the post-processing routine is not fully automated, nor is it efficient. Methods of adaptive signal processing or filtering will be investigated to assist in reaching this goal. The additional experimental data will be crucial.

The multipath correction theory will also be applied to dynamic as well as precise static platforms. To really be useful, the technique must be operable in a dynamic environment indicative of a spacecraft environment. In the current situation, theory may hold promise for high precision geodetic surveying and DGPS base stations.

4. Spinning Satellite Attitude Determination

Charles P. Behre

4.0 Introduction

The dynamical properties of spinning satellites allow for unique ways of determining spin rates and attitude [*Martin-Neira and Lucas*, 1992]. For the motion of a satellite that is spinning in the absence of applied torques, the motion of the kinematics can be modeled as the sum of sinusoids. If a GPS antenna is mounted on the spinning satellite, the signals it receives are related to this sinusoidal model. The frequencies of the signal oscillations correspond to the spin and nutation frequencies of the satellite. The amplitudes of the signals correspond to the attitude of the satellite.

This section describes two techniques for extracting the modes of a sinusoid from a sampled signal. These methods are then applied to a model of GPS phase measurements as would be received on spinning satellite. Finally, a simulation is described that is used to analyze the performance of the techniques.

4.1 Modal Analysis Techniques for Sinusoidal Signals

The two methods that are described are the Fast Fourier Transform (FFT) and the auto regressive model (AR). The ideal performance of each of the techniques are compared to their performance due to sampling and noise effects.

4.1.1 The FFT Method

To determine the modal frequencies and modal amplitudes of a signal the following steps are applied:

1) Apply an FFT algorithm to the sampled signal data.
2) Compute the power spectral density (PSD) of the transformed data in step 1.
3) Identify the peaks of the PSD.
4) Determine the frequency at which each peak occurs.
5) Relate these frequencies back to a kinematic model.

Using only the PSD values, the frequencies found in step 4 are the most likely estimate (MLE) of each signal mode. Ideally, they are the exact frequencies of the modes. However, the sampling properties of the signal can lead to errors.

Ideally, the signal should be sampled so that the modal frequencies are integer multiples of the frequency bin. The frequency bin size is determined by

$$\frac{f_{samp}}{\#\text{ of samples per window}}$$

where

f_{samp} is the sampling frequency in Hz.

For this case the peaks of the PSD occur exactly at the signal frequencies. The power contained in each of the peaks is the exact power of each mode. Figure 4.1 illustrates an ideal PSD.

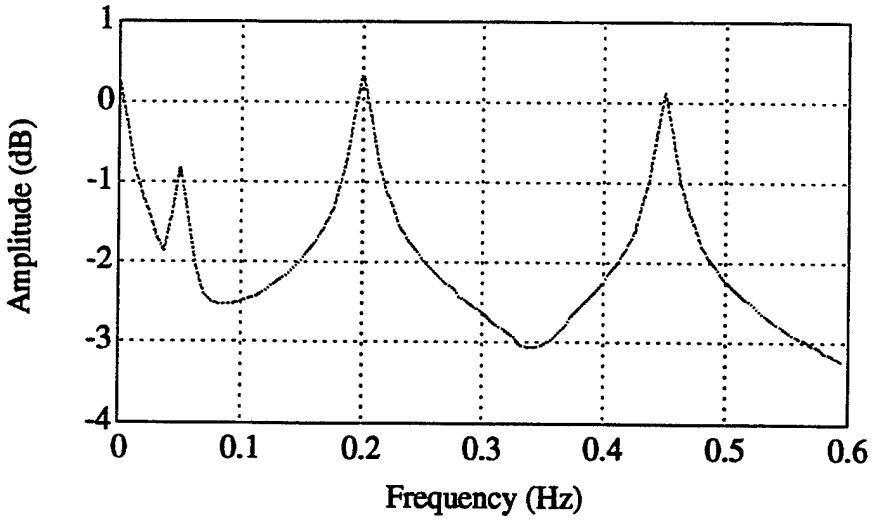

Figure 4.1. PSD of the FFT of GPS Phase Difference Measurements - Ideal Case

Realistically, the signal cannot be sampled with this condition because the modal frequencies are unknown. As a result, the frequency bins of the FFT do not line up exactly with each of the signal modes. The peaks of the PSD occur in the frequency bins that are closest to the correct modes. The signal power of each mode is spread over a range of frequency bins surrounding the correct frequency. This is known as bin leakage. One way to deal with this problem is to find the frequency center of the bins by weighting them. This is analogous to determining the mass center of a system of point masses. In the case of frequencies, the power contained in each bin is like the mass. The difference between the bin frequency and the center frequency is like the distance of one mass to the center of mass of a system. Another solution to the problem is to increase the sampling size. This reduces the size of each frequency bin. As a result, the signal modes are, on average, going to be closer to one of the bins.

Another problem that degrades the determination of the modal frequencies is noise in the signal. For the ideal sampling case, this is not a problem if the signal power is significantly larger than the noise level. The frequency of each mode still occurs exactly at one bin. All of the power contained in the mode is still only in that bin. There is a small amount of extra power, however, due to the noise power. If the signal power is very small, this extra noise power might significantly effect its estimation. For the non-ideal sampling case, there are some additional effects. One of the main problems is that the estimation of modal frequencies using the weighting of the bins is degraded. Normally, the power contained in the bin closest to the particular signal frequency is the greatest, while the power in the other surrounding bins is smaller. When bin weighting is used, extra power due to noise contained in these surrounding bins causes the estimation of the frequency center to be less accurate.

One way to decrease the effect of noise is to use a window function on the data. Ideally, the most accurate FFT would be of an infinite length of data. Because this is not possible, a finite set of data has to be used. Mathematically, this appears as an abrupt change from some sampled data value to an infinite number of zeros. This has the effect of amplifying the noise. If a window function is applied to the data, this abrupt change is smoothed. As a result, the noise level is decreased. Figure 4.2 shows the plot of a PSD which contains noise and is not ideally sampled.

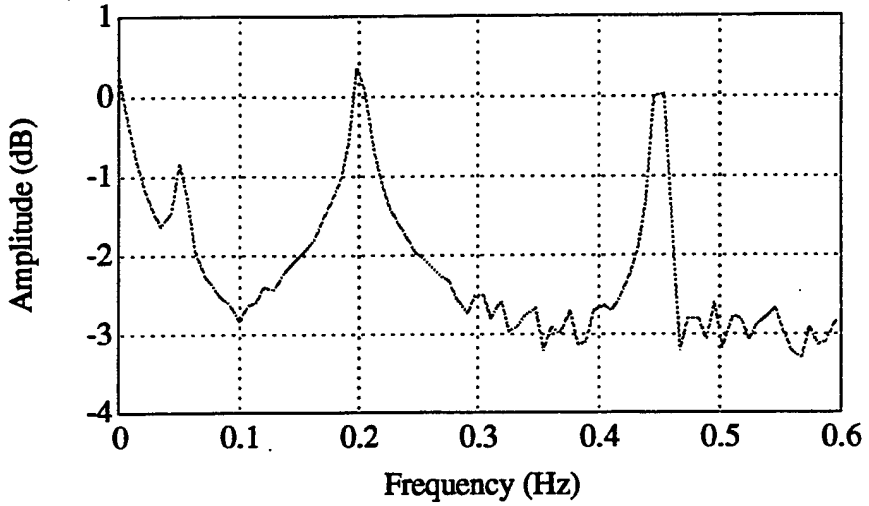

Figure 4.2. Effects of Noise and Sampling on PSD

In the implementation of an FFT algorithm there are no assumptions about the structure of the signal. In other words, the FFT can be applied to any type of signal. There are other frequency estimation methods, on the other hand, which can take advantage of the knowledge of the signal's structure. The next section discusses one of these methods called the auto regressive or AR method.

4.1.2 AR Modal Estimation

In general, a discrete-time process can be well approximated by a time series or rational transfer function model [*Kay*, 1988]. If the process is modeled as an AR process of order p, the sampled data $x[n]$ can be represented by the recursive difference relation

$$x[n] = -\sum_{k=1}^{p} a[k]x[n-k] + u[n] \qquad (4..1)$$

where the coefficients $a[k]$ are estimated from the sampled data. Taking the Z-transform of (4.1) yields the transfer function

$$\frac{X(z)}{U(z)} = \frac{1}{P(z)} \qquad (4..2)$$

where

$$P(z) = 1 + \sum_{k=1}^{p} a[k]z^{-k} = 1 + a[1]z^{-1} + a[2]z^{-2} + a[3]z^{-3} + \cdots + a[p]z^{-p} \qquad (4.3)$$

If the signal is composed of $2p$ complex sinusoids plus white Gaussian noise, then x can be written as

$$x[n] = \sum_{k=1}^{p} A_k \exp(j2\pi\bar{f}_k n) + A_k^* \exp(-j2\pi\bar{f}_k n) + v[n] \quad n = 1,\ 2,\ 3,\ \cdots,\ N \qquad (4.4)$$

where

N is the number of data samples,

A_k and A_k^* are complex conjugate amplitudes,

$\bar{f}_k = \dfrac{f_k}{f_{samp}}$ are the normalized sinusoidal frequencies

and

$v[n]$ is the noise.

As a result, z, in Equation (4.3) is found by

$$z = \exp\left(j2\pi\bar{f}_k\right). \qquad (4.5)$$

From the estimated $a[k]$ in (4.1) the roots of $P(z)$ are found from (4.3). The poles are in complex conjugate pairs and lie on a unit circle at angles corresponding to the sinusoidal frequencies $\bar{f}_k$ found in (4.4) as illustrated in Figure 4.3.

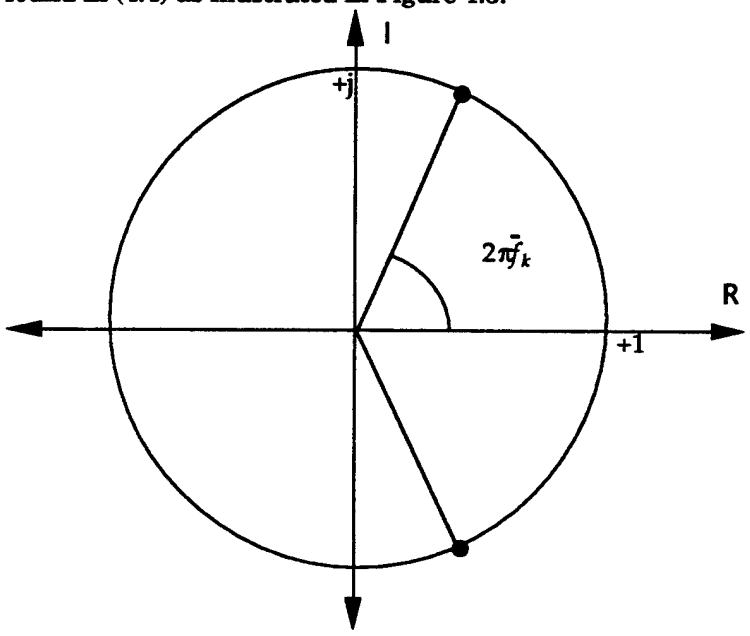

Figure 4.3. Relationship between Signal Frequency and Transfer Function Poles.

It should be noted that this technique directly estimates the frequencies $\bar{f}_k$, therefore it does not depend on the modal frequencies being multiples of the frequency bins.

Ideally for the case where there is no noise and the signal is perfectly modeled by (4.4), the signal is assumed to be composed of $2p$ sinusoids. This means that each pole of (4.2) lies exactly on the unit circle at the exact angle of $2\pi\bar{f}_k$.

For the non-ideal case, however, there is noise and the signal can not be perfectly modeled by (4.4). To take into account the noise, a higher order model than $2p$ is used. This allows for

the power contained in the noise to be spread among the non-modal frequencies. The poles of (4.2) corresponding to the modes now lie near the unit circle, while the poles corresponding to the noise lie farther away. The angles of the poles are only approximately equal to $2\pi\bar{f}_k$. As the model order is increased, there are more frequencies available for the noise. As a result, the poles for the modal frequencies get closer to the unit circle and the angles get closer to $2\pi\bar{f}_k$. If the model order is too high spurious frequencies might become dominant. Figure 4.4 illustrates this relationship.

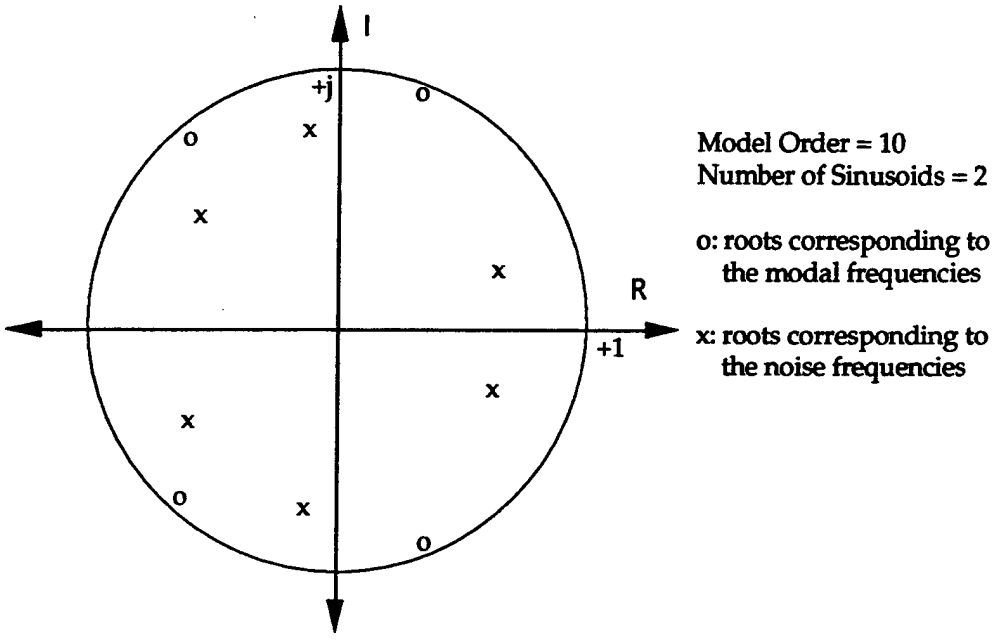

Figure 4.4. The Pole - Frequency Relationship For a Noisy Sampled Signal

4.1.3 FFT and AR Method Comparison

The performance of the FFT and AR methods are dependent on a variety of parameters. The FFT gives its best accuracy when the signal frequencies are multiples of the frequency bins. Increasing the sample size reduces the width of the bins and as a result, increases the accuracy. Computation time, however, increases with the size of the sample.

The AR method, on the other hand, does not depend on the frequency bin width (or sampling rate). Its accuracy increases as the assumed model order is increased. The choice of model number is limited to be no larger than the number of samples. Computation time, however, increases with an increase in model number because there are more coefficients in (4.1) to be computed.

4.2 Application of Modal Analysis to Spinning Satellites

The modal analysis methods as described in the last section can be used to determine the frequencies associated with a spinning satellite and to determine its attitude. In order to

employ these methods a dynamical model must be assumed for the satellite and some type of measurement signal must be taken which oscillates according to this model.

Figure 4.5 illustrates the model that is used. The rotating satellite has two principle angular velocities. The first is its spin about an inertially fixed axis ω_I or its inertial nutation rate. The second is its spin about a body axis ω_p or its body nutation rate. There are no applied torques.

Phase difference measurements $\Delta\phi$ from a GPS receiver mounted on the spinning satellite oscillate according to the satellite kinematics. These measurements can be used to compute displacement vectors for a GPS antenna which also oscillate with respect to time. The frequency estimation techniques can be applied to the displacements. The dominant frequencies as found from the FFT or AR methods correspond to the frequencies contained in the model.

After the frequencies are computed, other techniques can be used to determine the elements of the attitude matrix. These methods either use the kinematic model directly or use the amplitudes of the PSD spikes. This section describes a model of a spinning satellite and the application of the frequency and amplitude estimation methods to it.

4.2.1 Derivation of the Observation

The observation is found by reducing the raw measurement. In this case the raw measurements are the phase difference measurements of two GPS antennas and the observations are the displacement vectors of one antenna called the slave with respect to another antenna called the master.

The phase difference measurements to n satellites are modeled as

$$\Delta\phi = \mathbf{H}\mathbf{r} + k \tag{4.6}$$

where

$$\mathbf{H} = \begin{bmatrix} e_1^T \\ e_2^T \\ \vdots \\ e_i^T \end{bmatrix}^L \qquad i = 1,\ 2,\ 3,\ \cdots,\ n \tag{4.7}$$

n is the number of satellites, $\mathbf{r}$ is the displacement vector of the slave antenna, and k is an integer ambiguity. The superscript L means that the line-of-sight vectors are expressed in some local frame such as an orbital frame. Differencing the $\Delta\phi$ measurements at time t_m from the measurements at the initial time t_0 yields

$$y(t_m) = \Delta\phi(t_m) - \Delta\phi(t_0) = \mathbf{H}[\mathbf{r}(t_m) - \mathbf{r}(t_0)] \equiv \mathbf{H}\mathbf{dr}(t_m) \tag{4.8}$$

where m is the number of measurement epochs and $\mathbf{dr}$ is the displacement vector [*Cohen*, 1992]. Solving for $\mathbf{dr}$ results in

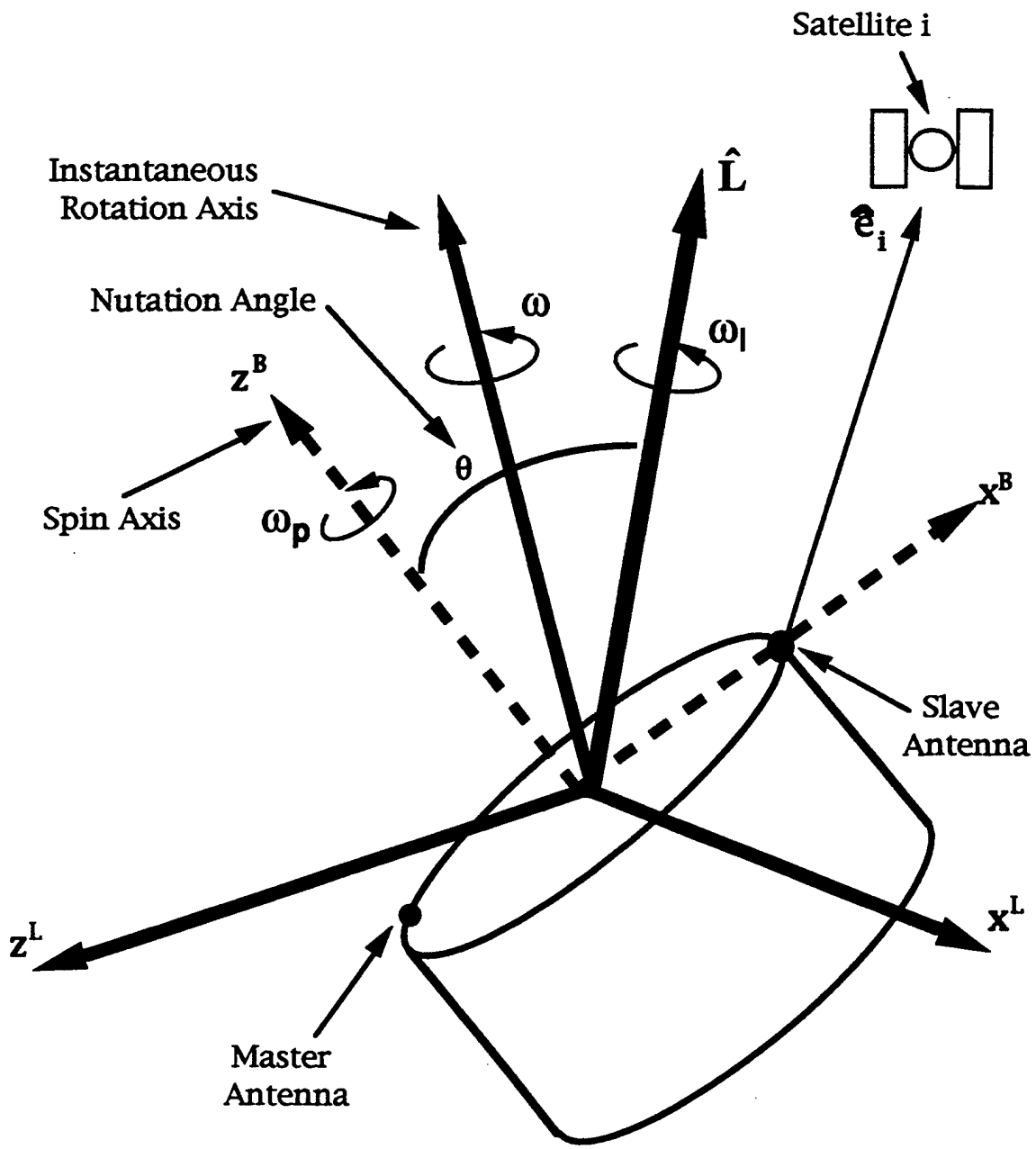

$$\omega_p = \frac{I_{xB} - I_{zB}}{I_{xB}} \omega_l \cos\theta$$

$$\omega^2 = \omega_p^2 + \omega_l^2 + 2\omega_p \omega_l \cos\theta$$

$\omega \equiv$ Inertial spin rate about the instantaneous rotation axis

$\omega_p \equiv$ body nutation rate

$\omega_l \equiv$ inertial nutation rate

$\theta \equiv$ nutation angle

Figure 4.5. Components of the Kinematic Model

$$\mathbf{dr}^{L}(t_m) = \left(\mathbf{H}^{T}\mathbf{H}\right)^{-1}\mathbf{H}^{T}y(t_m). \tag{4.9}$$

4.2.2 Derivation of the Kinematic Model

The displacement vector can also be related to the attitude and angular velocities of the satellite. Let ${}^{H}C^{B}$ be the rotation matrix of the slave antenna's coordinates from a body fixed system to an inertially fixed angular momentum system and define the antenna's body fixed coordinates to be

$$\mathbf{r}^{B} = \begin{bmatrix} d \\ 0 \\ 0 \end{bmatrix} \tag{4.10}$$

where d is the distance of the antenna from the body spin axis. Expanding ${}^{H}C^{B}$ to show the satellite angular velocities and multiplying by $\mathbf{r}^{B}$ yields

$$\mathbf{r}^{H} = {}^{H}\mathbf{C}^{B}(t_m)\mathbf{r}^{B} = d\begin{bmatrix} c\varphi c\lambda - c\theta s\varphi s\lambda \\ c\varphi s\lambda + c\theta s\varphi s\lambda \\ s\theta s\varphi \end{bmatrix} \tag{4.11}$$

where

$$\varphi = \omega_p t_m, \tag{4.12}$$

$$\lambda = \omega_l t_m, \tag{4.13}$$

and θ is the nutation angle.

Let ${}^{L}\mathbf{C}^{H}$ be the rotation matrix from the angular momentum system to the local system, i.e. the attitude matrix. At any measurement epoch the antenna's displacement is

$$\mathbf{dr}^{L}(t_m) = {}^{L}\mathbf{C}^{H}\left[{}^{H}\mathbf{C}^{B}(t_m) - {}^{H}\mathbf{C}^{B}(t_0)\right]\mathbf{r}^{B}. \tag{4.14}$$

Expanding (4.14) yields

$$\mathbf{dr}^{L}(t_m) = d\begin{bmatrix} a_{11}(c\varphi c\lambda - c\theta s\varphi s\lambda - 1) + a_{12}(c\varphi s\lambda + c\theta s\varphi s\lambda) + a_{13}s\theta s\varphi \\ a_{21}(c\varphi c\lambda - c\theta s\varphi s\lambda - 1) + a_{22}(c\varphi s\lambda + c\theta s\varphi s\lambda) + a_{23}s\theta s\varphi \\ a_{31}(c\varphi c\lambda - c\theta s\varphi s\lambda - 1) + a_{32}(c\varphi s\lambda + c\theta s\varphi s\lambda) + a_{33}s\theta s\varphi \end{bmatrix} \tag{4.15}$$

where the a_{ij} are the elements of the attitude matrix ${}^{L}\mathbf{C}^{H}$.

Applying the frequency estimation methods to the observations as computed by (4.9) yields the frequency components of (4.15). Knowing the frequencies, the elements of the attitude matrix can be found.

The **H** matrix in (4.9) is composed of line-of-sight vectors as shown in (4.7). This matrix changes with respect to time due to the orbital motion of both the spinning vehicle and the GPS satellite. This motion, however, is very small compared to the spinning of the satellite. As a result, it is treated as a fixed matrix in the application of the algorithms.

4.2.3 Application of Frequency Estimation Techniques to the Spinning Satellite Model

There are four frequencies that are contained in (4.15):

1) $f_0 = 0$ is a dc component corresponding to the constant,
2) $f_d = f_l - f_p$,

   where $f_l = \frac{\omega_l}{2\pi}$ and $f_p = \frac{\omega_p}{2\pi}$,
3) f_p,

and
4) $f_s = f_l + f_p$.

Applying an FFT algorithm to observations computed in (4.9) yields a PSD with spikes at these four frequencies. Figure 4.1 shows an ideal PSD with four frequency spikes. From this plot it can be seen that f_p= 0.2 Hz and f_l = 0.25 Hz. Applying the AR method to (4.9) yields four pairs of complex roots of (4.2). The positive angles on the unit circle are

$$\frac{2\pi f_0}{f_{samp}}, \frac{2\pi f_d}{f_{samp}}, \frac{2\pi f_p}{f_{samp}}, \text{ and } \frac{2\pi f_s}{f_{samp}}.$$

4.2.4 Attitude Estimation: Method I

The first technique for attitude estimation involves computing the elements of the attitude matrix directly from a fit of the observations to the kinematics. The steps involved are:

1) Collect a batch of data and apply (4.9) to get $\mathbf{dr}(t_m)$, m= 1, 2, 3, . . . N, where N is the number of measurement times;
2) Estimate the four frequencies using either the FFT or AR method;
3) Using these estimated frequencies accumulate the 5xN matrix

$$\begin{bmatrix} c\varphi c\lambda - 1 \\ s\varphi s\lambda \\ c\varphi s\lambda \\ s\varphi c\lambda \\ s\varphi \end{bmatrix} \tag{4.16}$$

   where φ and λ are found by Equations 4.12 and 4.13, respectively, at each measurement time;
4) Divide (4.15) into a product of the unknown elements multiplied by (4.16) yielding

$$\mathbf{dr}(t_m) = d \begin{bmatrix} a_{12} & -a_{11}c\theta & a_{12} & a_{12}c\theta & a_{13}s\theta \\ a_{21} & -a_{21}c\theta & a_{22} & a_{22}c\theta & a_{23}s\theta \\ a_{31} & -a_{31}c\theta & a_{32} & a_{32}c\theta & a_{33}s\theta \end{bmatrix} \begin{bmatrix} c\varphi c\lambda - 1 \\ s\varphi s\lambda \\ c\varphi s\lambda \\ s\varphi c\lambda \\ s\varphi \end{bmatrix}; \tag{4.17}$$

   and
5) Apply a least squares solution to determine the unknown attitude matrix elements a_{ij} and nutation angle θ.

4.2.5 Attitude Estimation: Method II & III

Both methods II and III determine the elements of the attitude matrix ${}^{L}\mathbf{C}^{H}$ from the amplitudes of the spikes in a PSD. The relation of these elements to the attitude matrix can be seen by taking the Fourier transform of row 1 of (4.15), i.e., the dx component of **dr**. This yields

$$\begin{aligned}
\Im(dx) = {} & \delta(s+f_s)\frac{1}{4}(a_{11}+a_{11}c\theta+ia_{12}+ia_{11}c\theta) \\
& +\delta(s-f_s)\frac{1}{4}(a_{11}+a_{11}c\theta-ia_{12}-ia_{11}c\theta) \\
& +\delta(s+f_d)\frac{1}{4}(a_{11}-a_{11}c\theta-ia_{12}+ia_{11}c\theta) \\
& +\delta(s-f_d)\frac{1}{4}(a_{11}-a_{11}c\theta+ia_{12}-ia_{11}c\theta) \\
& +\delta(s+f_p)i\frac{1}{2}a_{13}s\theta \\
& -\delta(s-f_p)i\frac{1}{2}a_{13}s\theta \\
& -\delta(s-0)a_{11}
\end{aligned} \tag{4.18}$$

where $\Im$ is the Fourier transform operator, δ is the delta function, and $i=\sqrt{-1}$. The Fourier transform is also applied to rows 2 and 3 of (4.15). The coefficients of the delta functions can then be grouped according to frequency to obtain

$$\begin{bmatrix} |A_1|_j \\ |A_2|_j \\ |A_3|_j \\ |A_4|_j \end{bmatrix} = \begin{bmatrix} a_{j1} \\ \dfrac{(1-c\theta)\sqrt{a_{j1}^2+a_{j2}^2}}{4} \\ \dfrac{a_{j3}s\theta}{2} \\ \dfrac{(1+c\theta)\sqrt{a_{j1}^2+a_{j2}^2}}{4} \end{bmatrix} \qquad j=1,2,3 \tag{4.19}$$

where the $|A_k|_j$ are the amplitudes of the PSD spikes and j corresponds to the three rows of (4.15) and to the three rows of ${}^{L}\mathbf{C}^{H}$.

In method II the amplitudes of the PSD spikes are estimated directly from the FFT of the data. In method III the amplitudes of the PSD spikes are computed from (4.4)

$$x[n]=\sum_{k=1}^{p} A_k \exp(j2\pi\bar{f}_k n)+A_k^* \exp(-j2\pi\bar{f}_k n)+v[n] \quad n=1,\ 2,\ 3,\ \cdots,\ N.$$

Knowing the four frequencies $\bar{f}_k$ and using the sampled data $x[n]$, a least squares algorithm can be applied to estimate A_k. Then Equation (4.19) can be used to compute a_{ij} and θ.

4.3 Spinning Satellite Simulation

In this section the performance of the frequency and attitude estimation algorithms is evaluated using a computer simulation of a spinning satellite. Phase difference measurements are simulated from the known locations of two GPS antennas. The true attitude matrix is computed from the known orientation of the angular momentum axis. This axis is fixed in time because there are no applied torques to the spinning satellite. The satellite also nutates about this axis at a fixed angle θ. The GPS satellites are held motionless in the sky. Therefore, the **H** matrix remains constant.

The phase difference measurements are simulated by propagating the satellite according to the kinematic model. Given an inertial spin rate f about the instantaneous rotation axis and a set of principle moments of inertia, the inertial nutation rate and body nutation rate are found from

$$f^2 = f_l^2 + f_p^2 + 2 f_p f_l \cos\theta \text{ and } f_p = \frac{I_{xB} - I_{zB}}{I_{xB}} f_l.$$

At each epoch t_m a $\Delta\phi$ measurement is generated from the truth. Noise is added on to $\Delta\phi$ to simulate actual GPS measurements. From each $\Delta\phi(t_m)$ a corresponding $\mathbf{dr}(t_m)$ is found. Both the FFT and AR methods are applied to dr to determine the four frequencies described in section 4.2.3. The attitude determination methods I, II, and III are applied to compute ${}^{L}C^{H}$ and θ.

4.3.1 Simulation Results: Frequency

Tables 4.1 and 4.2 show the results of the algorithms using two difference nutation angles. The inertial spin rate f about the instantaneous rotation axis is 3.1234 Hz and the sample frequency is 3 Hz. The cases which are investigated involve the case with no noise and ideal sampling, the case with noise and with ideal sampling, the case with no noise but with non-ideal sampling, and the case with both noise and sampling effects.

Table 4.1. Frequency Estimation with $\theta = 19.75°$

		Actual	Ideal	Noise	f_{samp}	Both
f_p	FFT	.2000	.2000	.2000	.2001	.2000
	AR	.2000	.2000	.2001	.2000	.2002
f_l	FFT	.2500	.2500	.2500	.2503	.2503
	AR	.2500	.2500	.2499	.2500	.2498
f_p+f_l	FFT	.4500	.4500	.4500	.4504	.4504
	AR	.4500	.4500	.4500	.4500	.4500
f_p-f_l	FFT	.0500	.0500	.0500	.0503	.0502
	AR	.0500	.0500	.0498	.0500	.0497

Table 4.2. Frequency Estimation with $\theta = 5°$

		Actual	Ideal	Noise	f_{samp}	Both
f_p	FFT	.2201	.2201	.2201	.2198	.2199
	AR	.2201	.2201	.2205	.2201	.2204
f_l	FFT	.2325	.2325	.2325	.2328	.2330
	AR	.2325	.2325	.2321	.2325	.2322
f_p+f_l	FFT	.4526	.4526	.4526	.4529	.4529
	AR	.4526	.4526	.4526	.4526	.4526
f_p-f_l	FFT	.0125	.0125	.2199	.0100	.0098
	AR	.0125	.0125	.0117	.0125	.0117

The AR method performs slightly better than the FFT. For the best results a model order of at least 15 must be used. At the sampling frequency of 3 Hz, the FFT method requires about 300 samples for a good degree of accuracy while the AR method only needs 150 samples. Larger nutation angles produced larger modal amplitudes. Both methods performed the best for the signals with the highest amplitudes. The effects of non-ideal sampling do not alter the AR results at all.

4.3.2 Simulation Results: Attitude Determination

The results using method I were highly dependent on having a high level of accuracy from the frequency estimation. Like the estimation of frequency, the accuracies were the best for the larger nutation angles. In Equation (4.17) the nutation angle was estimated along with the elements of the attitude matrix. If the nutation angle was accurately estimated in some other way, the estimation accuracy for the attitude matrix elements increased significantly. The accuracy did not, however, improve if the size of the batch was increased over a minimum size of about 500 samples.

The results using method II varied the most. Unlike method I, they were not strongly dependent on using a separate nutation angle estimation. A minimum batch size of about 600 samples was required for good results.

The results using method III were very dependent on an accurate frequency estimations. The accuracy improved as the nutation angle increased. Like method I, the accuracy significantly improved if the nutation angle was estimated in some other manner. The minimum batch size for good results was about the same as method II.

4.4 Future Plans

We plan to continue this research along several avenues. The simulation model will be upgraded to include user and GPS satellite orbital motion, external torques due to solar pressure and drag, satellite control maneuvers, and realistic GPS satellite visibilities. The attitude determination algorithms will also be modified to compensate for the additional features. In addition, the use of raw phase data rather than baseline difference vectors as the primary observable will be evaluated.

Another important step will be to test these algorithms on ground test data collected at the Naval Research Laboratory during the summer of 1994. The instrumented spin/tilt table which will be located at Maryland Point, provides a controlled environment and a "truth" reference for dynamic testing.

5. References

Axelrad, P. and L. M. Ward, "On-orbit GPS Based Attitude and Antenna Baseline Estimation", ION National Technical Meeting, San Diego, CA, Jan. 24-26, 1994.

Axelrad, P., B.C. Chesley, L. M. Ward, "GPS Based Spacecraft Attitude Determination", Final Report for October 1992-September 1993 to the Naval Research Laboratory, Sept. 1993.

Braasch, M.S., "Isolation of GPS Multipath and Receiver Tracking Errors," 1994 ION National Technical Meeting, San Diego, CA, January, 1994.

Braasch, M and F. van Grass, "Mitigation of Multipath in DGPS Ground Reference Stations," Proceedings of the Institute of Navigation National Technical Meeting, San Diego, CA, January, 1992.

Cohen, C.E., E. G. Lightsey, B.W. Parkinson, and W.A. Fees, "Space Flight Tests of Attitude Determination Using GPS: Preliminary Results", Preprint of paper presented at ION GPS-93, Salt Lake City, UT, Sept. 22-24, 1993.

Cohen, C.E. *Attitude Determination Using GPS*, Ph.D. Dissertation, Department of Aeronautics and Astronautics, Stanford University, Dec. 1992.

Cohen, C.E. and B.W. Parkinson, "Integer Ambiguity Resolution of the GPS Carrier for Spacecraft Attitude Determination," AAS 92-015, AAS Guidance and Control Conference, Keystone Colorado, Feb. 8-12, 1992b.

Cohen, C and B. Parkinson, ``Mitigating Multipath Error in GPS Based Attitude Determination," Guidance and Control 1991, Vol. 74, Advances in the Astronautical Sciences.

Counselman, C. and S. Gourevitch, ``Miniature Interferometer Terminals for Earth Surveying: Ambiguity and Multipath with Global Positioning System," IEEE Transactions on Geoscience and Remote Sensing, Vol. GE-19, No. 4, October, 1981.

Georgiadou, Y. and A. Kleusberg, ``On Carrier Signal Multipath Effects in Relative GPS Positioning," Manuscripta Geodaetica, Vol. 13, 1988.

Greenspan, R., A. Ng, J. Przyemski and J. Veale, ``Accuracy of Relative Positioning by Interferometry with Reconstructed Carrier GPS: Experimental Results," Proceedings of the Third International Geodetic Symposium on Satellite Doppler Positioning, Las Cruces, NM, February, 1982.

Kay, Steven M., *Modern Spectral Estimation Theory & Application*, Prentice Hall, 1988.

Lefferts, E.J., F.L. Markley, and M.D. Shuster, "Kalman Filtering for Spacecraft Attitude Estimation", *Journal of Guidance, Control, and Dynamics*, AIAA Paper 82-0070, AIAA 20th Aerospace Sciences Meeting, Orlando, FL, Jan. 1982.

Lightsey, E. G., C.E. Cohen, W. A. Feess, and B.W. Parkinson, "Analysis of Spacecraft Attitude Measurements Using Onboard GPS", Preprint of paper presented at AAS Guidance and Control Conference, Keystone, CO, February, 1994.

Martin-Niera, M. and R. Lucas, "GPS Attitude Determination of Spin Stabilized Satellites," Proceedings of ION GPS 92, Albuquerque, New Mexico, Sept. 16-18, 1992.

Press, W.H., S.A. Teukolsky, W.T. Vetterling, and B.P. Flannery, {\em Numerical Recipes in C}, pp. 575-580, Cambridge University Press, 1992.

Sennot,J, and D. Pietraszewski, "Experimental Measurement and Characterization of Ionospheric and Multipath Errors in Differential GPS," Journal of the Institude of Navigation, Vol. 34, No. 2, Summer, 1987.

Shuster, M. D., "A Survey of Attitude Representations", *The Journal of Astronautical Sciences*, Vol. 41, No. 4, Oct.-Dec. 1993.

van Nee, R., "Multiath Effects onf GPS Code Phase Measurements," ION GPS-92, Albuquerqe, NM, September, 1992.

van Nee, R., "The Multipath Estimating Delay Lock Loop," 1994 ION National Technical Meeting, San Diego, CA, January, 1994.

Wertz, J. R., ed. *Spacecraft Attitude Determination and Control*, D. Reidel Publishing Company Library in Astrophysics and Space Science, 1978.

APPENDIX A - Corrections to the Sept. 1993 Final Report to NRL

Equation 4.15, page 13

$$
\begin{aligned}
I_1\dot{\omega}_1 + \omega_2\omega_3(I_3 - I_2) + h_w\omega_2 &= N_1 \\
I_2\dot{\omega}_2 + \omega_1\omega_3(I_1 - I_3) - h_w\omega_1 &= N_2 \\
I_3\dot{\omega}_3 + \omega_1\omega_2(I_2 - I_1) &= N_3
\end{aligned}
$$

Equation A-1, page 78

$$
C(\theta_1, \theta_2, \theta_3) = \begin{bmatrix}
\cos\theta_2\cos\theta_3 & \cos\theta_2\sin\theta_3 & -\sin\theta_2 \\
\sin\theta_1\sin\theta_2\cos\theta_3 - \cos\theta_1\sin\theta_3 & \sin\theta_1\sin\theta_2\sin\theta_3 + \cos\theta_1\cos\theta_3 & \sin\theta_1\cos\theta_2 \\
\cos\theta_1\sin\theta_2\cos\theta_3 + sin\theta_1\sin\theta_3 & \cos\theta_1\sin\theta_2\sin\theta_3 - \sin\theta_1\cos\theta_3 & \cos\theta_1\cos\theta_2
\end{bmatrix}
$$

Equation B-2, page 79: See Section 2.10 above.

GPS BASED ATTITUDE DETERMINATION

FY'93-94 Technical Report II

to the Naval Research Laboratory

NRL Scientific Officer - Bernard Kaufman

Principal Investigator - Penina Axelrad
Co-Investigator - Peter F. MacDoran

Report Written By - Penina Axelrad
Bruce Chesley
Christopher J. Comp
Lisa M. Ward

Colorado Center for Astrodynamics Research
University of Colorado, CB 431
Boulder, CO 80309

October 14, 1994

Award: N00014-93-1-G030, Account: 153-7545

ABSTRACT

This report describes the research performed by the Colorado Center for Astrodynamics Research during the second half of FY'93-94 on spacecraft attitude determination using GPS. The specific topics currently under investigation are Kalman filtering approaches for Earth pointing satellites and multipath mitigation in GPS phase observations.

A bootstrapping algorithm for high accuracy attitude determination using GPS, comprising three steps - initialization, baseline estimation, and an attitude Kalman filter, is successfully applied to both simulated and actual flight data from the RADCAL satellite. Results from several data sets are presented showing agreement in the baseline and line bias estimates to within 5 mm. An attitude point solution method is also implemented to validate the filter results. Comparisons between filter and point solution methods are presented. Attitude results indicate pitch and roll oscillations which agree to within three percent with the frequencies computed based on vehicle mass properties, and an unexpected yaw rate which changes unexpectedly in some of the data sets.

A new multipath correction algorithm is described which makes use of signal to noise ratio data to create a GPS differential phase correction profile. This technique is evaluated based on both simulated and experimental data collected on a static antenna array. The profiling procedure both reduces the overal magnitude of the differential phase errors, and more importantly, removes a large portion of the low frequency, time correlated error characteristics.

A set of Kalman Filter algorithms for incorporating data from both GPS and Fiber Optic Gyros onboard a small satellite is described. This work is focused on implementation onboard the JAWSAT mission, but could be applied to other similar spacecraft configurations. In particular a measurement differencing approach which mitigates correlated errors produced by multipath is implemented and evaluated. Results from a computer simulation with experimentally based error models, are presented, which show performance in the range of 0.03 degrees, 1-σ, per axis.

Suggestions for further improvements and continued research in each of these areas are given.

TABLE OF CONTENTS

LIST OF FIGURES

LIST OF TABLES

1.0 OVERVIEW

This report describes the research performed by the Colorado Center for Astrodynamics Research during the second half of FY'93-94 on spacecraft attitude determination using GPS. The work is a continuation of research described in the the first technical report for FY'93-94 [*Axelrad, Behre, Comp, and Ward*, May 16, 1994].

The overall project encompasses various methods for using GPS to determine the attitude of a spacecraft in near Earth orbit. The specific topics covered in this technical report are Kalman filtering approaches for both attitude and baseline estimation, and a new technique for multipath mitigation in GPS phase observations.

The highlights of the technical advances made during the last six months are as follows:

- Comparison of attitude, baseline, and line bias solutions for several sets of data from RADCAL.
- Development and evaluation of an algorithm which uses receiver signal-to-noise ratio (SNR) to produce a multipath correction profile for differential phase observations.
- Development of a computer simulation of multipath interference for use in understanding the performance of the multipath correction method.
- Development of a Kalman filter which integrates GPS and Fiber Optic Gyro observations for attitude estimation onboard a small satellite.

Section 2 summarizes the bootstrapping attitude determination algorithms and presents results from both simulated and on-orbit data from the RADCAL satellite. Comparisons between results from different data sets are made as means for evaluating the performance of the algorithms. Plans for future work in this area are provided.

Section 3 describes analytical and experimental work performed to characterize and mitigate multipath errors in differential phase measurements. The new algorithm is a considerable improvement over the methodology described in our previous report. It has been shown to be successful using both simulated data, as well as experimental data collected in a highly reflective environment. Possible extensions of the technique to real time operation in a dynamic environment are discussed as well as opportunities for further accuracy improvements.

Section 4 provides information on research we have done on an integrated GPS/IFOG attitude determination Kalman filter. A measurement differencing technique to enhance the performance of the basic filter in the presence of multipath is described, and results from a computer simulation are presented and discussed. This work is currently geared toward operation on a small satellite, JAWSAT, but could be applied to any spacecraft equipped with both GPS and gyros.

2.0 SPACECRAFT ATTITUDE ESTIMATION USING GPS

Lisa M. Ward

2.1 INTRODUCTION

This report describes a sequence of algorithms, which begin with the most basic assumptions about the vehicle attitude and ultimately permit the highest accuracy attitude determination based on GPS measurements. The sequence begins with an attitude initialization step largely unchanged from that suggested in Cohen and Parkinson [1], followed by an extended Kalman estimator for the attitude and line biases, with the option for refinement of baseline estimates based on data collected on orbit rather than on the ground. These algorithms have been successfully used on both simulated and actual flight data collected onboard RADCAL. Because of the lack of another source of attitude information, the accuracy of the actual results can only be verified by consistency checks between data sets.

This section will first present the basic theory behind GPS based attitude determination followed by the specific methodology and implementation of each algorithm. Next, we describe of how each algorithm contributes to the attitude determination process. The results of each algorithm will be presented, and finally, a summary and discussion of future work.

2.2 GPS BASED ATTITUDE DETERMINATION METHODOLOGY

The theory of GPS based attitude determination has been described in a number of references, most notably in Cohen [2]. Here we provide an overview to aid in the discussion of our results.

2.2.1 THE GPS OBSERVABLES

The fractional difference in carrier phase between two antennas, $\Delta\varphi$, forms the principal observable for attitude determination using GPS. One antenna is designated as the master antenna, and the others are slaves. This phase difference can be expressed by

$$\Delta\varphi = \Delta r - k + \beta + \nu \tag{2.1}$$

where Δr is the difference in range between the two antennas and a GPS satellite, k is the integer number of carrier cycles in the differential range, β is the hardware line bias, and ν is the random measurement noise, all expressed in cycles.

As illustrated in Figure 2.1, the range difference is the projection of the baseline vector, $\mathbf{b}$ (directed from master to slave), onto the user-to-GPS line of sight vector, $\mathbf{e}$, which gives

$$\Delta r = \mathbf{b} \cdot \mathbf{e} = |\mathbf{b}| \cos\theta \tag{2.2}$$

If $\mathbf{e}$ is expressed in the orbit local reference frame and $\mathbf{b}$ is known in the body fixed reference frame, the range difference becomes

$$\Delta r = \left(\mathbf{b}^B\right)^{\mathrm{T}} {}^B\mathbf{C}^L \, \mathbf{e}^L \tag{2.3}$$

In this notation ${}^{B}\mathbf{C}^{L}$, which is the rotation matrix from the local frame to the body frame, represents the attitude of the vehicle. The superscripts on the vectors denote the reference frame in which each vector is expressed. Now the observed phase difference is given by

$$\Delta\varphi = (\mathbf{b}^{B})^{\mathrm{T}}\left({}^{B}\mathbf{C}^{L}\,\mathbf{e}^{L}\right) - k + \beta + \nu \qquad (2.4)$$

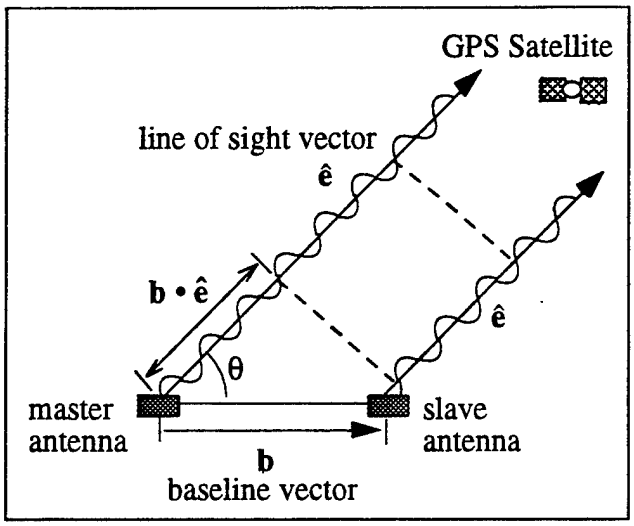

Figure 2.1. GPS Differential Phase Geometry

The reference frames discussed in this section are shown in Figure 2.2. One is the orbit local frame, L, which is centered on the spacecraft and aligned with the radial and orbit normal vectors. The other is the body fixed frame, B, which is aligned with the principal axes of the spacecraft.

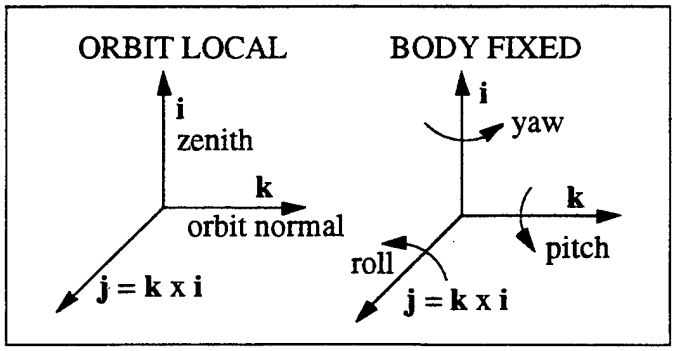

Figure 2.2. Reference Frames

2.2.2 GENERAL GPS BASED ATTITUDE DETERMINATION

Given a minimum number of observations, for example 3 baselines observing 2 satellites, the attitude can be solved deterministically. If more measurements are available, the solution can be optimized in some way. The general approach is to solve for the attitude matrix, ${}^{B}\hat{\mathbf{C}}^{L}$, that minimizes the phase difference residuals in the least squares sense. The phase difference residual, $\delta\varphi_{ij}$, for baseline i and satellite j is given by

$$\delta\varphi_{ij} \equiv \Delta\varphi_{ij} - \Delta\hat{\varphi}_{ij} \tag{2.5}$$

where $\Delta\varphi_{ij}$ is the observed phase difference measurement, and $\Delta\hat{\varphi}_{ij}$ is the predicted phase difference measurement.

Generally, the entire attitude matrix cannot be solved for directly but can be linearized about an a priori estimate, ${}^{B}\hat{\mathbf{C}}_0^{L}$, as follows:

$${}^{B}\hat{\mathbf{C}}^{L} = \delta\mathbf{C}\ {}^{B}\hat{\mathbf{C}}_0^{L} \equiv \left(\mathbf{I} + 2\mathbf{Q}^{\times}\right){}^{B}\hat{\mathbf{C}}_0^{L}. \tag{2.6}$$

where the transformation matrix, $\delta\mathbf{C}$, is expressed in terms of a small correction quaternion, $\delta\bar{q} = \begin{bmatrix}\delta q_1 & \delta q_2 & \delta q_3\end{bmatrix}^{\mathrm{T}}$, $\mathbf{I}$ is the identity matrix, and $\mathbf{Q}^{\times}$ is the cross product matrix associated with the elements of the vector $\delta\bar{q}$ given by

$$\mathbf{Q}^{\times} = \begin{bmatrix} 0 & \delta q_3 & -\delta q_2 \\ -\delta q_3 & 0 & \delta q_1 \\ \delta q_2 & -\delta q_1 & 0 \end{bmatrix}. \tag{2.7}$$

The full 4-element correction quaternion $\delta\mathbf{q}$ is defined by

$$\delta\mathbf{q} \equiv \mathbf{q} \otimes \hat{\mathbf{q}}^{-1} \tag{2.8}$$

where the symbol $\otimes$ signifies the quaternion composition operation, c.f. Wertz [3].

Substituting Equation 2.6 into Equation 2.4 and expanding leads to the following expression for the observed phase difference,

$$\Delta\varphi_{ij} = (\mathbf{b}_i^{B})^{\mathrm{T}}\left({}^{B}\hat{\mathbf{C}}_0^{L}\,\mathbf{e}_j^{L}\right) + (\mathbf{b}_i^{B})^{\mathrm{T}}\left(2\mathbf{Q}^{\times}\,{}^{B}\hat{\mathbf{C}}_0^{L}\,\mathbf{e}_j^{L}\right) - k_{ij} + \beta_i \tag{2.9}$$

where the predicted phase is given by

$$\Delta\hat{\varphi}_{ij} = \left(\mathbf{b}_i^{B}\right)^{\mathrm{T}}\left({}^{B}\hat{\mathbf{C}}_0^{L}\,\mathbf{e}_j^{L}\right) - k_{ij} + \beta_i. \tag{2.10}$$

The second term in Equation 9 can be rearranged as follows

$$\left(\mathbf{b}_i^{B}\right)^{\mathrm{T}}\left(2\mathbf{Q}^{\times}\,{}^{B}\hat{\mathbf{C}}_0^{L}\,\mathbf{e}_j^{L}\right) = 2\left({}^{B}\hat{\mathbf{C}}_0^{L}\,\mathbf{e}_j^{L}\right)^{\mathrm{T}}\mathbf{B}_i^{\times}\delta\bar{q} \tag{2.11}$$

where $\mathbf{B}_i^{\times}$ is the cross product matrix associated with the components of the vector $\mathbf{b}_i$. Now we can write

$$\delta\varphi_{ij} = 2\ ({}^{B}\hat{\mathbf{C}}_0^{L}\,\mathbf{e}_j^{L})^{\mathrm{T}}\ \mathbf{B}_i^{\times}\ \delta\bar{q} \tag{2.12}$$

and solve this equation for the $\delta\bar{q}$ that minimizes the residuals.

2.2.3 ATTITUDE POINT SOLUTION

The attitude point solution is an iterative least squares fit to a set of simultaneous observations. Since no information about the dynamics of the system is incorporated into the solution, the estimates are noisy. However, it does serve as a benchmark against which other methods can be compared.

The approach here is to solve for the state vector which is given by

$$\mathbf{x} = \begin{bmatrix}\delta q_1 & \delta q_2 & \delta q_3\end{bmatrix}^{\mathrm{T}}, \tag{2.13}$$

using the following equation to predict the phase difference:

$$\Delta\hat{\varphi}_{ij} = (\mathbf{b}_i^{B})^{\mathrm{T}}\left({}^{B}\hat{\mathbf{C}}_0^{L}\,\mathbf{e}_j^{L}\right) + \beta_i - \hat{k}_{ij}. \tag{2.14}$$

In this formulation the line bias is assumed to be known, and $\hat{k}$ is calculated as follows:

$$\Delta\hat{k}_{ij} = \text{int}\left[(\mathbf{b}_i^B)^{\mathrm{T}}\left({}^B\hat{\mathbf{C}}_0^L\ \mathbf{e}_j^L\right) + \beta_i - \Delta\varphi_{ij}\right] \tag{2.15}$$

where the int function rounds to the nearest integer. Then the measurement gradient matrix, $\mathbf{H} = \partial(\Delta\varphi)/\partial\mathbf{x}$, is given by

$$\mathbf{H}_{ij} = 2\left({}^B\hat{\mathbf{C}}_0^L\ \mathbf{e}_j^L\right)^{\mathrm{T}}\mathbf{B}_i^{\times} \tag{2.16}$$

for each baseline i and satellite j.

At each measurement epoch we solve the system of equations $\mathbf{H}_{ij}\delta\bar{q} = \delta\varphi_{ij}$ for $\delta\bar{q}$ and compute updated quaternion, $\hat{\mathbf{q}}^+$, by composing the correction quaternion with the a priori estimate, $\hat{\mathbf{q}}^-$, as follows

$$\hat{\mathbf{q}}^+ = \delta\mathbf{q} \otimes \hat{\mathbf{q}}^- \tag{2.17}$$

The process is repeated until $\delta\bar{q}$ gets sufficiently small.

2.2.4 ATTITUDE KALMAN FILTER

A Kalman filter, by using a dynamical model along with a measurement model, can produce a better solution than the point solution. An extended Kalman filter based on Lefferts, Markley, and Shuster [4] is presented below.

The state vector in this formulation is given by

$$\mathbf{x} = \left[\delta q_1 \quad \delta q_2 \quad \delta q_3 \mid \delta\omega_{I1} \quad \delta\omega_{I2} \quad \delta\omega_{I3} \mid \delta\beta_1 \quad \delta\beta_2 \quad \delta\beta_3\right]^{\mathrm{T}} \tag{2.18}$$

where δq, $\delta\omega_I$, and $\delta\beta$ represent corrections to the local to body quaternion, the inertial angular velocity, and the line biases, respectively. Here the predicted phase difference given by

$$\Delta\hat{\varphi}_{ij} = (\mathbf{b}_i^B)^{\mathrm{T}}\left({}^B\hat{\mathbf{C}}_0^L\ \mathbf{e}_j^L\right) + \hat{\beta}_i - \hat{k}_{ij}, \tag{2.19}$$

where $\hat{k}$ is calculated according to Equation 2.15.

Consider a measurement on baseline i. The elements of the measurement gradient matrix corresponding to the line bias, β_i, is 1. The elements for the quaternion states are calculated by the same equation used in the point solution. All other elements are zero. For example, if baseline 1 observes satellite j, then

$$\mathbf{H}_{1j} = \left[2\left({}^B\hat{\mathbf{C}}_0^L\ \mathbf{e}_j^L\right)^{\mathrm{T}}\mathbf{B}_1^{\times} \;\middle|\; 0 \quad 0 \quad 0 \;\middle|\; 1 \quad 0 \quad 0\right]. \tag{2.20}$$

Between measurement epochs, the quaternion and angular velocity states are advanced to the current measurement time by numerically integrating the appropriate equations of motion. The line biases are assumed to be constant. The covariance matrix is propagated forward with the state transition matrix derived from the linearized equations of motion. The equations of motion for a gravity gradient gyrostat can be found previous technical reports to NRL [5, 6].

2.2.5 ATTITUDE INITIALIZATION

Since the receiver only measures the fractional part of the phase difference, the range difference remains ambiguous until the integer part is resolved. Both the point solution and the Kalman filter require that the attitude, angular velocity, and line biases are known to an equivalent uncertainty of 1/4 of a wavelength so that the integers can be resolved directly.

The batch process presented here is a method of estimating the initial attitude, angular velocity, and integer ambiguities for a spacecraft. These values can then be used as starting points for the other attitude estimation algorithms. This algorithm is based on the method described by Cohen and Parkinson [1].

The vehicle is assumed to rotate with a constant angular velocity so that the attitude matrix can be represented as

$$ {}^{B}\mathbf{C}^{L} = \mathbf{C}(\omega t)\mathbf{C}(\mathbf{q}_0) \tag{2.21} $$

where the quaternion, $\mathbf{q}_0$, represents the attitude of the vehicle with respect to the local frame at some initial time, and ω is the (assumed) constant angular velocity vector of the vehicle with respect to the local frame. This algorithm also assumes that each ambiguity is constant; thus, an interval of data is chosen where there are at least 3 visible satellites that do not loose lock, or experience a cycle slip. In addition, the time span of the data must be short enough so that the angular velocity is approximately constant but long enough to obtain adequate information to resolve the ambiguities.

With an a priori initial attitude and angular velocity, $\bar{\mathbf{q}}_0$ and $\bar{\omega}$, respectively, we can estimate ${}^{B}\mathbf{C}^{L}$ using the following equation,

$$ {}^{B}\hat{\mathbf{C}}^{L} = \delta\mathbf{C}\ {}^{B}\bar{\mathbf{C}}^{L} \equiv (\mathbf{I} + \Theta^{\times})\ \mathbf{C}(\bar{\omega}t)\mathbf{C}(\bar{\mathbf{q}}_0) \tag{2.22} $$

The vector $\bar{\theta}$ represents small rotations about the initial estimate of the body axes and is given by

$$ \bar{\theta} = \begin{bmatrix} \delta\theta_1 \\ \delta\theta_2 \\ \delta\theta_3 \end{bmatrix} + \begin{bmatrix} \delta\omega_1 \\ \delta\omega_2 \\ \delta\omega_3 \end{bmatrix} t, \tag{2.23} $$

and $\Theta^{\times}$ is the cross product matrix associated with the components of $\bar{\theta}$.

The state vector is defined as

$$ \mathbf{x} = \left[\delta\theta_1 \quad \delta\theta_2 \quad \delta\theta_3 \mid \delta\omega_1 \quad \delta\omega_2 \quad \delta\omega_3 \mid \kappa_{11} \quad \cdots \quad \kappa_{mn}\right]^{\mathrm{T}}, \tag{2.24} $$

where κ_{ij} is the integer, k_{ij}, minus the line bias, β_i (i.e. κ_{ij} is a floating point number). The predicted phase difference for baseline i and satellite j is,

$$ \Delta\hat{\varphi}_{ij} = (\mathbf{b}_i^{B})^{\mathrm{T}} \left({}^{B}\bar{\mathbf{C}}^{L}\, \mathbf{e}_i^{L}\right). \tag{2.25} $$

Then the measurement gradient, $\mathbf{H}_{ij}$, for a single measurement is given by

$$ \mathbf{H}_{ij} = \left[\left({}^{B}\bar{\mathbf{C}}^{L}\, \mathbf{e}_j^{L}\right)^{\mathrm{T}} \mathrm{B}_i^{\times} \;\middle|\; \left({}^{B}\bar{\mathbf{C}}^{L}\, \mathbf{e}_j^{L}\right)^{\mathrm{T}} \mathrm{B}_i^{\times} t \;\middle|\; 0 \quad \cdots \quad 0 \quad -1 \quad 0 \quad \cdots \quad 0 \right]. \tag{2.26} $$

The measurement gradient vectors are concatenated into an m by n matrix, $\mathbf{H}$, where m is the number of measurements and n is the number of states. The measurement residuals are then combined into a m-vector, $\mathbf{z}$, to give

$$\mathbf{z} = \begin{bmatrix} \vdots \\ \Delta\varphi_{ijt} - \Delta\hat{\varphi}_{ijt} \\ \vdots \end{bmatrix}. \tag{2.27}$$

Now, to find the best estimate of the corrections solve the system of equations $\mathbf{Hx} = \mathbf{z}$ for $\mathbf{x}$. The small angle corrections are converted to a correction quaternion as follows,

$$\begin{aligned} \delta q_1 &= \delta\theta_1/2 \\ \delta q_2 &= \delta\theta_2/2 \\ \delta q_3 &= \delta\theta_3/2 \\ \delta q_4 &= \sqrt{1 - \delta q_1^2 - \delta q_2^2 - \delta q_3^2} \end{aligned} \tag{2.28}$$

which is in turn used to update the a priori estimate of $\mathbf{q}_0$ according to the quaternion composition rule. The angular velocity is updated in the traditional manner by adding the correction to the a priori estimate. This batch process is iterated until the corrections become sufficiently small.

Since the fractional part of each κ_{ij} represents the constant differential line bias between the two antennas, we can estimate the line bias associated with a baseline i by averaging over all satellites $j = 1,\ldots,l$, where l is the number of GPS satellites. Proximity of the fractional portions is used as an integrity check of the algorithm. If the unaveraged line biases for each baseline are not close to one another, the solution is deemed incorrect. Then another set of initial conditions is chosen and the procedure is repeated.

2.2.6 BASELINE ESTIMATION ALGORITHM

To properly estimate the attitude of a spacecraft, the body reference frame (B) must be clearly defined, and each of the baselines must be accurately known in this frame. A 1 centimeter error in antenna coordinates on a 1 meter baseline can result in a pointing error of 0.5 degrees. If the GPS antennas are not carefully surveyed prior to launch, some assumptions must be made about the relation of the body frame to the antenna array. Mechanical drawings of the spacecraft should provide the location of the antennas to within several centimeters. Refining these estimates is the purpose of the three-step algorithm developed here. First, a sequential filter is used to estimate the line biases, baseline vectors, and inertial angular velocity in the local reference frame. Next, the body fixed frame is defined by two of the local baselines, and all three baselines are transformed from the local frame to the body frame. Finally, the baseline coordinates in the body frame are averaged over time to obtain the best estimate. This method is similar to that presented in Axelrad and Ward [7].

The 15 element state vector for the sequential filter is given by

$$\mathbf{x} = \left[(\delta\mathbf{b}_1^L)^{\mathrm{T}} \quad (\delta\mathbf{b}_2^L)^{\mathrm{T}} \quad (\delta\mathbf{b}_3^L)^{\mathrm{T}} \mid \delta\omega_{I1}^L \quad \delta\omega_{I2}^L \quad \delta\omega_{I3}^L \mid \delta\beta_1 \quad \delta\beta_2 \quad \delta\beta_3 \right]^{\mathrm{T}}, \tag{2.29}$$

and the phase measurement prediction is

$$\Delta\hat{\varphi}_{ij} = (\mathbf{e}_j^L)^{\mathrm{T}} \quad \hat{\mathbf{b}}_i^L + \hat{\beta}_i - \hat{k}_{ij} \tag{2.30}$$

where $\hat{k}$ is calculated according to Equation 2.15.

Consider a measurement on baseline i observing satellite j. The elements of the measurement gradient matrix for baseline i are the elements of the line of sight vector $\mathbf{e}_j^L$. The element corresponding to the line bias, β_i, is 1. All other elements are zero. For example, if baseline 1 observes satellite j, then

$$\mathbf{H}_{1j} = \left[(\mathbf{e}_j^L)^{\mathrm{T}} \quad \bar{\mathbf{0}}^{\mathrm{T}} \quad \bar{\mathbf{0}}^{\mathrm{T}} \,\middle|\, 0 \;\; 0 \;\; 0 \,\middle|\, 1 \;\; 0 \;\; 0 \right]. \tag{2.31}$$

The dynamic model in the filter is given by

$$\left(\frac{d\mathbf{b}^L}{dt} \right)_I = \omega_I^L \times \mathbf{b}^L \qquad \left(\frac{d\omega_I^L}{dt} \right)_I = \mathbf{0} \tag{2.32}$$

where both $\mathbf{b}$ and ω_I (the angular velocity of the body frame with respect to the inertial frame) are expressed in local coordinates. Furthermore, $\mathbf{b}^B$ is assumed to be fixed.

After the baselines have been estimated in the local frame, the body frame is defined as follows:

$$\hat{\mathbf{j}}_B^L \equiv \frac{\hat{\mathbf{b}}_2^L}{\left| \hat{\mathbf{b}}_2^L \right|}, \qquad \hat{\mathbf{i}}_B^L \equiv \frac{\hat{\mathbf{b}}_2^L \times \hat{\mathbf{b}}_1^L}{\left| \hat{\mathbf{b}}_2^L \times \hat{\mathbf{b}}_1^L \right|}, \qquad \hat{\mathbf{k}}_B^L \equiv \hat{\mathbf{i}}_B^L \times \hat{\mathbf{j}}_B^L. \tag{2.33}$$

Figure 2.3 illustrates this definition of the body frame.

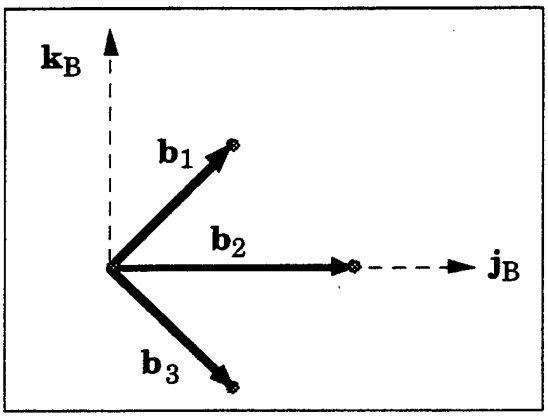

Figure 2.3. Definition of the Body Fixed Frame

Defining the body frame in this way makes use of the information that the baselines are fixed relative to one another. However, this definition assumes that the GPS antenna baselines describe the body frame of interest, which may not necessarily be the case. More likely, a body frame based on some other reference, such as the principal axes, is sought. This means that baselines must be related to the body frame of interest in some way. What we have done here is to simply assume that the baselines are aligned with the principal axes. A more rigorous method of developing this relationship is discussed under future work.

The estimate of the local to body transformation matrix is computed at each measurement epoch with the equation

$$ {}^{B}\hat{\mathbf{C}}^{L} = \begin{bmatrix} \left(\hat{\mathbf{i}}_B^L\right)^{\mathrm{T}} \\ \left(\hat{\mathbf{j}}_B^L\right)^{\mathrm{T}} \\ \left(\hat{\mathbf{k}}_B^L\right)^{\mathrm{T}} \end{bmatrix}, \tag{2.34} $$

and the estimated local baselines are transformed to the body frame. Since the baseline vectors in the body frame should remain constant, their coordinates can be averaged over time to obtain the best estimate.

2.3 BOOTSTRAPPING PROCESS

Assume the baselines, line biases, integer ambiguities, and attitude of a spacecraft are unknown. To begin the attitude estimation process, a rough estimate of both vehicle attitude and antenna locations are needed. Broad assumptions can be made about the attitude of a spacecraft based on vehicle design and/or GPS satellite visibility. For example, a gravity gradient satellite would most likely be nadir pointing. Checking received GPS signal strength could verify this assumption and provide additional attitude information. To determine the antenna locations in the spacecraft body frame, [2] developed a static self-survey algorithm to provide baseline and bias estimates to an accuracy of several millimeters. Without the self-survey, however, we must rely on a mechanical drawing of the spacecraft which should provide the location of antennas to within several centimeters.

The ad hoc attitude and baseline estimates described above are sufficient to start the bootstrapping process. First, the attitude initialization algorithm is employed to improve the a priori estimate of the initial attitude to within 5 degrees. With accurate baselines, enough information is now available to apply the attitude Kalman Filter with accurate results. However, if the baselines are not well known, the baseline estimator is used to improve the knowledge of the relative antenna coordinates and the line biases before running the attitude filter.

For a highly accurate attitude solution, the point solution would not be used directly in the bootstrapping process. However, it can provide valuable information about measurement and process noise in the data. Table 2.1 lists the input requirements and expected performance of each algorithm.

Table 2.1. Bootstrapping Algorithm Requirements and Performance

Parameter	Input Requirements	Output Performance
Initial Attitude Determination		
attitude	unknown	5 deg
baselines	2 cm	n/a
line biases	no knowledge	1/4 cycle
Baseline Estimator		
attitude	5 deg	n/a
baselines	2 cm	5 mm
line biases	1/4 cycle	0.03 cycles
Attitude Kalman Filter		
attitude	5 deg	0.2 deg
baselines	5 mm	n/a
line biases	1/4 cycle	0.03 cycles
Point Solution		
attitude	5 deg	1.0 deg
baselines	5 mm	n/a
line biases	1/4 cycle	n/a

2.4 RESULTS

2.4.1 RADCAL DATA

The Air Force RADCAL satellite is the first known spacecraft to demonstrate the operation of attitude determination using GPS [8]. RADCAL is a gravity gradient stabilized satellite in a circular, polar orbit at an altitude of 815 kilometers. The main body of the spacecraft is about 76 centimeters in diameter with a 6 meter boom. Four GPS antennas are mounted on the zenith face of the main body and canted outward 17.5 degrees. A Trimble Quadrex receiver collects the raw differential carrier phase data which is transmitted to the ground for attitude post-processing. GPS receiver data collected on board RADCAL are posted on the TECNET. RADCAL navigation solutions which have been corrected for Selective Availability are also on the TECNET. With the help of Bill Feess and Robert Smith of Aerospace Corporation we have obtained access to the TECNET and can download RADCAL data to a local computer. In addition, with Dave Starr's assistance, we have obtained the Jet Propulsion Laboratory's precise GPS orbits via anonymous FTP.

2.4.2 SIMULATED DATA

A FORTRAN simulation modeling a spacecraft using GPS for attitude determination has been developed. The simulation generates GPS differential phase measurements and user-to-GPS line of sight data for the purpose of testing these algorithms. The attitude dynamics of the user satellite are based on a gravity gradient satellite (either with or without a spinning wheel). The user satellite orbit dynamics are based on a two-body orbit with oblate Earth perturbations. The position and velocity of the GPS satellites are calculated using a simpler model which includes only two-body effects. After the true range difference between antennas is calculated, the measurement error, modeled as a discrete first order Markov process, is added.

2.4.3 ATTITUDE INITIALIZATION RESULTS

A number of data sets have been processed and analyzed. The RADCAL data used to produce the results presented below was collected on day 160 of this year (9 June 1994). The data starts at noon and spans almost 18 hours. The a priori yaw, roll, and pitch for the Attitude Initialization were all chosen to be zero. The a priori values for the angular velocity and line biases were also set to zero. The baseline vectors were fixed to the values reported in [9] which are based on the vehicle mechanical drawings. Using a 10 minute span of data, the algorithm converged to an attitude solution in 15 iterations. The results are reported in Table 2.2. The standard deviation (STD) of the line bias estimates is also given.

Table 2.2. Attitude Initialization Results
RADCAL - Day 160

Euler Angles (deg)		Angular Velocity (deg/sec)		Line Biases (cycles)		Line Bias STD (cycles)	
yaw:	-163.9	ω_{I1}:	-0.86×10^{-3}	β_1:	0.66	σ_1:	0.09
roll:	-4.0	ω_{I2}:	-0.19×10^{-3}	β_2:	0.46	σ_2:	0.10
pitch:	5.3	ω_{I3}:	1.13×10^{-3}	β_3:	0.37	σ_3:	0.06

2.4.4 ATTITUDE KALMAN FILTER RESULTS

The initial attitude estimated above was used to start the Attitude Kalman Filter. The standard deviation of the measurement noise was assumed to be 1 centimeter. A small process noise was chosen corresponding to a change in the quaternion of 0.001 over a 1 second interval. Differential phase measurements with signal-to-noise ratios of less that 3 AMU* were screened out of filter solution. Refinement of these input values is still in progress.

The attitude solutions are shown in Figure 2.4, and they are typical of the results obtained with other data sets. The 1-σ uncertainties reported by the Kalman filter are less than 0.2 degrees for yaw, roll, and pitch angles. The 1-σ uncertainties in each of the angular velocities is less than 1.2×10^{-3} degrees/second. Figure 2.5 shows the line biases. Although, they take almost one hour to converge, the estimates remain constant for the remainder of the run, as expected.

2.4.5 ATTITUDE POINT SOLUTION RESULTS

The initial attitude estimated above, was used to initialize the point solution algorithm. The line biases were fixed to the estimates calculated in the Kalman filter. Again, measurements with signal-to-noise ratios of less than 3 AMU were excluded from the solution. The results are shown in Figure 2.6. Although the point solutions are noisier than the filter solutions, they are qualitatively similar. The attitude difference resulting from subtracting the point

* Amplitude Measurement Unit. Corresponds to the amplitude of recovered carrier in a bandwidth of 1KHz.

solutions from the filter solutions is shown in Figure 2.7. The RMS of these differences is 0.81 degrees for yaw, 0.72 degrees for roll, and 0.79 degrees for pitch.

2.4.6 BASELINE ESTIMATION RESULTS

Since baselines 1 and 2 were used to define the rotation matrix from body to local coordinates, we look at the results for baseline 3 as an indication of how well the algorithm works. Figure 2.8 shows the estimated body frame coordinates of baseline 3. As expected the average of each coordinate remains constant.

2.4.7 ADDITIONAL RESULTS - DAY 189

The most recently processed data set was collected on Day 189 (8 July 1994). Figures 2.9 and 2.10 show the Euler angle and line bias estimates from attitude filter. One difference between these results and previous ones is the 5 hour period where the yaw angle is constant. Reasons for this type of motion are under investigation.

We note that the attitude initialization algorithm did not work as expected on this particular data set. Although the initial attitude converged to a reasonable answer, the line biases were inconsistent. Perhaps there was not enough motion observed to resolve the integers. To work around this problem, we used the line bias attitude filter estimates from Day 160. This approach produced the results shown in Figures 2.9 and 2.10. Using this approach to initialize the point solution algorithm also produced similar results. The RMS of the attitude difference between the point and filter solutions is less than 0.6 degrees for each angle.

Figure 2.4. Attitude Kalman Filter Euler Angles
RADCAL - Day 160

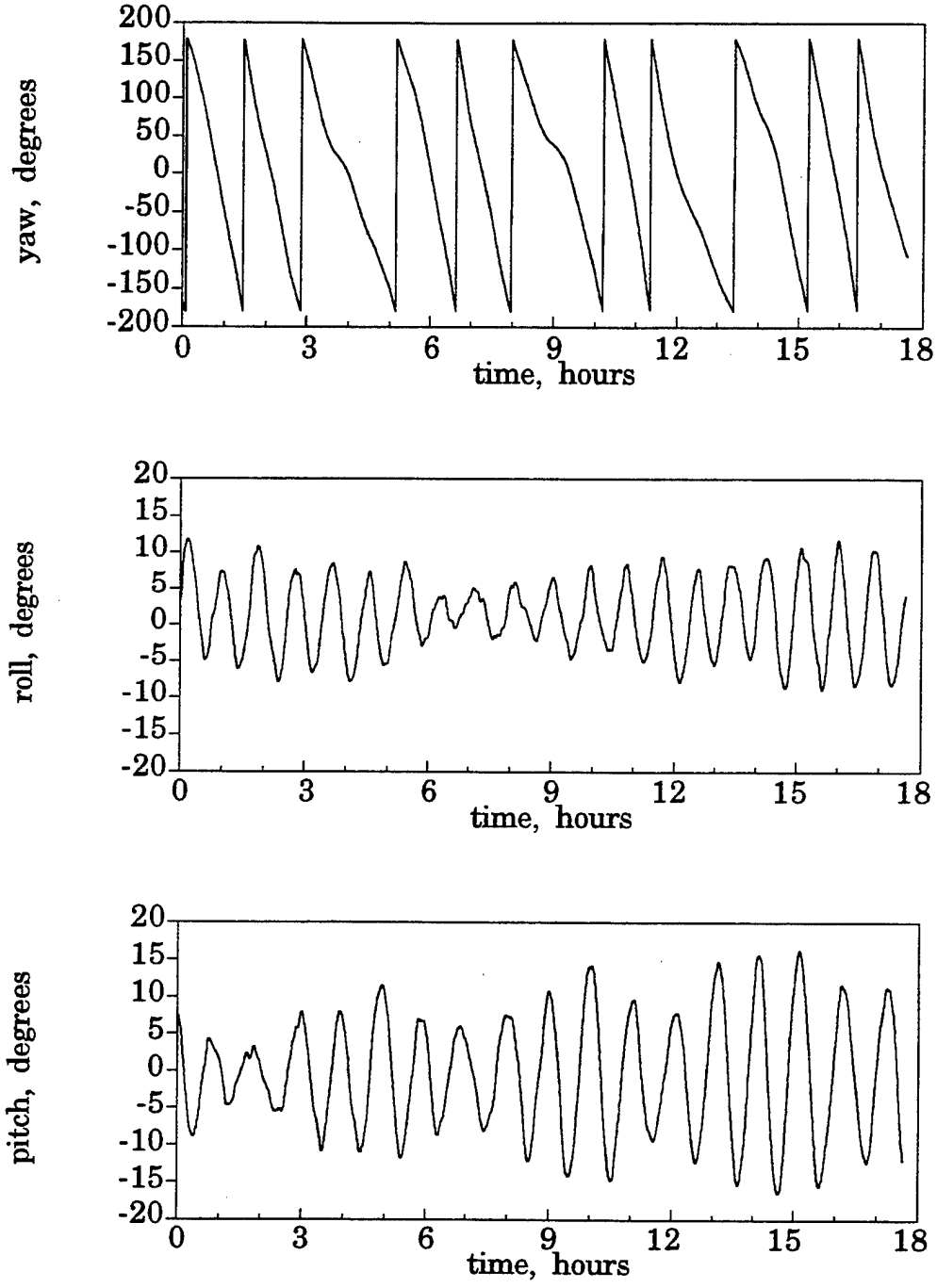

Figure 2.5. Attitude Kalman Filter Line Biases
RADCAL - Day 160

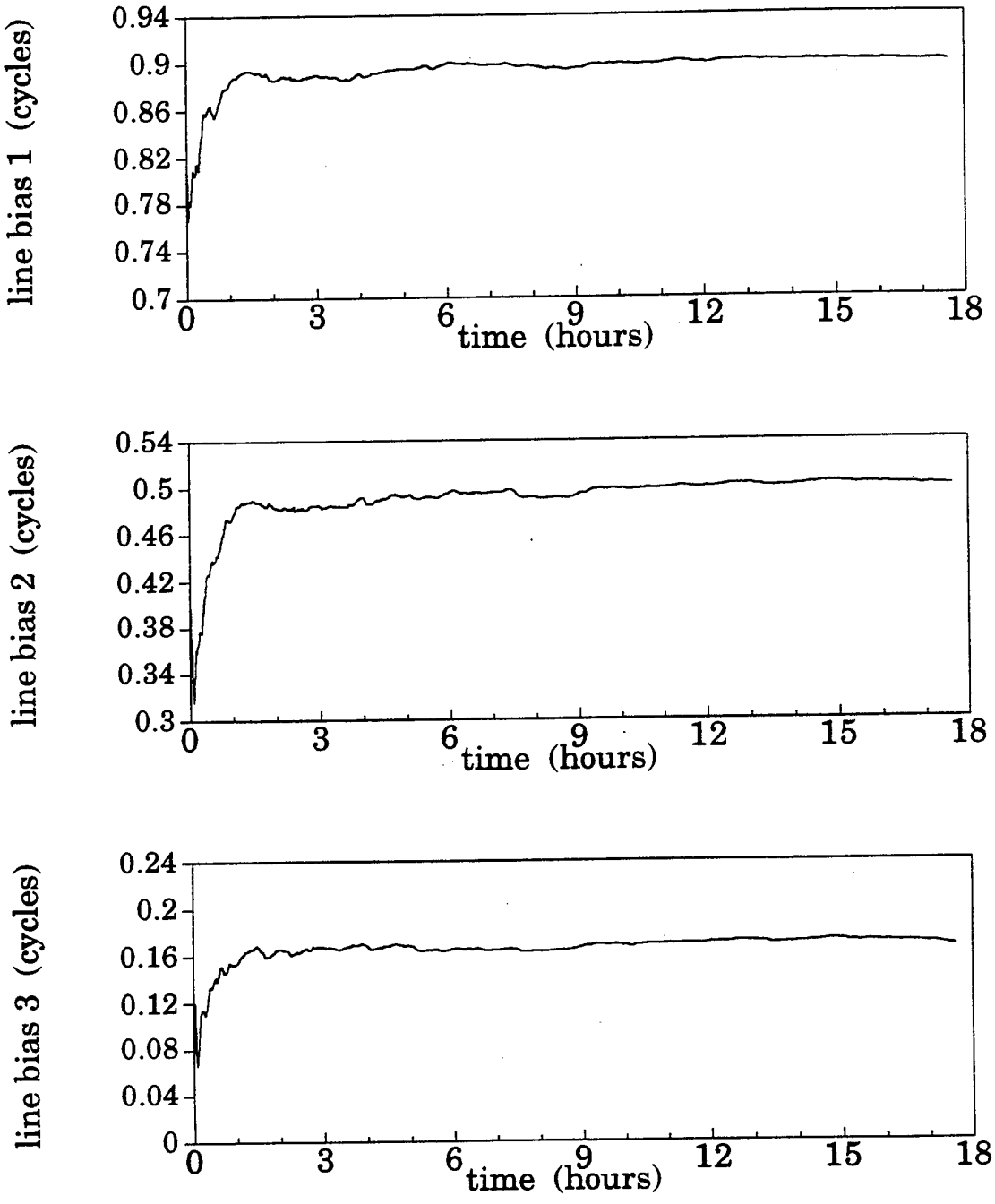

Figure 2.6. Attitude Point Solution Results
RADCAL - Day 160

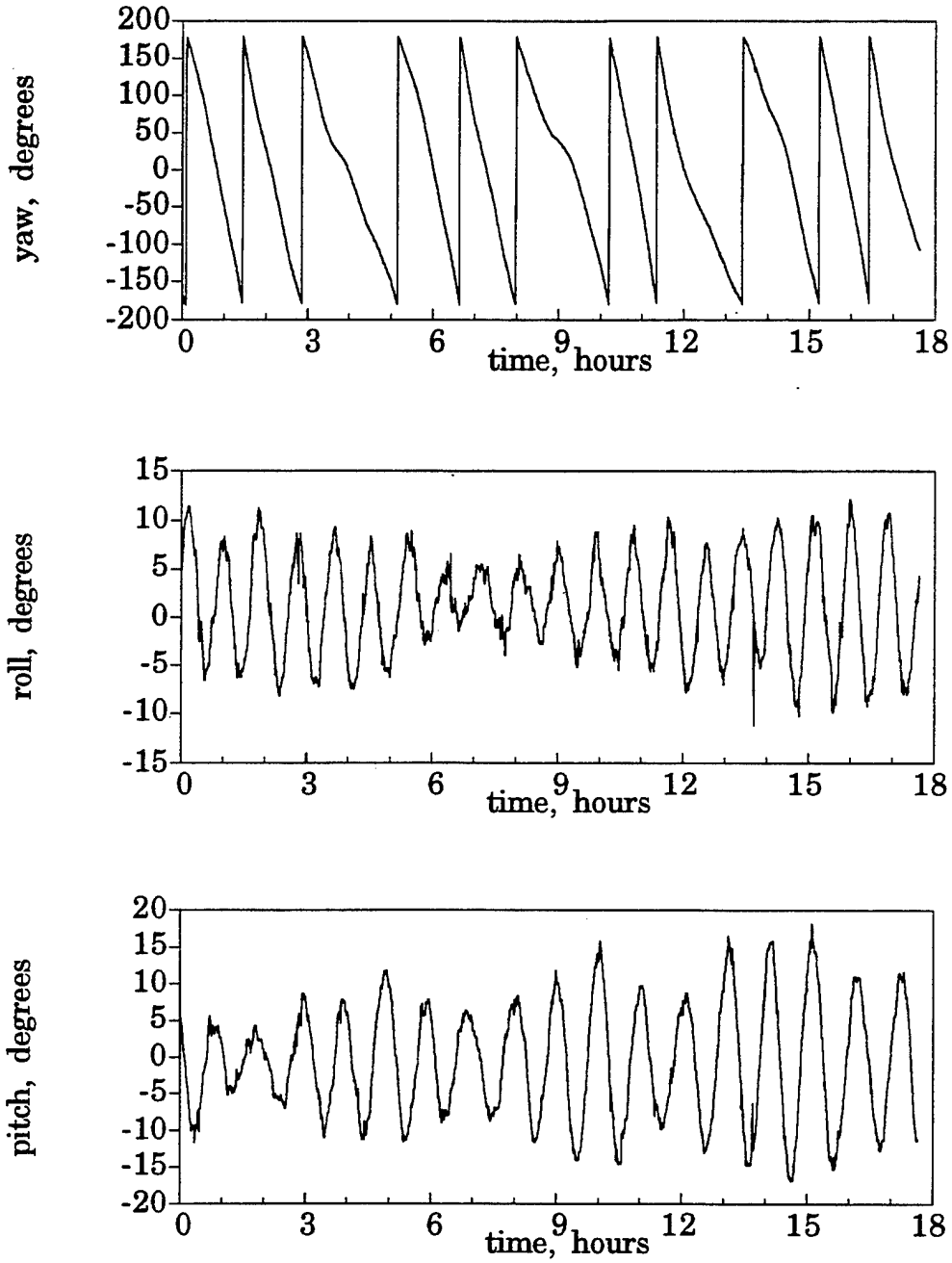

Figure 2.7. Point vs. Filter Attitude Difference
RADCAL - Day 160

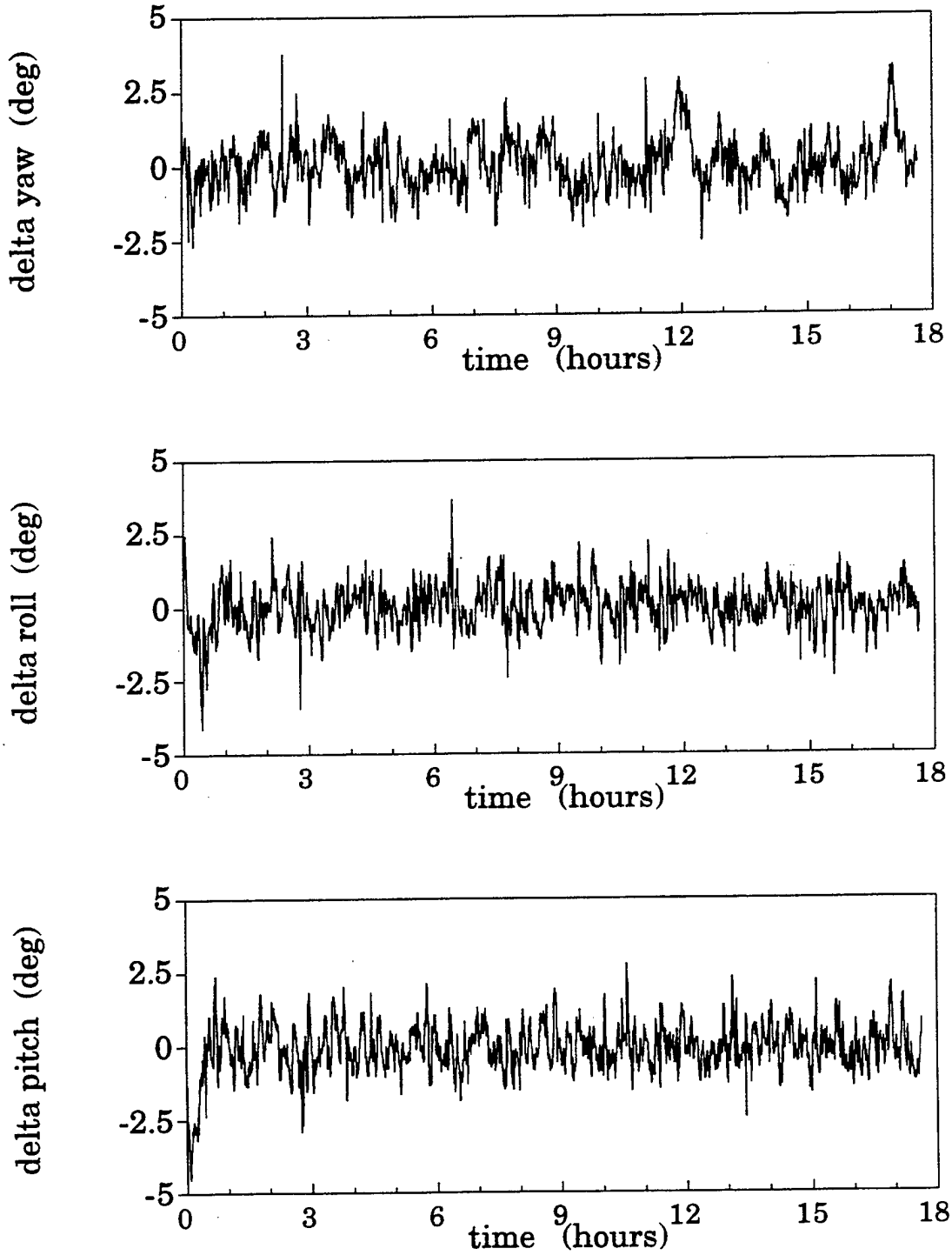

Figure 2.8. Baseline Estimation Results
Baseline 3 Coordinates in the Body Frame
RADCAL - Day 160

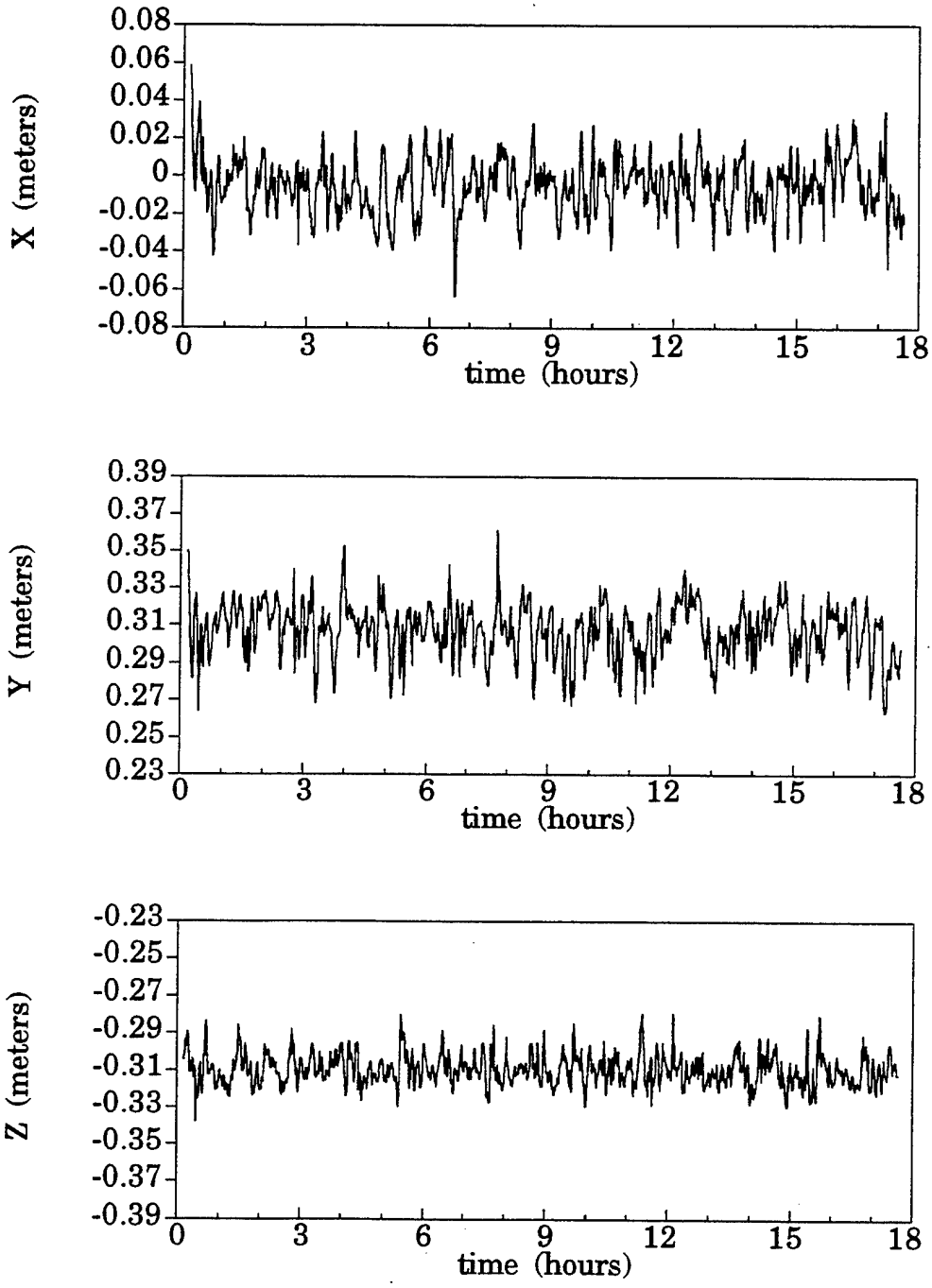

Figure 2.9. Attitude Kalman Filter Euler Angles
RADCAL - Day 189

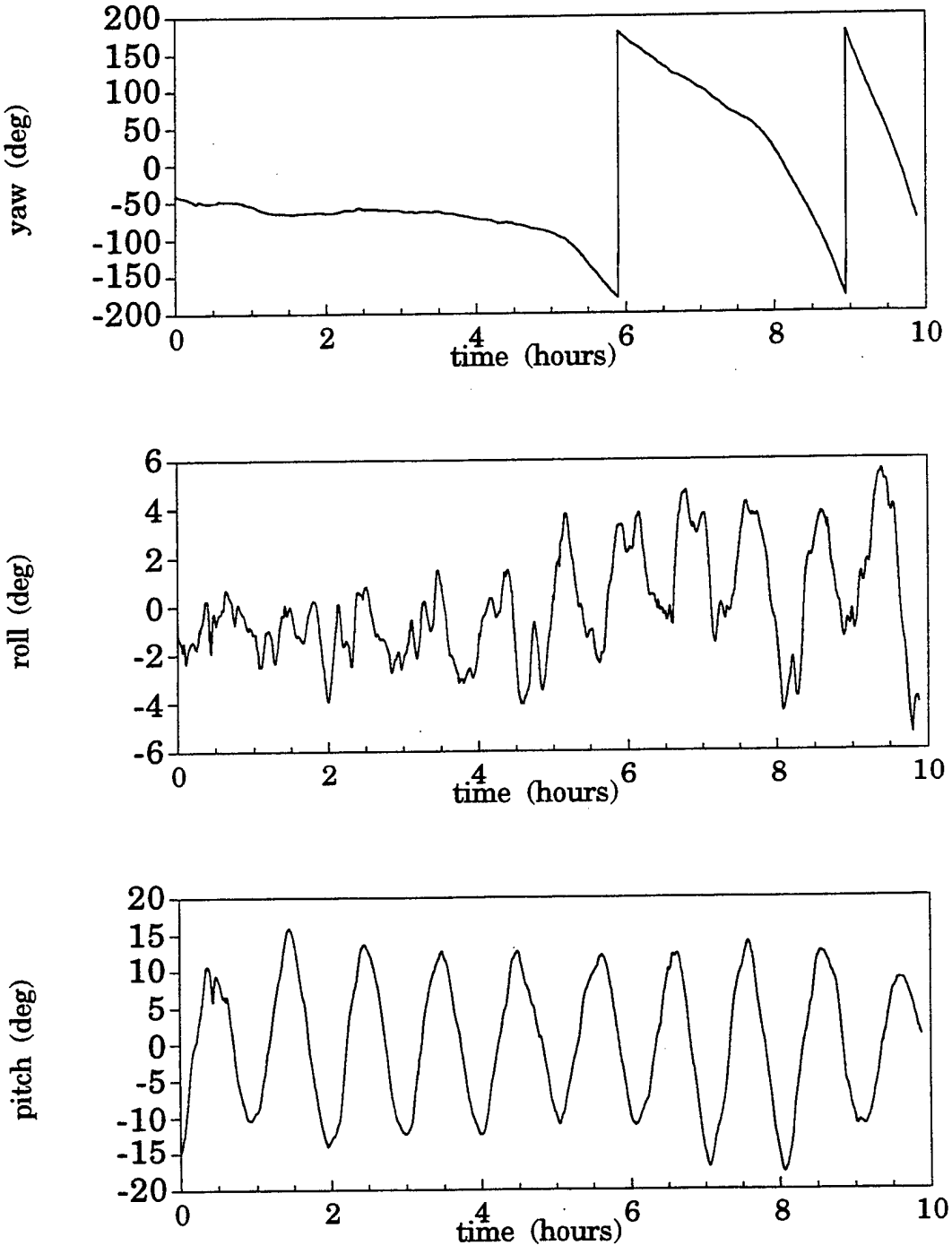

Figure 2.10. Attitude Kalman Filter Line Biases
RADCAL - Day 189

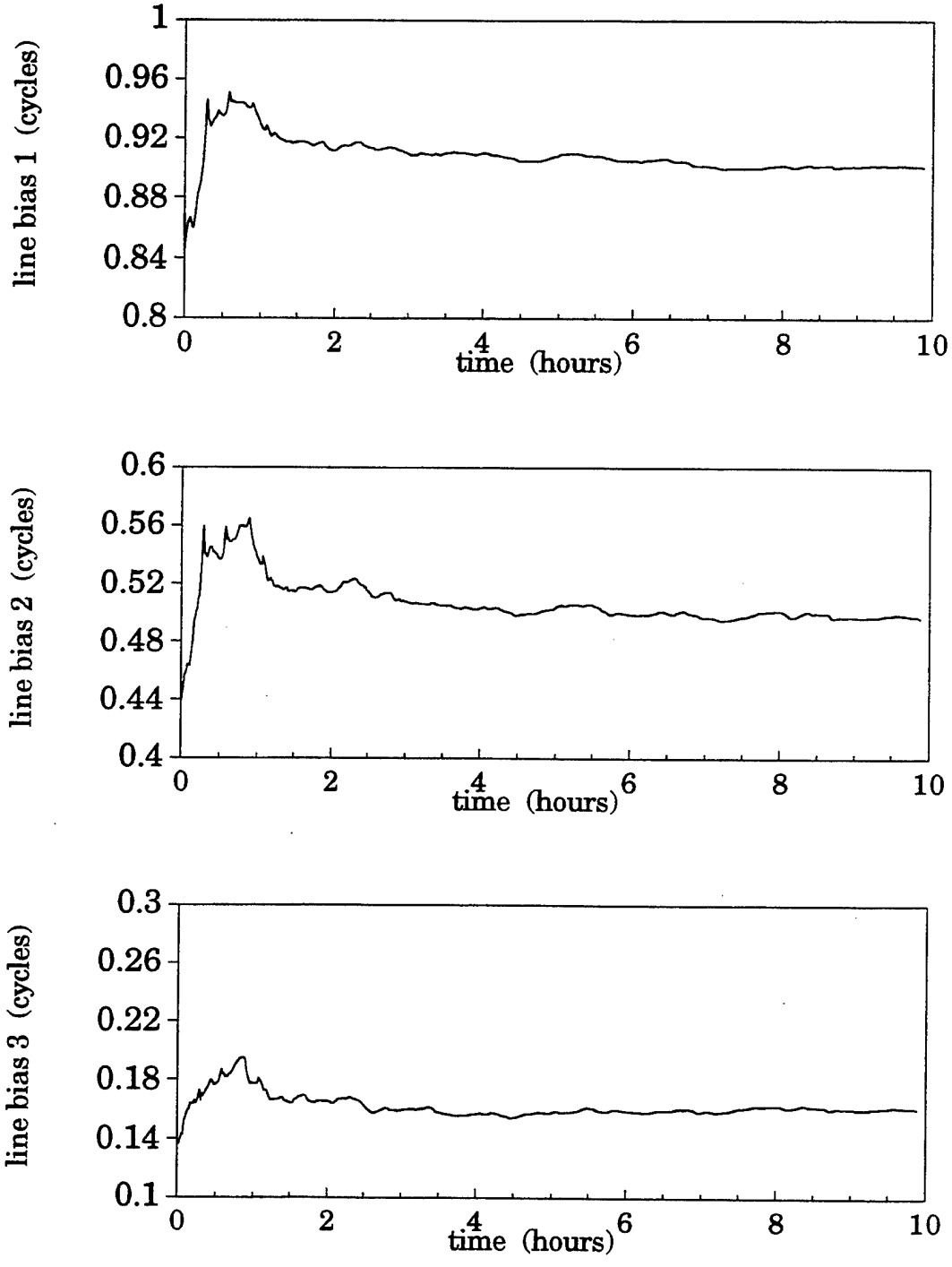

2.4.8 DISCUSSION

Currently, there is no external "truth" against which to compare the RADCAL attitude solutions. We can, however, compare results from different methods and/or different data sets to obtain a measure of quality. Furthermore, evaluating the consistency between data sets of relatively fixed parameters, such as baselines and line biases, provides a measure of accuracy.

The expected natural pitch and roll frequencies for a gravity gradient satellite with RADCAL's moments of inertia, I, and orbital motion, n, can be calculated with the following equations:

$$\omega_p = n\sqrt{3(I_2 - I_1)/I_3} \qquad (2.35)$$
$$\omega_r = n\sqrt{4(I_3 - I_1)/I_2}$$

The observed frequencies can be determined by taking a Fast Fourier Transform (FFT) of the RADCAL attitude solutions. From Figure 2.11, which shows an FFT of the pitch angle for day 160, it is clear that most of the power is concentrated at the natural frequency (~1.7 x10^{-3} rad/sec), with very little power at the orbital frequency (~ 1.03 x10^{-3} rad/sec). The results of both methods are compiled in Table 2.3. The expected periods of the pitch and roll motions agree with the observed periods to within 2.7 percent.

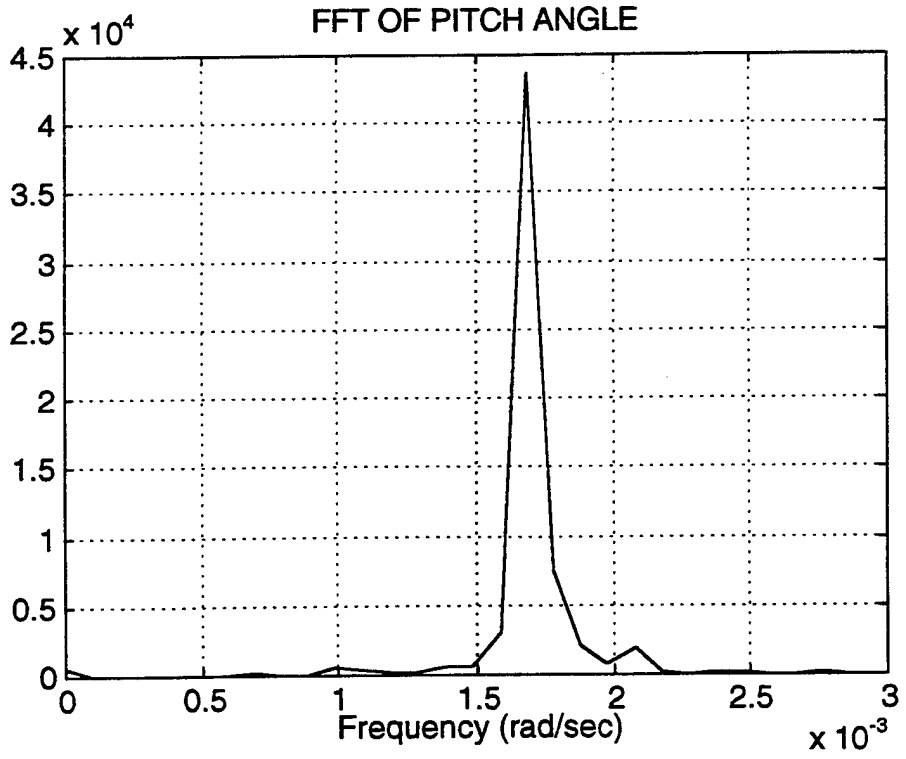

Figure 2.11 FFT of Pitch Angle
RADCAL - Day 160

Table 2.3. RADCAL Pitch and Roll Periods

	Expected (min)	Day 160 FFT (min)
pitch period	60.85	60.22
roll period	52.47	53.90

Table 2.4 contains the Baseline Estimator results for days 107, 160, and 189. The maximum difference between these coordinates is 3 millimeters. Also included in Table 2.4 are the estimates obtained from the mechanical drawings. The maximum difference between the mechanical drawings and any of the Baseline Estimator results is 12 millimeters.

Table 2.4. Baseline Vector Estimates in meters

Baselines		Day 107	Day 160	Day 189	Mechanical
1	x	0.0	0.0	0.0	0.0
	y	0.306	0.303	0.304	0.313
	z	0.310	0.308	0.309	0.313
2	x	0.0	0.0	0.0	0.0
	y	0.616	0.614	0.615	0.626
	z	0.0	0.0	0.0	0.0
3	x	-0.003	-0.005	-0.004	0.0
	y	0.309	0.307	0.308	0.313
	z	-0.310	-0.309	-0.309	-0.313

In Table 2.5 we also compare the line bias results from both the Baseline Estimator (BE) and Attitude Kalman Filter (AKF). The largest maximum difference, which occurs on line bias 2, is 0.026 cycles or 5 millimeters.

Table 2.5. Line Bias Estimates in cycles

Line Bias	Day 107		Day 160		Day 189	
	AKF	BE	AKF	BE	AKF	BE
β_1	0.8909	0.8992	0.8995	0.8925	0.9008	0.9030
β_2	0.4954	0.4859	0.5005	0.5013	0.4967	0.4751
β_3	0.1611	0.1668	0.1673	0.1727	0.1608	0.1668

2.5 SUMMARY AND FUTURE WORK

In summary, this section described a methodology for attitude determination onboard a gravity gradient stabilized near-Earth satellite using GPS. We have presented a sequence of algorithms -- attitude initialization, attitude point solution, attitude Kalman Filter, and on-orbit baseline estimation, which have been successfully applied to both simulated and actual flight data collected onboard the Air Force RADCAL satellite. Each algorithm represents increasing requirements for a priori knowledge of the vehicle state and dynamics, which consequently, improves output accuracies. The accuracy of the final attitude estimates, based on data from RADCAL is assessed to be at the level of 15 arc minutes.

The work still to be addressed falls into two main categories: improving robustness and improving accuracy. Robustness issues include evaluating the convergence region of the

attitude initialization algorithm. More specifically, we will determine how much motion is needed to resolve the integers, and how much change in angular velocity can be tolerated. We will also develop an automated data selection process which takes these factors into account.

To increase the accuracy of the baseline estimation process, we plan to combine the attitude and baseline filters into one comprehensive package. One approach we are considering is to estimate corrections to the baselines in the attitude filter. Another approach would be to pass the current estimate of the attitude into the baseline estimator to ensure that the most accurate attitude information is used. In the same manner, baseline information could be passed back to the attitude filter to allow for flexing baselines.

We will also investigate how unmodeled torques affect the accuracy of the attitude filter by first identifying significant perturbations and including them in the simulation. Errors in the attitude solution resulting from these perturbations should be easily quantifiable. We will also determine which perturbations, if any, should be added to the attitude filter dynamics to obtain the required performance.

2.6 REFERENCES

[1] Cohen, C.E. and B.W. Parkinson, "Integer Ambiguity Resolution of the GPS Carrier for Spacecraft Attitude Determination," AAS 92-015, AAS Guidance and Control Conference, Keystone Colorado, Feb. 8-12, 1992.

[2] Cohen, C.E. *Attitude Determination Using GPS*, Ph.D. Dissertation, Department of Aeronautics and Astronautics, Stanford University, Dec. 1992.

[3] Wertz, J.A., Ed., *Spacecraft Attitude Determination and Control*, Kluwer Academic Publishers, Netherlands, 1978.

[4] Lefferts, E.J., F.L. Markley, and M.D. Shuster, "Kalman Filtering for Spacecraft Attitude Estimation", *Journal of Guidance, Control, and Dynamics*, AIAA Paper 82-0070, AIAA 20th Aerospace Sciences Meeting, Orlando, FL, Jan. 1982.

[5] Axelrad, P., P.F. MacDoran, C.P. Behre, C.J. Comp, L. M. Ward, "GPS Based Attitude Determination", FY'93-94 Technical Report I to the Naval Research Laboratory, May 16, 1994.

[6] Axelrad, P., B.C. Chesley, L. M. Ward, "GPS Based Spacecraft Attitude Determination", Final Report for October 1992-September 1993 to the Naval Research Laboratory, Sept. 1993.

[7] Axelrad, P. and L.M. Ward, "On-Orbit GPS Based Attitude and Antenna Baseline Estimation," Proceedings of the ION National Technical Meeting, San Diego, CA, Jan 24-26, 1994.

[8] Cohen, C.E., E. G. Lightsey, B.W. Parkinson, and W.A. Fees, "Space Flight Tests of Attitude Determination Using GPS: Preliminary Results", Preprint of paper presented at ION GPS-93, Salt Lake City, Sept. 22-24, 1993.

[9] Lightsey, E.G., C.E. Cohen, W. A. Feess, and B.W. Parkinson, "Analysis for Spacecraft Attitude Measurements Using Onboard GPS", AAS Guidance and Control Conference, Keystone, CO, February, 1994.

3.0 MULTIPATH CORRECTION

Christopher J. Comp

3.1 INTRODUCTION

High precision measurements of the GPS L-Band carrier phase have been used for a wide variety of surveying applications ranging from worldwide geodetic networks to kinematic survey on both land and sea. More recently, attitude determination systems based on the carrier phase observable have been developed and demonstrated on land [1], sea [2], air [3,4], and in space [5,6]. The key observable in each of these systems is the difference in the received phase measured by two antennas to a single satellite, known as the differential phase. When two separate receivers are used to track the two antennas, as is the case in a survey application or in some attitude determination systems [c.f. 1,2,4], the difference between differential phase measurements for two satellites (double difference) is used as the observable. This eliminates the effect of the different receiver clocks on the observations.

The limiting factor on performance in almost all attitude determination applications has been identified as multipath. Similarly, in some high precision surveying environments, multipath appears to be the dominant error source. Multipath is the corruption of the direct GPS signal by one or more signals reflected from the local surroundings. Figure 3.1 shows an example of differential phase residuals between two fixed antennas. The structured oscillations are characteristic of multipath interference. The residual data has the first order GPS satellite motion removed, leaving the multipath and receiver measurement noise. In this particular set of data, the multipath produced peak errors of 8 millimeters with low frequency components. Uncorrected, these measurement errors would produce corresponding attitude errors at the level of 8 milliradians (0.46 degrees) for a 1 meter antenna baseline length.

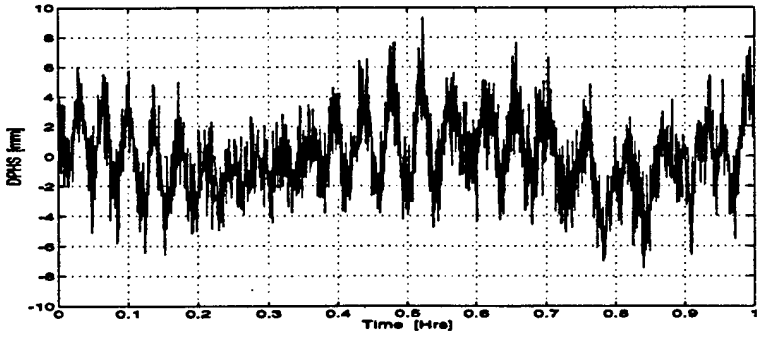

Figure 3.1: Differential phase data for a 1 meter patch antenna baseline. *The data was collected May 24, 1994, with a Trimble Vector attitude receiver. The horizontal axis is time in minutes, the vertical axis is differential phase residual in millimeters.*

The topic of multipath mitigation in GPS phase measurements has received considerable attention in the literature. Several researchers have recommended various means of devising maps of the multipath environment surrounding an antenna. These maps provide multipath

corrections for each satellite signal as a function of its azimuth and elevation. Hajj [7] at JPL developed a simulator specifically for spacecraft multipath characterization. This software package has been used to predict the multipath characteristics on board TOPEX and other satellites. Cohen and Parkinson [8,9] at Stanford University compiled a multipath map based on experimental results. By tracking all satellites in view for 24 hours, they compiled a set of differential phase data to which a spherical harmonic model was adjusted. Clark [10] at NASA Goddard Space Flight Center suggested that phase and amplitude data could be useful to make a holographic map of the multipath environment, but the receivers he had access to at the time did not provide sufficient amplitude resolution. The limitation of these approaches is that they only work well if the antenna environment remains constant. While it has been widely demonstrated that code multipath is highly repeatable, our experiments have shown (unintentionally) that phase multipath is quite sensitive to even small environmental changes.

Other researchers have investigated the use of the data itself to identify or correct multipath. Georgiadou and Kleusberg [11] describe methods for identifying the presence of multipath by looking at the difference between L1 and L2 phase observations. Their technique could possibly be used to reduce multipath errors in an attitude determination system, but it does require dual frequency capability.

The approach described here overcomes many of the shortcomings of previously recommended techniques. It utilizes the ratio of the amplitude of the recovered carrier signal to the noise ratio (SNR) and the known antenna gain pattern to create a multipath correction profile. Thus, a new correction profile is generated for each data set, eliminating the requirement that the environment remain unchanged. The technique has been successfully used in a post processing mode on data collected during static ground tests with the Trimble Vector receiver.

Section 3.2 provides background theory and Section 3.3 details the multipath profiling procedure. Sections 3.4 and 3.5 describe the ground tests and results for a static antenna array. Section 3.6 contains a discussion of the results. Section 3.7 suggests applications and future enhancements of the proposed methodology.

3.2 MULTIPATH THEORY

The GPS 1575.42 MHz carrier signal is biphase modulated with the C/A and P-codes. The typical modern receiver downconverts the received signal to an IF frequency, and digitally samples to produce in-phase (I) and quadrature (Q) components. It then aligns the received signal with a locally generated replica using a delay lock loop (DLL). The output of the punctual correlator is the recovered carrier signal. The standard definition of the signal to noise ratio (SNR) has the recovered carrier power as the numerator and the noise power as the denominator. The SNR is an indication of the magnitude of the recovered carrier signal. The SNR is affected by correlator performance, antenna gain characteristics, and multipath.

The recovered IF signal, consisting of both direct and multipath components, serves as one input to a phase-lock loop (PLL). The other input to the PLL is a local replica of the carrier generated by an NCO. In a standard receiver, the output frequency of the NCO is controlled so as to make the local signal align with the received signal. Thus, when the PLL first achieves frequency lock between the local and incoming signals, a phase comparator can measure the fractional phase difference of the two signals - this is the phase offset. Thereafter, subsequent commands to the NCO essentially keep track of changes in this phase difference. This value is what we refer to as the phase of the signal, but is more accurately described as accumulated doppler.

The Trimble Vector receiver provides a comparable measurement in a somewhat different manner. The signal from the antenna designated as the master is used to control the NCO in the PLL. The phase measurement reported for the master corresponds to that described above. The slave antennas, on the other hand, only report the phase difference between the signal coming from the slave and the signal generated by locking to the master signal. Hence, the channel directly outputs the phase difference between the each slave and the master antenna. The Trimble Vector receiver measures the amplitude of the recovered carrier within the channel bandwidth. This amplitude is reported separately for each antenna as the SNR in Trimble Amplitude Units (AMU). In keeping with the measurements, we will use SNR to mean an amplitude ratio rather than the more common power ratio.

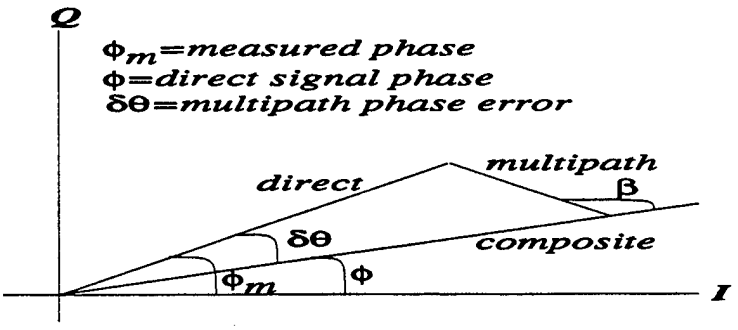

Figure 3.2: Phasor diagram. *Depicts the relationship between the composite, direct, and multipath signals. The horizontal and vertical axes represent the in-phase and quadrature phasor components, respectively.*

A phasor diagram such as that in Figure 3.2 is a useful way to represent the relationship between the direct signal, one or more multipath signals, and the composite signal which is tracked by the PLL. Each signal is represented by a complex number $r = Ae^{j\theta}$, where A is the amplitude of the signal, and θ is the phase. In addition to reporting the phase of the composite signal θ_c, the PLL also reports the amplitude of the composite signal A_c, as the signal to noise ratio.

$$A_c = SNR \tag{3.1}$$

The direct signal is modeled as $r_d = A_d e^{j\theta_d}$, where the amplitude A_d is the product of two factors, one constant and the other a function of the antenna gain pattern and the azimuth

and elevation of the satellite as seen by the antenna.

$$A_d \equiv A_o A(antgain, az, el) = A_o A_a \tag{3.2}$$

Each multipath signal is modeled as $r_i = A_i e^{j(\theta_d+\beta_i)}$, with $A_i = \alpha_i A_o$, where α_i is the ratio of the multipath amplitude to the constant part of the direct signal amplitude, and β_i is the phase of the multipath signal relative to the direct. Generally, $\alpha_i = \frac{A_i}{A_o} < 0.1$.

The composite signal can be written as:

$$\begin{aligned} r_c &= r_d + \sum_i r_i \\ &= [A_o A_a)]e^{j\theta_d} + \sum_i \alpha_i A_o e^{j(\theta_d+\beta_i)} \end{aligned} \tag{3.3}$$

where i is summed over all multipath signals present. The composite signal, that which is truly tracked in the receiver PLL, has magnitude:

$$A_c = \sqrt{(A_o A_a + \sum_i \alpha_i A_o \cos(\beta_i))^2 + (\sum_i \alpha_i A_o \sin(\beta_i))^2} \tag{3.4}$$

which is expressed in the form of the SNR by the receiver. The difference in the phase between the composite and direct phasors, or the phase error, is given by:

$$\tan(\delta\theta) = \frac{\sum_i \alpha_i A_o \sin(\beta_i)}{A_o A_a + \sum_i \alpha_i A_o \cos(\beta_i)} \tag{3.5}$$

For small α_i the magnitude and phase error expressions can be approximated as follows:

$$A_c \approx (A_o A_a)\left[1 + \frac{\sum_i \alpha_i A_o \cos(\beta_i)}{A_o A_a}\right] \tag{3.6}$$

and

$$\begin{aligned} \delta\theta &\approx \frac{\sum_i \alpha_i A_o \sin(\beta_i)}{A_o A_a + \sum_i \alpha_i A_o \cos(\beta_i)} \\ &= \frac{\sum_i \alpha_i A_o \sin(\beta_i)}{A_c} \end{aligned} \tag{3.7}$$

As an example, we now look at the direct signal plus a single multipath component, as displayed in Figure 3.2. For the moment, assume that the amplitudes of both the direct and multipath signals are constant. The changes in relative phase of the multipath component due to satellite motion can be seen to produce changes in the amplitude of the resultant, and hence in the SNR. The amplitude is maximized when β =0, and minimized when

β=180 degrees. As β increases, the multipath phasor rotates around the tip of the direct, producing an oscillation in the phase error and the SNR. The maximum phase error occurs when β =90 or 270, and is equal to $max(\delta\theta) = \frac{\alpha A_a}{A_c}$. Note that the phase error is 90 degrees out of phase with the amplitude. In effect when β =0 or 180 degrees, the phase error due to multipath is zero.

What we now propose to do is use SNR data to determine the amplitude and phase of each multipath constituent, and then construct an estimate of the resulting phase error. The sum of these estimates constitutes a multipath correction profile.

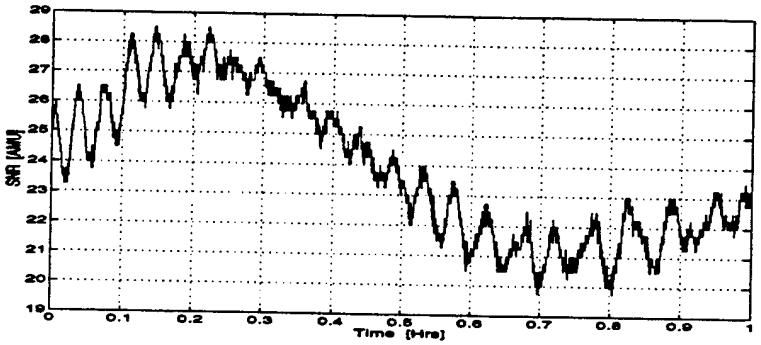

Figure 3.3: SNR data showing multipath. *The resultant SNR signal contains a direct and one or more multipath components. The direct signal accounts for the large offset of the multipath signature. The data was collected May 24, 1994, with a Trimble Vector receiver. The horizontal axis is time in minutes, the vertical axis is SNR in units of Trimble amplitude measurement units (AMU).*

Figure 3.3 shows the reported SNR for a single antenna. If the data spanned a longer time frame, a parabolic signature would be visible due to the gain differences as the satellite line of sight traverses the gain pattern. For the time shown, it appears as a constant offset. The SNR data can be adjusted by subtracting off the gain pattern effect. It is assumed that the gain pattern variations in azimuth and elevation are smooth, such that little or no residual gain pattern effects contaminate the adjusted SNR.

The remaining oscillations are produced by multipath, the frequency of which is dictated by the vector connecting the antenna to the reflector, and the rate of change of the direction of the line of sight vector. Basically, a reflector placed near an antenna produces multipath with a lower frequency than an antenna at a distance.

If we assume that this frequency is constant, then the relative phase of the multipath signal compared to the direct can be modeled as:

$$\beta = \omega t + \phi \tag{3.8}$$

where β was described previously, t is measured relative to any convenient time, and ϕ is the relative phase offset of the multipath signal at t =0. The fact that the multipath components have distinct frequencies enables them to be identified by spectral analysis.

In reality, the frequency is not constant because the the satellite motion relative to the antenna-reflector vector is not constant. We will discuss this further in Section 3.3.

3.3 MULTIPATH PROFILING PROCEDURE

The multipath induced amplitude variations of the resultant carrier can be observed in the SNR. The proposed developed algorithm uses the SNR data to create a profile of the multipath induced differential phase errors. To summarize the assumptions made:

- The amplitude of the direct signal arriving at the antenna is constant.
- The amplitudes of the multipath signals arriving at the antenna are constant.
- The antenna gain pattern is fairly smooth and not very sensitive to azimuth and elevation.
- The multipath frequencies are constant for a meaningful period of time.

The steps for computing a differential phase multipath profile are listed below. The major points of interest for the procedure are described thereafter.

1. Remove first order satellite and vehicle motion from the SNR data to produce the adjusted SNR.
2. Identify significant multipath frequencies based on the adjusted SNR data.
3. Solve for the amplitude $\alpha_i A_o$ and phase offset ϕ_i for each multipath constituent in the SNR.
4. Construct the phase multipath estimate based on the multipath parameters identified above.
5. Difference multipath estimates for two antennas to form a differential phase correction profile for each multipath constituent.
6. Solve for the correct sign of the correction based on the phase residuals.
7. Subtract the differential profile from the actual differential phase data to remove multipath.

The first step is to remove variations in the SNR due to gain changes. The composite SNR contains variations due to vehicle and GPS satellite motion, resulting from the direct signal passing through different parts of the antenna gain pattern. Along the lines of the amplitude derivation in section 2, the SNR variations due to multipath can be isolated by:

$$SNR_{mp} \approx SNR_c - SNR_d \tag{3.9}$$

for small multipath signal amplitude relative to the direct, where SNR_c is the composite SNR reported by the receiver, SNR_d is the direct SNR, and $SNR_{mp} = \sum \alpha A_o \cos(\beta)$ in Equation 3.6. The small multipath amplitude assumption enables the simple subtraction of the direct SNR from the resultant SNR, leaving the SNR multipath.

For static applications, the direct SNR is computed in the following manner. A satellite elevation time series is derived from the known antenna locations and GPS almanac. Using the antenna gain pattern, the elevation angles are mapped into normalized signal power, and scaled by a nominal SNR.

For dynamic applications, the satellite line of sight vectors will be utilized in conjunction with the gain pattern to compute the direct SNR signal. In this method, approximate vehicle attitude is needed to compute the appropriate gain compensation.

Assuming several multipath frequencies exist, the predominant frequences are identified by spectral estimation of the SNR data. This is presently done graphically with the Lomb periodogram (detailed in [12]). The periodogram has some desirable features over an FFT based approach, such as greater precision and non-constant sample rate capability.

Multipath is not a stationary process because the frequency varies according to the rate of change of the satellite line of sight vector, projected onto the vector between the antenna and reflector. Thus spectral estimation must be performed on a span of data long enough to provide excellent accuracy, yet short enough such that the frequency appears nearly constant. Typically, about two cycles of the SNR multipath are required to ensure sufficient frequency identification. Multiple multipath constituents at different frequencies are analyzed separately using different data lengths. This is implemented with a double pass routine to improve accuracy. The first pass is performed on the entire data set, which is suitable for accurate analysis of long period multipath signals. In the process, short period multipath frequencies are roughly identified, and used to determine appropriate time intervals for their accurate analysis in the second pass.

Using the frequencies identified above, determine the amplitude and offset of the SNR multipath constituents. This is done for each interval based on a least squares fit to the model:

$$\begin{bmatrix} \cos(\omega_1 t_k) & -\sin(\omega_1 t_k) & \dots & \cos(\omega_n t_k) & -\sin(\omega_n t_k) \\ \vdots & \vdots & & \vdots & \vdots \end{bmatrix} \times \begin{bmatrix} \alpha_1 A_o \cos\phi_1 \\ \alpha_1 A_o \sin\phi_1 \\ \vdots \\ \alpha_n A_o \cos\phi_n \\ \alpha_n A_o \sin\phi_n \end{bmatrix} = \begin{bmatrix} SNR_{mp}(t_k) \\ \vdots \end{bmatrix} \tag{3.10}$$

where n is the number of multipath constituents, $t_k \epsilon [tstart, tstop]$ are the measurement times, and recall from section 2 that the $\alpha_i A_o$'s are the multipath amplitudes. Two multipath constituents at each antenna were used for the scenarios described in this research, requiring a four element least squares solution. Both the matrix containing sinusoidal ar-

guments and the SNR data vector are accumulated in columnar fashion.

Having identified the frequencies, amplitudes, and offsets of the SNR multipath, the quantity β in Equation 3.8, computed at antenna j, for multipath constituents $i = 1, \ldots, n$, and for the time t_k, is:

$$\beta_{ij}(t_k) = \omega_{ij} t_k + \phi_{ij} \tag{3.11}$$

where ω_{ij} is the frequency of the multipath observed in the SNR, ϕ_{ij} is the phase offset, and t_k is the measurement time.

The multipath phase error was derived in Section 3.2 for small relative amplitude. The error in a carrier phase measurement at antenna j, for multipath constituent i, and time t_k, is given as:

$$\delta\theta_{ij}(t_k) \approx \frac{\alpha_i A_o \sin(\beta_{ij})}{A_c} \tag{3.12}$$

Again, the small multipath amplitude assumption allows simple addition of the multipath contributions from all constituents $i = 1, \ldots, n$:

$$\delta\theta_j \approx \sum_{i=1}^{n} \delta\theta_{ij} \tag{3.13}$$

The $\delta\theta_j$ sequence is essentially a profile of the phase multipath derived from the SNR data, which may be subtracted from the phase data to correct for the multipath.

The direction of rotation of the multipath phasor determines the signof the multipath error. The spectral estimation procedure leaves the sign of the SNR multipath frequency ambiguous. All signs are initially assumed positive and the multipath error profile is constructed. The multipath constituent signs from both antennas are then determined based on a least squares fit to the following model:

$$\begin{bmatrix} \delta\theta_{11}(t_k) & \cdots & \delta\theta_{n1}(t_k) & \delta\theta_{12}(t_k) & \cdots & \delta\theta_{n2}(t_k) \\ \vdots & & \vdots & \vdots & & \vdots \end{bmatrix} \times \begin{bmatrix} s_{11} \\ \vdots \\ s_{1n} \\ s_{21} \\ \vdots \\ s_{2n} \end{bmatrix} = \begin{bmatrix} DPHS_{residual}(t_i) \\ \vdots \end{bmatrix} \tag{3.14}$$

where in this situation the multipath profile constituents $\delta\theta_{ij}$ are kept separate to solve for the individual signs, and $DPHS_{residual}$ is the differential phase residual.

Vehicle and GPS satellite motion are also present in the differential phase data. While this is critical information for the vehicle attitude determination, it is undesirable when solving for the signs of the multipath constituents. For this step we use the differential

phase residual, which is the measured differential phase minus the motion effects. For static applications, the satellite motion is removed by subtracting a third order polynomial fit. When vehicle motion is added in the dynamic case, the total motion effects are derived from initial attitude solutions and baseline geometry, and then subtracted. Both are a rough approximations, but are sufficient enough to solve for the correct signs of the phase multipath correction.

The multipath profiles may be differenced between two antennas corresponding to a differential phase measurement. The s_{ij}'s are determined as real numbers which should be close to ± 1. The correct multipath profile is then:

$$\delta\theta = \sum_{j=1}^{2}\sum_{i=1}^{n} sign(s_{ij})\delta\theta_{ij} \tag{3.15}$$

3.4 MULTIPATH EXPERIMENTS

3.4.1 SIMULATION

The first step in evaluating the performance of the multipath profiling algorithm was to test it under ideal conditions. This was done by composing a Matlab signal simulation program which generated multipath corrupted SNR and differential phase data, based on models of a single master-slave antenna pair, a single GPS satellite in orbit passing directly overhead, and one or more reflectors. Figure 3.4 illustrates the simulated antenna/reflector configuration. The baseline length was 1 meter, and two reflectors were located 1 meter and 10 meters from the master antenna. The relative amplitudes of the multipath produced by the near and far reflectors were set to 0.1 and 0.05, respectively. Out of the 12 hour GPS orbit, a one hour segment was chosen that produced a good balance of low and high frequency multipath, from the 1 and 10 meter reflectors, respectively. Receiver noise of 2 millimeters $1-\sigma$ was added to the phase values, and the antenna gain was assumed to be constant for all satellite elevations. The SNR's were quantized to the level of 1/4 AMU, corresponding to the characteristics of the Trimble Vector receiver.

3.4.2 REFLECTOR EXPERIMENTS

The motivation for the experiments was to test the multipath correction techniques described in Section 3.3 on a static platform, and to compare with the simulated results. Two sets of experiments were performed in which multipath was deliberately injected into the received GPS signal.

The multipath injection by reflection experiments were conducted May 23-27, 1994, on the engineering center roof, at the University of Colorado, Boulder. There were high concrete walls adjacent to the site covering about 90 degrees of the western horizon. The site

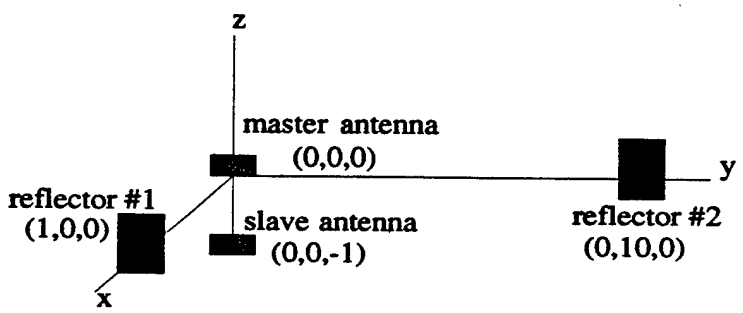

Figure 3.4: Multipath simulation configuration. *Shown are the positions of the two antennas and reflectors. The coordinates are specified in the local system with the master antenna at the origin, and the axes are aligned with the ECEF system.*

was a multipath nightmare, which ironically made it ideal to test the correction technique. The Trimble Vector receiver was used in conjunction with four Trimble patch antennas. The antennas were mounted on a rigid, nonreflective support structure, with possible baseline lengths of 0.5, 1.0, and 1.1 meters. Receiver control and data storage was achieved with a laptop computer. In these experiments, intentional multipath was reflected by an aluminum plate measuring 0.60 x 1.22 meters. The reflector was positioned next to the antenna array and canted upwards at 53 degrees. This configuration reflected a signal ray from a satellite at an elevation angle of 80 degrees approximately to the center of the antenna array.

3.4.3 ELECTRONIC INJECTION EXPERIMENTS

The electronic multipath injection experiments were conducted March 1-6, 1994. The location was a remote site 10 miles north of Boulder that was nearly devoid of naturally occurring multipath. The Trimble Vector receiver was again used alongside the laptop computer, and two Trimble microstrip patch antennas were replaced by narrow beam helical antennas placed within metallic parabolic bowls, named *helibowls*. The antenna configuration allowed for patch and helibowl baseline lengths of 1 meter. Narrow beam antenna performance in the presence of multipath was also being investigated at the time. Intentional multipath was electronically injected such that a single multipath ray could be observed. The electronic multipath injection was achieved using a satellite near zenith and additional collection and retransmission antennas. As the satellite passed overhead both the antenna array and a high gain helical antenna positioned several meters away, the signal was sent from the high gain antenna, through a low noise amplifier and 15 meters of RG-214 cable, and was projected towards the array by means of a second helical transmission antenna. The retransmitting antenna was placed 2.4 meters horizontally and 2.1 meters vertically from the center of the array. The signal power balance was accounted for by considering the gain of the helical collection and retransmitting antennas, the LNA, power loss from the cable, and space loss from the retransmitting antenna to the array. The received power of the multipath signal relative to the direct could be adjusted with a variable step RF

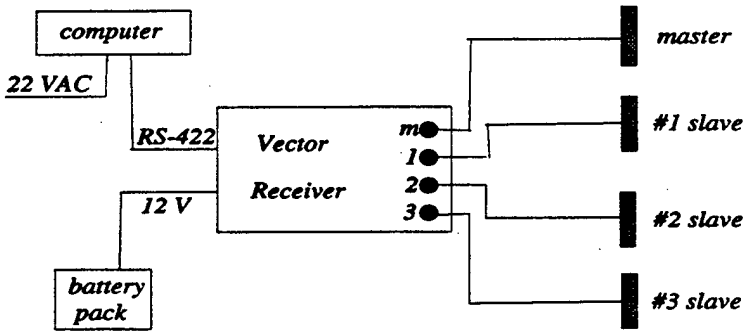

Figure 3.5: Experimental block diagram. *Shown are the important connections for the Trimble Vector receiver, the laptop computer, power supplies, and wiring. In the case of the electronic injection experiment, the number 1 and 3 slave antennas were replaced with the helibowl antennas.*

Table 3.1. Summary of multipath experiments.

Date	Duration (Hrs)	MP Injection	PRN
3-5-94	2	electronic	29
3-6-94	2	electronic	29
5-24-94	1	reflective	7
5-24-94	1	reflective	6
5-25-94	1	reflective	27

attenuator, located just prior to the retransmitting antenna. The multipath relative power was set to 0.10, a typical value for reflectivities associated with a spacecraft environment.

A block diagram describing the receiver and associated hardware setup is provided in Figure 3.5. The antennas shown are for the electronic injection experiments. Note that the helibowls required low noise amplifiers to boost the signal to appropriate levels. As stated above, they were replaced with patch antennas for the reflection experiments. The gain patterns for each type of antenna was measured in the University of Colorado anechoic chamber prior to the experiments. This ensured that the gain patterns were consistent among the antenna types. The antennas were also mounted to the support structure such that their orientations were kept the same throughout the experiments. In the differential mode, this compensated for small azimuthal variations in gain patterns and antenna phase center motion. Table 3.1 summarizes the successful multipath injection experiments by providing the date, duration, type of multipath injection, and observed PRN. Differential phase and SNR data were collected for the duration of each experiment. The longer duration of the electronic multipath injection experiment was chosen such that the GPS satellite could traverse completely through the helical collection antenna main lobe.

3.5 RESULTS

The frequencies of the predominant multipath in the adjusted SNR data were identified using spectral analysis. Two constituents were used to model the multipath for both the simulated and experimental data. In each case, there were distinct high and low frequency multipath signatures, produced by a distant and nearby reflector, respectively. A sample of the multipath frequencies encountered is given in Table 3.2. The values given are from a 1 meter patch baseline for the reflective multipath experiment with PRN 27, on March 25, 1994. They were averaged over the 1 hour duration. The length of time used for spectral estimation of the frequency, amplitude, and relative phase offset of the multipath constituents is also provided in Table 3.2.

Table 3.2. Predominant multipath frequencies and time spans for spectral estimation.

Antenna	Constituent	Frequency $(10)^{-3}$Hz	Time Span [sec]
master	high	7.0	300
master	low	0.41	3600
1 slave	high	6.6	300
1 slave	low	0.27	3600

The actual adjusted SNR showing multipath, together with the SNR derived from the estimated multipath parameters, for two antennas that make up a differential baseline, are shown in Figure 3.6. Note that they do not align precisely, indicating that the frequency or amplitude were not estimated correctly, or that additional multipath frequencies are present that were not accounted for in the least squares model. Also, if gain effects remain in the adjusted SNR, they will be absorbed into the estimated multipath parameters.

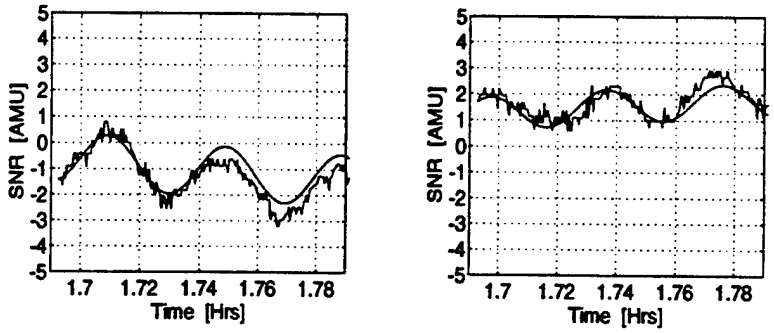

Figure 3.6: Adjusted SNR data and estimated SNR multipath. *The adjusted SNR data and the SNR multipath estimates are for the master antenna (left) and the number 1 slave antenna (right) that make up a 1 meter baseline.*

The differential phase residual, accompanied by the SNR derived multipath profile, are displayed in Figure 3.7 for the simulated data. The multipath profile estimated with the adjusted SNR data closely tracks the differential phase multipath, which has been smoothed

by a low-pass filter. A 720 second time span was used to estimate parameters for the rapidly varying multipath, produced by the nearby reflector. The slowly varying multipath, produced by the distant reflector, was estimated with a 3600 second time span (the entire 1 hour data set).

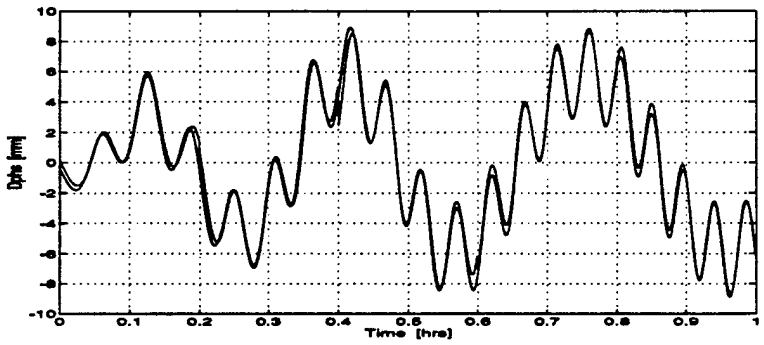

Figure 3.7: Simulated differential phase residual and estimated multipath profile. *The phase residual was low-pass filtered with a 30 Hz cutoff frequency. The horizontal axis is the time in units of hours, and the vertical axis is the differential phase residual in units of millimeters.*

The multipath correction result for the simulated data is contained in Figure 3.8. The simulation results exemplify what is expected from the correction technique: the elimination of multipath to the level of the noise. There exists residual multipath which is usually less than 1 millimeter, but extends to 2 millimeters on several occasions. The most visible excursions, which occur at multiples of 0.2 hours (720 seconds), are not really multipath. They are discontinuities at the borders of the data segments used to perform the high frequency spectral estimation. The reduction in error is from 10.6 to 3.3 millimeters. The reported errors from this point on are 99.73 percentile errors. This statistic is given because the multipath errors are not normally distributed. If they were, a 3-σ error would be equivalent.

The multipath correction results from a reflective multipath injection experiment are exhibited in Figure 3.9. This is for the 1 meter patch baseline, observing PRN 27, on May 25, and is indicative of what was achieved with the other experimental data. The result shows a reduction of multipath error from 7.3 to 5.6 millimeters. The slowly varying multipath was produced by the nearby placed aluminum plate reflector, and its SNR parameters were estimated with a 3600 second time span. As shown, the slow constituents were nearly eliminated. The rapidly varying multipath was produced by a distant concrete and metallic wall structure, one of many on the engineering center roof. The SNR parameters were estimated with a 300 time span. The fast constituents were reduced significantly, in fact 70 percent of the data lies within ± 2 millimeters.

The multipath correction results from a electronic multipath injection experiment are exhibited in Figure 3.10. This is for the 1 meter patch baseline, observing PRN 29, on March 6. The error was lowered from 8.0 to 6.8 millimeters, and the two hour segment of

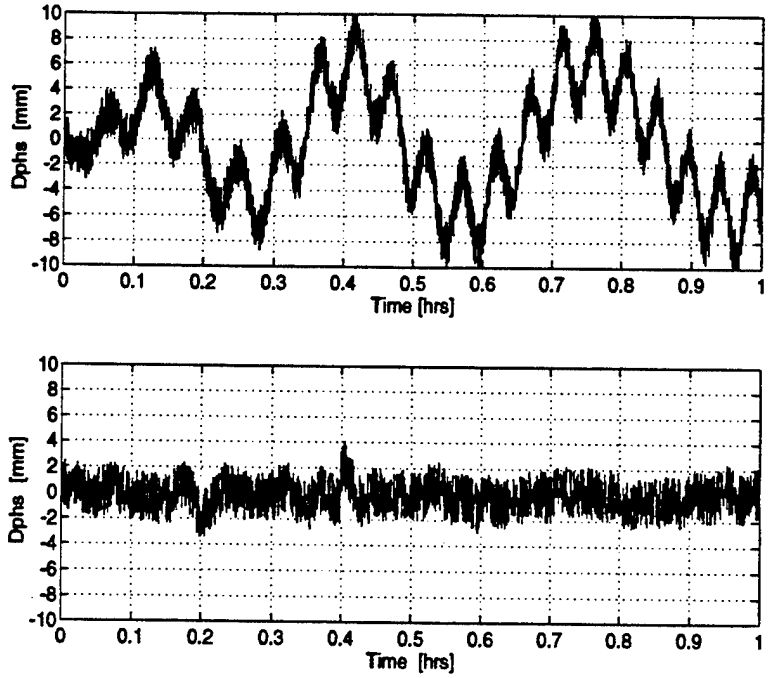

Figure 3.8: Simulation results. *Shown are the differential phase residual (top), and the differential phase residual after subtracting the SNR derived multipath (bottom). The horizontal axes are the time in units of hours, the vertical axes are the differential phases in units of millimeters.*

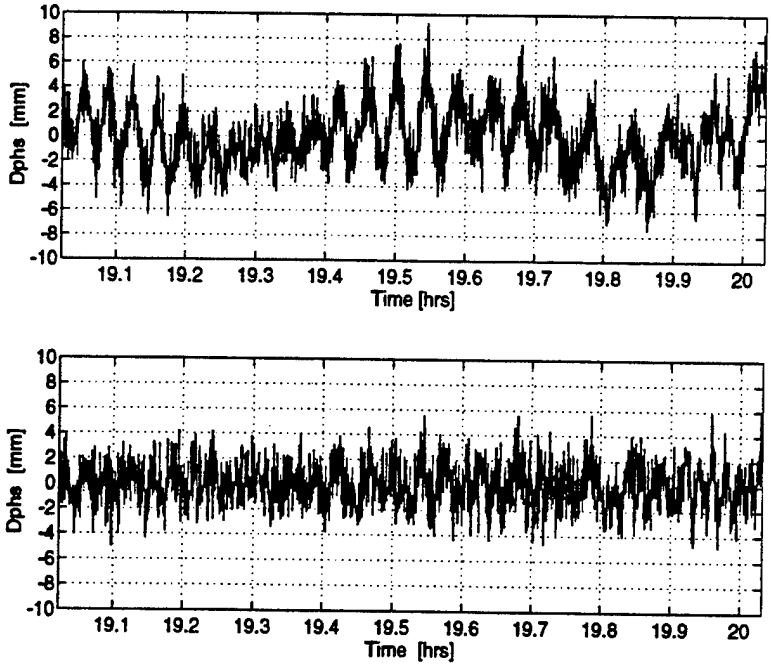

Figure 3.9: Reflective multipath injection results. *Shown are the phase residual (top), and the differential phase residual after subtracting the SNR derived multipath (bottom). This data is for PRN 27, collected with a 1 meter patch baseline on May 25, 1994, over a 1 hour time period. The horizontal axes are the time of day in units of hours, the vertical axes are the differential phases in units of millimeters.*

data displays excursions of residual multipath well above the receiver noise level. The slowly varying multipath was produced by reflectors from the metallic bowls of the nearby heli-bowl antennas, and the rapidly varying multipath was produced by the distant electronic injection apparatus. Both SNR constituent parameters were estimated with a 1500 second time span, which may explain why the high frequency errors were not removed very effectively.

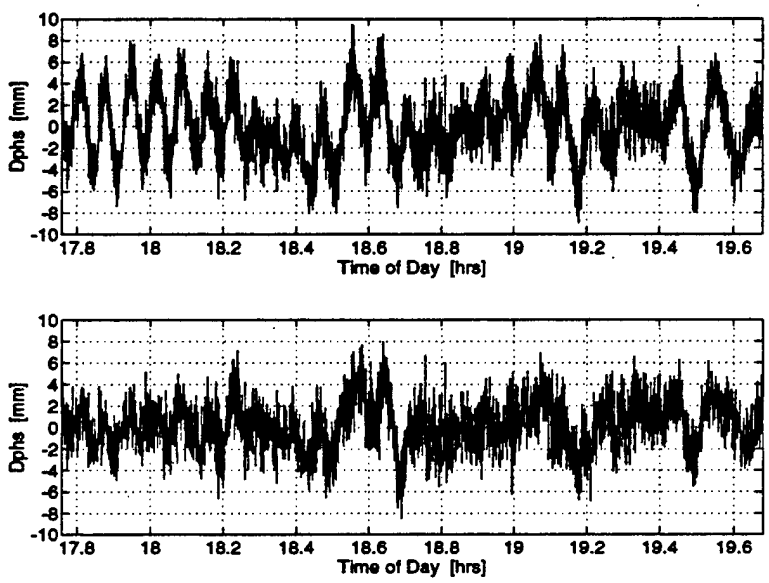

Figure 3.10: Electronic multipath injection results. *Shown is the phase residual (top), and the differential phase residual after subtracting the SNR derived multipath (bottom). This data is for PRN 29, and was collected with a 1 meter patch baseline on March 6, 1994, over a 2 hour time period. The horizontal axes are the time of day in units of hours, the vertical axes are the differential phases in units of millimeters.*

Table 3.3: Summary of multipath correction results.

Type of Experiment	PRN	MP Error Before [mm]	MP Error After [mm]
Simulation	N/A	10.4	3.3
Reflection	PRN 27	7.4	5.5
Reflection	PRN 7	7.3	5.6
Reflection	PRN 6	6.2	5.2
Electronic	PRN 29	8.0	6.8

Table 3.3 summarizes the multipath correction results for all the cases discussed in this paper, in addition to the other reflection experiment results not shown. The 99.73 percentile multipath errors in the differential phase residual are provided for the before and after correction scenarios. The rows for PRN 27, PRN 7, and PRN 6, are for the reflective multipath injection experiments. The PRN 29 row is for the electronic multipath injection experiment.

3.6 DISCUSSION OF RESULTS

The multipath correction results are extremely promising. For the reflective tests in particular, which most closely represent real world operating conditions, the multipath contribution to the phase error was reduced to levels that approach the receiver noise. Furthermore, since the low frequency components of the phase error have been virtually eliminated, high frequency receiver noise can now be easily removed by smoothing, or Kalman filtering.

The effectiveness of the multipath correction is largely dependent on the quality of the frequency estimates, which is limited by two factors: the precision with which the frequencies can be estimated, and the fact that the frequencies are actually time varying. We found that FFT methods do not provide sufficient resolution at the low multipath frequencies. The Lomb periodogram technique is satisfactory; however, our current implementation requires significant user interaction. Future enhancements will automate this process. Methods for estimating the time varying frequencies will also be investigated.

The performance of the multipath correction technique is also dependent on the accuracy of the SNR measurements, the assumed antenna gain pattern, and the assumptions made that the direct and multipath signals have constant amplitudes. We are fortunate in that the Trimble Vector provides very accurate SNR data and does not appear to be a limiting factor in the results presented here. The gain patterns we generated were quite coarse and did not include azimuthal variations. Improved patterns can be expected to improve the performance of the technique. Finally, the because of the success in the reflective tests, we conclude that the assumption of constant direct and multipath amplitude is reasonable.

The relatively poor performance in the electronic tests can be attributed to two amplitude related factors - 1) the amplitude of the "multipath" may have been larger than the assumed 0.1 ratio; and 2) because of the sharp cutoff of the high gain antenna used to generate the multipath, the amplitude was in fact not constant. (We did not compensate for the high gain antenna pattern.) Furthermore, we did not estimate the high frequency components using shorter time spans, as was done for the reflector experiment data, because of time constraints.

3.7 SUMMARY AND FUTURE WORK

A highly effective technique for the correction of multipath errors in GPS phase data, based on SNR measurements, has been described and demonstrated. The technique, applied to data sets collected on static baselines in severe multipath environments, reduced the differential phase errors to near receiver noise levels. The phase accuracy improvements gained by this algorithm have potential to enhance performance for high precision survey as well as attitude determination on dynamic vehicles.

In its current post-processing mode, the algorithm could be readily applied to survey data collected using two static receivers. The only modification required would be for the effect of the different station clocks at the two sites to be removed via double differencing of the phase measurements, or estimation of the clock errors *apriori*. The different clock errors make it impossible to use single difference phase data (between stations) to identify the correct sign of the multipath profile components. Application of this technique could produce significantly improved results, especially for short baseline surveys where one or more of the antennas is subject to many multipath reflections. One difficulty, pointed out by T. Clark [10], is that most survey receivers do not provide sufficient resolution for the amplitude data. In fact, the RINEX format does not allow for useful SNR data to be reported.

Our next area of focus is to test the performance of the multipath profiling technique on dynamic data, again in a post-mission mode. The first step in the procedure is to compute an initial time history of the vehicle attitude. This information serves as the basis for computing the correct antenna gain to be removed from each amplitude observation and for removing the expected phase difference from the phase observables to permit the constituent sign determination. Post-mission accuracy refinement is a valuable tool for analysis of spacecraft data, and airborne altimetry or photogrammetry.

Finally, the obvious extension of the proposed method is to develop a means for implementation of multipath profiling in near real-time. The two key challenges to this are the selection of the appropriate sequential or adaptive frequency estimation techniques and a reduction in the computational load. We believe that such an approach is achievable in near real-time for applications demanding the highest accuracy possible.

REFERENCES: MULTIPATH CORRECTION

[1] Schwarz, K.P., A. El-Mowafy, and M. Wei, "Testing GPS Attitude System in Kinematic Mode," Proceedings of ION GPS-92, Albuquerque, NM, Sept. 16-18, 1992.

[2] Lu, G., M.E. Cannon, and G. Lachapelle, "Attitude Determination in a Survey Launch Using Multi-Antenna GPS Technologies," Proceedings of ION National Technical Meeting, San Francisco, CA, Jan. 20-22, 1993.

[3] Cohen, C.E., B.W. Parkinson, "Aircraft Applications of GPS-Based Attitude Determination," Proceedings of ION GPS-92, Albuquerque, NM, Sept. 16-18, 1992.

[4] Cannon, M.E., and M. Haverland, "Experiments of GPS Attitude Determination Within A Helicopter Pod," Proceedings of ION GPS-93, Salt Lake City, UT, Sept. 22-24, 1993.

[5] Cohen, C.E., E.G. Lightsey, B.W. Parkinson, and W.A. Fees, "Space Flight Tests of Attitude Determination Using GPS: Preliminary Results," Preprint of paper presented at ION GPS-93, Salt Lake City, UT, Sept. 22-24, 1993.

[6] Ward, L.M., "Spacecraft Attitude Estimation Using GPS: Methodology and Results," Ph.D. Dissertation Prospectus, University of Colorado, Dept. of Aerospace Engineering Sciences, August 12, 1994.

[7] Hajj, G.A., "The Multipath Simulator: A Tool Toward Controlling Multipath," Proceedings of the 2nd Symposium on GPS Applications in Space, Hanscom AFB, MA, Feb. 1990.

[8] Cohen, C.E., Attitude Determination Using GPS, Ph.D. Dissertation, Department of Aeronautics and Astronautics, Stanford University, Dec. 1992.

[9] Cohen, C and B. Parkinson, "Mitigating Multipath Error in GPS Based Attitude Determination," Guidance and Control, Vol. 74, Advances in the Astronautical Sciences, 1991.

[10] Clark, T., "GPS Antennas: De-Mystifying Multipath," NASA Goddard Internal Memorandum, March 5, 1992.

[11] Georgiadou, Y. and A. Kleusberg, "On Carrier Signal Multipath Effects in Relative GPS Positioning," Manuscripta Geodaetica, Vol. 13, 1988.

[12] Press, W.H., S.A. Teukolsky, W.T. Vetterling, and B.P. Flannery, *Numerical Recipes in C*, pp. 575-580, Cambridge University Press, 1992.

4.0 AN INTEGRATED GPS ATTITUDE DETERMINATION SYSTEM FOR JAWSAT

Bruce C. Chesley

4.1 OVERVIEW

This chapter discusses the development of an onboard attitude determination system using GPS, Fiber Optic Gyros (FOG), and sun sensors for JAWSAT. JAWSAT is a small, three-axis stabilized spacecraft scheduled for launch in 1996. It is being designed and built by students and faculty at the U.S. Air Force Academy and Weber State University, primarily to meet educational objectives. This paper provides an overview of the satellite design and technology demonstration experiments, and then focuses on an integrated attitude determination system using GPS and FOGs.

The attitude determination system for JAWSAT is designed around a Trimble Navigation TANS Vector receiver, augmented by fiber optic gyros and sun sensors. The required attitude performance is 1 degree in heading, pitch, and roll; however, our goal is to attain the best performance possible while meeting the size, power, and real-time processing constraints of the satellite design.

This chapter describes estimation and filtering approaches developed for the JAWSAT attitude determination system. First we consider an extended Kalman filter algorithm. This algorithm uses FOG measurements to determine the satellite dynamics and uses GPS measurements to estimate the FOG drift. The primary source of error in this approach is time-correlated measurement errors in the GPS attitude solution due to multipath. To address this, we have developed a measurement differencing Kalman filter algorithm to mitigate the effects of these time-correlated errors. This measurement differencing approach reduces both the standard deviation and the maximum value of the attitude estimation error. We also consider limiting the on-time of the GPS receiver to reduce power consumption. The approach developed for JAWSAT could be of value for other near-Earth, low cost small satellite missions.

4.2 JAWSAT MISSION OBJECTIVES AND DESIGN

The Global Positioning System (GPS) has the capability to provide position, velocity, attitude, and timing information to a satellite in low Earth orbit. This combination of many functions in one instrument is attractive for small satellites, where size, power, and cost are limited. A recent report by the National Research Council advocates incorporation of GPS into small satellite designs for orbit and attitude determination [Montgomery, 1994]. The motivation for this research is to integrate GPS based attitude with other on-board sensors for both coarse attitude acquisition and fine attitude tracking. A demonstration vehicle for this design is JAWSAT, the Joint Air Force Academy - Weber State University Satellite.

JAWSAT is a combined effort to build, launch, and operate a small, three-axis stabilized satellite in low Earth orbit [Smith and Liefer, 1993]. The mission of JAWSAT is to demonstrate technologies for future space missions and to meet educational objectives for students at the sponsoring institutions and at various secondary schools. Technology demonstrations on the satellite include a GPS based attitude determination system, two experimental pulse plasma thrusters (PPTs) for low-thrust orbit transfer, a CCD camera, and a high energy particle detector.

JAWSAT will be approximately 0.7m $\times$ 0.5m $\times$ 0.3m and weigh less than 100 kg at launch (Figure 4.1). The baseline design calls for JAWSAT to be Earth-pointing in a sun-synchronous noon-midnight orbit at

an altitude of 720 km. Three-axis stabilization will be achieved using reaction wheels and magnetic torque rods. Four GPS antennas will be mounted at the corners of the zenith face.

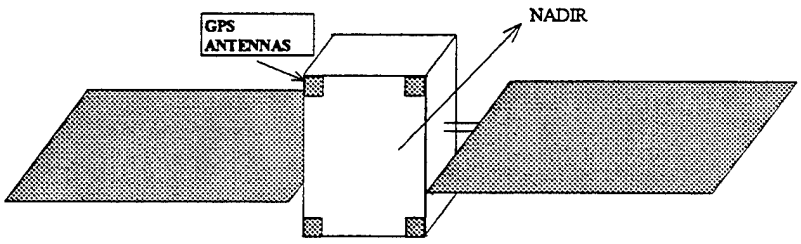

Figure 4.1. JAWSAT Structure with Solar Panels Deployed.

The attitude determination system for JAWSAT must satisfy constraints on power, size, weight, cost, and processor capabilities while meeting mission requirements. The attitude control specifications require the spacecraft to point within ± 5 degrees of nadir. Attitude knowledge needs to be maintained within ± 1 degrees in heading, pitch, and roll to ensure adequate margin for the control system. Cost and size constraints limit the accuracy of the attitude determination sensors available as well as the complexity of the flight software.

The experience of designing, fabricating, and operating a small satellite is an important objective for undergraduate students at the Air Force Academy and Weber State University. Students at primary and secondary schools will also be involved in JAWSAT once it is on orbit by receiving synthesized voice messages and video images directly in their classrooms. The messages and images will be received with a personal computer and a low cost receiver (less than $300).

The remainder of this chapter describes the design and analysis of an integrated GPS attitude determination system for JAWSAT. The principles of operation and performance characteristics of each of the three main attitude determination sensors (GPS, FOG, and SSA) are discussed. These characteristics form the basis of a simulation used to evaluate Kalman filtering algorithms which integrate GPS and FOG attitude measurements. Improved performance is achieved using a measurement differencing Kalman filter approach. Finally, the effects of minimizing GPS receiver on-time are investigated to conserve satellite power during orbital operations.

4.3 GPS BASED ATTITUDE DETERMINATION

GPS based attitude determination for JAWSAT will be performed using the Trimble Vector attitude receiver. The Vector is a six-channel, four-antenna, C/A code receiver that reports instantaneous attitude solutions in addition to navigation information. The receiver measures 127 mm × 241 mm × 56 mm, weighs 1.42 kg, and requires 4 W at 9-18 Volts DC. The receiver is connected to four microstrip patch antennas with coaxial cables. The antennas measure 96 mm × 102 mm × 13 mm and weigh 0.19 kg each. The antennas will be mounted on the extreme corners of the zenith face of the satellite. The receiver has an RS-422 port for data output at a rate of 38.4 kbaud, and attitude solutions are available at a nominal rate of 2 Hz [Trimble, 1994].

The Vector receiver observes the differential phase of the Doppler shifted L1 carrier signals received at two or more antennas. Converting this observable to attitude requires several quantities to be known--the integer ambiguities, the antenna baseline vectors, and the hardware biases. These parameters are computed by the receiver prior to generating attitude solutions. The baselines and hardware biases are estimated off-line during a survey lasting at least eight hours. Determining the integer ambiguities for attitude determination requires an initialization step. Assuming the baselines and hardware biases are known from the static survey, the integer ambiguities can be resolved by motion-based or integer search techniques. Details of these procedures are contained in Cohen [1992] and Trimble [1994]. The receiver can report attitude represented by Euler angles or quaternions.

The Vector receiver hardware has not been formally space qualified, but receiver software designed for use on orbit has been developed. Small satellite designs frequently use terrestrial hardware in the interest of keeping costs low. Certain electrical components, such as electrolytic capacitors, need to be avoided and additional shielding of terrestrial equipment may be needed to ruggedize hardware for use in space [Reeves, 1994].

A precursor to the Vector receiver is currently successfully operating in space on the Air Force RADCAL satellite. This receiver, the Trimble Quadrex, has been used to form attitude estimation solutions reported by Lightsey, et al. [1994] and Ward [1994].

Preliminary ground based performance testing of the Vector receiver was reported by Axelrad and Chesley [1993]. Further ground based testing will be conducted using a JAWSAT mock up. The JAWSAT test structure is an aluminum box with a plate for mounting the four GPS antennas. The plate measures 66 cm $\times$ 53 cm, with the four GPS patch antennas are mounted at the extreme corners. The JAWSAT mock up with GPS antennas and Vector receiver is shown in Figure 4.2 on the roof of the Engineering Center at the University of Colorado.

Test results for a representative small satellite structure will be used in the remainder of this chapter. The generic small satellite test structure is an aluminum square with sides 71 cm long. The four GPS antennas are mounted at the corners of the square. This test structure was described in Axelrad and Chesley [1993]. Further ground testing with the JAWSAT mock up structure will be conducted shortly.

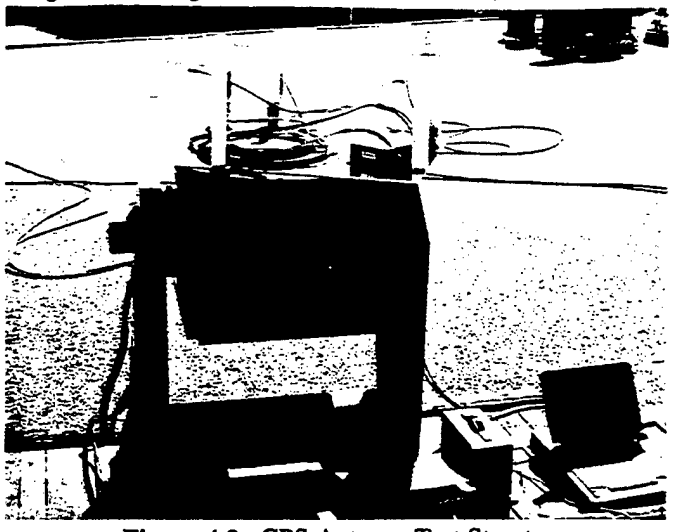

Figure 4.2. GPS Antenna Test Structure.

Sample results from a static test run are shown in Figure 4.3. No filtering of the receiver output or integration with measurements from other sensors was included in this test. Note that for the short baselines used, the attitude accuracy is approximately 0.5 degrees, one-sigma. Also note the apparent time correlation in the attitude solutions indicative of multipath errors affecting the raw signal phase observable.

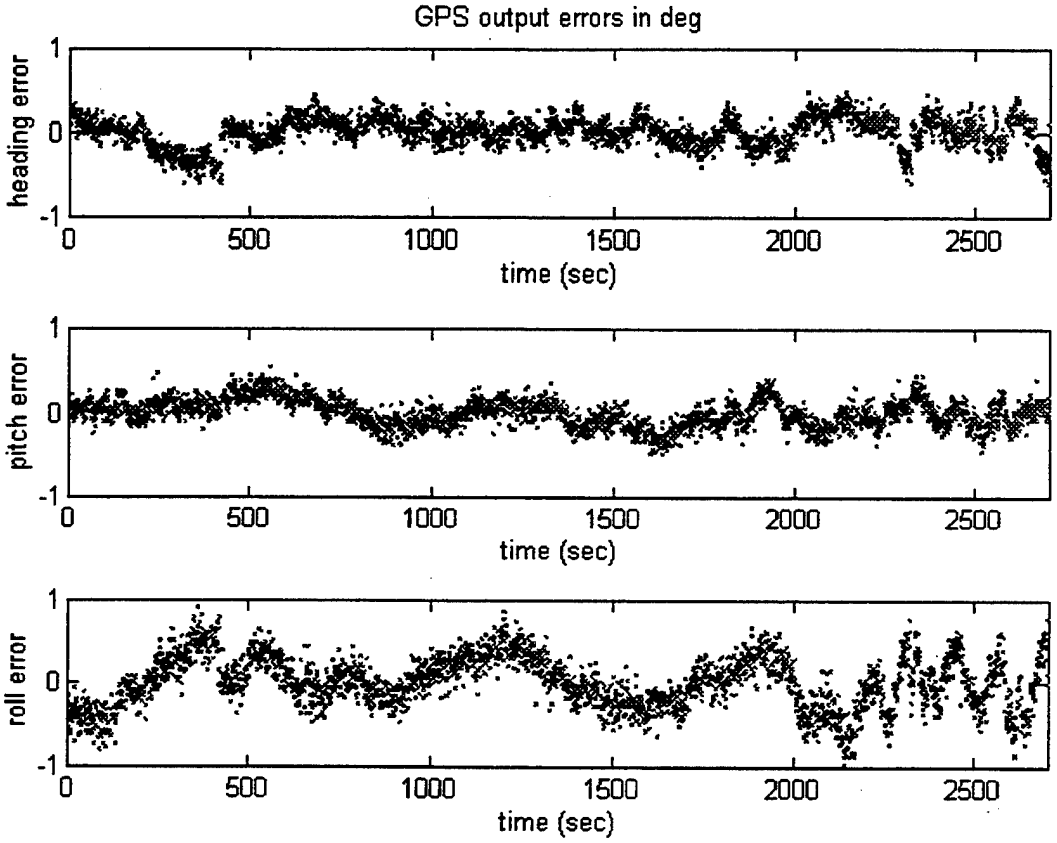

Figure 4.3. Sample GPS Attitude Output.

In this case we know the attitude was fixed, so any variations in the results are assumed to be measurement errors. These attitude error characteristics shown in Figure 4.3 were used in a simulation of an integrated GPS attitude determination system described later in this chapter.

4.4 FOG ATTITUDE DETERMINATION

Fiber Optic Gyros (FOG) are attitude rate sensors that measure changes in transit times of counter rotating beams of light in a closed optical path. FOG technology is considered very promising as an accurate, low-cost attitude rate sensor since many of the components (such as optical fiber and superluminescent diodes) are already produced in relatively large quantities for telecommunications systems [Mark, et al., 1991]. The Clementine spacecraft launched in January 1994 included FOGs in its attitude sensor suite.

FOGs operate by splitting light from a superluminescent diode into two beams. One rotates clockwise through a coil of optical fiber, the other beam rotates counterclockwise. The counter rotating light beams

can be used to sense rotation since the light (photons) moving in opposite directions around the ring will travel different path lengths if the ring is rotating. When the beams are recombined after traveling the same optical path in opposite directions, the interference pattern can be used to measure the rotation rate. These sensor are sometimes called interferometric fiber optic gyros (IFOG) for this reason.
The basic principle of FOG rotation sensing is shown in Figure 4.4. The phase shift as the fiber coil rotates through the angle $\Delta\theta$ is sensed by a photodetector.

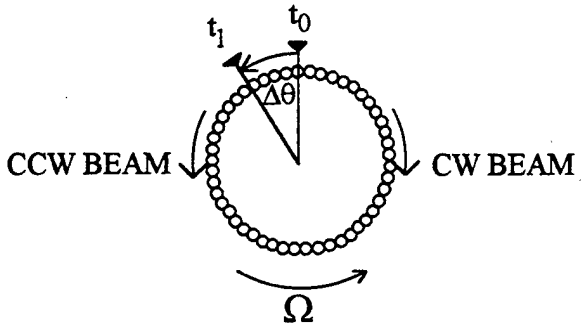

Figure 4.4. Standing Wave Interference Pattern in Fiber Optic Gyro.

For an optical gyro with N fiber coils and diameter D the optical path length is $L = N\pi D$ and the difference in transit time for the clockwise and counter clockwise paths becomes

$$\Delta T = \frac{-LD}{c^2}\Omega \tag{4.1}$$

If the period of the light source is $T = \lambda/c$, then the fractional fringe interference is

$$\frac{\Delta T}{T} = \frac{-LD}{c^2 T}\Omega = \frac{-LD}{c\,\lambda}\Omega \tag{4.2}$$

The Sagnac phase shift measured by an optical gyro is 2π times the fringe interference and is given by

$$\Psi_s = \frac{-2\pi LD}{c^2 T}\Omega \equiv -K_s\Omega \tag{4.3}$$

where K_s is the Sagnac scale factor for the gyro. For a typical gyro with $L \approx 1000$ m, $D \approx 10$ cm, and $\lambda = 820$ nm, the Sagnac scale factor is $K_S = 2.51$ arcsec/(deg/hr) [Mathews, 1990].

The primary error sources for FOGs are random drifts in the angular rate bias. The angular rate bias is an offset between the FOG measurement and the true angular velocity. These bias drifts arise due to imperfections in the optical fiber that cause the clockwise and counter clockwise beams to experience slightly nonreciprocal paths. The drift in the rate bias can be characterized by random walk behavior. Environmental effects such as thermal and magnetic disturbances also contribute to the random bias drift [Lefèvre, et al., 1984]. Significant improvements have been made in calibrating and compensating for these bias drifts, and high accuracy FOGs are available with drift rates on the order of 0.01 deg/hr.

Error characteristics for the JAWSAT gyros are not available since the specific FOG hardware has not been finalized. Low cost FOGs available for JAWSAT are anticipated to have bias drifts in the 1-5 deg/hr range.

Figure 4.5 shows simulated output of a gyro with characteristics typical of what will be launched on JAWSAT. FOG model parameters were adapted from Siouris [1993] for use in the attitude estimation simulation described below. The gyro simulation includes parameters for gyro drift due to fiber imperfections, temperature dependence, magnetic dependence, and acceleration dependence, as well as input axis misalignment errors.

The general error characteristics described in this section will be modified to match the flight hardware when that data becomes available.

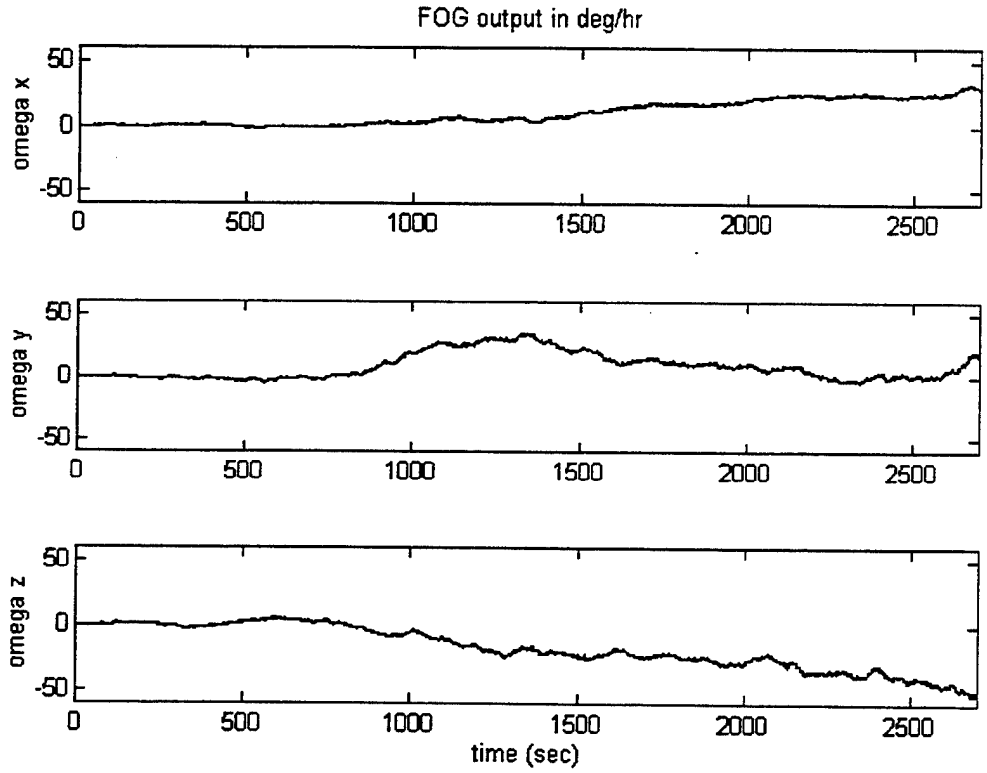

Figure 4.5. Simulated FOG Angular Rate Drift. *Graphs show random walk characteristics for gyros aligned with each of the three body axes. Angular velocity input is zero for each axis.*

4.5 SSA ATTITUDE DETERMINATION

Virtually every satellite has flown with some sort of sun sensor for attitude estimation. Sun sensors use photodetectors to determine the angle of incidence of the sun's energy, thereby giving an estimate of the spacecraft orientation. The Sun Sensor Assembly (SSA) for JAWSAT will be a two-slit sensor with direct digital output [Reeves, 1994]. It will be designed and fabricated at the USAF Academy.

The principle of operation of the SSA relies on strips of photocells located beneath a light entrance slit as shown in Figure 4.6. The pattern of the photocell detectors illuminated by the sun image through the slit can be used to determine the angle to the sun. The photocell strips have alternating active and passive elements as shown in the diagram. The composite of photocell bits that are activated by the incident solar energy comprise the digital word that represents the angle between the sunline and the normal to the sensor face.

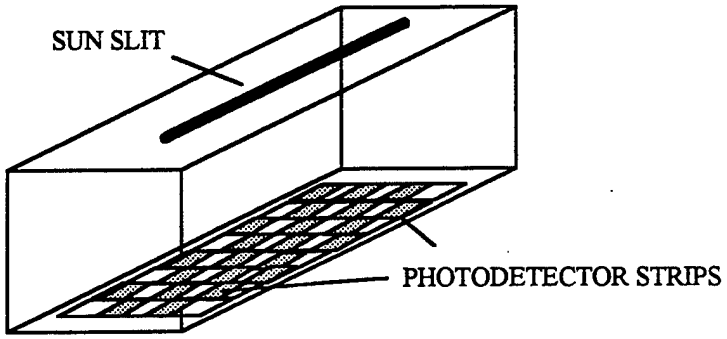

Figure 4.6. Sun Sensor Assembly. *Photodetector strips showing alternating active/passive pattern.*

The SSA for JAWSAT will consist of six two-slit sensors to provide a field of view of approximately 2πsr. The direct readout from the sensor will be an 8-bit digital word, with the least significant bit representing 0.5 deg. This quantization is expected to be the largest error source.

4.6 ATTITUDE ESTIMATION SIMULATION

A simulation of the spacecraft attitude determination using GPS and FOG has been developed in MATLAB to test attitude estimation algorithms. The simulation is composed of three primary sections as shown in Figure 4.7--a truth model of controlled attitude dynamics, measurement models of the FOG and GPS sensors, and an estimation model for vehicle attitude determination and gyro bias correction. Preliminary results demonstrate that the integrated GPS/FOG attitude determination system is capable of meeting JAWSAT mission requirements. The simulation currently concentrates on achieving improved performance for integrated GPS/FOG measurements; simulated SSA measurements will be added in the future.

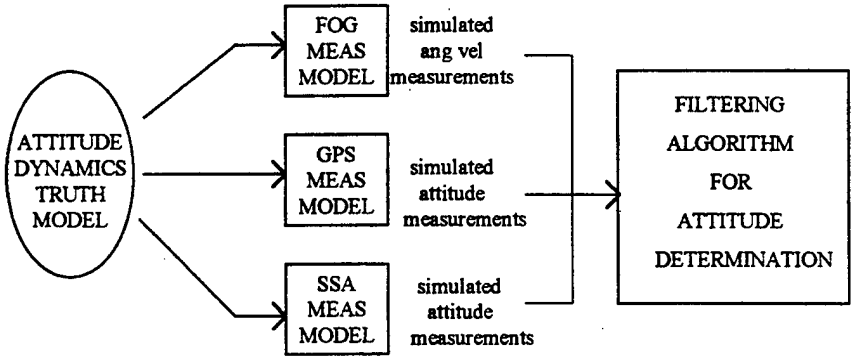

Figure 4.7. Simulation Data Flow

The true attitude dynamics are computed based on expected performance of the attitude control system, and simulated sensor measurements are generated from this truth data. The FOG model applies drift rate bias and random walk terms that account for errors in the bias, errors in scale factor, and axis misalignment errors. The combination of these effects for the error parameters chosen provides attitude errors that drift on approximately 3 deg/hr. An example of simulated FOG output was shown in Figure 4.5. The simulation adds GPS attitude errors from ground test data to the simulated true dynamics. GPS attitude errors used in the simulation were shown in Figure 4.2.

4.7 EXTENDED KALMAN FILTER ALGORITHM

An extended Kalman filter algorithm to estimate spacecraft attitude and gyro bias parameters using FOG and GPS measurements was developed. The full state vector has seven dimensions: four states for the attitude quaternion, $\bar{q} = \begin{bmatrix} q_1 & q_2 & q_3 & q_4 \end{bmatrix}^T$, and three gyro bias states, $b = \begin{bmatrix} b_1 & b_2 & b_3 \end{bmatrix}^T$, (one for each axis). The Kalman filter implementation uses only three of the quaternion states since inclusion of all four gives rise to a singularity in the covariance matrix time update; therefore, a six-state formulation is used following Lefferts, Markley, and Shuster [1982]. The fourth quaternion state can be computed at any time from the other three to give the full seven dimensional state. The time propagation and measurement update processes are shown in Figure 4.8.

Time propagation of the quaternion state estimate and the covariance matrix is performed using FOG angular rate measurements. The GPS quaternion measurements are then compared with the propagated state vector estimate to form the measurement residual at each state update epoch. The extended Kalman filter then forms a quaternion state correction term from which a new estimate of the total quaternion of rotation can be determined by quaternion composition. The gyro bias terms are accumulated in the usual way by adding the incremental update to the reference trajectory. Details are in Lefferts, et al. [1982], and summarized below. Additional information on general Kalman filter theory can be found in Gelb [1974] and Maybeck [1982].

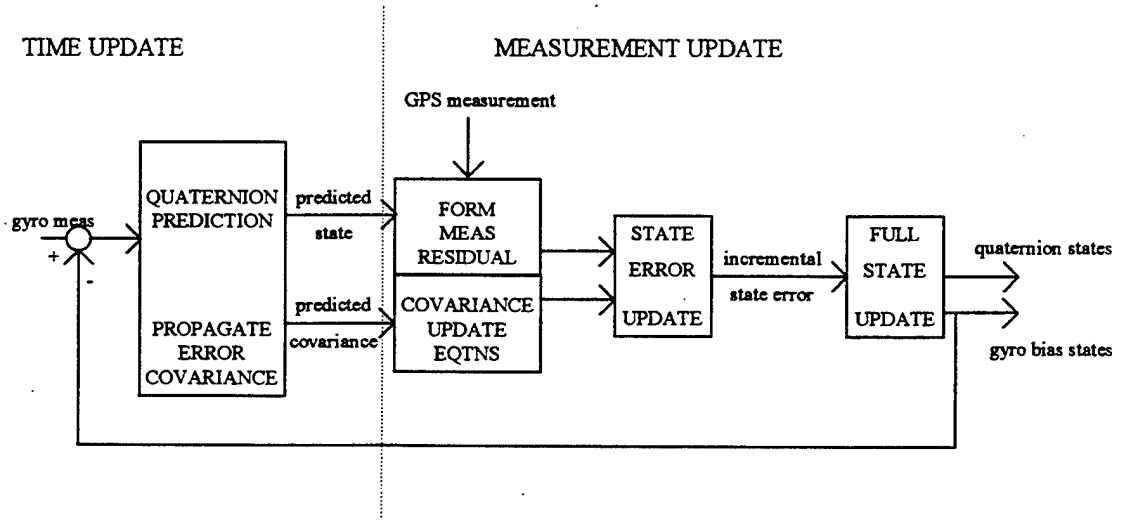

Figure 4.8. Extended Kalman Filter Algorithm

The dynamic model for the full state $\hat{x}$ is given by

$$\frac{\mathrm{d}}{\mathrm{d}t}\hat{\bar{q}} = \tfrac{1}{2}\Omega^{\times}\hat{\bar{q}} \tag{4.4}$$

$$\frac{\mathrm{d}}{\mathrm{d}t}\hat{b} = 0 \tag{4.5}$$

$$\hat{x} = \begin{bmatrix} \hat{\bar{q}} \\ \hat{b} \end{bmatrix} \tag{4.6}$$

where the cross product matrix $\Omega^{\times}$ is given by

$$\Omega^{\times} = \begin{bmatrix} 0 & \hat{\omega}_3 & -\hat{\omega}_2 & \hat{\omega}_1 \\ -\hat{\omega}_3 & 0 & \hat{\omega}_1 & \hat{\omega}_2 \\ \hat{\omega}_2 & -\hat{\omega}_1 & 0 & \hat{\omega}_3 \\ -\hat{\omega}_1 & -\hat{\omega}_2 & -\hat{\omega}_3 & 0 \end{bmatrix} \tag{4.7}$$

and the angular velocity estimate $\hat{\omega}$ is obtained from

$$\hat{\omega} = \omega_{\text{meas}} - \hat{b} \tag{4.8}$$

where ω_{meas} is the raw (biased) gyro measurement vector and $\hat{b}$ is the best estimate of the gyro bias vector. Note that the dynamic model for the controlled spacecraft motion is derived directly from the gyro measurements.

The time propagation for the total attitude quaternion $\hat{\bar{q}}$ from time *k-1* to *k* is obtained from the gyro angular velocity measurements and the attitude kinematics described by

$$\hat{\bar{q}}_k = e^{\frac{1}{2}\Omega^{\times}\Delta t}\hat{\bar{q}}_{k-1}. \tag{4.9}$$

Following Lefferts, et al. [1982], we formulate the covariance propagation and measurement update equations in terms of a six-dimensional state vector to avoid singularities. The six-dimensional state vector is defined as

$$\tilde{x} \equiv \begin{bmatrix} \delta q \\ b \end{bmatrix} \tag{4.10}$$

where δq represents the three components of the small quaternion correction. Thus, the four dimensional quaternion $\delta\bar{q}$ represent the rotation between the true state and the estimated state, as defined by

$$\delta\bar{q} \equiv \bar{q} \otimes \hat{\bar{q}}^{-1} \tag{4.11}$$

where an overbar indicates a four-dimensional quaternion, a carat indicates an estimated quantity and $\otimes$ denotes quaternion composition.

Next we linearize about the reference trajectory provided by the angular velocity, and formulate the extended Kalman filter for the state error vector, noting that

$$\Delta\tilde{x} \equiv \begin{bmatrix} \delta q \\ \Delta b \end{bmatrix}. \tag{4.12}$$

The dynamic equations for the state error are then

$$\frac{d}{dt}\Delta\tilde{x} = F\Delta\tilde{x} + Gw \tag{4.13}$$

where

$$\mathbf{F}(t_k) = \begin{bmatrix} 0 & \hat{\omega}_3(t_k) & -\hat{\omega}_2(t_k) & -\frac{1}{2} & 0 & 0 \\ -\hat{\omega}_3(t_k) & 0 & \hat{\omega}_1(t_k) & 0 & -\frac{1}{2} & 0 \\ \hat{\omega}_2(t_k) & -\hat{\omega}_1(t_k) & 0 & 0 & 0 & -\frac{1}{2} \\ 0 & 0 & 0 & 0 & 0 & 0 \\ 0 & 0 & 0 & 0 & 0 & 0 \\ 0 & 0 & 0 & 0 & 0 & 0 \end{bmatrix} \tag{4.14}$$

$$G = \begin{bmatrix} -\frac{1}{2}I_{3\times3} & 0_{3\times3} \\ 0_{3\times3} & I_{3\times3} \end{bmatrix} \tag{4.15}$$

and $w \sim \mathrm{N}(0, Q_d)$.

To propagate the state error covariance matrix P, compute the state transition matrix, Φ, from this linearized model

$$\Phi(k+N|k) = e^{\mathbf{F}(t_{k+N}-t_k)} \tag{4.16}$$

where N is the number of time propagation steps between measurement updates.

Then the time propagation for the covariance matrix is given by

$$P_{k+1}^{-} = \Phi P_k^{+} \Phi^T + Q_d. \tag{4.17}$$

Next we define a transformed measurement residual vector that relates the GPS measurement $\bar{q}_{GPS}$ to the state vector correction $\Delta\tilde{x} = \begin{bmatrix} \delta q & \Delta b \end{bmatrix}^T$. First we form the measurement residual

$$\Delta z = \Delta\bar{q} \equiv \bar{q}_{GPS} - \hat{\bar{q}}^{-} . \tag{4.18}$$

This measurement residual is not a quaternion, but it is related to the state according to equation (127) in Lefferts, et al. [1982], if we take

$$\bar{q}_{GPS} = \bar{q} + \Xi(\bar{q})v \tag{4.19}$$

where

$$\Xi\left(\hat{\bar{q}}\right) = \begin{bmatrix} \hat{q}_4 & -\hat{q}_3 & \hat{q}_2 \\ \hat{q}_3 & \hat{q}_4 & -\hat{q}_1 \\ -\hat{q}_2 & \hat{q}_1 & \hat{q}_4 \\ -\hat{q}_1 & -\hat{q}_2 & -\hat{q}_3 \end{bmatrix} \tag{4.20}$$

and the three independent quantities representing the small angle measurement error, v, are described by

$$v \sim \mathrm{N}\left(0, R_{3\times 3}\right). \tag{4.21}$$

Then

$$\Delta z = \Delta\bar{q} = \Xi\left(\hat{\bar{q}}\right)\delta q + \Xi\left(\hat{\bar{q}}\right)v \tag{4.22}$$

where the matrix $\Xi\left(\hat{\bar{q}}\right)$ accounts for the combination of quaternion components. A filter using this form gives rise to a singularity in the gain equation. To avoid this problem, we define the transformed measurement residual of dimension three as

$$\Delta\tilde{z} = \Xi^{T}\left(\hat{\bar{q}}\right)\Delta z = \delta q + v . \tag{4.23}$$

Note that the transformed measurements contain three quantities that retain all the information contained in the original four-dimensional measurement residual.

The measurement observation matrix for the transformed measurement residual is just

$$H = \left[I_{3\times 3} \quad 0_{3\times 3}\right]. \tag{4.24}$$

The optimal updated state and covariance are then given by

$$K = P^{-}H^{T}\left(HP^{-}H^{T} + R\right)^{-1} \tag{4.25}$$

$$\Delta\hat{\tilde{x}} = K(\Delta\tilde{z}) \tag{4.26}$$

$$P^{+} = (I - KH)P^{-}(I - KH)^{T} + KRK^{T}. \tag{4.27}$$

The updated total state can be obtained as in Lefferts, et al. [1982], using the following relations

$$\Delta\tilde{x}^{+} \equiv \begin{bmatrix} \delta\hat{q}^{+} \\ \Delta\hat{b}^{+} \end{bmatrix} \tag{4.28}$$

$$\delta\hat{\tilde{q}}^{+} \equiv \begin{bmatrix} \delta\hat{q}^{+} \\ 1 \end{bmatrix} \tag{4.29}$$

$$\hat{\tilde{q}}^{+} = \delta\hat{\tilde{q}}^{+} \otimes \hat{\tilde{q}}^{-} \tag{4.30}$$

$$\hat{b}^{+} = \hat{b}^{-} + \Delta\hat{b}^{+}. \tag{4.31}$$

4.8 MEASUREMENT DIFFERENCING ESTIMATION ALGORITHM

A technique for improved Kalman filtering in the presence of time correlated measurement errors involves differencing successive measurements to "whiten" the errors. This approach was first suggested by Bryson and Henrickson [1968], and was discussed further by Bryson and Ho [1975]. Provided the time constant of the measurement error correlation is large compared to the sampling frequency, the errors in successive differenced measurements will not be correlated in time. The disadvantage of this approach is that the measurement noise at each epoch is increased. However, measurement differencing is preferred over state vector augmentation to account for the non-white measurement errors because increasing the dimension of the state vector is inconvenient for real-time applications and, more importantly, computations of the filter gains are typically ill-conditioned [Bryson and Ho, 1975].

Measurement differencing requires a very good dynamic model or measurements with little high frequency noise to successfully overcome the increased measurement noise introduced by the approach. In the present case, FOG measurements provide the dynamic model very accurately for short time spans relative to the gyro drift. The prediction equations for the measurement differencing case are the same as those given by equations (4.9-4.17). The measurement update equations are modified from Bryson and Henrickson [1968] to relate the transformed (three-dimensional) measurement residual to the total state, as in the previous section. Transformed measurement residuals are used to account for quaternion composition relations and prevent singularities in the covariance update equations. The new model for the transformed measurement residual is given as

$$\Delta\tilde{z}_k = H\begin{bmatrix} \delta q \\ b \end{bmatrix}_k + \varepsilon_k \tag{4.32}$$

where

$$\varepsilon_k = \Psi \varepsilon_{k-1} + w_k \tag{4.33}$$

$$\Psi = e^{-\beta \Delta t} I_{3\times 3}. \tag{4.34}$$

Note that ε_k is first order Markov process described by the transition matrix Ψ. β is the inverse time constant of the Markov process that models the multipath errors, Δt is the interval between GPS measurements, and w_k is a Gaussian white noise parameter with covariance Q_{df}. The measurement observation matrix, H, is as defined in equation (4.23).

The pseudo measurement is defined to be the difference

$$\zeta_{k-1} = \Delta\tilde{z}_k - \Psi \Delta\tilde{z}_{k-1}. \tag{4.35}$$

The pseudo measurement error covariance matrix is given by

$$R = HGQ_dG^TH^T + Q_{df} \tag{4.36}$$

where Q_{df} is the covariance of the gyro noise.

Note that the (pseudo) measurement and process noises are now correlated according to the covariance matrix

$$C \equiv \mathrm{E}\left[w\varepsilon^T\right] = Q_dG^TH^T. \tag{4.37}$$

Following Bryson and Ho [1975], we define the matrix D to be

$$D = GCR^{-1}. \tag{4.38}$$

Then the Kalman filter measurement update equations become

$$K = P_k^- H_r^T \left(H_r P_k^- H_r^T + R\right)^{-1} \tag{4.39}$$

$$\begin{aligned} P_{k-1|k} &= \left(I - KH_r\right)P_{k-1}^-\left(I - KH_r\right)^T \\ &\quad + KRK^T \end{aligned} \tag{4.40}$$

$$\begin{aligned} P_{k|k} &= \left(\Phi - DH_r\right)P_{k-1|k}\left(\Phi - DH_r\right)^T \\ &\quad + Q_d - DRD^T \end{aligned} \tag{4.41}$$

$$\Delta\hat{\tilde{x}}_{k-1|k} = K\left(\zeta_{k-1}\right) \tag{4.42}$$

$$\Delta\hat{\tilde{x}}_{k|k} = \Phi\Delta\hat{\tilde{x}}_{k-1|k} + D\left(\zeta_{k-1} - H_r\Delta\hat{\tilde{x}}_{k-1|k}\right) \tag{4.43}$$

where

$$H_r = H\Phi - \Psi H\,. \tag{4.44}$$

The notation *k-1|k* is used to denote quantities computed at time step *k-1* given a GPS measurement at time *k*. This time lag of one update epoch is introduced by the pseudo measurement which includes measurements at time *k-1* and *k*. Equations (4.41) and (4.43) propagate the covariance and state estimates to the current measurement epoch.

4.9 SIMULATION RESULTS AND DISCUSSION

Figure 4.9 shows Kalman filter error plots for the attitude angles using the extended Kalman filter algorithm. Attitude quaternion output has been converted to yaw, pitch, and roll for easier interpretation. Note that the errors are time correlated due to multipath errors in the GPS measurements. These time correlated errors will be reduced using the measurement differencing algorithm.

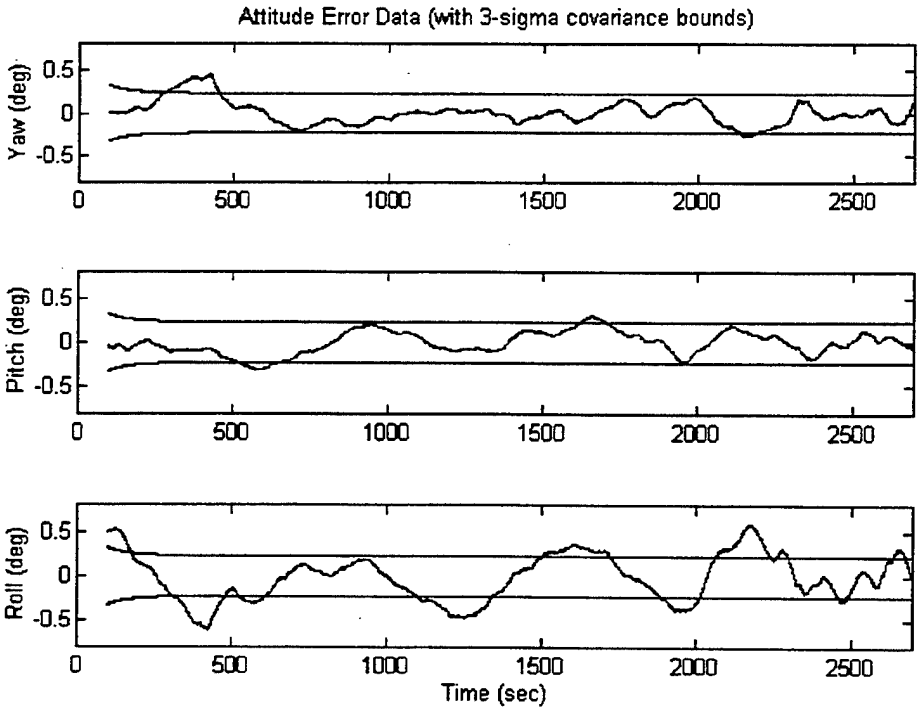

Figure 4.9. Kalman Filter Error Plot.

A sample comparison of simulation results for the two filter approaches is shown in Figure 4.10.

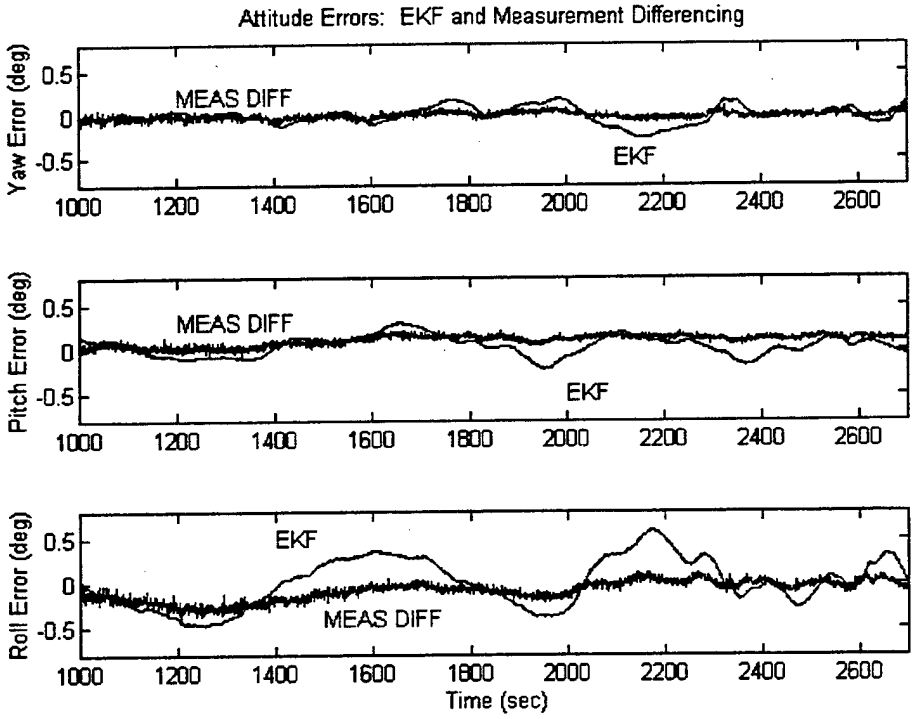

Figure 4.10. Comparison of Kalman Filter and Measurement Differencing Kalman Filter for Integrated GPS/FOG Measurements.

The measurement differencing approach successfully reduces the effect of GPS errors due to multipath in the combined GPS/FOG solution. The standard deviation of the yaw errors in Figure 4.10 is 0.03 deg using the measurement differencing algorithm compared to 0.10 deg using the standard Kalman filter. The maximum errors are also reduced using measurement differencing from 0.27 deg to 0.11 deg for the yaw error data shown. Similar reductions apply to the pitch and roll error performance of the measurement differencing algorithm.

Extended periods where attitude errors have a non-zero mean are also greatly reduced with the measurement differencing approach, a feature which could prove important in a closed loop attitude control system. Improved performance of measurement differencing approach is due to the fact that the GPS errors can be approximated by a first-order Markov process and that an accurate dynamic model is available from the FOG measurements.

Convergence of the measurement difference error covariance is slower than with the extended Kalman filter algorithm. This is due to the increased measurement error covariance that arises in the measurement differencing formulation. Convergence times for the measurement differencing algorithm are nonetheless short compared with the orbit period, so this does not appear to be a significant limitation of this approach when applied to small satellites.

It should also be noted that estimates of the gyro bias states are not improved using the measurement differencing approach since they are not observed directly. Smoothing of the measurement differencing algorithm results may also be possible, and will be considered in future research.

Further study of the sensitivity of the measurement differencing algorithm to uncertainties in the time constants in the correlated measurement error transfer function will be conducted to asses the viability of this approach for a broad range of multipath conditions. Preliminary simulation results indicate that errors in the time constant of 100 sec out of 300 sec do not appreciably effect estimation accuracy. Future ground testing will be conducted to characterize multipath reflections from the JAWSAT solar panels.

4.10 MINIMIZING RECEIVER ON-TIME

The mission profile for JAWSAT involves the use of PPT thrusters to perform gradual maneuvering of the spacecraft orbit. To prevent radio frequency interference (RFI) and provide sufficient power for all subsystems, the PPT will not be operated simultaneously with communications transceivers and the GPS receiver. During thrust maneuvers (which could last several months or even years) pulses will be performed for half of each orbit period, and the GPS receiver and communications equipment will operate for the other half. Since the FOG attitude errors and bias errors grow rather slowly with time, the use of intermittent GPS measurements was studied to see if attitude knowledge could be maintained within JAWSAT requirements.

A parametric covariance analysis was performed to determine how long the GPS receiver can be idle while still maintaining attitude knowledge within 1 deg. The allowable idle time was only about 5 min. Simulation results were generated using GPS measurements every 1 sec until the filter reached steady state. After this initialization period GPS measurements were alternately available and unavailable for spans of 5 min. The extended Kalman filtering algorithm (not the measurement differencing filter) was used in this simulation of intermittent GPS measurements. Attitude error plots for this case are shown in Figure 4.11.

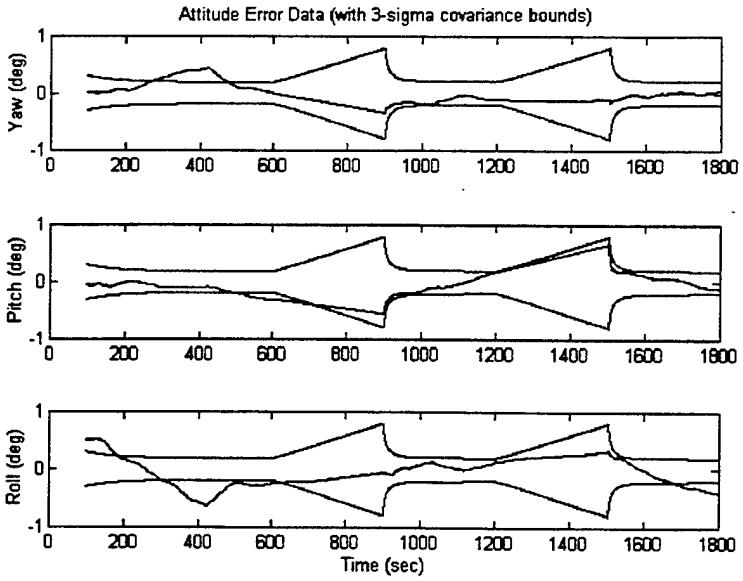

Figure 4.11. Attitude Estimation Errors: Intermittent Use of GPS. *Covariance bounds grow when there are no GPS measurements to estimate FOG bias parameters.*

Note that the uncertainty in the attitude error (represented by the covariance) grows when there are no GPS measurements available to provide information to update the gyro bias estimates. The 5 min. idle periods shown in Figure 4.11 do not satisfy the JAWSAT operational constraint to deactivate the GPS receiver for a 45 min. period each orbit that the PPTs are in use. Therefore, additional measurements from other instruments such as the sun sensors will be needed to estimate gyro drift during the GPS idle period. Incorporation of sun sensor data into the integrated attitude determination algorithms discussed in this chapter is a topic for future research.

4.11 SUMMARY

This chapter described an integrated attitude determination system using GPS and FOGs for JAWSAT. JAWSAT is planned to be the first three-axis stabilized university sponsored satellite [Smith and Liefer, 1993]. The attitude determination system is being designed to incorporate several sensors for improved reliability and technology demonstration. The reasons for designing an integrated attitude determination system for JAWSAT include improved accuracy over stand-alone sensors and failure detection of attitude sensors. This chapter demonstrates a method for improving the accuracy of integrated GPS and gyro attitude measurements using a measurement differencing Kalman filter algorithm.

Future work will address an integrated attitude determination system containing sun sensors in addition to GPS and FOGs. This effort will focus on failure detection algorithms and extending the idle time of the GPS receiver to conserve power. Ground testing will be extended to include characterization of multipath reflections due to the JAWSAT solar panels. Dynamic testing of an integrated attitude determination system using GPS and gyros will also be performed.

REFERENCES FOR JAWSAT ATTITUDE DETERMINATION

AXELRAD, P. and CHESLEY, B.C. "Performance Testing of a GPS Based Attitude Determination System," AIAA-93-3787, AIAA GN&C, Monterey, California, August 9-11, 1993, pp. 809-819.

BRYSON, A.E. and L.J. HENRICKSON "Estimation Using Sampled Data Containing Sequentially Correlated Noise," *Journal of Spacecraft and Rockets*, Vol. 5, No. 6, June 1968, pp. 662-665.

BRYSON, ARTHUR E. and YU-CHI HO *Applied Optimal Control.* Hemisphere Publishing, New York, 1975.

COHEN, C.E. *Attitude Determination Using GPS,* Ph.D. Dissertation, Stanford University, December 1992.

GELB, ARTHUR (ed.) *Applied Optimal Estimation.* MIT Press, Cambridge, Massachusetts, 1974.

LEFÈVRE, H.C., BERGH, R.A., and SHAW, H.J. "An Overview of Fiber-Optic Gyroscopes," *Journal of Lightwave Technology*, Vol. LT-2, No. 2, April 1984, pp. 91-107.

LEFFERTS, E.J., MARKLEY F.L., and SHUSTER, M.D. "Kalman Filtering for Spacecraft Attitude Estimation," *Journal of Guidance, Control and Dynamics,* Vol. 5, No. 5, September-October 1982, pp. 417-429.

LIGHTSEY, E.G., C.E. COHEN, W.A. FEESS, and B.W. PARKINSON, "Analysis of Spacecraft Attitude Measurements Using Onboard GPS," AAS Guidance and Control Conference, Keystone, Colorado, Februrary, 1994.

MARK, J., TAZARTES, D., FIDRIC, B., and CORDOVA, A. "A Rate Integrating Fiber Optic Gyro," *Navigation*, Vol. 38, No. 4, Winter 1991-92, pp. 341-353.

MATHEWS, A. "Utilization of Fiber Optic Gyros in Inertial Measurement Units," *Navigation*, Vol. 37, No. 1, Spring 1990, pp. 17-38.

MAYBECK, PETER S. *Stochastic Models, Estimation, and Control.* Academic Press, Orlando, Florida, 1979.

MONTGOMERY, HALE. "Washington View," *GPS World*, Vol. 5, No. 9, September 1994, p 16.

REEVES, EMERY I. U.S. Air Force Academy Department of Astronautics. Personal communication. August 31, 1994.

SIOURIS, G.M. *Aerospace Avionics Systems: A Modern Synthesis.* Academic Press, San Diego, 1993.

SMITH, JAY L. and LIEFER, RANDALL "Exploring Space with a Microsat...Where No Microsat has Gone Before," SPIE Small-Satellite Technology and Applications III (1993), Vol. 1940, pp. 12-18.

TRIMBLE NAVIGATION, "TANS Vector Specification and User's Manual," May 1994.

WARD, LISA M. "Spacecraft Attitude Estimation Using GPS: Methodology and Results," Ph.D. Dissertation Prospectus, University of Colorado, Boulder, August 12, 1994.

GPS BASED ATTITUDE DETERMINATION

FY'94-95 Technical Report I

to the Naval Research Laboratory

NRL Scientific Officer - Bernard Kaufman

Principal Investigator - Penina Axelrad

Report Written By - Penina Axelrad
Charles P. Behre
Christopher J. Comp
Lisa M. Ward

Colorado Center for Astrodynamics Research
University of Colorado, CB 431
Boulder, CO 80309

October 6, 1995

Award: N00014-93-1-G030, Account: 153-7545

ABSTRACT

This report describes the research performed by the Colorado Center for Astrodynamics Research during the first half of FY'94-95 on spacecraft attitude determination using GPS. The specific topics currently under investigation are attitude determination algorithms for Earth pointing and spinning satellites and multipath mitigation in GPS phase observations.

Enhancements to the previously developed bootstrapping algorithms for attitude and baseline estimation have been implemented and tested on flight data from RADCAL. These include improvements to the attitude initialization procedure and augmentation of the attitude filter state to include disturbing torques. The computer simulation used to study these algorithms was also improved to include multipath and receiver noise models. Results are presented for each of five data sets collected on RADCAL. Performance is evaluated by comparing filter and point solutions. Plans for future work include improving the dynamic model for the disturbing torque states and developing a combined attitude and baseline filter.

A study of adaptive signal processing techniques was conducted with the goal of improving the performance of the multipath correction algorithm developed previously. Two classes of algorithms were considered - sequential estimation including the short-time FFT, the data-adaptive evolutionary periodogram, and adaptive least squares, and adaptive filtering approaches including both system modelling and predictive formulations. These methods were tested on both time varying sinusoidal signals as well as simulated multipath data. The most promising techniques were found to be the infinite impulse response notch filter and the adaptive least squares. Continued research in these areas is recommended.

Several techniques for the determination of attitude of a spinning satellite are described and compared. The analysis focuses on the effect of the nutation angle on the accuracy with which each procedure determines the spin frequencies, nutation angle, and orientation of the angular momentum vector. A simulation of the vehicle dynamics and the GPS measurements was developed to evaluate the algorithm performance. This research was presented at the ION GPS'95 conference in Palm Springs.

TABLE OF CONTENTS

LIST OF FIGURES

LIST OF TABLES

1.0 OVERVIEW

This report describes the research performed by the Colorado Center for Astrodynamics Research during the first half of FY'94-95 on spacecraft attitude determination using GPS. The work is a continuation of research described in the first and second technical reports for FY'93-94 [1,2]. Portions of this research have been reported in conference papers [3-5].

The overall project encompasses various methods for using GPS to determine the attitude of a spacecraft in near Earth orbit. The specific topics covered in this technical report are point solution and Kalman filtering approaches for both attitude and baseline estimation, adaptive signal processing techniques which are being considered for use in multipath mitigation, and frequency and time domain approaches to attitude estimation of a spinning satellite.

The highlights of the technical advances made during the first half of FY'94-95 are as follows:

- Improvement to attitude initialization procedure.
- Augmentation of the attitude Kalman filter to include disturbance torques.
- Improved modeling of receiver noise and multipath in the attitude simulation.
- Continued analysis of flight data from RADCAL.
- Investigation and identification of candidate adaptive signal processing algorithms for use with the SNR based multipath correction technique.
- Development of angular velocity and nutation angle filters for attitude determination of a spinning satellite.
- Comparison of frequency and time domain approaches for attitude determination of a spinning satellite.

Section 2 summarizes the bootstrapping attitude determination algorithms and presents results from both simulated and on-orbit data from the RADCAL satellite. Comparisons between results from different data sets are made as means for evaluating the performance of the algorithms. Plans for future work in this area are provided.

Section 3 presents preliminary research on adaptive signal processing techniques we plan to apply to the multipath mitigation problem. The previous technical report discussed a post processing method which used SNR data to aid in correcting the differential phase measurements. The current investigation aims to correct some deficiencies in the previous approach including the need for human interaction with the algorithm and the need for measurement post-processing as opposed to real-time operation. This section discusses the advantages and disadvantages of various techniques which were considered, and identifies the most promising methods to be pursued further.

Section 4 describes algorithms and simulation results for attitude determination on a spinning satellite. Both time domain and frequency domain approaches are considered and comparisons are made among the various methods. This section is derived from a technical paper presented at the ION GPS-95 conference on September 15, 1995 in Palm Springs [5].

[1] Axelrad, P., C.P. Behre, C.J. Comp, and L.M. Ward, "GPS Based Spacecraft Attitude Determination", FY'93-94 Technical Report I to the Naval Research Laboratory, May 16, 1994.

[2] Axelrad, P., B.C. Chesley, C.J. Comp, and L.M. Ward, "GPS Based Spacecraft Attitude Determination", FY'93-94 Technical Report II to the Naval Research Laboratory, October 16, 1994.

[3] Ward, L.M. and P. Axelrad, "Spacecraft Attitude Estimation Using GPS: Methodology and Results for RADCAL," Presented at the ION National Technical Meeting, Anaheim, CA, January 20, 1995.

[4] Melvin, P.J., L.M. Ward, and P. Axelrad, "The Analysis of GPS Attitude Data from a Slowly Rotating, Symmetrical Gravity Gradient Satellite," Presented at the AAS/AIAA Spaceflight Mechanics Meeting, Albuquerque, NM, February 13-16, 1995, AAS 95-133.

[5] Axelrad, P. and C.P. Behre, "A Comparison of GPS-Based Attitude Estimation Techniques for Spinning Satellites," Presented at ION GPS-95, Palm Springs, September 15, 1995.

2.0 Attitude and Baseline Estimation

Lisa M. Ward

2.1 Introduction

Previous reports to NRL [1], [2], and [3] describe a sequence of algorithms that begin with the most basic assumptions about the vehicle attitude and ultimately provide highly accurate attitude estimates using GPS measurements. The four algorithms are an attitude initialization process, an attitude point solution, an extended Kalman filter for attitude estimation, and an on-orbit baseline refinement algorithm. These algorithms have been tested on both simulated data and flight data collected on board the RADCAL satellite.

In this section of the report, a brief description of each of the attitude estimation algorithms is presented. The remainder of the report focuses on enhancements to the previous work which include:

- Improved data selection for the initialization process. (Section 2.3.1)
- Further analysis of the contribution of baseline errors to the attitude solution. (Section 2.3.2)
- Augmented state vector in the Kalman filter to include disturbance torques. (Section 2.3.3)
- Analysis of additional RADCAL data. (Section 2.4)
- Addition of two multipath models to the simulation. (Sections 2.5.2 and 2.5.3)
- Addition of a receiver noise model that is based on the antenna gain pattern. (Section 2.5.1)
- Analysis of simulated REX II data. (Section 2.6)

2.2 Summary of Estimation Algorithms

A brief review of each of the estimation algorithms is given below. Detailed descriptions can be found in Reference [1].

2.2.1 Attitude Initialization

A rough estimate of both vehicle attitude and antenna locations are needed before accurate attitude estimation may begin. The initialization algorithm estimates the initial attitude, angular velocity, and line biases using a least squares batch process based on Cohen and Parkinson [4]. A simplified dynamical model is employed whereby the angular velocity of the vehicle (with respect to the orbit local frame) is assumed constant. The process, using very little *a priori* information, is iterated until the corrections become sufficiently small. The other algorithms require the attitude errors to be small enough to resolve the integers directly. This means that the combined attitude, line bias, and baseline errors must be less than 1/4 of a wavelength.

2.2.2 Baseline Estimation

Knowledge of the GPS antenna baselines are a crucial part of obtaining accurate attitude estimates. Without a conclusive survey of the baselines prior to launch, as is the case with RADCAL, we refine *a priori* estimates based on the mechanical drawings with a three-step algorithm. First, a sequential filter is used to estimate the line biases, baseline vectors, and inertial angular velocity in the local reference frame. Next, the body fixed frame is defined by two of the local baselines, and all three baseline are transformed from the local frame to the body frame. Finally, the baseline coordinates in the body frame are averaged over time to obtain the best estimate.

2.2.3 Attitude Kalman Filter

After determining an initial attitude estimate and obtaining accurate baseline estimates, an extended Kalman filter based on Lefferts, Markley, and Shuster [5] is used for ongoing attitude determination. The filter combines GPS measurements and dynamic information to accurately estimate the attitude of a spacecraft in addition to other parameters.

2.2.4 Attitude Point Solution

An attitude point solution is also used in this study to estimate the local to body quaternion. This algorithm is an iterative least squares fit to a set of simultaneous observations. Since no information about the dynamics of the system is incorporated into the solution, the estimates are noisy. However, it does serve as a benchmark against which other methods can be compared.

2.3 Estimation Algorithm Enhancements

2.3.1 Initialization Enhancements

A number of issues have been raised concerning the use of the initialization algorithm. Although the content of the algorithm has not been changed, we have addressed these issues as presented below.

One of the main questions concerning the initialization algorithm was: How close does the intial guess have to be in order for the process to converge? For a gravity gradient stabilized satellite, like RADCAL the pitch and roll angles are usually known to within 20 degrees. The yaw angle, however, is completely unknown. In this situation, choosing four sets of initial conditions with the yaw angles separated by 90 degrees will produce at least one convergent

Another question concerning this algorithm was: What constitutes a valid solution? Sometimes the algorithm would converge to a solution that was clearly invalid (e.g. not nadir pointing). How do we know if a solution that looks correct actually is? The line bias estimates provide the answer. We know that the line bias estimates for a particular baseline should all be closely clustered. The largest difference between line bias estimates for a baseline provides a measurement of proximity. If the largest difference is at most 1/4 of a cycle for two out of three baselines, the solutions is deemed correct.

Since this algorithm uses very little *a priori* information, it is very sensitive to the input data. A third question that arose was: How do we select data that will produce a valid

solution? To answer this question we have developed a set of data selection criteria which insures the success of the algorithm. These criteria are:

Interval Length: The length of the interval must be long enough to obtain adequate information to resolve the ambiguities, but short enough so that the assumption that angular velocity is constant is not violated. We found 10 minutes of data to be optimal for RADCAL.

Number of GPS Satellites: Since the number of GPS satellites dictates the number of states to be estimated, the number of satellites must be chosen prior to running the algorithm. With too few satellites not enough information will be available to resolve the integers. But too many satellites (and hence, too many states) could decrease the algorithm's performance. We found that using 3 or 4 satellites produced the best results.

Satellite Motion: Being a motion based technique, we look for GPS satellites with large motion relative to the user satellite. Large satellite motion will translate into a large change in the differential phase measurements. Measuring the change in phase measurement over each baseline for a particular satellite provides a gauge of how much satellite motion is present. Satellites with cycle slips or changes in the master antenna are eliminated. For RADCAL, satellites with a change in phase measurement of less than 0.25 cycle over each baseline are also eliminated. If at least 3 satellites remain and the cumulative phase change for the interval is more than 8 cycles then this interval is considered a good candidate. (The cumulative change is calculated by adding the change in phase over each baseline to produce a total change for a satellite, then adding the total change for each satellite to produce a cumulative change for the interval). In addition to looking for large phase changes, to insure that the geometry is favorable we required at least one of the satellites to attain an elevation of 50 degrees or more.

Reliable Data: Poor data produced by low signal levels or corrupted by multipath will degrade the performance of this algorithm. Furthermore, data from satellites low on the horizon will be particularly susceptible to producing poor results. To account for this, measurements with a low signal-to-noise ratio (SNR) were filtered out. We found that during the satellite selection process described above, filtering data with SNR's below 6 AMU* indicated intervals that would yield a consistent solution with a very high probability of success.

Sometimes no intervals contained data that satisfied the above requirements. In these cases the constraints were loosened either by lowering the SNR cutoff or lowering the phase change per baseline cutoff. While loosening the constraints usually indicated a usable interval of data, the probability of success was decreased.

2.3.2 Baseline Error Analysis

It is well known that errors in the baseline estimates produce errors in the attitude solutions. This relationship, however, is not a direct one. The attitude error caused by a baseline error

*Amplitude Measurement Unit. Corresponds to the amplitude of recovered carrier in a bandwidth of 1KHz.

is dependent not only on the baseline error itself, but also on the baseline. Furthermore, the orientation of each of these vectors with respect to the line-of-sight vector is also an important factor.

To determine the extent to which a baseline error, $\delta\mathbf{b}$, affects the attitude solution, recall that the observed phase measurement, $\Delta\phi$, for baseline i observing satellite j, is given by the equation

$$\Delta\phi_{ij} = \left(\mathbf{b}_i^B\right)^T \mathbf{C}\mathbf{e}_j^L \tag{2.1}$$

where $\mathbf{b}_i^B$ is the baseline vector in the body frame, $\mathbf{C}$ is the local-to-body transformation matrix, and $\mathbf{e}_j^L$ is the line-of-sight vector. Equation 2.1 also assumes the measurement noise, cycle integer, and differential line bias are all zero.

Consider that we have an *a priori* estimate of the attitude, $\hat{\mathbf{C}}$, and an *apriori* estimate of the baseline, $\hat{\mathbf{b}}_i^B$, so that

$$\mathbf{b}_i = \hat{\mathbf{b}}_i + \delta\mathbf{b}_i \tag{2.2}$$

$$\mathbf{C} = \delta\mathbf{C}\hat{\mathbf{C}} = \left[\mathbf{I} + \Theta^\times + \mathcal{O}\left(\delta\theta^\in\right)\right]\hat{\mathbf{C}} \tag{2.3}$$

where the small rotation matrix, $\delta\mathbf{C}$, is a function of the small angle rotation vector, $\delta\theta$, and $\Theta^\times$ is the cross product matrix associated with $\delta\theta$.

Let $\hat{\mathbf{e}}_j = \hat{\mathbf{C}}\mathbf{e}_j^L$. Furthermore, assume that all quantities are given in the body frame. This allows us to drop the reference frame superscripts and simplify notation.

After making the substitutions described in Equations 2.2 and 2.3 and neglecting second order terms, it follows that the Equation 2.1 can be rewritten as

$$\Delta\phi_{ij} = \left(\hat{\mathbf{b}}_i + \delta\mathbf{b}_i\right)^T \hat{\mathbf{e}}_j + \left(\hat{\mathbf{b}}_i + \delta\mathbf{b}_i\right)^T \Theta^\times \hat{\mathbf{e}}_j \tag{2.4}$$

Also recall that the predicted phase, which is a function of the *a priori* quantities only, is calculated by the equation

$$\Delta\hat{\phi}_{ij} = \hat{\mathbf{b}}_i^T \hat{\mathbf{e}}_j \tag{2.5}$$

Now the phase residual, $\delta\phi_{ij}$, which is the difference between the predicted and observed phase, is given by

$$\delta\phi_{ij} = \delta\mathbf{b}_i^T \hat{\mathbf{e}}_j + \left(\mathbf{b}_i + \delta\mathbf{b}_i\right)^T \Theta^\times \hat{\mathbf{e}}_j \tag{2.6}$$

or

$$\delta\phi_{ij} = \hat{\mathbf{e}}_j^T \delta\mathbf{b}_i + \hat{\mathbf{e}}_j^T \hat{\mathbf{B}}_i^\times \delta\theta + \hat{\mathbf{e}}_j^T \delta\mathbf{B}_i^\times \delta\theta \tag{2.7}$$

where $\hat{\mathbf{B}}_i^\times$ and $\delta\mathbf{B}_i^\times$ are the cross product matrices associated with the vectors $\hat{\mathbf{b}}_i$ and $\delta\mathbf{b}_i$, respectively.

The measurement gradient matrix which is also is calculated from *a priori* quantities, is given by the equation

$$\mathbf{H}_{ij} = \hat{\mathbf{e}}_j^T \hat{\mathbf{B}}_i^\times \tag{2.8}$$

Given enough observations we could solve for $\delta\theta$ and $\delta\mathbf{b}$. However, typically we ignore $\delta\mathbf{b}$ and solve the following equation

$$\mathbf{H}\delta\hat{\theta} = \delta\phi \tag{2.9}$$

to find the correction vector, $\delta\hat{\theta}$, to the *a priori* attitude. By substituting Equations 2.7 and 2.8 into the above equation, we can rewrite Equation 2.9 as follows:

$$\hat{\mathbf{e}}^T \hat{\mathbf{B}}^\times \delta\hat{\theta} = \delta\mathbf{b}^T \hat{\mathbf{e}} + \hat{\mathbf{e}}^T \hat{\mathbf{B}}^\times \delta\theta + \hat{\mathbf{e}}^T \delta\mathbf{B}^\times \delta\theta \tag{2.10}$$

Then the error in $\delta\theta$ due to $\delta\mathbf{b}$ which we define as

$$\delta\tilde{\theta} = \delta\theta - \delta\hat{\theta} \tag{2.11}$$

can be found with the equation

$$\hat{\mathbf{e}}^T \hat{\mathbf{B}}^{\times} \delta\tilde{\theta} = -\delta\mathbf{b}^T \hat{\mathbf{e}} \tag{2.12}$$

And for a single baseline and satellite, Equation 2.12 is equivalent to

$$\left(\hat{\mathbf{e}}_j \times \hat{\mathbf{b}}_i\right)^T \delta\tilde{\theta} = \delta\mathbf{b}_i \cdot \hat{\mathbf{e}}_j \tag{2.13}$$

If $\hat{\mathbf{e}}_j \times \hat{\mathbf{b}}_i = 0$ (i.e. if the line-of-sight and and baseline vectors are aligned), then the rotation about $\hat{\mathbf{b}}_i$ is not observable. However, if $\hat{\mathbf{e}}_j \times \hat{\mathbf{b}}_i \neq 0$, then we can approximate the magnitude of $\delta\tilde{\theta}$ with the equation

$$|\delta\tilde{\theta}| \approx \frac{|\delta\mathbf{b}_i \cdot \hat{\mathbf{e}}_j|}{|\hat{\mathbf{e}}_j \times \hat{\mathbf{b}}_i|} \tag{2.14}$$

To demonstrate, consider the case where the estimated baseline is perpendicular to the line-of-sight vector, and the baseline error is aligned with the line-of-sight vector as illustrated in Figure 2.1. The resulting error in the attitude solution will be on the order of $\delta\mathbf{b}/\mathbf{b}$ for small $\delta\mathbf{b}$. On the other hand, if the baseline error is also perpendicular to the line of sight vector, then resulting error in the attitude solution will be zero.

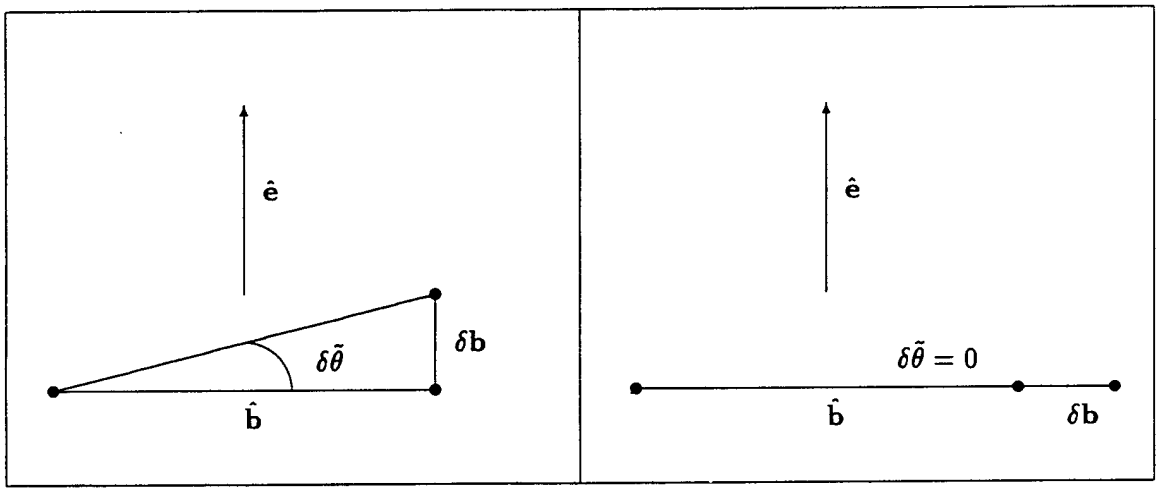

Figure 2.1: Effect of Baseline Error

2.3.3 Kalman Filter Enhancements

In the original formulation of the filter, given in [1], the attitude quaternion, angular velocity, and line biases were estimated. The state vector has now been augmented to estimate

disturbing torques as follows:

$$\mathbf{x} = \left[\begin{array}{ccc|ccc|ccc|ccc} \delta q_1 & \delta q_2 & \delta q_3 & \delta\omega_1 & \delta\omega_2 & \delta\omega_3 & \delta\tau_1 & \delta\tau_2 & \delta\tau_3 & \delta\beta_1 & \delta\beta_2 & \delta\beta_3 \end{array} \right]^T \tag{2.15}$$

where $\delta\mathbf{q}$, $\delta\omega$, $\delta\tau$, and $\delta\beta$ represent corrections to the local to body quaternion, the inertial angular velocity, the disturbing torque, and the line biases, respectively. The equation for the predicted phase difference is unchanged from the previous implementation. The measurement gradient $\mathbf{H}_{ij}$ for baseline i and satellite j is slightly modified as follows:

$$\mathbf{H}_{ij} = \left[\begin{array}{c|ccc|ccc|ccc} 2\left(\hat{\mathbf{C}}\,\mathbf{e}_j^L\right)^T \mathbf{B}_i^\times & 0 & 0 & 0 & 0 & 0 & 0 & h_{\beta_1} & h_{\beta_2} & h_{\beta_3} \end{array} \right] \tag{2.16}$$

where h_{β_n} is 1 if $i = n$ and zero otherwise.

Between measurement epochs, the quaternion and angular velocity states are advanced to the current measurement time by numerically integrating the nonlinear equations of motion for a gravity gradient stabilized satellite. These equations now are

$$\dot{q}_1 = \frac{1}{2}(\omega_1 q_4 - \omega_2 q_3 + \omega_3 q_2 + \Omega q_2) \tag{2.17}$$

$$\dot{q}_2 = \frac{1}{2}(\omega_1 q_3 + \omega_2 q_4 - \omega_3 q_1 - \Omega q_1) \tag{2.18}$$

$$\dot{q}_3 = \frac{1}{2}(-\omega_1 q_2 + \omega_2 q_1 + \omega_3 q_4 - \Omega q_4) \tag{2.19}$$

$$\dot{q}_4 = \frac{1}{2}(-\omega_1 q_1 - \omega_2 q_2 - \omega_3 q_3 + \Omega q_3) \tag{2.20}$$

$$\dot{\omega}_1 = K_1\omega_2\omega_3 - 3\Omega^2 K_1 C_{21} C_{31} + \frac{\tau_1}{I_1} \tag{2.21}$$

$$\dot{\omega}_2 = K_2\omega_1\omega_3 - 3\Omega^2 K_2 C_{11} C_{31} + \frac{\tau_2}{I_2} \tag{2.22}$$

$$\dot{\omega}_3 = K_3\omega_1\omega_2 - 3\Omega^2 K_3 C_{11} C_{21} + \frac{\tau_3}{I_3} \tag{2.23}$$

where Ω is the orbital rate of the spacecraft (i.e. the angular velocity of the local frame in inertial space), I_1, I_2, and I_3 are the principal moments of inertia, and K_1, K_2, and K_3 are defined as follows:

$$K_1 = (I_2 - I_3)/I_1 \tag{2.24}$$

$$K_2 = (I_3 - I_1)/I_2 \tag{2.25}$$

$$K_3 = (I_1 - I_2)/I_3 \tag{2.26}$$

The derivatives of the disturbing torque, τ, and line biases, β, are equal to zero. Derivations of the above equations can be found in Kane [6].

The covariance matrix is propagated forward with the state transition matrix derived from the linearized dynamical equations. Linearizing Equations 2.17-2.23 about the current estimate and neglecting second order terms leads to the following equations:

$$\delta\dot{\mathbf{q}} = \omega^\times\,\delta\mathbf{q} + \frac{1}{2}\delta\omega \tag{2.27}$$

and

$$\delta\dot{\omega}_1 = K_1 6\Omega^2\left[(C_{21}^2 - C_{31}^2)\delta q_1 - C_{11}C_{21}\delta q_2 + C_{11}C_{31}\delta q_3\right] \tag{2.28}$$

$$+K_1\left[\omega_3\delta\omega_2+\omega_2\delta\omega_3\right]+\delta\tau_1/I_1 \tag{2.29}$$

$$\delta\dot{\omega}_2 = K_2 6\Omega^2\left[C_{11}C_{21}\delta q_1+(C_{31}^2-C_{11}^2)\delta q_2-C_{21}C_{31}\delta q_3\right] \tag{2.30}$$

$$+K_2\left[\omega_3\delta\omega_1+\omega_1\delta\omega_3\right]+\delta\tau_2/I_2 \tag{2.31}$$

$$\delta\dot{\omega}_3 = K_3 6\Omega^2\left[-C_{11}C_{31}\delta q_1+C_{21}C_{31}\delta q_2+(C_{11}^2-C_{21}^2)\delta q_3\right] \tag{2.32}$$

$$+K_3\left[\omega_2\delta\omega_1+\omega_1\delta\omega_2\right]+\delta\tau_3/I_3 \tag{2.33}$$

Again, the derivatives of $\delta\dot{\tau}$ and $\delta\dot{\beta}$ are equal to zero.

2.4 Results for RADCAL

The following sections contain a compilation of attitude solutions and other results for RADCAL obtained with the improved methods described above. Recall that RADCAL is a symmetrical spacecraft in a near-circular, polar orbit at an altitude of 815 km, used by the U.S. Air Force for radar calibration. The physical parameters for RADCAL are given in Table 2.1. It is passively stabilized to a nadir pointing attitude by a gravity gradient boom and magnetic nutation dampers. RADCAL carries a Trimble Navigation TANS Quadrex receiver modified by Stanford to measure the differential phase of GPS signals arriving at four microstrip patch antennas mounted on the zenith face of the vehicle and canted outward 17.5 degrees.

The phase differences between each of 3 slaves and a master antenna are downloaded to the ground for post processing. In addition to the phase observation files, we also use the RADCAL GPS navigation solutions corrected for Selective Availability by the Air Force, and the precise GPS orbits calculated by the Jet Propulsion Laboratory. A total of 5 data sets have been processed and analyzed as listed in Table 2.2.

Table 2.1: RADCAL Parameters

	parameter	value	units
nominal orbit†	semimajor axis	1793	km
	eccentricity	0.01	
	inclination	90.0	deg
size†	body height	40.6	cm
	body diameter	76.2	cm
	boom height	6.069	m
	weight	89.3	kg
moment of inertia‡	radial	6.234	kg · m
	transverse	96.242	kg · m
	normal	96.675	kg · m

2.4.1 Attitude Initialization Results

Using the data selection criteria outlined in Section 2.2.1 we found the that each time a consistent solution was obtained, it proved to be within 10 degrees of the filter estimate

†Nominal orbit and size parameters are taken from Reference [7].

‡Moments of inertial are taken from the mechanical drawings.

Table 2.2: RADCAL Data Sets

Day	Date	Length	Data Rate
079	20 Mar 94	2.2 hrs	15 sec
107	17 Apr 95	5.9 hrs	12 sec
160	9 June 94	17.6 hrs	30 sec
165	14 Jun 94	11.2 hrs	30 sec
189	8 Jul 94	16.8 hrs	30 sec

for all data sets. However, since the quality of the RADCAL data is rather poor, finding a criteria that would produce good results without eliminating most of the data was not easy. Seventy-five percent of the measurements had an SNR of less than 9 AMU, and only two percent of the measurements had an SNR above 15 AMU. Ideally, we would like to filter out data with SNR's less than 8 or 10. With RADCAL, however, we had to settle for the lax requirement of 6 AMU. Even so, on three of the days the minimum phase change per baseline requirement had to be lowered to find any candidate intervals. On Day 189 the length of the interval had to be increased as well. Loosening the constraints to this extent resulted in occasionally having to try more than one interval before finding one that produced a consistent solution.

2.4.2 Baseline Estimation Results

The attitude and line biases from the initialization and baselines from the mechanical drawing provided the *a priori* values for the filter. The standard deviation of the measurement noise was set to 1 centimeter, and the process noise was chosen to allow for a 1 millimeter change in the baselines (expressed in local coordinates) over a 1 second interval. Differential phase measurements with an SNR of less than 3 AMU were eliminated from the solution. Table 2.3 contains the baseline estimation results for all days processed. The baselines from the mechanical drawings are also included in the table. After examining the baseline results from each of the five data sets, the estimates from Day 160 were chosen as the nominal baseline values to be used subsequently in the attitude filter and point solutions algorithms.

The estimates for each baseline coordinate are closely clustered. The maximum difference in baseline length between data sets is 7 millimeters. The maximum difference in baseline direction between data sets is 1 degree.

2.4.3 Attitude Kalman Filter Results

The attitude Kalman filter was run on the 5 data sets using the *a priori* attitude provided by the initialization routine. The Day 160 baselines and line biases were provided by the baseline estimator. The standard deviation of the measurement noise was set to 1 centimeter. The process noise covariance for each state are listed in Table 2.4; the values correspond to a 1 second interval. Figures 2.2-2.6 present the attitude filter solutions for each of the five data sets. Measurements with SNR's of less than 3 AMU are excluded from the solutions.

The Kalman filter results for Day 106 are shown in Figure 2.4. Here the spacecraft is slowly spinning about the yaw axis, and the rate of spin is near the orbit rate but opposite

Table 2.3: RADCAL Baseline Estimates

Day	Baseline 1 (m)			Baseline 2 (m)			Baseline 3 (m)		
	b_x	b_y	b_z	b_x	b_y	b_z	b_x	b_y	b_z
079	0.0	0.310	0.304	0.0	0.618	0.0	-.006	0.305	-.308
107	0.0	0.306	0.311	0.0	0.615	0.0	-.002	0.309	-.310
160	0.0	0.303	0.308	0.0	0.614	0.0	-.004	0.307	-.309
165	0.0	0.306	0.307	0.0	0.620	0.0	-.005	0.311	-.312
189	0.0	0.304	0.309	0.0	0.621	0.0	-.009	0.307	-.309
Mech.	0.0	0.313	0.313	0.0	0.626	0.0	0.0	0.313	-.313

in direction. Harmonic oscillations about the roll and pitch axes are also apparent which is typical of gravity gradient motion. On Day 107 the spacecraft displays similar behavior, shown in Figure 2.3.

Results from Day 189, however, indicate a different type of motion. In Figure 2.6, which shows the attitude solutions for Day 189, the yaw angle is seen to be fairly constant for the first four hours. The yaw rate then speeds up to the "normal" mode observed on RADCAL. Furthermore, the satellite exhibits a bias in the roll angle which agrees with the Likins-Pringle theory discussed in Melvin [8]. The results for Day 165 also show a similar period where the yaw is constant, as illustrated in Figure 2.5.

To gain a better understanding of the observed motion we examine estimates of disturbing torques acting on the spacecraft during these periods. Figures 2.7 and 2.8 show a time history of the disturbance torques about the body axes for Days 160 and 189, respectively. By taking a Fast Fourier Transform (FFT) of the torques we can plot the frequency content of the of the data as shown in Figure 2.9. For these plots the output of the FFT is converted to amplitude and plotted against frequency.

The FFT's for the x-axis torques for both days show that most of the power is at lower frequencies of 0.02 cycles/minute and less. These frequencies correspond to periods of 50 minutes ($\approx$ twice orbital rate) and longer. On Day 189 we also observe a large spike at zero that is not apparent in the Day 160 data. This spike is probably due to the disturbance producing the constant yaw angle on Day 189. The cause of these various disturbing torques is unknown although we speculate that some of the disturbance is related to the magnetic hysteresis rods.

In addition, the FFT for the y-axis torque for Day 189 contains an anomalous spike at 0.05 cycles/minute (or 20 minutes/cycle). Since it seems unlikely that a disturbing torque with this short of a period is acting on the spacecraft we suspect this could be the effect of poor filter tuning.

2.4.4 Attitude Filter Performance

As a method of evaluating our results we compared the expected and observed roll and pitch frequencies. The observed frequencies can be determined by taking an FFT of the RADCAL attitude solutions. The results are compiled in Table 2.5. The observed periods of the roll and pitch motions agree with the expected periods within 5.6 and 6.5 percent, respectively.

The FFT for Day 189 also showed a strong secondary peak at 545 minutes due to the

Table 2.4: Kalman Filter Process Noise Parameters

State	Process Noise	Units
quaternion	1×10^{-14}	dimensionless
angular velocity	2×10^{-18}	$(\text{rad/sec})^2$
radial torque	6×10^{-16}	$(\text{N}\cdot\text{m})^2$
normal, transverse torque	1×10^{-14}	$(\text{N}\cdot\text{m})^2$
line bias	1×10^{-14}	$(\text{cy})^2$

Table 2.5: Roll and Pitch Periods for RADCAL

Day	Roll Period	Pitch Period
Expected	**52.47**	**60.85**
107	54.01	64.80
160	52.94	62.30
165	51.84	61.28
189	49.54	60.57

disturbing torque producing the constant yaw angle. The data for Day 079 spanned less than two orbital periods, and hence, was too short to produce meaningful results.

Line bias consistency is yet another indication of filter performance. Line bias estimates in cycles for all days are compiled in Table 2.6. There is strong agreement in line bias estimates across each day. The largest difference of 4.4 millimeters occurs on line bias 2.

2.4.5 Solution Accuracy Analysis

Because there is no accurate attitude reference for RADCAL, it is difficult to quantify the accuracy of the attitude solutions. One way of determining approximate accuracy is by comparing the point and filter solutions. Computing the difference between the point and Kalman filter solutions at each measurement epoch will give the combined error from both solution types. The point solutions track the measurement data exactly, so point solution errors are likely to be dominated by errors in the GPS measurements. The GPS

Table 2.6: Line Bias Estimates for RADCAL

Day	Line Bias (cycles)		
	β_1	β_2	β_3
079	0.918	0.515	0.184
107	0.902	0.493	0.172
160	0.906	0.496	0.180
165	0.910	0.493	0.179
189	0.900	0.494	0.180

Table 2.7: RMS of Point and Filter Solution Differences

Day	Δyaw			Δroll			Δpitch		
	RAW	HPF	LPF	RAW	HPF	LPF	RAW	HPF	LPF
107	0.59	0.55	0.20	0.82	0.60	0.38	0.98	0.64	0.37
160	0.62	0.50	0.30	0.83	0.58	0.43	0.88	0.58	0.50
165	0.60	0.55	0.20	0.90	0.59	0.45	0.95	0.64	0.49
189	0.50	0.46	0.19	0.95	0.59	0.49	0.87	0.53	0.66

measurement errors include receiver noise and multipath which generally have periods less than 10 minutes. Because each GPS satellite pass is fairly short (20 minutes), there is no viable mechanism for low frequency errors to appear in the point solutions. The filter solution has removed or smoothed the measurement errors by establishing a fairly high confidence in the dynamic model; i.e. by setting the process noise values low. Filter solution errors are caused by dynamic mismodeling and are evident in the lower frequency components of the solution differences, with periods of 50 minutes and above. Errors common to both methods, such as baseline or line bias errors, are not apparent in the difference data as these errors will cancel out in the computation.

Hence, in addition to the Kalman filter solutions we also computed point solutions from the RADCAL data. Again, the attitude from the initialization algorithm was used to start the process. The line biases were fixed to the estimates calculated in the attitude Kalman filter. Measurements with SNR's of less than 3 AMU were excluded from the solution.

To separate and quantify the errors attributed to each solution type, we performed both a high and low pass filter on the difference data. The high pass filter (HPF) should remove Kalman filter solution errors, leaving only errors due to the point solutions. The low pass filter (LPF), on the other hand, should remove the point solution errors, leaving only Kalman filter solution errors. A Butterworth filter with a 25 minute cutoff was used for both band pass filters. The root-mean-square (RMS) of the raw data was computed. The RMS of the high and low pass filtered data with the initial transient (30 minutes) removed was also computed. The results are given in Table 2.7. Day 079 is excluded because it is too short to produce meaningful results.

In all cases the yaw errors are smaller than pitch and roll errors since there are two baselines observing yaw, while only one baseline observing each of the other angles. The raw data produced roll and pitch RMS errors ranging from 0.82 to 0.98 degrees and yaw RMS errors ranging from 0.50 to 0.62 degrees. The high pass filtered data, which represents the point solution errors, produced smaller roll and pitch errors of 0.53 to 0.64 degrees. The improvement in yaw, however, is not as pronouced. Since the yaw motion is uncoupled, we beleive that the dynamic model for yaw is more accurate which would account for this phenomenon. The low pass filtered data, which represents the filter solution errors, produced the best results as expected. The one exception was the pitch errors for Day 189 where the low pass filtered data produced greater errors than the high pass filtered data. This is possibly due to poor modeling of the disturbing torques on that day.

2.4.6 RADCAL Multipath Analysis

In addition to looking at attitude solutions, we also looked at measurement residuals from the filter to gain insight on its performance. Figure 2.10 shows post-fit phase difference measurement residuals for PRN 23 on Day 107. The residuals for baseline 2 are clearly structured with a time constant of approximately 4 minutes. Using an approximation given in Georgiadou and Kleusberg [9], we calculated the minimum distance to a reflector that would cause this type of oscillation. The reflector turned out to be 6 meters away, which is close to the distance from antenna 2 to the top of the boom.

Multipath in the residuals for baselines 1 and 3, however, do not look the same. An explanation is illustrated in Figure 2.11 which is a sky plot of the line-of-sight vector expressed in the body fixed frame for PRN 23. The GPS antenna positions are also shown with the boom at the center of the plot. As the GPS satellite moves across the sky, each antenna will be affected by multipath differently. Since the boom is in the center of the antennas, it may be corrupting measurements to one antenna, but not to another. Furthermore, the antennas are canted outward and look in different directions, which exacerbates this phenomenon.

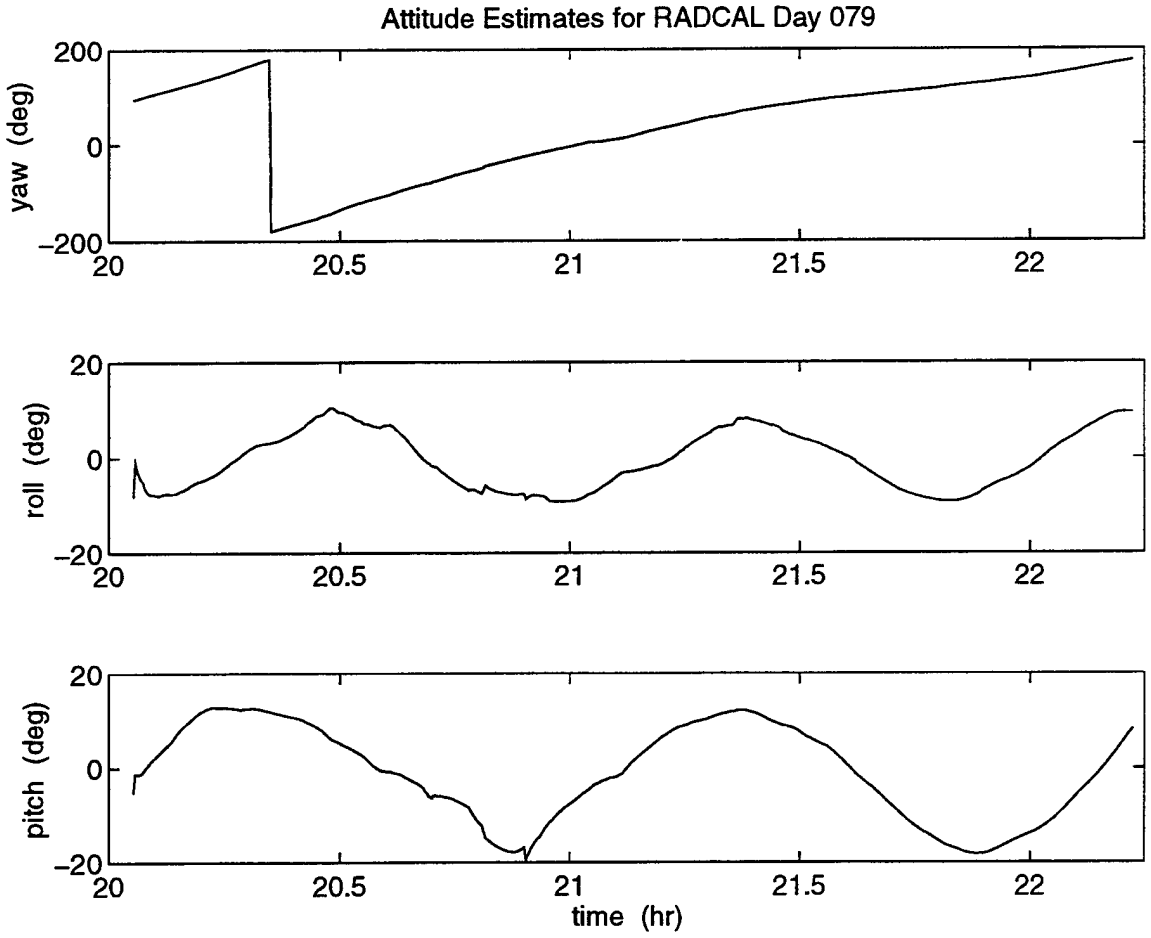

Figure 2.2: Attitude Kalman Filter Estimates for RADCAL Day 079

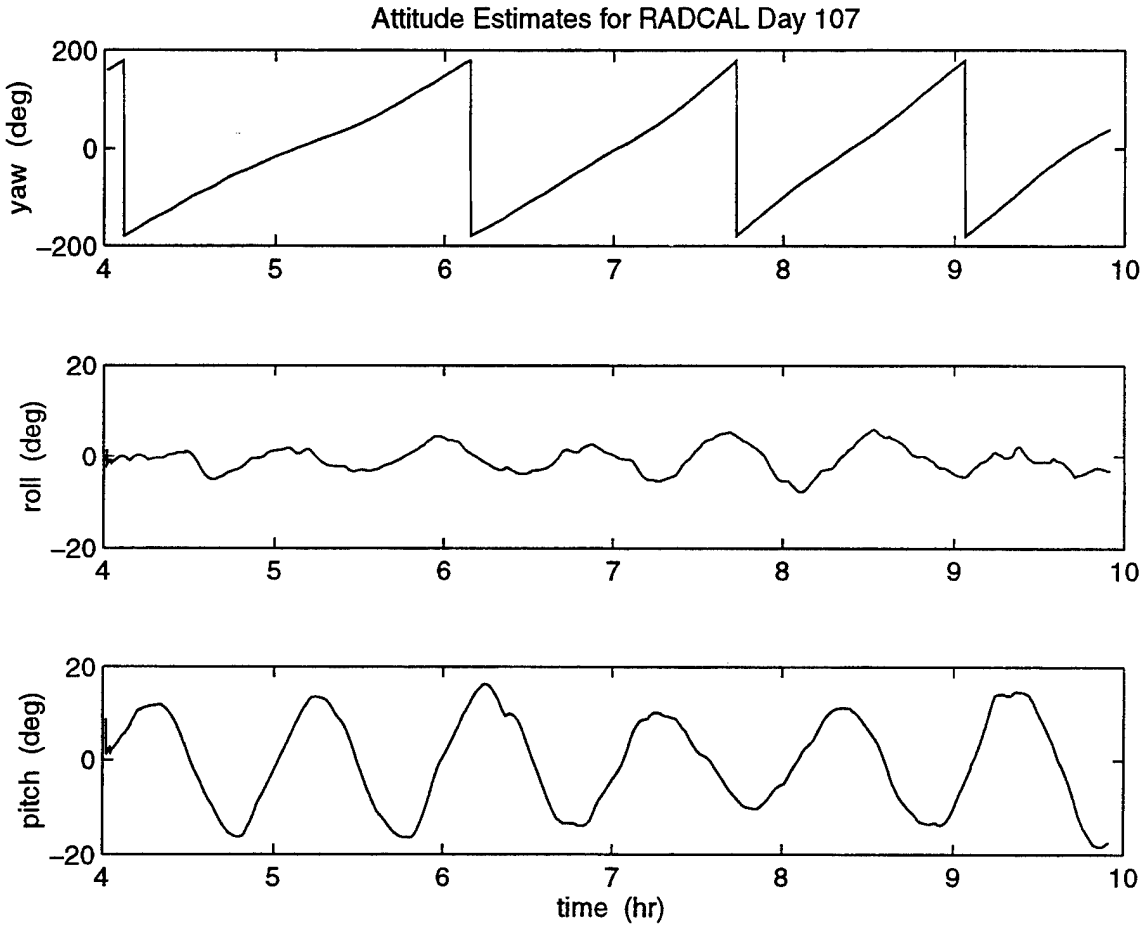

Figure 2.3: Attitude Kalman Filter Estimates for RADCAL Day 107

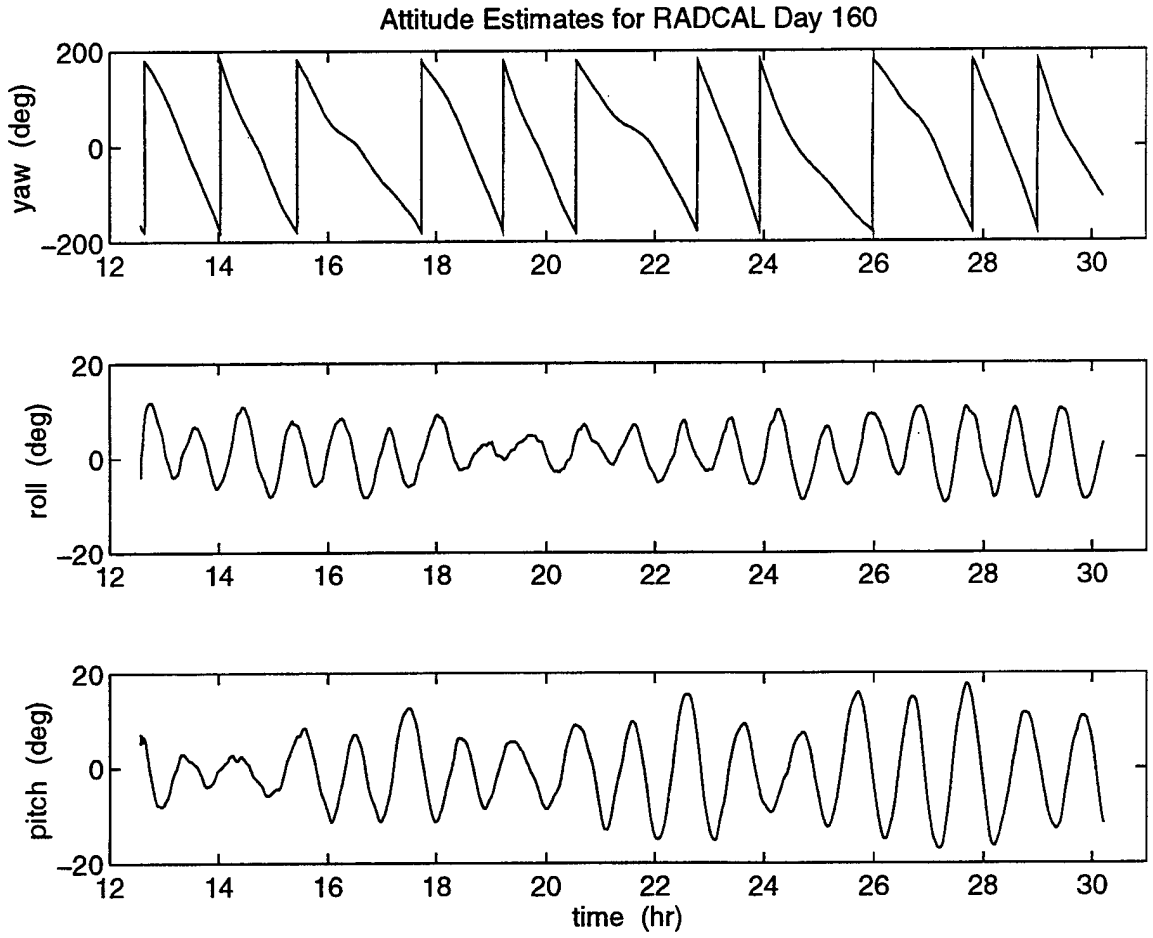

Figure 2.4: Attitude Kalman Filter Estimates for RADCAL Day 160

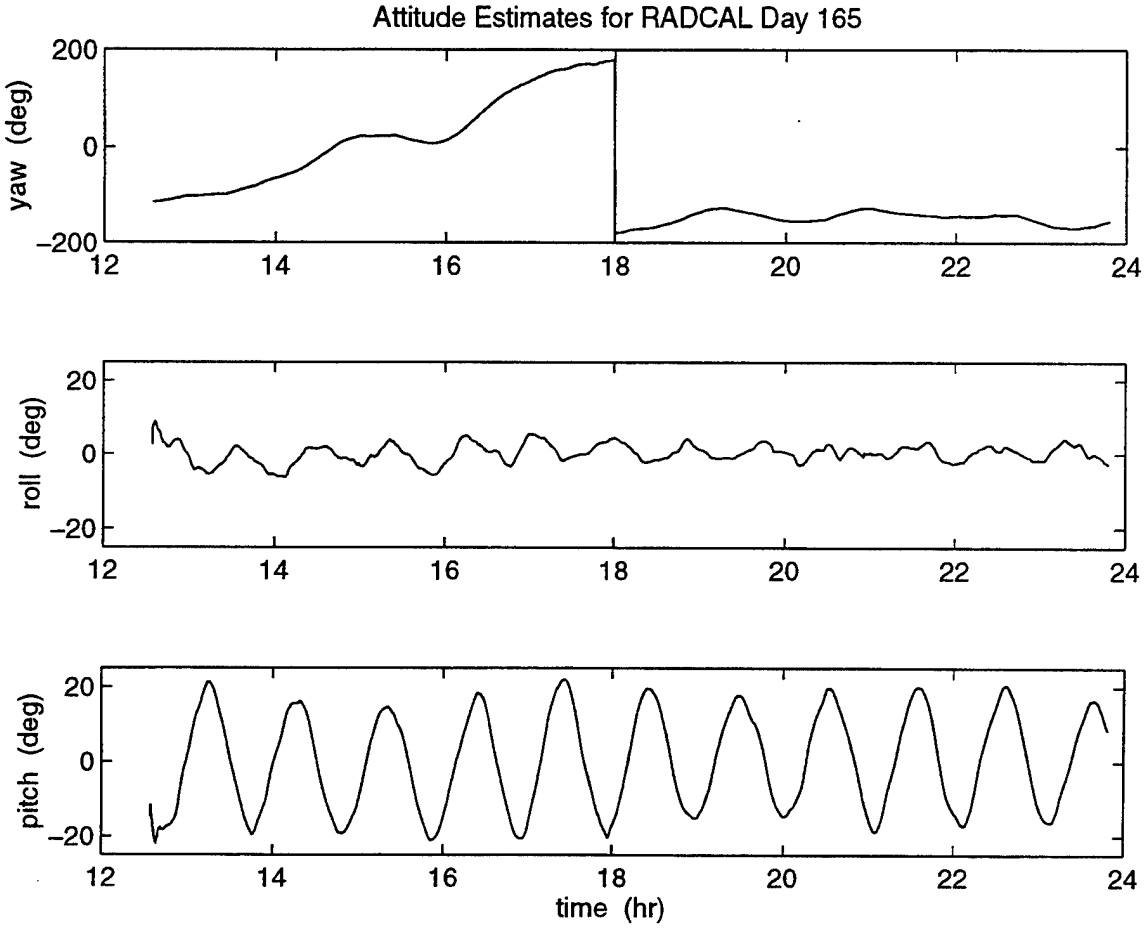

Figure 2.5: Attitude Kalman Filter Estimates for RADCAL Day 165

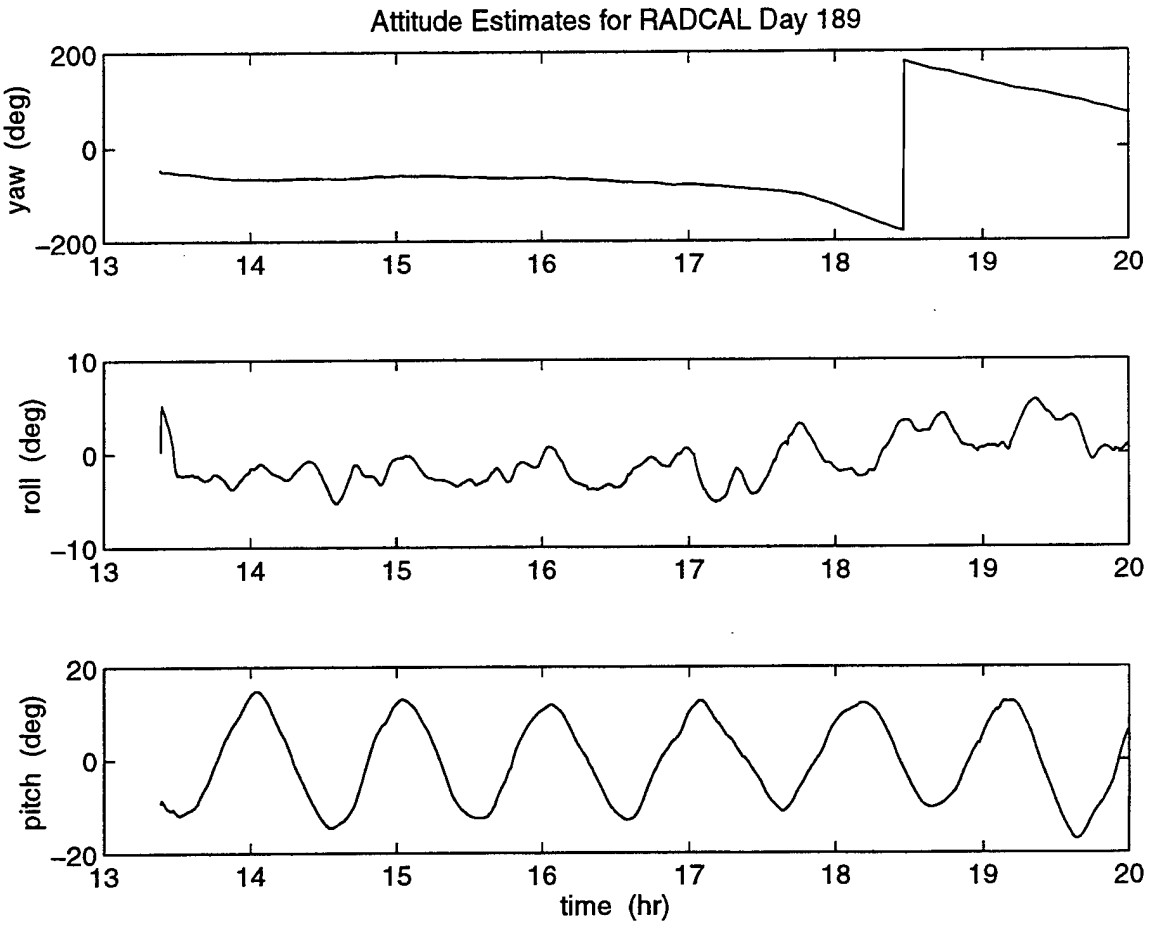

Figure 2.6: Attitude Kalman Filter Estimates for RADCAL Day 189

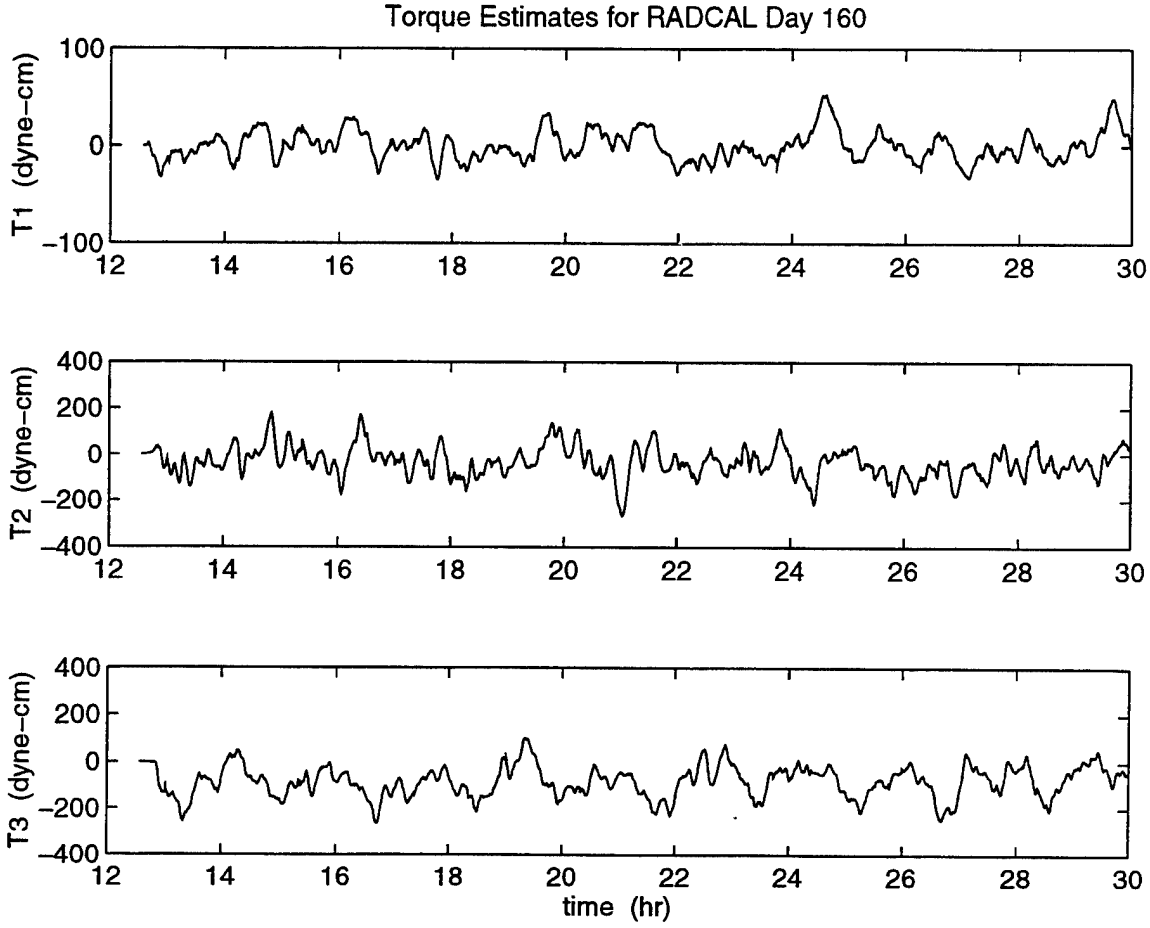

Figure 2.7: Torque Estimates for RADCAL Day 160

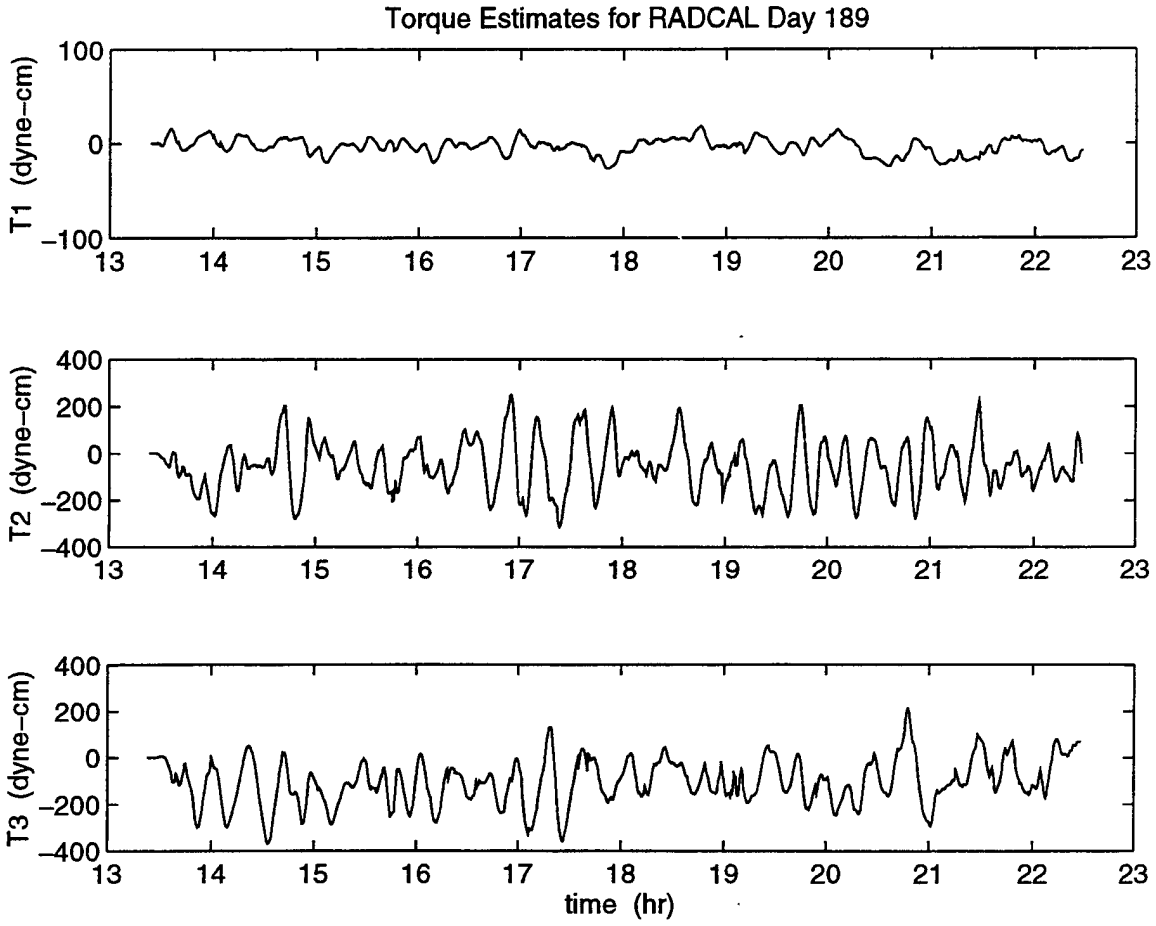

Figure 2.8: Torque Estimates for RADCAL Day 189

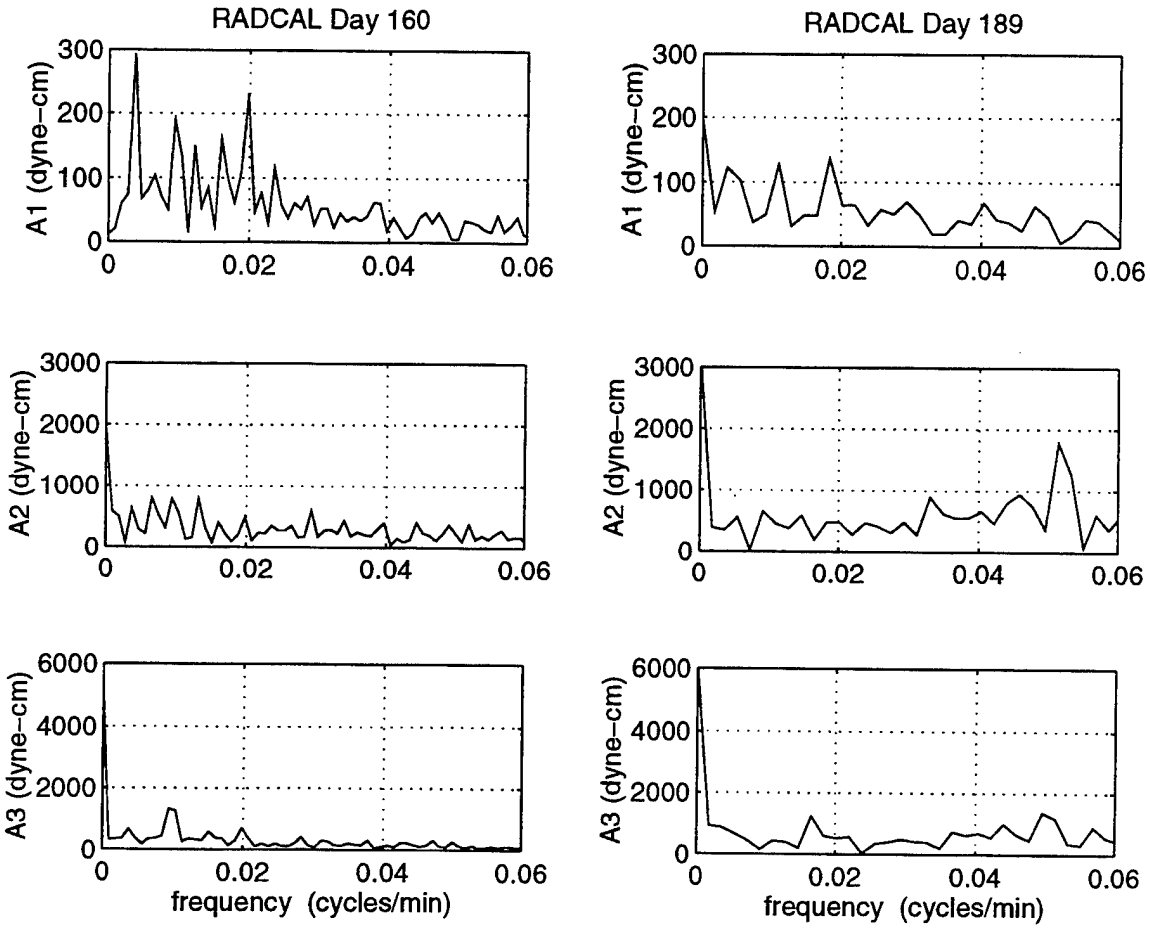

Figure 2.9: Spectral estimates of disturbing torques acting about the body axes. For each plot, the x-axis corresponds to frequency in cycles/minute, and the y-axis corresponds to amplitude in dyne-cm.

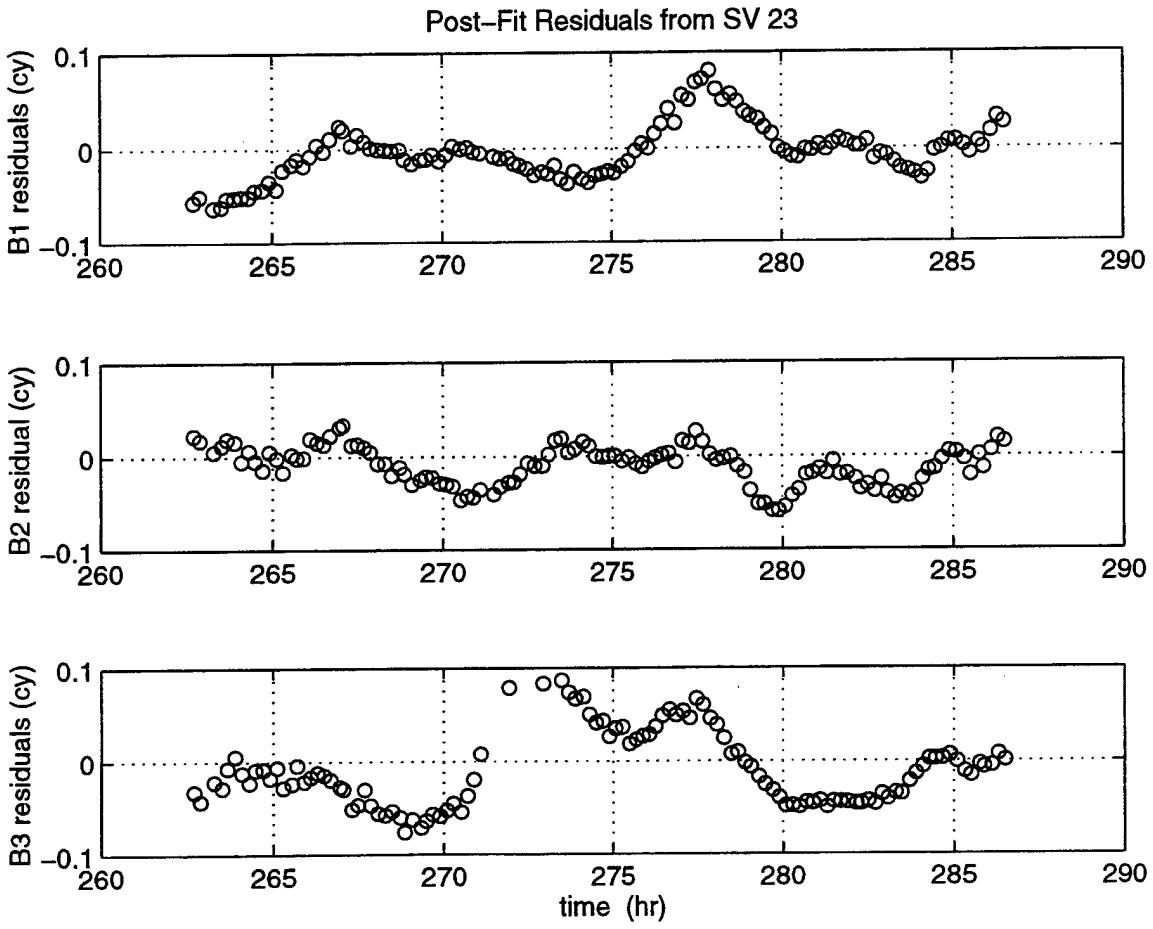

Figure 2.10: Post-Fit Measurement Residuals for PRN 23 on Day 107

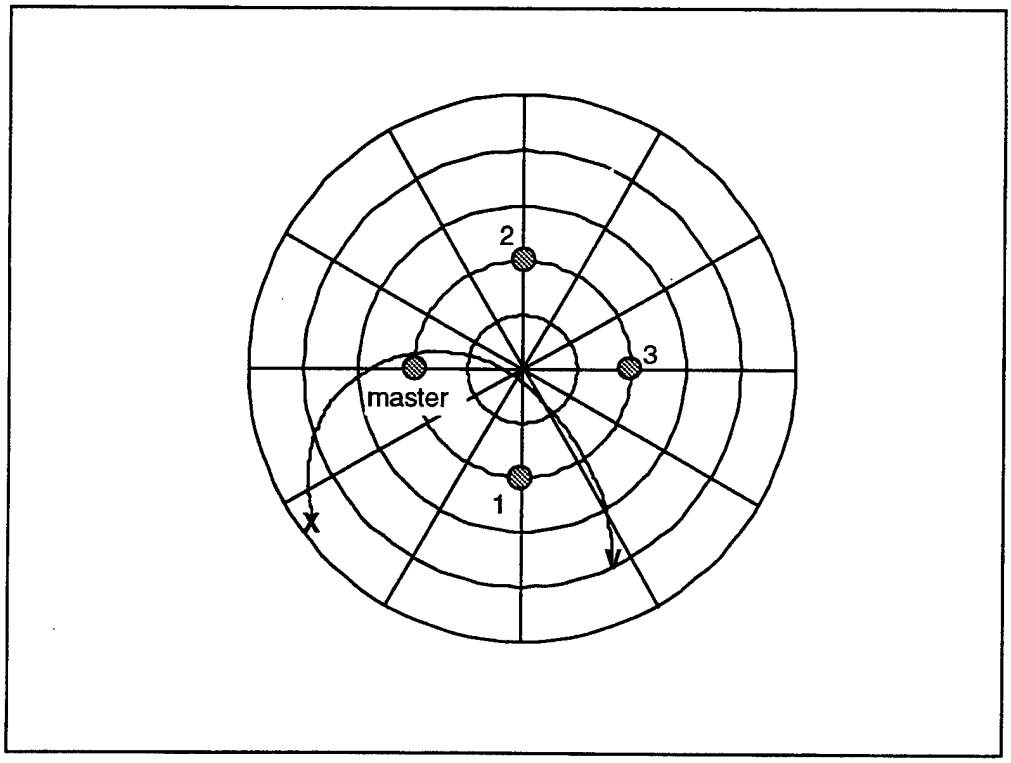

Figure 2.11: Sky Plot for PRN 23 on Day 107

2.5 New Phase Error Models

As described in previous reports, we have developed a computer simulation which models a spacecraft with a GPS-based attitude determination system. The spacecraft's orbital and attitude motion are modeled as are the GPS satellite positions. Phase measurements observed by an on board GPS receiver are also modeled. In the past a discrete first order Markov process was used to model a combination of phase measurement errors. While this method is straightforward and easy to implement, it only serves as a crude approximation to the total measurement error. In another study for CTA Space Systems we evaluated the performance of the GPS-based attitude determination system on board the spacecraft REX II, a follow-on to RADCAL. This study required a deeper understanding of how different error sources affect the attitude solutions. Since multipath is clearly the dominant source of error for RADCAL we developed several models to analyze how multipath contributes to the phase errors. A more accurate model of receiver noise, another important contribution to the phase errors, has also been developed. Since REX II and RADCAL are so similar, the algorithms are applicable to both spacecraft.

2.5.1 Receiver Noise Model

Receiver thermal noise introduces a high frequency contribution to the phase observations. This effect is typically modeled as a white Gaussian random variable with variance related to the carrier-power-to-noise density C/N_0 and the tracking parameters of the receiver phase lock loop. The C/N_0 is a function of the incoming signal strength, the zenith angle of the signal with respect to the antenna, and the gain pattern of the antenna. In our simulation, we model the receiver noise as a discrete Gaussian random variable with variance computed as follows:

$$\sigma_R^2 = \frac{f_N}{(C/N_0)\ G} \tag{2.34}$$

where σ_R^2 is the variance of the receiver noise, the tracking loop bandwidth f_N is 10 Hz for the Trimble Vector, C/N_0 is 10^4 Hz (40 dB-Hz), and G is the gain of the antenna.

A gain pattern for the antenna, measured by Bruce Schupler and Roger Allshouse at NASA Goddard, as a function of satellite azimuth and zenith angle, is illustrated in Figure 2.12. This pattern has been normalized to a maximum value of 1. The receiver noise generated according to equation 2.34 has a minimum variance of $(1\text{mm})^2$ at a zenith angle of 28 degrees and a maximum variance of $(6\ \text{mm})^2$ at a zenith angle of 90 degrees. The nominal C/N_0 was based primarily on experience with ground test data. The theoretical variance values computed based on the SNR reported by the receiver predicts receiver noise errors as little as 0.1 mm, 1-σ. We have never observed such high quality measurements. More typical results based on experiments conducted at CU show noise levels to be in the 1-2 mm range, 1-σ. To be somewhat conservative in modeling the performance for REX II and RADCAL we have used the low C/N_0 value as a means of scaling the receiver noise variance to better match our experimental results.

2.5.2 Geometric Multipath Model

Multipath refers to the error that is introduced into an observation when, in addition to the direct satellite signal, reflected signals from nearby objects arrive at the GPS antenna. Reflected signals are always delayed relative to the direct and generally are weaker than the direct. To properly simulate the multipath environment on board a spacecraft one would

construct a geometric optics model of the vehicle surfaces as well as the signal and antenna properties. The development of such a model is beyond the scope of this analysis; however, a more sophisticated geometrical optics simulation [10] is available and could be used in the future to model the spacecraft's environment. In the meantime we use a simplified geometrical model as follows. The reflector is assumed to perfectly redirect all signals to the receiving antenna. The phase of the indirect signal ϕ_M is

$$\phi_M = |\mathbf{d}| - \mathbf{e} \cdot \mathbf{d} \tag{2.35}$$

where $\mathbf{d}$ is the vector from the antenna to the reflector, and $\mathbf{e}$ is the line GPS line-of-sight vector. When combined with the direct signal, this leads to a phase error given by

$$\tan \theta_M = \frac{\alpha \ \sin \phi_M}{1 + \cos \phi_M} \tag{2.36}$$

where α is the amplitude of the reflected signal relative to the direct signal. These multipath errors are added to phase measurements for any satellite-antenna pair for which the unit vector from the antenna to the satellite lies within a specified bi-directional cone of the unit vector from the antenna to the reflector, as illustrated in Figure 2.13. The assumption is that a signal coming in at a more obtuse angle will not reflect into the antenna. Clearly, this is a simplified model. While it does not take into account the complexities of microwave refraction, it does produce errors representative of those observed on RADCAL. Figure 2.14 illustrates the multipath error produced by a point reflector located at the top of the boom as a GPS satellite flies overhead. The periodic structure of the errors is the well known signature of multipath.

To simulate the environment on REX II we placed a series of 32 reflectors along the 6 meter boom with a valid cone angle of 25 degrees. A cluster of reflectors near the top and bottom are meant to simulate the larger reflective areas of the tip mass and baseplate respectively. This configuration produces multipath errors on approximately 25 percent of the measurements.

2.5.3 Sinusoidal Multipath Model

As a secondary model which does not specifically require knowledge of the reflector location we also developed a sinusoidal model that produces a multipath type of error signal. In the RADCAL attitude error data we observed a significant level of signal power in the frequency range of 5-20 Hz which is probably attributable to multipath. As such we generated sinusoidal phase errors in this frequency range for the REX II simulation. For each satellite that comes into view, we construct the multipath error at time t with the equation:

$$\theta_M = A \ \sin(\omega_M \ t + \varphi) \tag{2.37}$$

where ω_M, A, and φ, are all uniformly distributed random variables over a specified range. Figure 2.15 illustrates the multipath errors produced with this model. For this plot the frequency range of is 0.02 to 0.0054 radians/second which corresponds to periods of approximately 5 to 20 minutes. The amplitude range (A) is from 0 to 10 mm, and the phase shifts range from 0 to 2π radians.

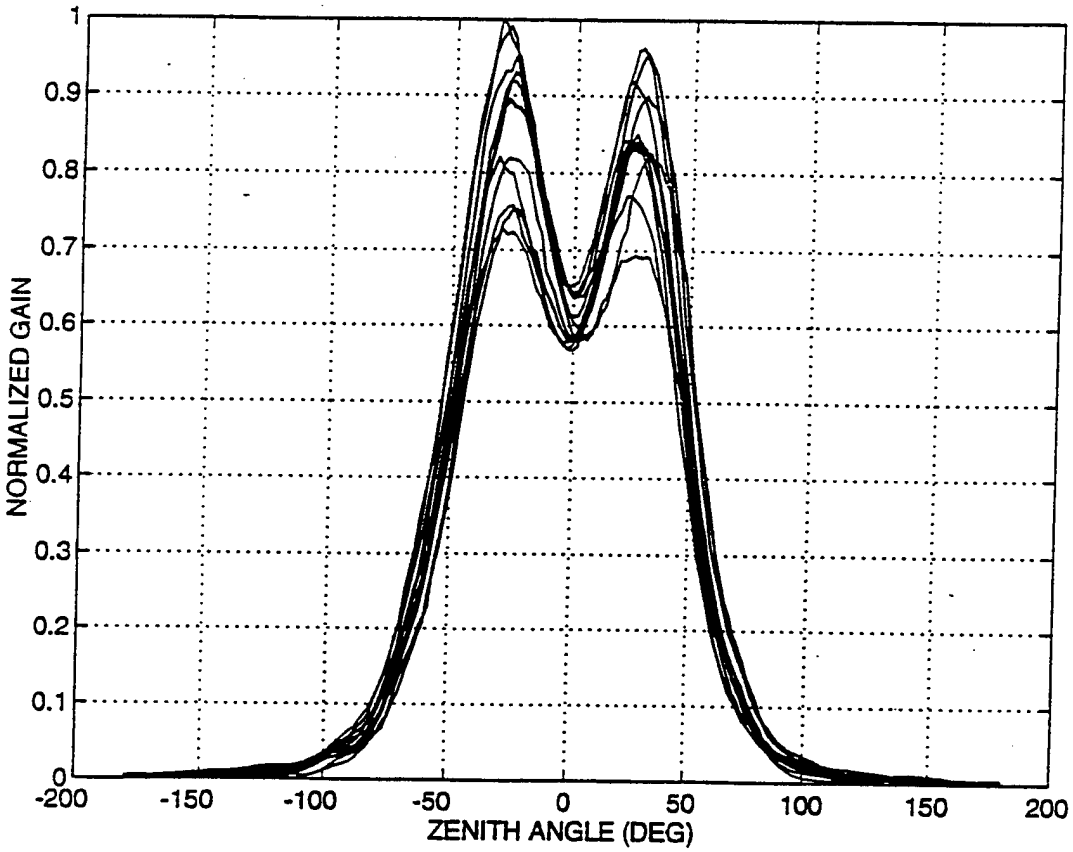

Figure 2.12: Antenna Gain Pattern

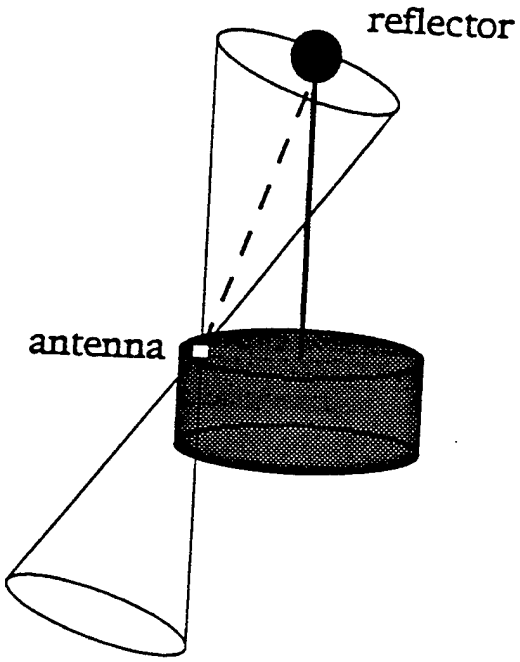

Figure 2.13: Geometrical Multipath Diagram

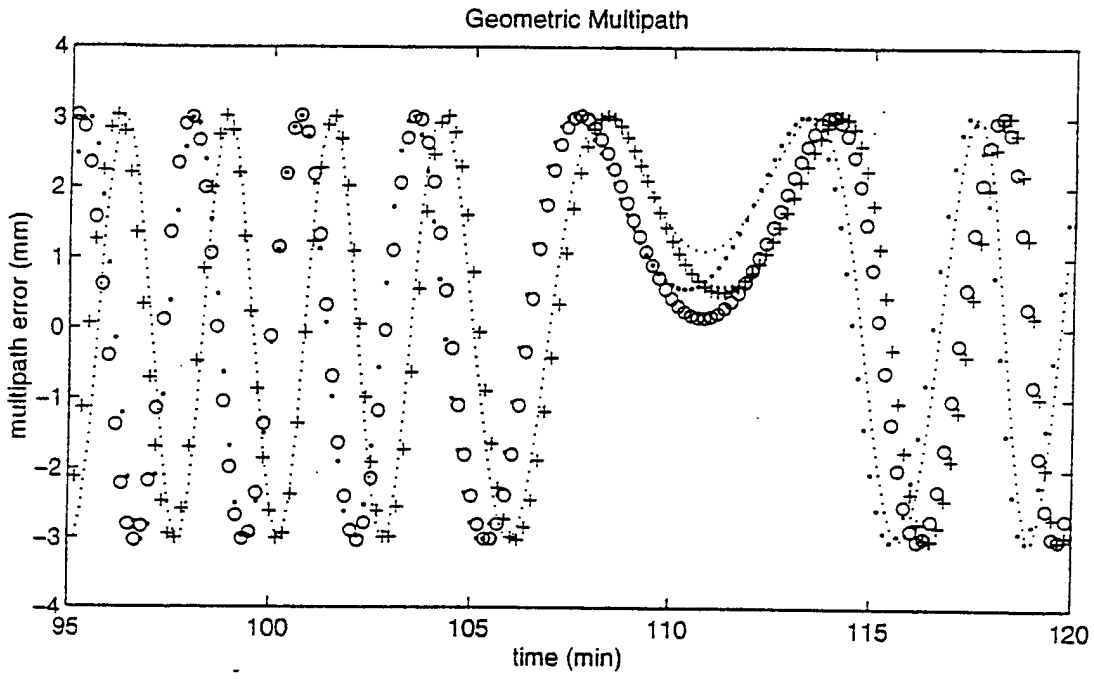

Figure 2.14: Example of Geometrical Multipath

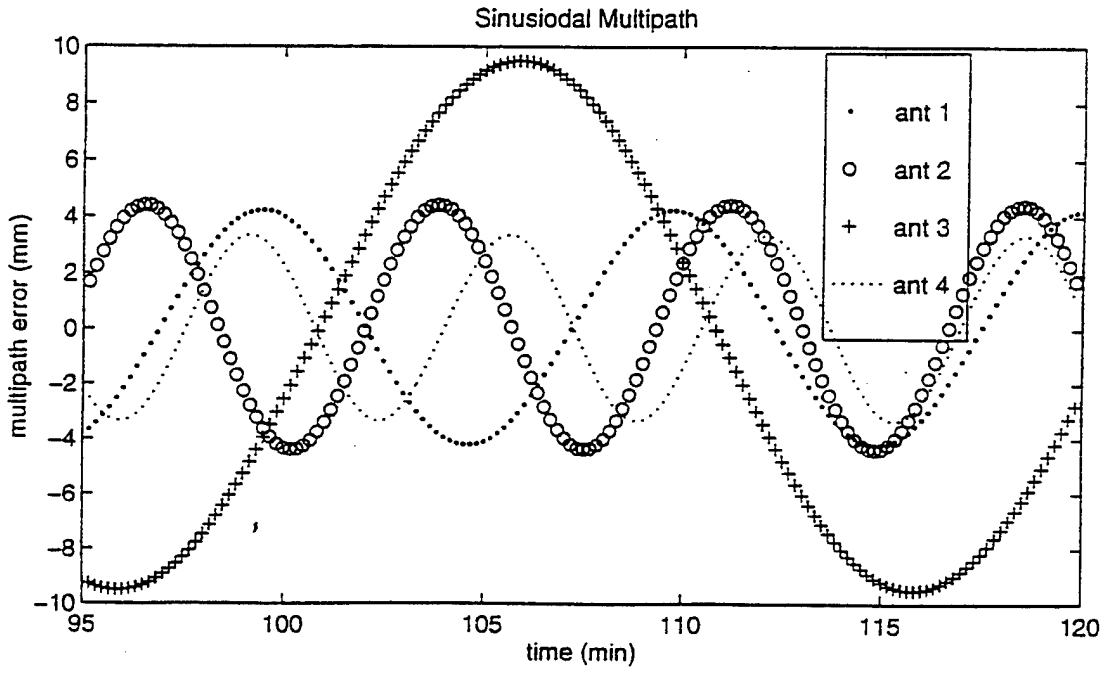

Figure 2.15: Example of Sinusoidal Multipath

2.6 REX II Simulation Results

REX II is very similar in design to RADCAL. It is a gravity-gradient, axis-symmetric satellite with a 6 meter boom. The planned orbit is circular with an inclination of 82 degrees at an altitude of 834 km. REX II has a momentum wheel for 3-axis stabilization, but this attribute is not modeled here. The main difference between the two spacecraft that affects this analysis is antenna placement. There are four co-planar antennas on board REX II. However, they are not canted outward as on RADCAL, but lie flat on the zenith face of the vehicle.

The primary scenario that we investigated is similar in character to the motion observed on RADCAL for Day 160. The yaw rate of the vehicle was -1x10^{-3} radians/second, the pitch oscillations peaked at 12.3 degrees and the roll oscillations peaked at 6.7 degrees, as illustrated in Figure 2.16. The simulations we performed were 5 hours in length with GPS measurements generated every 1 second. At each measurement epoch the point solution algorithm was run using measurements from up to six visible satellites. The parameters selected for the multipath models are intended to be representative of the errors observed for RADCAL.

2.6.1 Geometric Multipath Results

Two different cases of geometric multipath were investigated. One simulates a low multipath environment, and the other simulates a high multipath environment. For the low multipath case, the magnitude of the multipath relative to the direct signal was chosen to be 0.06. This produced phase errors, including receiver noise, of approximately 8.8 mm, 1-σ. Figure 2.17 shows the attitude point solutions using low multipath model. The high frequency error in the signal is due to receiver noise, while the lower frequency "bumps" superimposed on the attitude motion are caused by multipath. These bumps occur when a GPS satellite passes overhead and its signal interferes with a large portion of the boom (which is also overhead of the antennas). If the root-sum-square (RSS) of the errors are plotted against argument of latitude, as in Figure 2.18, it is evident that the errors decrease as REX II moves over the Earth's poles. Since the GPS orbits are inclined 55 degrees, no GPS satellites pass directly overhead when REX II is near the poles which accounts for lower multipath errors. With this multipath case the RMS of the error in yaw, roll, and pitch are 0.34, 0.55, and 0.50 degrees, respectively. On the other hand, for the high multipath case the magnitude of the multipath relative to the direct signal was chosen to be 0.10. This case produced phase errors of approximately 11.8 mm, 1-σ. While the multipath bumps occur in the same place as they do in the low multipath case, they have larger amplitude. This translates into larger solution errors - almost 0.3 degree worse in roll and pitch compared to the low multipath case. Knowledge of the yaw angle, however, was not reduced to the same extent because signals from the lower elevation satellites that determine the yaw angle are not affected by the boom as much as signals from overhead satellites.

2.6.2 Sinusoidal Multipath Results

Low and high multipath environments were also simulated using the sinusoidal model. The maximum amplitude of the multipath errors was chosen to be 1 centimeter for the low multipath environment and 1.5 centimeters for the high multipath environment. This produced total phase errors, including receiver noise, at the level of 8.2 and 10.2 mm (1-σ), respectively. Figure 2.19 shows the attitude point solutions from using the high multipath

Table 2.8: RMS of Simulated REX II Errors

Multipath Model	RMS of Solution Errors (deg)		
	yaw	roll	pitch
geometric/low	0.34	0.55	0.50
geometric/high	0.38	0.84	0.84
sinusoidal/low	0.45	0.41	0.40
sinusoidal/high	0.59	0.58	0.55

model. Here the bumps are more regularly spaced and occur more frequently than with the geometric multipath model. Furthermore, the errors are about the same magnitude in all three angles, unlike the geometric multipath model where the roll and pitch errors were larger than the yaw. The RMS of solution errors for the high multipath case range from 0.55 to 0.59 degrees. A summary of results from both the sinusoidal and geometric models is given in Table 2.8.

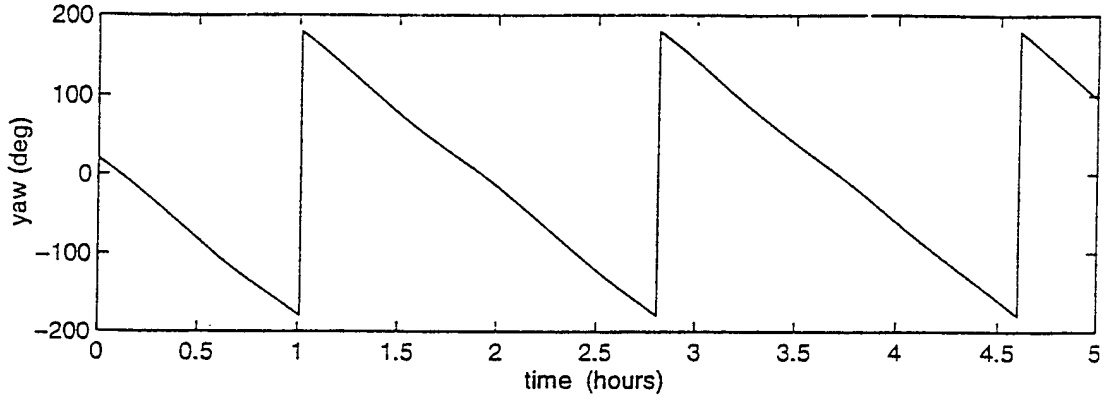

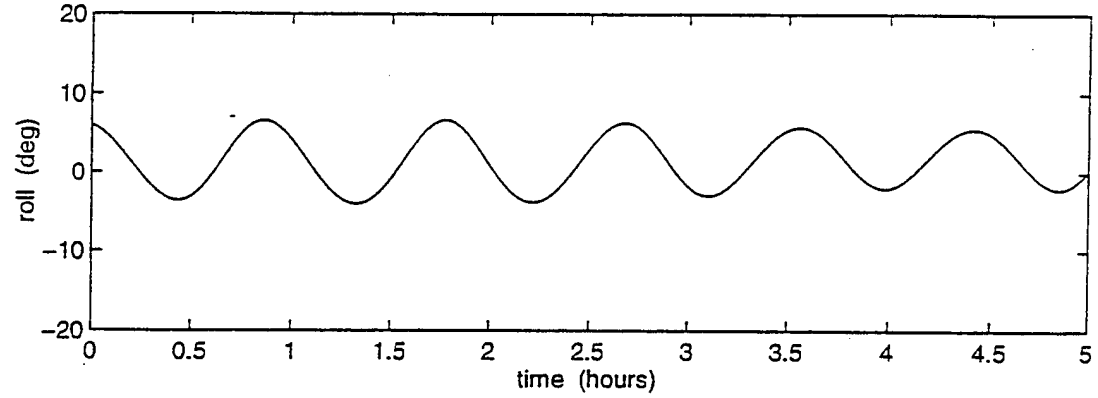

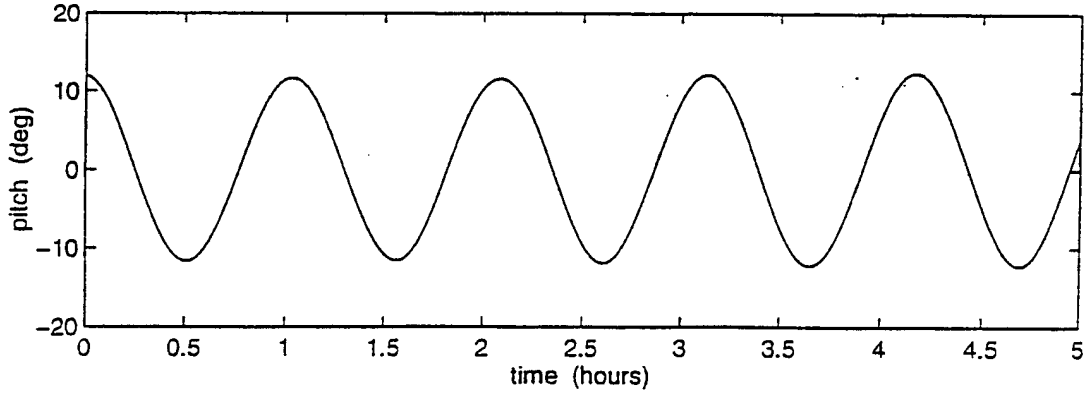

Figure 2.16: Simulated REX II Attitude

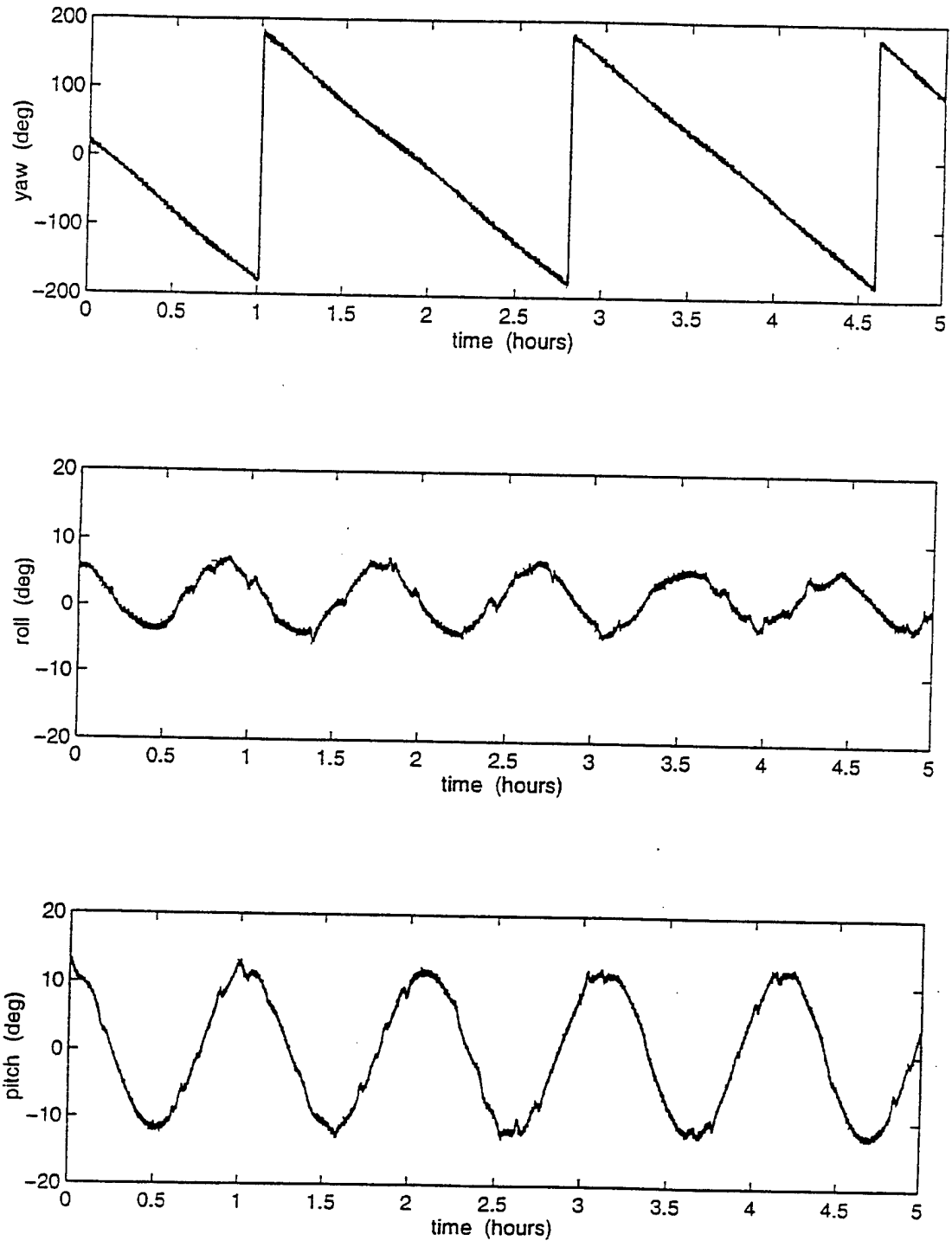

Figure 2.17: Point Solutions for Geometric Multipath: Low Case

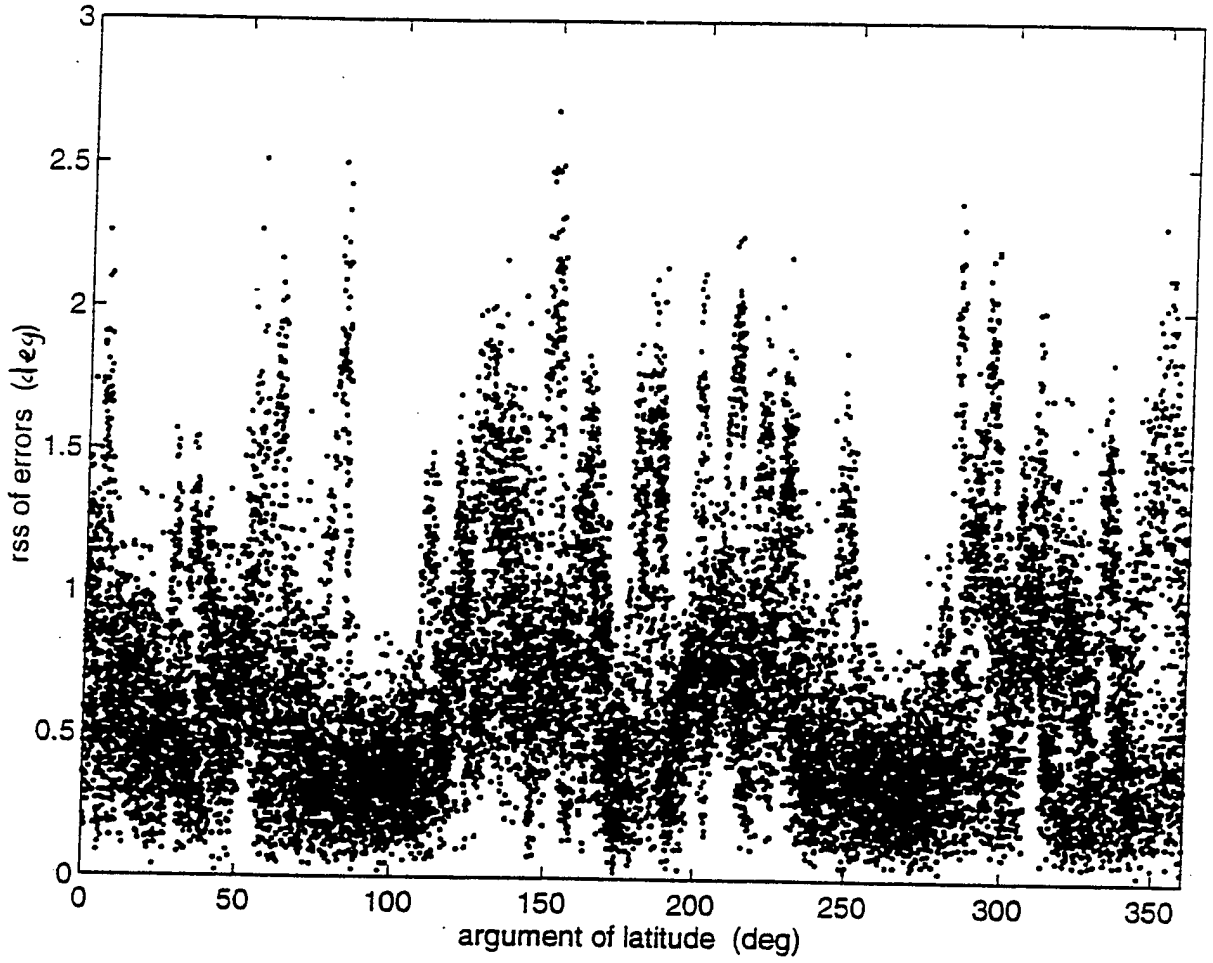

Figure 2.18: RSS of Solution Errors vs. Argument of Latitude

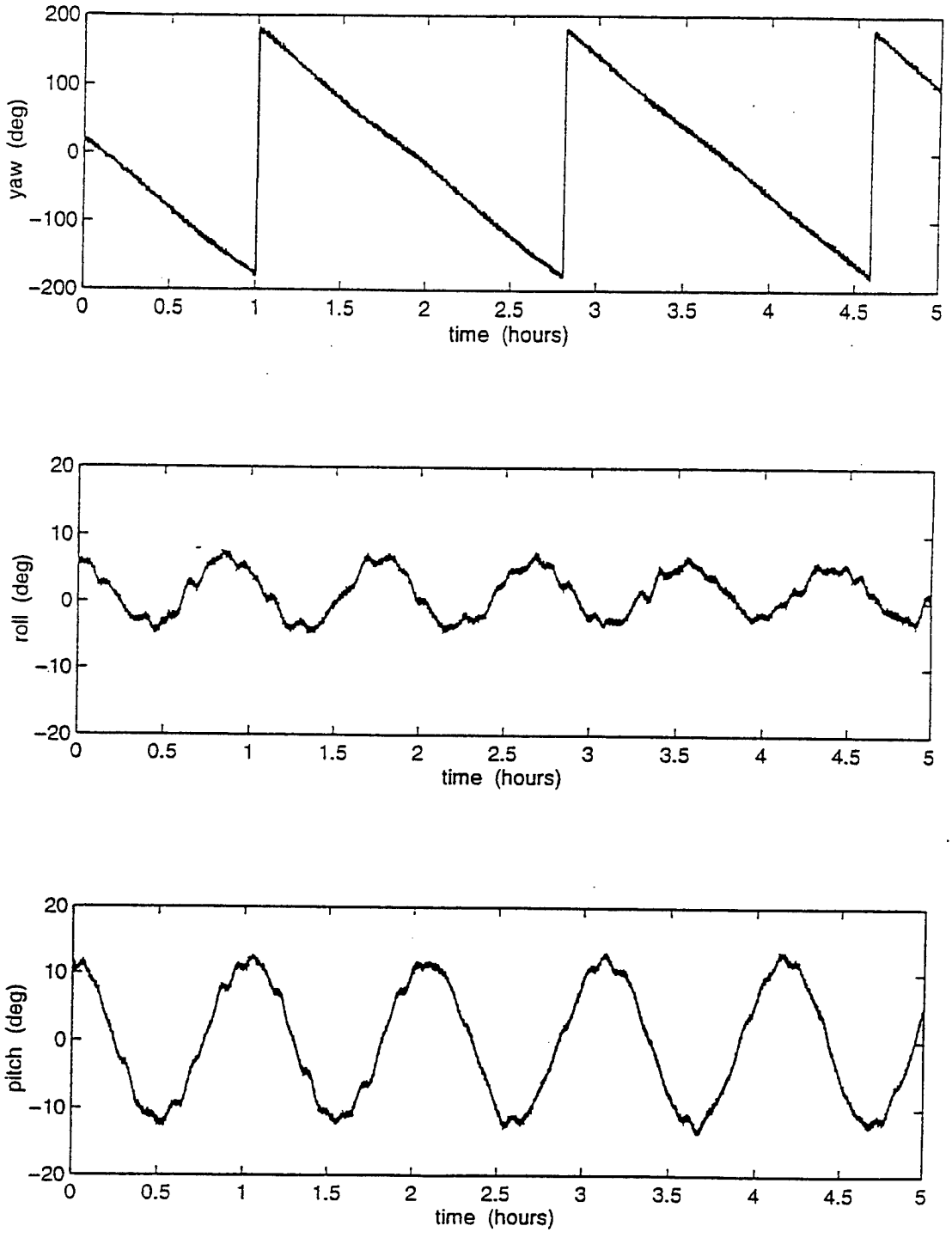

Figure 2.19: Point Solutions for Sinusoidal Multipath: High Case

2.7 Future Work

This study demonstrates a series of attitude and baseline estimation algorithms for use with GPS. Since these two processes are closely coupled, the next step is to develop a combined filter that will estimate the attitude and baselines simultaneously. The main concern with this approach is observability. baselines simultaneously. The main concern with this approach is observability. We know that estimating the attitude along with the three coordinates for each baseline does not provide enough observability to distinguish attitude errors from baseline errors. However, our investigations show that reducing the number of baseline parameters to estimate will provide the necessary observability. The planned method is to compute a vector correction to two of the baselines and a scalar correction to the third.

The baseline estimation process uses the electronic baselines as a basis for the body frame. Generally speaking, all instruments and principal axes can be expressed in a mechanically-defined reference frame. In order to accurately estimate the attitude of the "body frame", these two reference frames must be reconciled. We believe that errors in baseline length as well as errors in the direction of one baseline relative to another can be observed with this method. However, a pure rotation between these reference frames will remain transparent (i.e. will appear as an attitude error). A pure rotation would need to be resolved by some external means.

In the current implementation of the point solution algorithm, only the attitude is estimated. The line biases are assumed constant, and their values are fixed to the *a priori* estimates. However, our observability studies also show that with enough measurements the point solution has enough information to resolve both attitude and line bias parameters. Furthermore, using a minimum variance approach we can incorporate knowledge of the baseline errors, as well as attitude and line bias errors, into the solution.

Another improvement would be to modify the torque estimation procedure in the Kalman filter by including a correlated process noise model. This could increase the accuracy of the dynamic model without having to model the specific disturbing torques acting on the spacecraft. Along with improving the filter, adding disturbing torques in the simulation would aid in the testing and analysis of the improved filter as well as promote our understanding of spacecraft dynamics.

In addition to the RADCAL data, we have also received GPS data from a TANS Vector receiver flown on the Daimler-Benz Aerospace CRISTA-SPAS satellite [11]. GPS Navigation and attitude solutions computed on board as well as raw differential phase data is available for our analysis. We plan to compute attitude solutions with the raw phase data using the algorithms described herein. Also on board the satellite was a a stellar-inertial attitude determination system which will provide an excellent attitude reference for comparison with our results.

References

[1] Penina Axelrad, Bruce C. Chesley, Christopher J. Comp, and Lisa M. Ward. GPS Based Attitude Determination. FY'93-94 Technical Report II, Naval Research Laboratory, October 1994.

[2] Penina Axelrad, Charles P. Behre, Christopher J. Comp, and Lisa M. Ward. GPS Based Attitude Determination. FY'93-94 Technical Report I, Naval Research Laboratory, May 1994.

[3] Penina Axelrad, Bruce C. Chesley, and Lisa M. Ward. GPS Based Spacecraft Attitude Determination. Final Report for FY'92-93, Naval Research Laboratory, September 1993.

[4] Clark E. Cohen and Brad W. Parkinson. Integer Ambiguity Resolution of the GPS Carrier for Spacecraft Attitude Determination. In *AAS Guidance and Control Conference*, pages 107–118, Keystone, CO, February 1992. AAS 92-015.

[5] E. G. Lefferts, F. L. Markley, and M. D. Shuster. Kalman Filtering for Spacecraft Attitude Estimation. *Journal of Guidance, Control, and Dynamics*, 5(5):414–429, Sep - Oct 1982.

[6] Thomas R. Kane, Peter W. Likins, and David A. Levinson. *Spacecraft Dynamics.* McGraw Hill, Inc., 1983.

[7] Clark E. Cohen, E. G. Lightsey, William A. Fees, and Brad W. Parkinson. Space Flight Tests of Attitude Determination Using GPS: Preliminary Results. In *Proccedings of ION GPS-93*, pages 625–632, Salt Lake City, UT, September 1993.

[8] Peter J. Melvin, Lisa M. Ward, and Penina Axelrad. The Analysis of GPS Attitude Data from a Slowly Rotating, Symetrical Gravity Gradient Satellite. In *AAS/AIAA Spaceflight Mechanics Meeting*, Albuquerque, NM, February 1995.

[9] Y. Georgiadou and A. Kleusberg. On Carrier Signal Multipath Effects in Relative GPS Positioning. *Manuscripta Geodaetica*, 13, 1988.

[10] R. J. Marhefka and J. W. Silvestro. Near Zone - Basic Scattering Code: User's Manual with Space Station Applications. NASA Technical Report 716199-13, Ohio State University, March 1989.

[11] J. K. Brock, R. Fuller, B. Kemper, D. Mleczko, J. Rodden, and A. Tadros. GPS Attitude Determination and Navigation Flight Experiment. In *Proccedings of ION GPS-95*, Palm Springs, CA, September 1995. Draft.

3 MULTIPATH MODELLING AND CORRECTION

Christopher J. Comp

3.1 INTRODUCTION AND OVERVIEW

High precision measurements of the GPS L-Band carrier phase have been used for a wide variety of surveying applications ranging from worldwide geodetic networks to kinematic survey on both land and sea. More recently, attitude determination systems based on the carrier phase observable have been developed and demonstrated on land [17], sea [14], air [7, 3], and in space [8, 18]. The key measurement in each of these systems is the difference in the received phase measured by two antennas to a single satellite, known as the differential phase. When two separate receivers are used to track the two antennas, as is the case in a survey application or in some attitude determination systems [17, 14, 3]. The difference between differential phase measurements for two satellites (double difference) is used as the measurement, eliminating the effect of the different receiver clocks.

The limiting factor on performance in almost all attitude determination applications has been identified as multipath. Similarly, in some high precision surveying environments, multipath appears to be the dominant error source. Multipath is the corruption of the direct GPS signal by one or more signals reflected from the local surroundings. Figure 3.1 shows an example of differential phase residuals between two fixed antennas. The structured oscillations are characteristic of multipath interference. The residual data has the first order GPS satellite motion removed, leaving the multipath and receiver measurement noise. In this particular set of data, the multipath produced peak errors of 8 millimeters with low frequency components. Uncorrected, these measurement errors would produce attitude errors at the level of 8 milliradians (0.46 degrees) for a 1 meter antenna baseline length.

The primary goal of this research is to develop and implement a technique to correct for multipath in GPS carrier phase measurements. The technique should be successful in reducing multipath to the level of receiver measurement noise. The technique should also work in a variety of precise GPS applications involving both static and dynamic platforms, and also in a changing multipath environment. The research will emphasize multipath correction for attitude determination onboard near-earth spacecraft. Generality is desired to include commercially viable areas such as terrestrial attitude determination and differential surveying. A distant goal is to implement the technique in a near real-time operational mode.

The theoretical foundation of multipath with the GPS carrier signal has been studied, and was laid out in detail in the September, 1994 Technical Report [2]. Based on that knowledge, a procedure for estimating the multipath present in the phase measurement of the carrier signal was devised. The multipath correction approach described in [2] overcomes many of the shortcomings of previously recommended techniques. It utilizes the ratio of the amplitude of the recovered carrier signal to the noise (SNR) and the known antenna gain pattern to create a multipath correction profile for the carrier phase measurements. Thus, a new correction profile is generated for each data set, eliminating the constraint that the environment remain unchanged.

The relationship between the direct GPS signal, one or more multipath signals, and the resulting composite signal which is reported by the receiver, was developed as in [9]. The relationship was then used to derive the phase error due to multipath, based on information obtained from the amplitude of the composite signal (*i.e.* the SNR). When the multipath signal strength relative

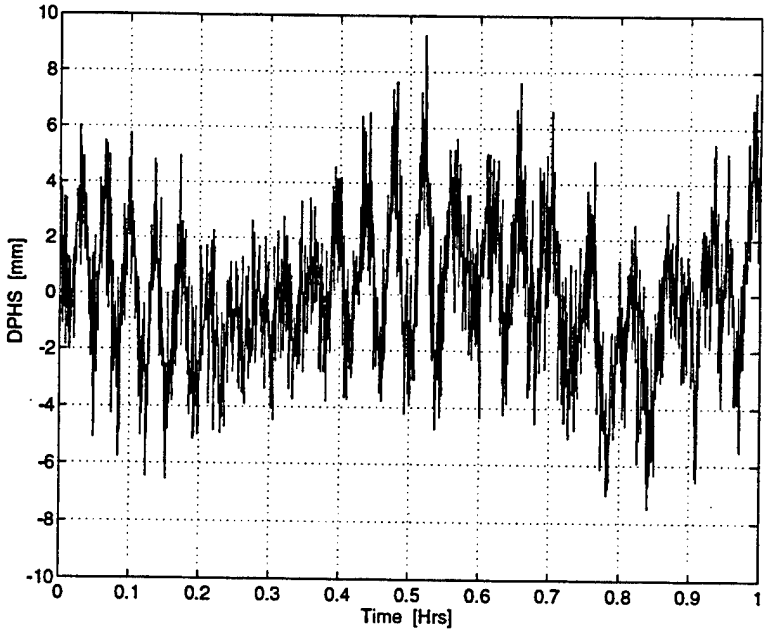

Figure 3.1: Differential phase data for a 1 meter patch antenna baseline. *The data was collected May 24, 1994, with a Trimble Vector attitude receiver. The horizontal axis is time in minutes, the vertical axis is differential phase residual in millimeters.*

to the direct signal is small, the expression for the phase error due to multipath is given by the following approximate formula:

$$\delta\phi \approx \frac{\sum_i \alpha_i A_o \sin(\omega_i t + \theta_i)}{A_o A_a + \sum_i \alpha_i A_o \cos(\omega_i t + \theta_i)} \tag{3.1}$$

where i is summed over all multipath signals present. The $\alpha_i A_o$ is the amplitude of the multipath fluctuations, ω_i is the frequency of the multipath, t is a time reference, θ_i is the phase offset of the multipath in the SNR, and A_c is the actual composite SNR.

The frequency, amplitude, and phase offset of the multipath are determined from the SNR data using spectral estimation techniques. Inserting the parameters into Equation 3.1 creates a profile of the multipath error in the phase data. This profile is subtracted from the phase data to eliminate the multipath error, leaving uncorrupted navigation information. Modeling and subsequent subtraction of multipath error that is identified directly from the phase data would be incorrect, due to the risk of removing fluctuations from actual vehicle dynamics.

The technique has proven successful for correcting multipath in differential phase measurements to near the receiver noise level, in limited trials. The technique was used in a post-processing mode on data from static terrestrial platforms. The data was generated by a model of a generic code-correlating receiver for the simulations, and was collected by a Trimble Vector code-correlating attitude receiver for the experiments. Simulations have been performed which analyze the effect of multipath on a dynamic orbiting spacecraft, in so doing the multipath characteristics are well

understood. At this time, however, the correction technique has been used only with simulated and experimental static scenarios.

The research conducted since the last progress report has concentrated on the development of a procedure to better estimate the spectral content of the multipath in the SNR data. The procedure must be capable of identifying non-stationary constituents from varying amounts of data, and must also lend itself to automation. This constitutes the basic criteria of what we consider successful adaptive spectral estimation.

Various candidate methods have been identified, all of which can be classified within two general areas of spectral estimation. Namely, the short-time FFT, data-adaptive evolutionary periodogram, and adaptive least squares, are different types of sequential estimation. Others, such as the FIR system modelling and predictive filter, and the IIR adaptive notch filter, are types of adaptive filtering. Presently, the short-time FFT, data-adaptive evolutionary periodogram, and FIR adaptive filters have been implemented. The performance of each has not met the criteria stated above for what we consider a successful adaptive spectral estimation. However, as the research has evolved, it now appears that the IIR and adaptive least squares approaches are the best qualified.

A computer multipath simulator that employs electromagnetic principles is desired. The design of such software would involve months of extensive research that is beyond the limits of this research. Nonetheless, the finished product would benefit in the modelling and verification areas of the multipath correction work. A software package has been obtained from the Ohio State University that we believe will satisfy our needs.

Section 3.2 discusses the planned work involving the Ohio State electromagnetic scattering code for multipath modelling purposes. Sections 3.3 and 3.4 explain the sequential estimation and adaptive filtering approaches, respectively. Section 3.5 discusses the results of the methods implemented thus far. Section 3.6 concludes the multipath coverage by outlining future research.

3.2 MULTIPATH MODELLING

Reliable modelling software is needed to help in the modelling and verification areas of the multipath correction research. A software package has been obtained from the Ohio State University ElectroScience Laboratory [16], called "Near Zone - Basic Scattering Code." The device utilizes the theories of electromagnetics and geometrical optics to analyze radiation from antennas in the presence of interfering structures. For this research, the GPS satellites and receiver antennas are modelled as right hand circular polarized and microstrip patch sources, respectively. Interfering structures that from complex shapes are modeled as combinations of simple flat plate and cylinder type reflectors. The software takes the following inputs: parameters describing the analysis frequency, source types and locations, structure types and locations, and what format of output is desired. The output is the radiated power from the antennas in the E_r and E_l electromagnetic planes, from which the amplitude and phase can be extracted. The theory of reciprocity is key, meaning that antennas posess similar radiation and reception characteristics.

A user's manual and FORTRAN 77 source code are provided. The program is currently operational on a UNIX workstation at CCAR. At this time, only test cases have been done to ensure the software is running correctly. Elsewhere, the code has been used extensively in conjunction with NASA Langley Research Center to study communications applications onboard the space station.

3.3 SPECTRAL ESTIMATION

The field of spectral estimation has received considerable attention in the past three decades. However, most of the progress has been made under the ideal setting of stationary signals. In the real world, the vast majority of signals are nonstationary. The most popular approach to this problem has been to modify existing techniques to estimate the time-varying spectrum. This usually assumes that the signals are slowly varying and remain locally stationary within specified time windows. An example of this is the short-time Fourier transform [1]. Although computationally efficient and easy to implement, it suffers from poor time-frequency resolution. A myriad of other methods exist, such as the set of autoregressive techniques [11, 15, 10], or the Wigner [5] and bilinear [4, 5, 6] distributions. In the end, these methods are plagued by faults that render their performance unsatisfactory for precise applications with nonstationary signals.

The data-adaptive evolutionary periodogram models the nonstationary signal in terms of its complex sinusoidal contributions at all frequencies. From the model, an expression for the time-varying amplitude is derived, which is a function of both time and frequency. The evolutionary spectrum for a given time and frequency is then computed as the power of the associated amplitude estimate. The data-adaptive evolutionary periodogram will be described in Section 3.3.2. But first, the classical approach of the short-time FFT will be described, which will serve as a baseline from which to compare the other methods.

3.3.1 SHORT-TIME FFT

The well-known discrete Fourier transform (DFT) produces samples of the Fourier transform that are discrete in frequency, of a periodic signal that is likewise discrete in time. Given a finite-length sequence $x(n)$ of length N, the DFT $X(n)$ is defined as

$$X(k) = \sum_{n=0}^{N-1} x(n) W_N^{kn}, \quad W_N = e^{-j2\pi/N}, \quad k = 0, \ldots, N-1 \tag{3.2}$$

and is equal to N samples of the Fourier transform separated equally in frequency. The complex frequency domain representation of the signal in 3.2 is easily converted to a power spectrum, or power versus frequency, by

$$P(\omega) = \|X(k)\| \tag{3.3}$$

which contains the frequency content of the signal. However, heavy computational cost prevents the DFT from practical use. The number of complex arithmetic operations are on the order of N^2. Storage space is also needed for the $x(n)$, $X(k)$, and W_N terms. The DFT has two main properties which may be used to its advantage: symmetry and periodicity of W_N^{kn}.

The symmetry and periodicity properties of the DFT were exploited to form a fast and efficient means of computation in the fast Fourier transform (FFT). In simple terms, the N-pt DFT operation is incrementally decomposed into $log(N)$ 2-pt DFT operations, for N an integer power of 2. The total number of complex arithmetic operations is then on the order of $Nlog(N)$. The procedure is also accompanied by a reduction in storage space. The operation may be done entirely in place, eliminating space to store the $X(k)$ terms. Further, the redundant 2-pt DFT needs only 2 W_N terms in storage. Despite the savings, the N length conglomerate output of the FFT is equal

to that of the N-pt DFT. The FFT has subsequently experienced widespread use in a number of signal processing applications, from convolution and filter design, to spectral estimation. The latter of which forms the basis of the short-time FFT (STFFT).

The FFT provides the spectrum of a signal over a time span equivalent to N samples. The spectrum is divided into N sections, or bins, in the range from DC to the Nyquist frequency. With greater N comes narrower bin width, and hence finer precision in the spectrum. A necessary condition to preserve the spectral effects (spikes, bumps, etc.) is that the signal is stationary, or not time-varying. For nonstationary signals, the effects move across and into other frequency bins as time passes. The FFT averages the changing effects over the total time span, resulting in a smeared image of the spectrum.

The STFFT consists of a series of consecutive short-length FFTs. It operates on shorter segments of the sequence in an attempt to reduce the amount of smearing. To explain, return to the length N sequence $x(n)$. The standard FFT effectively operates on the entire sequence, whereas the STFFT operates on an L length window of the sequence that is shifted along in time (typically $L \leq N/2$). Therefore, the STFFT is actually a concatenation in time of short-length FFTs of the windowed segments. The resolution of the STFFT spectrum is directly dependent on L, which is ultimately limited by N. Because the consecutively windowed segments are of shorter length, the spectral images tend to be coarse due to poor resolution. A windowing function (Blackman, Hanning, etc.) is usually employed to smooth the spectrum.

3.3.2 DATA-ADAPTIVE EVOLUTIONARY PERIODOGRAM

In its simplest form, the evolutionary spectral estimator may be viewed as a periodogram at each measurement time of the data sequence under analysis. As the spectrum is computed at each discrete frequency, the contributions from all other frequencies are minimized by assuming they are uncorrelated. The output is a snapshot of the spectrum at each data sample, thus showing the evolution of the signal contributions at each frequency over time. This technique is proposed as the evolutionary periodogram (EP) in [12]. Among the EP strong points are: a unique spectrum for a given signal, excellent frequency resolution, guaranteed positive spectral power, and the absence of cross-terms among multiple signal constituents.

To enhance the performance of the EP, the data-adaptive evolutionary periodogram (DAEP) was proposed in [13]. Rather than assuming that the signal components at frequencies different than that under analysis are uncorrelated, which is unrealistic, the information of those signal components is used to the advantage of the DAEP. As a result, the DAEP retains all the qualities of the EP while boasting an improvement in frequency resolution. The DAEP has shown to outperform the other methods mentioned above in estimating the spectrum of nonstationary signals.

3.3.2.1 THEORETICAL DEVELOPMENT

The following theoretical development contains the fundamental steps that are taken from the more detailed derivation in [12, 13]. Given a nonstationary process $x(n)$, which is available over the range $0 \leq n \leq N-1$, where N is the number of data samples, the contribution at the distinct frequency ω_0 can be represented as a complex variable

$$x_{\omega_0} = A(n, \omega_0) e^{jn\omega_0} \tag{3.4}$$

where $A(n,\omega_0)$ is an amplitude function, and $e^{jn\omega_0}$ is the complex argument. The nonstationary process may be modelled as the contribution from the frequency ω_0 and those from all other frequencies. We can write

$$\begin{aligned} x(n) &= x_{\omega_0}(n) + y_{\omega_0}(n) \\ &= A(n,\omega_0)e^{jn\omega_0} + y_{\omega_0}(n) \end{aligned} \tag{3.5}$$

where y_{ω_0} is the contribution from all frequencies other than ω_0, is zero-mean, and is uncorrelated with x_{ω_0} because they are at different frequencies. The variance of the amplitude function is related to the spectral density of x_{ω_0}, signified by $S(n,\omega_0)$, as given by the relation

$$E\{|A(n,\omega_0)|^2\} = S(n,\omega_0)\frac{d\omega_0}{2\pi} \tag{3.6}$$

Therefore, using $x(n)$ to estimate $A(n,\omega_0)$, one can in effect estimate $S(n,\omega_0)$. Performing this operation over all frequencies, the time-dependent spectral function can eventually be determined

$$S(n,\omega) = \frac{1}{2\pi}\int_{-\pi}^{\pi} S(n,\omega_0)d\omega_0 \tag{3.7}$$

Assuming the amplitude $A(n,\omega_0)$ varies with time, and it can be represented by an expansion of orthonormal functions $\{\beta_i(n)\}$, then

$$\begin{aligned} A(n,\omega_0) &= \sum_{i=0}^{M-1} \beta_i^*(n)a_i(\omega_0) \\ &= \mathbf{b}^H(n)\mathbf{a}(\omega_0) \end{aligned} \tag{3.8}$$

where

$$\mathbf{b}(n) = [\beta_0(n)\beta_1(n)\cdots\beta_{M-1}(n)]^T \tag{3.9}$$

is a vector of orthonormal functions at time n, and

$$\mathbf{a}(n) = [0(\omega_0)1(\omega_0)\cdots M-1(\omega_0)]^T \tag{3.10}$$

is a vector of expansion coefficients at ω_0. The order of expansion M dictates the rate at which the amplitude $A(n,\omega_0)$ is modeled to change, *i.e* increasing M creates a better model for rapidly changing amplitudes. However, as will be shown later, large M hinders the frequency resolution.

Combining (3.5) and (3.8), $x(n)$ can be written as

$$x(n) = \sum_{i=0}^{M-1} \beta_i^*(n)a_i(\omega_0)e^{jn\omega_0} + y_{\omega_0},\ 0 \le n \le N-1$$

If we let

$$\begin{aligned} &\{f_{n+1,i+1}\} = \beta_i^*(n)e^{jn\omega_0}, \\ &0 \le n \le N-1,\ 0 \le i \le M-1 \end{aligned} \tag{3.11}$$

be the entries for the $N \times M$ matrix $\mathbf{F}_{\omega_0}$, and also

$$\mathbf{x} = [x(0)x(1)\cdots x(N-1)]^T \tag{3.12}$$

$$\mathbf{y}(\omega_0) = [y_{\omega_0}(0)y_{\omega_0}(1)\cdots y_{\omega_0}(N-1)]^T \tag{3.13}$$

then $x(n)$ may be expressed in the following matrix form

$$\mathbf{x} = \mathbf{F}(\omega_0)\mathbf{a}(\omega_0) + \mathbf{y}(\omega_0) \tag{3.14}$$

Define a linear estimator for the amplitude function as

$$\begin{aligned} \hat{A}(n,\omega_0) &= \sum_{k=0}^{N-1} w_n^* x(k) \\ &= \mathbf{w}^H(n)\mathbf{x} \end{aligned} \tag{3.15}$$

where the $w_n(k)$ are time varying weights. The $*$ and H stand for the complex conjugate and Hermitian transpose operations, respectively. Substitution of (3.14) into (3.15) gives

$$\hat{A}(n,\omega_0) = \mathbf{w}^H(n)\mathbf{F}\mathbf{a} + \mathbf{w}^H(n)\mathbf{y} \tag{3.16}$$

where the ω_0 has been and will be omitted for simplicity, but the dependence as in (3.14) is still implied. Studying (3.16), the first term on the right hand side depends solely on x_{ω_0}, whereas the second depends on y_{ω_0}. To estimate the proper amplitude function at ω_0, the influence of the second term must be minimized. We impose the constraint towards this goal

$$\hat{A}(n,\omega_0) = \mathbf{w}^H(n)\mathbf{F}\mathbf{a} = \mathbf{b}^H(n)\mathbf{a} \tag{3.17}$$

or in other words

$$\mathbf{w}^H(n)\mathbf{F} = \mathbf{b}^H(n) \tag{3.18}$$

We now define a performance function as the mean squared error ξ, or the variance of the true minus estimated amplitude.

$$\begin{aligned} \xi &= \frac{1}{2}E\{|A(n,\omega_0) - \hat{A}(n,\omega_0)|^2\} \\ &= \frac{1}{2}E\{|\mathbf{b}^H(n)\mathbf{a} - \mathbf{w}^H(n)\mathbf{F}\mathbf{a} + \mathbf{w}^H(n)\mathbf{y}|^2\} \end{aligned} \tag{3.19}$$

Recall that x_{ω_0} and y_{ω_0} are uncorrelated. Let $\mathbf{R}_{yy}$ and $\mathbf{R}_{aa}$ be the correlation matrices for the data sequence $\mathbf{y}(\omega_0)$ and the expansion coefficients $\mathbf{a}$, respectively. Precisely,

$$\mathbf{R}_{xx} = E\{\mathbf{x}\mathbf{x}^H\} = \mathbf{R}_{yy} + \mathbf{F}\mathbf{R}_{aa}\mathbf{F}^H \tag{3.20}$$

Using the relation in (3.20), and applying the constraint in (3.18), the expression for ξ in (3.19) takes the following matrix form

$$\xi = \frac{1}{2}[\mathbf{w}^H(n)\mathbf{R}_{xx}\mathbf{w}(n) - \mathbf{b}^H(n)\mathbf{R}_{aa}\mathbf{b}(n)] \tag{3.21}$$

The ξ given by (3.21), subject to the constraint (3.18), is minimized using Lagrange multipliers. Define the augmented cost function

$$\begin{aligned} J &= \xi + C\Lambda \\ &= \frac{1}{2}[\mathbf{w}^H(n)\mathbf{R}_{xx}\mathbf{w}(n) - \mathbf{b}^H(n)\mathbf{R}_{aa}\mathbf{b}(n)] \\ &\quad -[\mathbf{w}^H\mathbf{F} - \mathbf{b}]\Lambda \end{aligned} \tag{3.22}$$

where C is the constraint function, and $\mathbf{\Lambda}$ is an $M \times 1$ vector of Lagrange multipliers. Differentiating (3.22) with respect to the weights $\mathbf{w}(n)$, and setting it equal to zero gives

$$\frac{\partial J}{\partial \mathbf{w}} = \mathbf{R}_{xx}\mathbf{w}_{opt}(n) - \mathbf{F}\mathbf{\Lambda} = 0 \tag{3.23}$$

Isolating $\mathbf{\Lambda}$ and applying (3.18) yields

$$\mathbf{\Lambda} = [\mathbf{F}^H\mathbf{R}_{xx}^{-1}\mathbf{F}]^{-1}\mathbf{b}(n) \tag{3.24}$$

Inserting (3.24) back into (3.23) and solving the optimum weight vector results in

$$\mathbf{w}_{opt}(n) = \mathbf{R}_{xx}^{-1}\mathbf{F}[\mathbf{F}^H\mathbf{R}_{xx}^{-1}\mathbf{F}]^{-1}\mathbf{b}(n) \tag{3.25}$$

Correspondingly, substituting (3.25) into (3.21) and simplifying terms produces the following expression for the minimum ξ

$$\xi_{min} = \frac{1}{2}\mathbf{b}^H(n)[\mathbf{F}^{-1}\mathbf{R}_{xx}\mathbf{F}^{-H} - \mathbf{R}_{aa}]\mathbf{b}(n)$$

Inserting the expression in (3.20) for $\mathbf{R}_{xx}$ finally yields

$$\xi_{min} = \frac{1}{2}\mathbf{b}^H(n)[\mathbf{F}^H\mathbf{R}_{yy}^{-1}\mathbf{F}]^{-1}\mathbf{b}(n) \tag{3.26}$$

Interestingly, the minimum ξ depends only on the correlation matrix $\mathbf{R}_{yy}$ and the expansion functions $\mathbf{b}(n)$. This is the effect of minimizing the contributions of the $\mathbf{y}(\omega_0)$ term in (3.16) by means of the constraint in (3.18). In the minimal case where $\mathbf{R}_{yy} = \mathbf{I}$, (3.26) is scaled down to

$$\xi_{min_{EP}} = \mathbf{b}^H(n)\mathbf{b}(n) \tag{3.27}$$

which is used for the evolutionary periodogram (EP) [12].

Lastly, substitution of (3.25) into (3.15) yields the minimum ξ estimate of the time-varying amplitude at the analysis frequency ω_0

$$\hat{A}(n,\omega_0) = \mathbf{b}^H(n)[\mathbf{F}^H\mathbf{R}_{xx}^{-1}\mathbf{F}]^{-1}\mathbf{F}^H\mathbf{R}_{xx}^{-1}\mathbf{x} \tag{3.28}$$

It will be shown that this expression plays an integral role in the data-adaptive evolutionary periodogram (DAEP) spectral estimator. As for the EP ($\mathbf{R}_{xx} = \mathbf{I}$), the amplitude is given by

$$\hat{A}_{EP}(n,\omega) = \mathbf{b}^H(n)\mathbf{F}^H\mathbf{x} \tag{3.29}$$

The data-adaptive estimate of the evolutionary spectrum at time n and frequency ω_0 is written using (3.6).

$$\hat{S}(n,\omega_0) = E\{\hat{A}(n,\omega)\hat{A}^H(n,\omega)\}$$

Inserting (3.28), and varying $\hat{S}(n,\omega_0)$ over $-\pi \leq \omega \leq \pi$ to produce the time-varying spectral estimate over all possible frequencies, the evolutionary spectral estimate eventually consolidates to

$$\hat{S}(n,\omega) = \mathbf{b}^H(n)[\mathbf{F}^H(\omega)\mathbf{R}_{xx}^{-1}\mathbf{F}(\omega)]^{-1}\mathbf{b}(n) \tag{3.30}$$

The evolutionary spectral estimator has been derived along the same lines as the minimum variance spectral estimator for a stationary setting. To show this, let $M = 1$ and $\beta_i = \beta_0 = 1$, then

$$\mathbf{F}(\omega) = bfe^H(\omega) = [1 \; e^{-j\omega} \; e^{-2j\omega} \; \cdots] \tag{3.31}$$

As a consequence, the evolutionary spectral estimator in (3.30) collapses to

$$\hat{S}(n,\omega) \;\; = \;\; [\mathbf{e}^H(\omega)\mathbf{R}_{xx}^{-1}\mathbf{e}(\omega)]^{-1} \tag{3.32}$$

which is the minimum variance spectral estimator (c.f. [11], pp. 378-380).

Experiments have shown [13] that the DAEP estimate provides the best frequency resolution, while exhibiting pseudo-linearity and minimal cross-term error among multiple signal components. Furthermore, the DAEP guarantees positive spectral estimates, and is robust in the presence of noise.

The main drawback of the DAEP is computational cost. This is due in part to the computation and inversion thereof of the correlation matrix $\mathbf{R}_{xx}$. It is worth noting that an efficient means of estimating the autocorrelation $\mathbf{R}_{xx}$ is detailed in [13] that is based on the evolutionary spectrum itself. Fortunately, computational burden is of no concern for the research at this time.

For the EP, using (3.29) instead of (3.28) results in an expression for $\hat{S}(n,\omega)$ that does not require any statistical information of the input signal $\mathbf{x}$. This is the end result of the $\mathbf{R}_{yy} = \mathbf{I}$ assumption discussed earlier. The complexity of the algorithm is diminished by ignoring the statistical information, but at a cost in frequency resolution.

3.3.2.2 DAEP ALGORITHM

The DAEP spectral estimator is implemented by means of the vector formula in 3.30, which is repeated here.

$$\hat{S}_{DAEP}(n,\omega) = \mathbf{b}^H(n)[\mathbf{F}^H(\omega)\mathbf{R}_{xx}^{-1}\mathbf{F}(\omega)]^{-1}\mathbf{b}(n) \tag{3.33}$$

The DAEP parallels the static periodogram detailed in [11], and actually reduces to the standard periodogram for the stationary setting ($M = 1, \beta_i = \beta_0 = 1/\sqrt{N}$).

The DAEP spectral estimate has the desirable feature of excellent frequency resolution that is common to periodograms in general. Consider that the spectral estimate $\hat{S}_{DAEP}(n,\omega)$ in (3.33) may be computed for any chosen frequency. If computational load is of no concern, a range of frequencies could be used with infinitesimal separation or resolution. However in theory, the minimum resolution is limited by the quantity $2\pi M/N$. This is true for the standard sets of expansion functions such as Fourier or Legendre. As eluded to before, the resolution is controlled by the order of the orthonormal expansion and the length of the data sequence. To ensure the best possible frequency resolution, it is advisable to keep M at a minimum by utilizing any *apriori* information available on $\mathbf{x}$.

The DAEP can be viewed as a linear time-varying band-pass filter with evolutionary filter response $\sum_{k=0}^{N-1} w_n^*(k)e^{-jk\omega}$. In effect, the bandwidth of the band-pass filter is equal to the frequency resolution. The center of the band-pass filter is then varied through a selected range of frequencies, and the spectrum estimate $\hat{S}_{DAEP}(n,\omega_0)$ is computed by squaring the magnitude of the filter output.

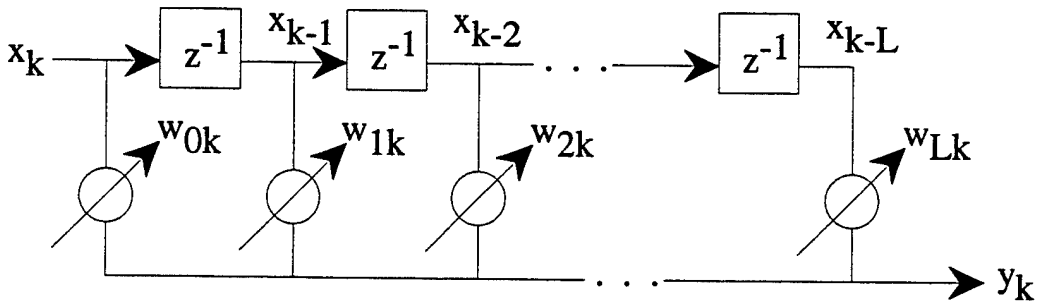

Figure 3.2: Adaptive Linear Combiner for FIR adaptive filter.

3.4 ADAPTIVE FILTERING

Digital filtering can be used to solve a wide variety of engineering tasks. A standard Finite Impulse Response (FIR) filter consists of a series of signal taps and delays, and associated multipliers or weights. The tap-delay and weight elements collectively form what is generally known as a linear combiner. The delays and weights dictate what the filter output will be given an input signal. The delays and weights are tuned for the specific problem at hand, based on the assumptions that the problem is well known and time-invariant.

The adaptive filter differs from the standard one in that the weights vary over time as they adapt to the specific problem. In this case the system of taps, delays, and weights, is known as the Adaptive Linear Combiner (ALC), and is portrayed in Figure 3.2. The ALC is the main ingredient of the adaptive filter. The ALC is utilized in different filtering configurations, which are suited for the class of problem at hand. Although the class of problem is known, the specifics are usually not, and they may or may not be time-varying. Two adaptive filtering configurations were used for this research, one system modelling and the other prediction. They will be described after the basic theory of adaptive filtering has been explained.

3.4.1 THEORETICAL DEVELOPMENT

A generic adaptive filtering configuration is furnished in Figure 3.3. The input signal is represented by x_n, the ALC (filtered) output by y_n, and the desired signal by d_n, where n is the time index. The error signal is defined as

$$e_n = d_n - y_n \tag{3.34}$$

Let $\mathbf{X}_n = [x_n, x_{n-1}, \ldots, x_{n-L}]^T$ be a vector composed of the L inputs ordered in reverse. Also let $\mathbf{W}_n = [w_{0n}, w_{1n}, \ldots, w_{Ln}]^T$ be a vector composed of the L adaptive weights in the ALC. The error signal becomes

$$e_n = d_n - \mathbf{W}_n^T \mathbf{X}_n \tag{3.35}$$

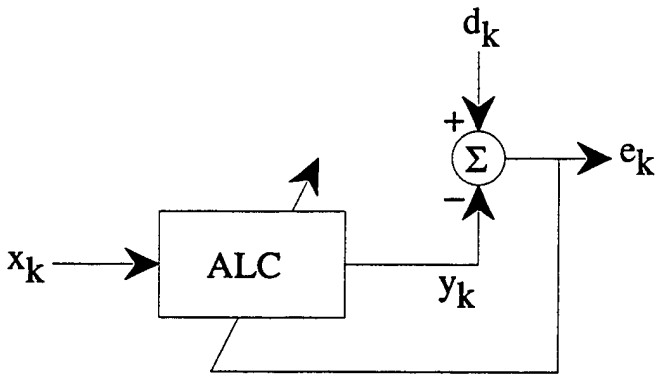

Figure 3.3: Generic adaptive filtering configuration.

Next define the performance index to be the expected value of the squared error (*i.e.* the mean squared error or ξ)

$$\xi = E[e_n] = E[d_n^2] + \mathbf{W}_n^T E[\mathbf{X}_n \mathbf{X}_n^T] \mathbf{W}_n - 2E[d_n \mathbf{X}_n^T] \mathbf{W}_n \tag{3.36}$$

The $E[d_n^2]$ term is interpreted as the correlation of the desired signal. Similarly, the $E[\mathbf{X}_n \mathbf{X}_n^T]$ term is interpreted as the correlation matrix of the input signal, and is signified by $\mathbf{R}$. The $E[d_n \mathbf{X}_n^T]$ term is the cross-correlation vector of the input and desired signals, given as $\mathbf{P}$. The ξ in 3.36 is now written as

$$\xi \;=\; E[d_n^2] + \mathbf{W}_n^T \mathbf{R} \mathbf{W}_n - 2\mathbf{P}^T \mathbf{W}_n \tag{3.37}$$

The ξ defines a quadratic performance surface with respect to the weights, w_{in}. The dimension of the hyperparaboloid surface is equal to the number of weights L. An example of a 2-weight ξ performance surface is displayed in Figure 3.4. The ξ has a single global minimum, which is either zero or positive due to the quadratic nature. The weight vector corresponding to the minimum point is therefore optimal, as in the following

$$\xi_{min} \;=\; \mathcal{F}(\mathbf{W}^*)$$

The optimal weight vector may be determined analytically, assuming the statistical properties of the signals ($E[d_n^2]$, $\mathbf{R}$, $\mathbf{P}$) are known. First form the gradient of the ξ

$$\nabla \doteq \frac{\partial \xi}{\partial \mathbf{W}_n} = 2\mathbf{R}\mathbf{W}_n - 2\mathbf{P} \tag{3.38}$$

Setting Equation 3.38 to zero and assuming $\mathbf{R}$ is nonsingular, the optimal weight vector is determined

$$W^* \;=\; \mathbf{R}^{-1}\mathbf{P} \tag{3.39}$$

Equation 3.39 may be recognized as the Wiener equation. The minimum ξ may be obtained by inserting 3.39 into 3.37, and then simplifying.

$$\xi_{min} \;=\; E[d_n^2] - 2\mathbf{P}^T \mathbf{W}_n^* \tag{3.40}$$

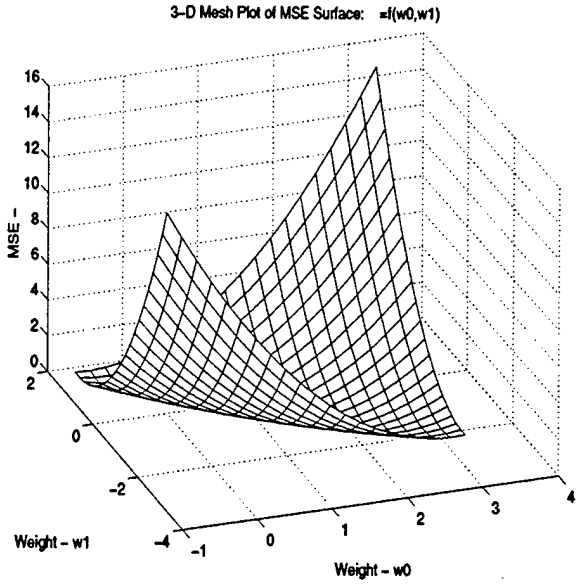

Figure 3.4: Example 2-weight ξ surface.

3.4.2 LMS WEIGHT UPDATE

In the real world, where the signal statistics are unknown, the optimal weight vector and minimum ξ must be determined using numerical techniques. The most common approach is to use a gradient search technique. The least-mean-squares (LMS) algorithm is one of the most widely accepted because of its simplicity and efficiency. It is superior to other gradient search techniques such as steepest-descent, which estimate the gradient by differencing short-term averages of the error signal.

A typical scenario exists where one has access to only the input and error signals, $\mathbf{X}_n$ and e_n, respectively. The LMS algorithm utilizes this information to estimate the gradient of the ξ as follows

$$\hat{\nabla}_n = \left[\frac{\partial e_n^2}{\partial \mathbf{W}_n}\right] = 2e_n\left[\frac{\partial e_n}{\partial \mathbf{W}_n}\right] = -2e_n\mathbf{X}_n \tag{3.41}$$

recalling Equation 3.35. The quantity $E[e_n^2]$ is effectively estimated by e_n^2 itself. A weight update recursion is then formulated

$$\hat{\mathbf{W}}_{n+1} = \hat{\mathbf{W}}_n - \mu\hat{\nabla}_n = \mathbf{W}_n + 2\mu e_n\mathbf{X}_n \tag{3.42}$$

which uses 3.41. The μ term is a convergence parameter that is adjusted to control the speed and stability of adaptation. For μ approaching unity, the convergence is slowed, and the variance of the weight estimates as they evolve over time is decreased.

Figure 3.3 together with Equation 3.42 depict the feedback relationship of the adaptive filter. For a time index n, the updated weights produce a filter output that subsequently produces an error signal, which in turn is used to update the weights at the $(n+1)^{th}$ index. The minimum

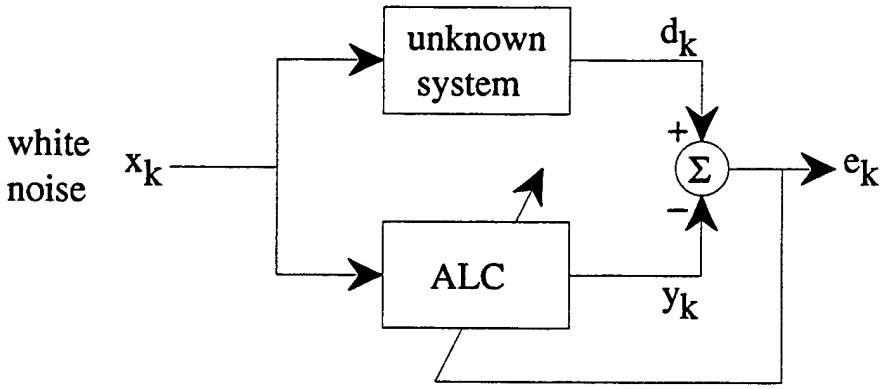

Figure 3.5: System modelling adaptive filter configuration.

ξ may also be estimated by taking a moving average of the resulting error signal. Finally, since the true optimal terminal conditions are unknown, convergence criterion for either the weights or ξ must be set.

3.4.3 SYSTEM MODELLING CONFIGURATION

When considering the system modelling configuration of adaptive filter, the goal is to match the transfer function of an unknown system. The configuration is shown in Figure 3.5. The adaptive filter accepts the same input x_n as the unknown system. The weights are adjusted such that the adaptive filter output y_n matches the unknown systems output d_n, which is the desired signal in Figure 3.3. The filter is essentially driving the error signal e_n to zero. The filter will continue to adapt if the unknown response is changing, e_n never quite reaching zero.

A system is defined as any process that has an input and output signal. The input-output relationship of the system is called the transfer function. The function is ordinarily represented as magnitude versus frequency. This is easily achieved by converting the time-domain weight values to the frequency-domain. As an example, the weights of a low-pass filter would form a *sinc* function in the time-domain. In the frequency-domain, the transfer function would be flat across the operational bandwidth, except for a notch at the stop frequency. In the trivial setting, a unity gain all-pass filter (a filter which does nothing to the input signal) would have a neutral flat-line function throughout the operational bandwidth.

In this application, the unknown system is the multipath process as a whole. The multipath process may be visualized as one that takes as input a set of sinusoidal signals spanning the entire spectrum, but only ouputs several distinct signals. The transfer function would be equivalent to a series of band pass filters. For the system modelling configuration, the adaptive filter actually takes Gaussian noise as input. The multipath system is only assumed to have the same input. The filter weights are then adapted such that the output signal matches the desired signal, which in this case is the SNR multipath.

The transfer function of the adaptive filter indicates the spectrum of the multipath system. The function closely resembles that of the system, which is a series of band pass filters. The pass

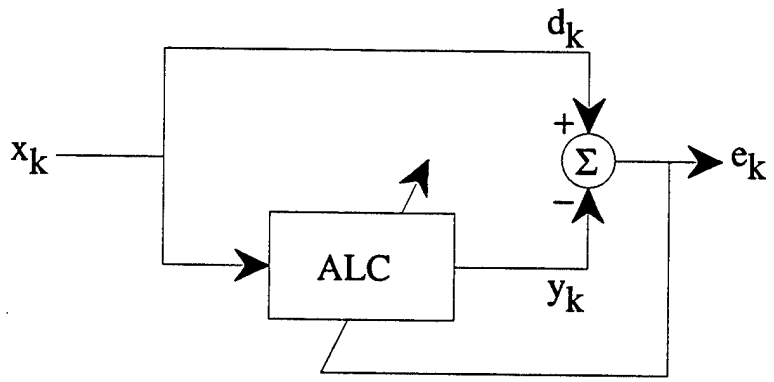

Figure 3.6: Predictor adaptive filter configuration.

bands will be located at the frequencies corresponding to the multipath constituents. In practice, the spectrum manifested by the adaptive filter transfer function is searched for band peaks that are related to the frequencies fo the multipath constituents. The width of the bands is decreased, and hence the frequency resolution is improved, by increasing the number of weights L. The resolution is limited by the length of the data sequence by following the rule $L \leq N$.

3.4.4 PREDICTION CONFIGURATION

This configuration of adaptive filter predicts the desired signal at the $(n+1)^{th}$ time index based on the previous L input signals. The configuration is shown in Figure 3.6. The signal x_n acts both as adaptive filter input and desired signal d_n. The weights are adjusted such that the filter output y_n mimics the desired signal at the next time index, d_{n+1}. Like the system modelling, the error signal e_n is driven to zero. Also, if the desired signal is changing, the filter will continue to adapt, e_n never quite reaching zero.

The predictor filter provides the spectrum of the multipath, much like the system modelling. Although the configurations are different, they share the same fundamental elements. For this research, the adaptive filter predicts the SNR multipath signal. During the process, the sinusoidal components excite the filter weights in their frequency range. The frequency-domain representation of the transfer function exhibits spikes at the multipath frequencies. As in the system modelling, the spectrum manifested by the adaptive filter transfer function is searched for peaks that are related to the frequencies fo the multipath constituents. The width of the spikes is decreased, and hence the frequency resolution is improved, by increasing the number of weights L. The resolution is limited by the length of the data sequence by following the rule $L \leq N$.

3.5 SPECTRAL ESTIMATION RESULTS

In order to properly demonstrate the effectiveness of the spectral techniques, two types of non-stationary signals were analyzed. The first was a dual chirp signal, the second simulated GPS multipath. Both signals will be described later. For each technique and signal combination, the

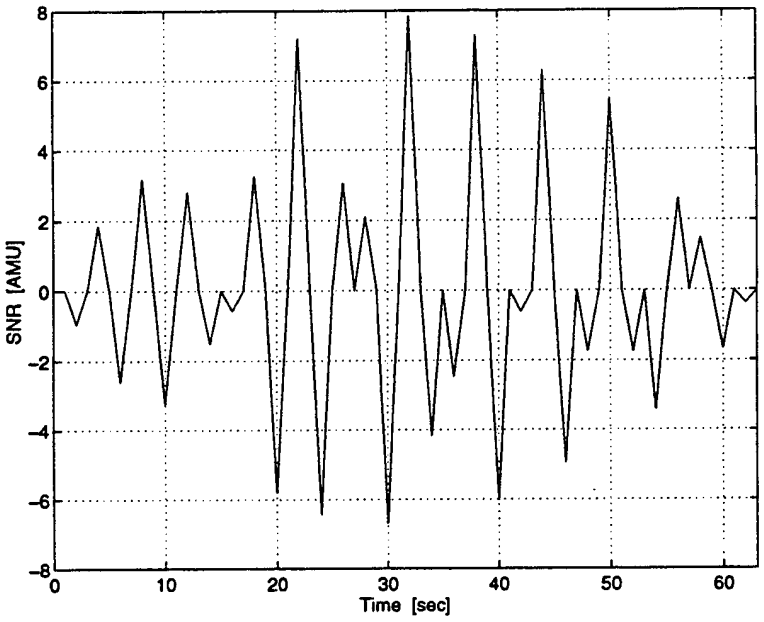

Figure 3.7: Time history of the dual chirp signal.

spectrum is presented in the forms of a mesh and contour plot. The mesh plot illustrates the spectrum as it evolves in time. The horizontal axes are frequency in Hz and time in seconds, and the vertical axis is the normalized spectral power. The contour plot is a rendering of the mesh plot as viewed from above. Accordingly, the horizontal frequency and time axes in the mesh plot appear as the horizontal and vertical axes in the contour plot. Two solid lines traverse the spectral ridges. The straight one represents the true frequency, the jagged one the estimated frequency. The estimate is simply the frequency corresponding to the maximum power at each time index.

3.5.1 DUAL CHIRP SIGNAL

The first data sequence analyzed was a dual chirp signal. A chirp signal is normally a sinusoid with frequency that is linearly swept through a specified range. The sequence in this example contained two chirps. The two frequencies began at the same value, and then diverged with equal measure as the sequence progressed. In addition to tracking the changing frequencies, the ability to distinguish the closely located frequencies was also examined. The dual chirp signal was implemented using the following expression.

$$x_n = A\left[\sin\left(2\pi\sum_{k=0}^{n}(f_{1n})\right) + \sin\left(2\pi\sum_{k=0}^{n}(f_{2n})\right)\right] \tag{3.43}$$

with time index $n = [1, N]$, amplitude $A = 2$, and frequencies $f_{1,2n} = 0.25 \pm n/8N$. The summation is the numerical equivalent to integrating the constantly changing frequency over the time interval $[0, t_n]$, defining the frequency and phase at each time index.

$$f_{in}t_n + \phi_n = \int_0^n f_i dt \tag{3.44}$$

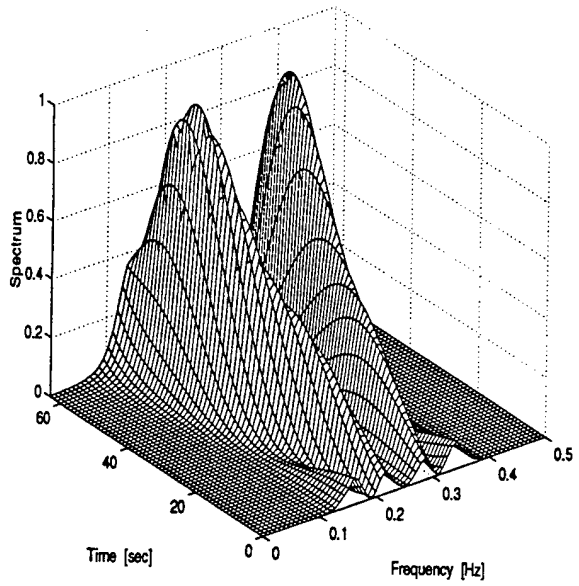

Figure 3.8: Mesh plot of DAEP produced spectrum for the dual chirp signal.

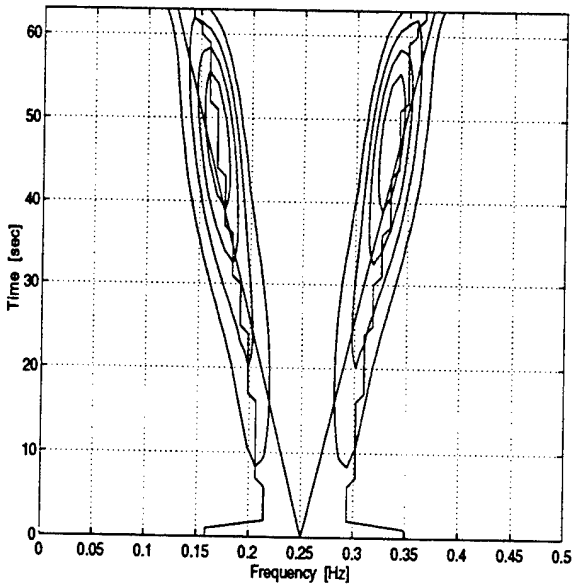

Figure 3.9: Contour plot of DAEP produced spectrum for the dual chirp signal.

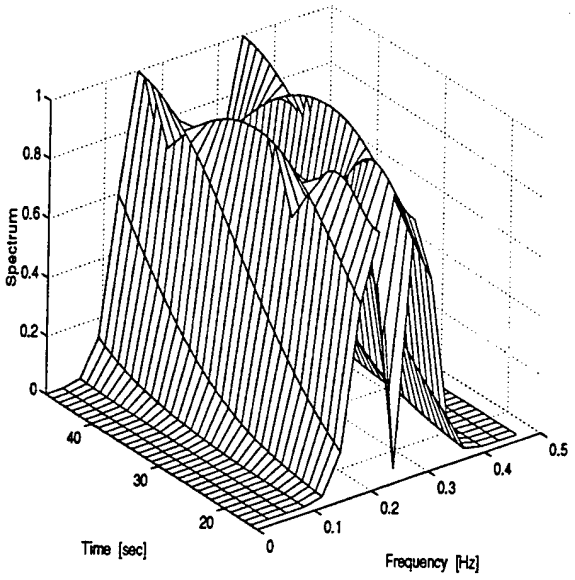

Figure 3.10: Mesh plot of STFFT produced spectrum for the dual chirp signal.

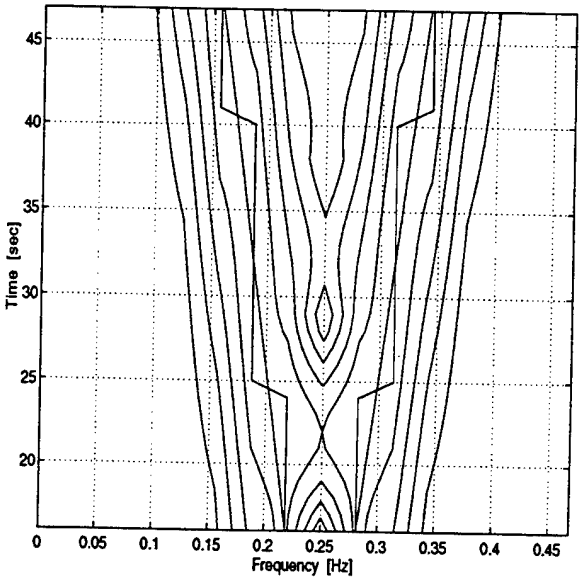

Figure 3.11: Contour plot of STFFT produced spectrum for the dual chirp signal.

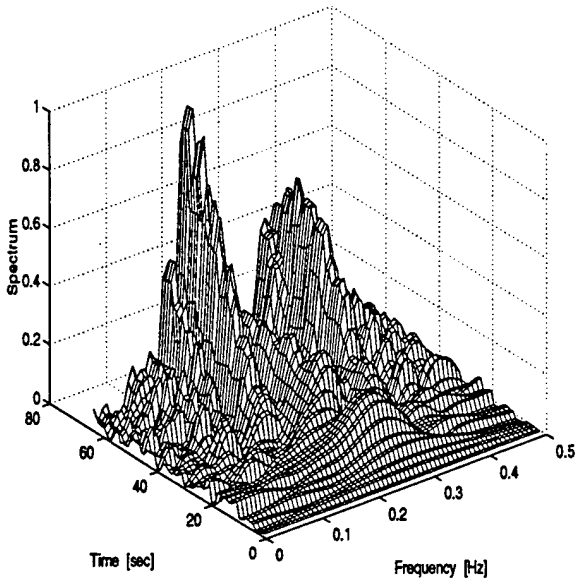

Figure 3.12: Mesh plot of system modelling adaptive filter produced spectrum for the dual chirp signal.

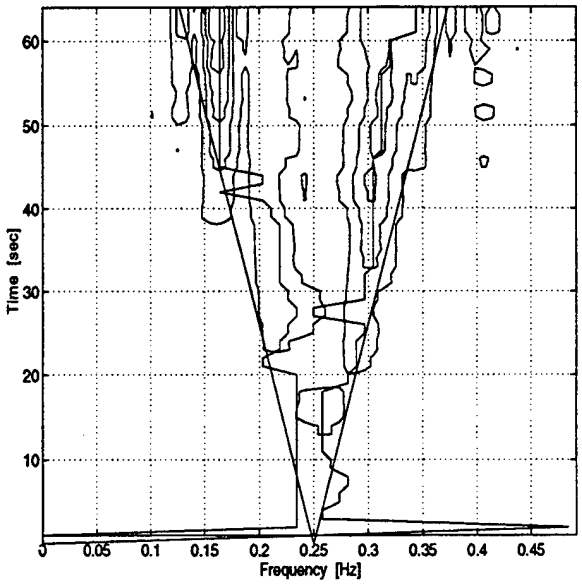

Figure 3.13: Contour plot of system modelling adaptive filter produced spectrum for the dual chirp signal.

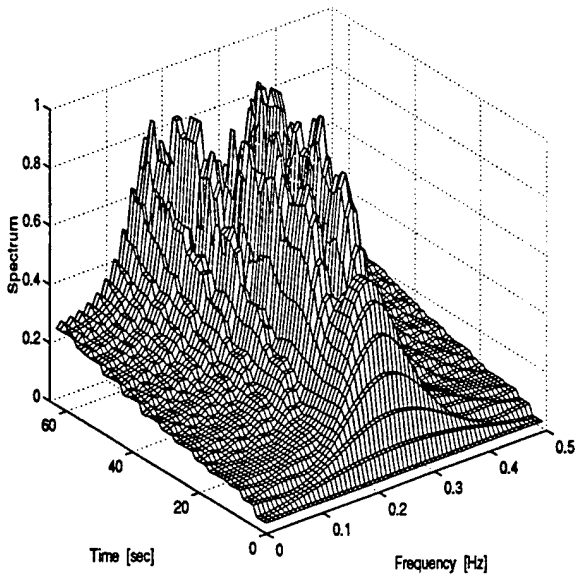

Figure 3.14: Mesh plot of predictor adaptive filter produced spectrum for the dual chirp signal.

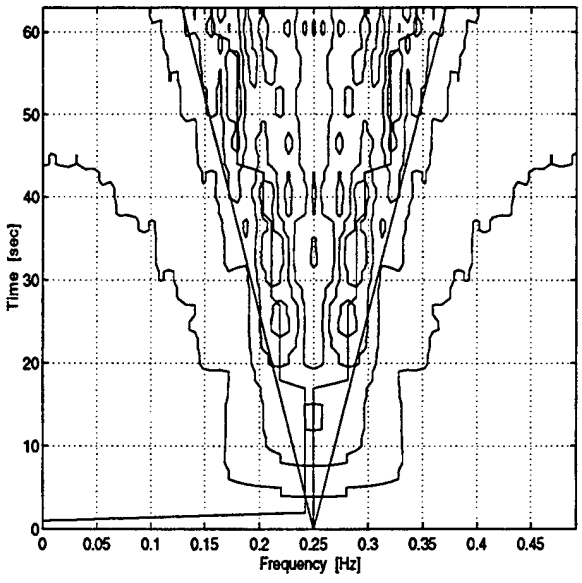

Figure 3.15: Contour plot of predictor adaptive filter produced spectrum for the dual chirp signal.

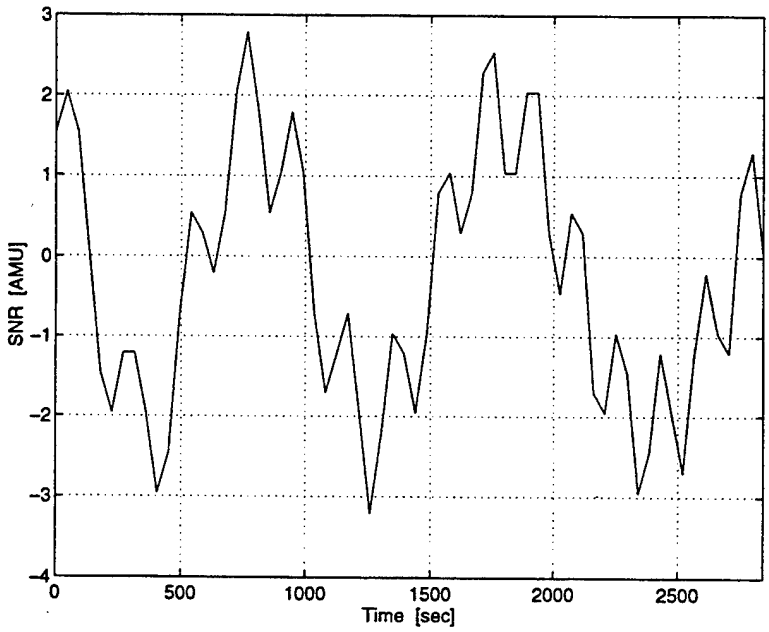

Figure 3.16: Time history of the SNR multipath signal.

Figure 3.7 shows the dual chirp signal time history. The horizontal axis is time in seconds, the vertical is the signal value. The sequence contains 64 seconds of data sampled at 1 Hz, meaning that $N = 64$.

The dual chirp signal was analyzed by the spectral estimation techniques using MATLAB. Figures 3.8 and 3.9 display mesh and contour plots of the DAEP produced spectrum. An order $M = 5$ Legendre function was used for the orthonormal expansion. Figures 3.10 and 3.11 display mesh and contour plots of the STFFT spectrum. The length of the window for the FFT operation was $L = 32$. Figures 3.12 and 3.13 display mesh and contour plots of the system modelling adaptive filter spectrum. Figures 3.14 and 3.15 display mesh and contour plots of the predictor adaptive filter spectrum. The number of weights for both filters was $L = 64$.

3.5.2 GPS SNR MULTIPATH SIGNAL

The second data sequence consists of simulated SNR measurements of a GPS signal that is corrupted by multipath [9]. The data was created with a Matlab signal simulation program which generated multipath corrupted SNR and differential phase data. The simulation was based on a simplified model of a single master-slave antenna pair, a single GPS satellite in orbit passing directly overhead, and one or more reflectors. The baseline length was 1 meter, and two reflectors were located 1 meter and 10 meters from the master antenna. The relative amplitudes of the multipath produced by the near and far reflectors were set to 0.1 and 0.05, respectively. The model is simplified because signals arriving from any direction are reflected into isotropic antennas.

Out of a 12 hour span relating to the GPS orbit, a one hour segment was chosen that produced a good balance of low and high frequency multipath, from the 1 and 10 meter reflectors, respectively. From previous analysis, it is known that there are two predominant multipath frequencies [9]. One

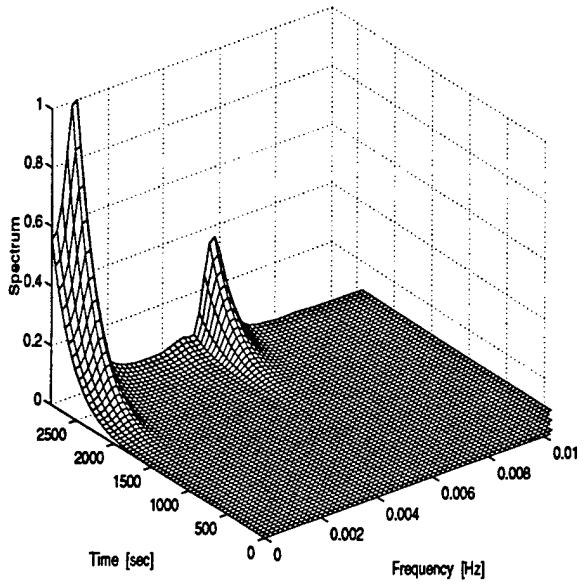

Figure 3.17: Mesh plot of DAEP produced spectrum for the SNR multipath signal.

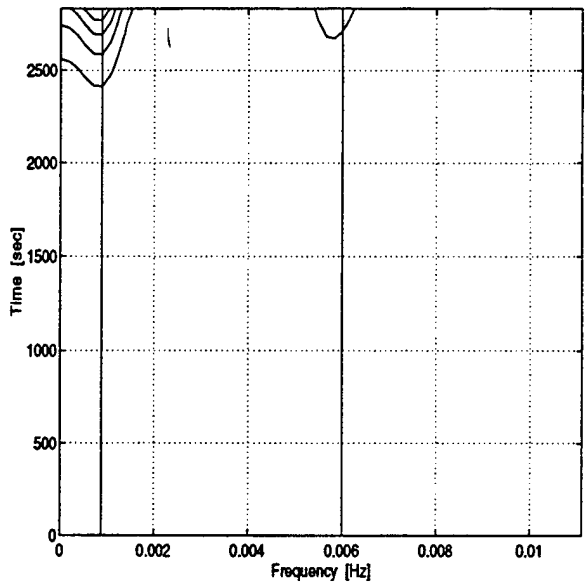

Figure 3.18: Contour plot of DAEP produced spectrum for the SNR multipath signal.

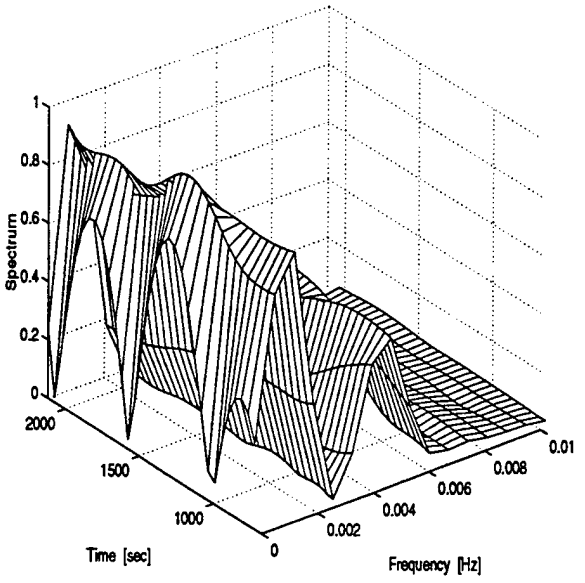

Figure 3.19: Mesh plot of STFFT produced spectrum for the SNR multipath signal.

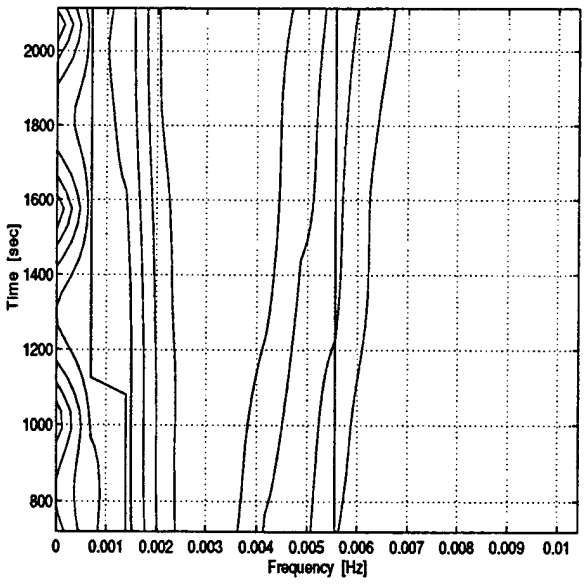

Figure 3.20: Contour plot of STFFT produced spectrum for the SNR multipath signal.

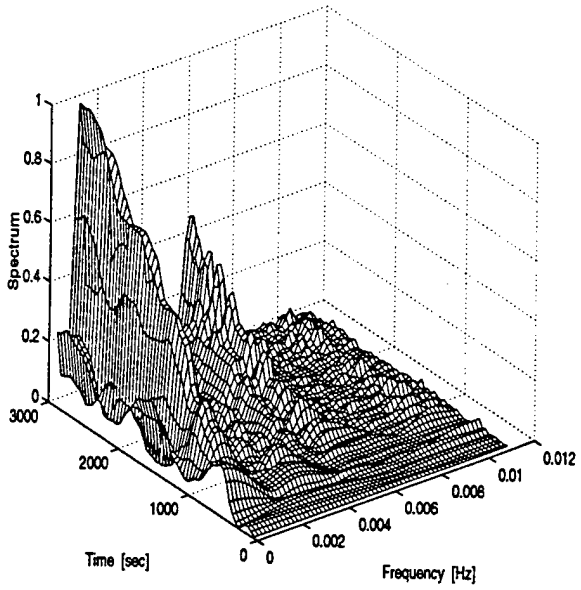

Figure 3.21: Mesh plot of system modelling adaptive filter produced spectrum for the SNR multipath signal.

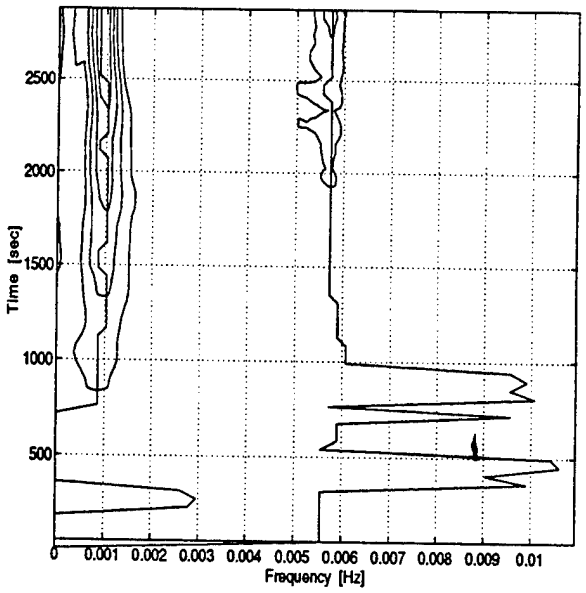

Figure 3.22: Contour plot of system modelling adaptive filter produced spectrum for the SNR multipath signal.

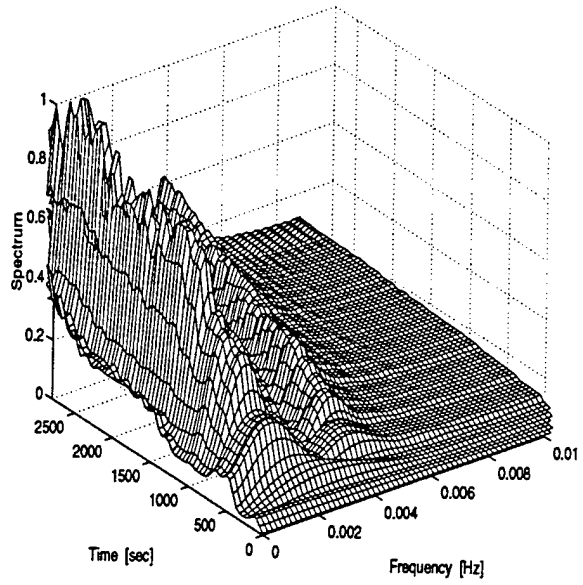

Figure 3.23: Mesh plot of predictor adaptive filter produced spectrum for the SNR multipath signal.

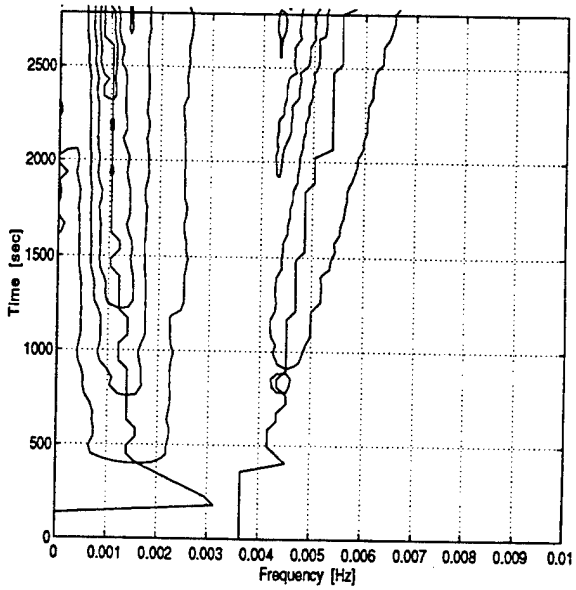

Figure 3.24: Contour plot of predictor adaptive filter produced spectrum for the SNR multipath signal.

frequency is in the range of 4-8 $\times 10^{-3}$ Hz, and time-varying. The other is practically constant and on the order of 10^{-4} Hz. The data was originally sampled at 1.5 second intervals. For the analysis, the data was decimated by a factor of 30, giving an effective sampling rate of 0.022 Hz (45 second intervals). Also, only $N = 64$ samples of the available data were used.

The simulated SNR multipath signal was analyzed by the spectral estimation techniques using MATLAB. Figures 3.17 and 3.18 display mesh and contour plots of the DAEP produced spectrum. An order $M = 5$ Legendre function was used for the orthonormal expansion. Figures 3.19 and 3.20 display mesh and contour plots of the STFFT spectrum. The length of the window for the FFT operation was $L = 32$. Figures 3.21 and 3.22 display mesh and contour plots of the system modelling adaptive filter spectrum. Figures 3.24 and 3.24 display mesh and contour plots of the predictor adaptive filter spectrum. The number of weights for both filters was $L = 64$. Note that there are no lines for the true frequencies since they are unknown in this example.

3.5.3 DISCUSSION OF RESULTS

The dual chirp signal allows one to evaluate the accuracy of the frequency estimates. Table 1 contains the mean (μ) and 1-σ errors of the frequency estimates for each technique. The numbers surprisingly indicate that the STFFT performs best at estimating the changing frequencies. The mean error in the STFFT estimate is half that of the DAEP, and surpasses those of the adaptive filters by at least an order of magnitude. The 1-σ errors follow the same trend.

Table 1: Mean and 1-σ errors of frequency estimates for the dual-chirp signal.

	DAEP	STFFT	System Modelling	Predictor
μ [Hz]	0.0179	0.0078	0.1178	0.0574
σ [Hz]	0.0171	0.0047	0.0701	0.0460

Although the STFFT outperforms the DAEP in estimating the frequency for the dual-chirp exercise, difficulties may arise in more challenging situations. The shape of the spectral surfaces gives evidence to this observation. The spectral ridges produced by the DAEP are steep and separated. By comparison, the STFFT ridges are shallow and often become interconnected. If the true frequencies were closer together, or were changing more rapidly, the performance of the STFFT would likely degrade considerably. Additionally, the routine for determining the frequency estimates was rudimentary. A more sophisticated centroid type technique would exploit the preferable DAEP spectra to refine the frequency estimates.

The FIR adaptive filters supplied unfavorable estimates of the dual-chirp frequencies. The shape of the spectra is jagged, not as regular as the DAEP or STFFT. This causes jitter when estimating the frequency. The effect is more pronounced in the system modelling spectrum, which was expected because of the random noise input. The predictor yields improved estimates, but the spectrum exhibits poor frequency separation in the early stages.

Working with the simulated multipath data provides an initial qualitative assessment of how the spectral analysis techniques perform on such complicated signals. There are no precise truth

values from which to compare the frequency estimates.

The DAEP spectrum begins to show the multipath frequencies after 1500 seconds has passed. This is because the spectral power of the two signals overshadows the rest of the spectrum. The DAEP spectral power builds up over time even for constant amplitude signals. The source of this characteristic is found in Equation 3.33, where the $\beta(n)$ terms increases with n. As a result, the mesh and contour plots have little meaning. The frequency estimates are computed independently each time index, however, and they are valid as they appear in the contour plot. The estimates are in the neighborhood of what is expected. The 0.006 Hz estimate is constant, which is not representative of the multipath data.

The STFFT presents a good spectral image of the multipath. Two distinct frequencies with constant amplitudes of correct proportion are seen. The frequency estimates are again in what is considered a permissible region. But like the DAEP, the higher (0.0055 Hz) estimate is constant, and is not indicative of the multipath data.

The predictor adaptive filter produced spectra may in fact provide the best representation of the multipath. The evidence supporting this conjecture lie in the frequency estimates. Not only do they lie in the acceptable range, they exhibit nonstationarity. The estimates settle down after 1000 seconds for the system modelling, and 500 seconds for the predictor, have passed. For the remainder of the data, both adaptive filter estimates seem to track frequencies relating to the multipath. The predictor results look more credible, based on knowledge gained during previous research with this data.

3.6 SUMMARY AND FUTURE WORK

A highly effective technique for the correction of multipath errors in GPS phase data, based on SNR measurements, was been described and demonstrated in [2]. The technique, applied to data sets collected on static baselines in severe multipath environments, reduced the differential phase errors to near receiver noise levels.

The recent phase of research was spent investigating methods of spectral analysis. In the current implementation of the multipath correction technique, the most substantial weakness is the estimation of the multipath frequencies. Classical algorithms, such as the periodogram, performed inadequately and demanded extensive user interaction. A method suited for time-varying frequencies, and requiring minimal external interaction, was desired.

Four methods of spectral analysis were studied: the data-adaptive evolutionary periodogram (DAEP), the short-time FFT, the system modelling and predictor type of adaptive filters. They were tested on two kinds of signals: the dual-chirp and the simulated multipath. The STFFT performed best on the dual-chirp signal. The predictor adaptive filter performed best on the simulated multipath. The STFFT produced spectra with poor resolution compared to the others. The adaptive filters were more sensitive to the input signals. None of the procedures needed user input during operation. The DAEP calls for an *apriori* guess of the number of signals being dealt with.

While the spectral analysis methods are an improvement over the classical ones, they don't meet the stringent requirements of the multipath correction technique. Errors in the frequency

estimates should be less than 10^{-3} Hz. The STFFT approached that level with the dual-chirp signal. It is difficult to ascertain the extent of performance when the true frequencies are unknown. Nonetheless, not one of the estimates appeared to be close with the simulated multipath.

The next step of research will be to examine more advanced adaptive estimation mechanisms. Based on a literature survey, the IIR adaptive filter and adaptive least squares approaches look very promising. The IIR adaptive filter is fundamentally similar to the FIR types described in this report. It has the advantage that one filter weight per signal achieves the same performance of an FIR filter with hundreds of weights. This means shorter convergence times and reduced computational complexity. The IIR filter also reports the frequency estimates directly, eliminating the search for peaks in the spectrum. The adaptive least squares is another efficient but powerful routine that directly reports the amplitude, and phase estimates in addition to the frequency.

Once a successful spectral analysis procedure has been found, the area of focus will be to test the performance of the multipath profiling technique on dynamic data, again in a post-mission mode. The first step in the procedure is to compute an initial time history of the vehicle attitude. This information serves as the basis for computing the correct antenna gain to be removed from each amplitude observation, and for removing the expected phase difference from the phase observables to permit the constituent sign determination. Post-mission accuracy refinement is a valuable tool for analysis of spacecraft data, and airborne altimetry or photogrammetry.

Work will continue on the multipath modelling software. The procedure of creating the basic GPS transmitting and receiving sources needs to be understood. Progress in this area will be accelerated with the assistance of Wendy Lippincott and Peter Melvin at NRL. After that, sophisticated models may be developed to aid the multipath research.

References

[1] Allen, J.B. and L.R. Rabiner, "A Unified Approach to Short-Time Fourier Analysis and Synthesis," Proceedings IEEE, Vol. 65, pp. 1558-1564, Nov. 1977.

[2] Axelrad, P., C. Behre, C.J. Comp, and L.M. Ward, "GPS Based Attitude Determination," NRL FY'93-94 Technical Report II, October 14, 1994.

[3] Cannon, M.E., and M. Haverland, "Experiments of GPS Attitude Determination Within A Helicopter Pod," Proceedings of ION GPS-93, Salt Lake City, UT, Sept. 22-24, 1993.

[4] Choi, H.I. and W.J. Williams, "Improved Time-Frequency Representation of Multicomponent Signals Using Exponential Kernels," IEEE Transactions on Acoustics, Speech and Signal Processing, Vol. 37, No. 6, pp. 826-871, 1989.

[5] Claasen, T.A.C.M. and W.F.G. Mecklenbrauker, "The Wigner Distribution - A Tool For Time-Frequency Analysis," Phillips Journal of Research, Vol. 35, No. 4, pp. 276-300, 1980.

[6] Cohen, L., "Time-Frequency Distributions - A Review," Proceedings IEEE, Vol. 77, No. 17, pp. 941-981, July, 1989.

[7] Cohen, C.E., B.W. Parkinson, "Aircraft Applications of GPS-Based Attitude Determination," Proceedings of ION GPS-92, Albuquerque, NM, Sept. 16-18, 1992.

[8] Cohen, C.E., E.G. Lightsey, B.W. Parkinson, and W.A. Fees, "Space Flight Tests of Attitude Determination Using GPS: Preliminary Results," Preprint of paper presented at ION GPS-93, Salt Lake City, UT, Sept. 22-24, 1993.

[9] Comp, C.J., "Carrier Phase Multipath Characterization and Mitigation For High Precision GPS Applications," Ph.D. Dissertation Prospectus, University of Colorado, Dept. of Aerospace Engineering Sciences, January 16, 1995.

[10] Kahn, M., L.F. Chaparro and E.W. Kamen, "Frequency Analysis of Nonstationary Signal Models," Proceedings of the Conference on Information Scientific Systems, pp. 617-622, Baltimore, MD, March, 1988.

[11] Kay, S.M., *Modern Spectral Estimation*, Prentice-Hall, Englewood Cliffs, N.J., 1988.

[12] Kayhan, A.S., A. El-Jaroudi and L.F. Chaparro, "Evolutionary Periodogram for Nonstationary Signals," IEEE Transactions on Signal Processing, Vol. 42, No. 6, pp. 1527-1536, June, 1994.

[13] Kayhan, A.S., A. El-Jaroudi and L.F. Chaparro, "Data-Adaptive Evolutionary Spectral Estimation," IEEE Transactions on Signal Processing, Vol. 43, No. 1, pp. 204-213, Jan., 1995.

[14] Lu, G., M.E. Cannon, and G. Lachapelle, "Attitude Determination in a Survey Launch Using Multi-Antenna GPS Technologies," Proceedings of ION National Technical Meeting, San Francisco, CA, Jan. 20-22, 1993.

[15] Melard, G. and A. Herteler de Schuter, "Contributions to Evolutionary Spectral Theory," Journal of Time Series Analysis, Vol. 10, No. 1, pp. 41-63, 1989.

[16] Marhefka, R.J. and J.W. Sivestro, "Near Zone - Basic Scattering Code User's Manual with Space Station Applications," Technical Report 716199-13, The Ohio State University Electro-Science Laboratory, Columbus, OH, March, 1989.

[17] Schwarz, K.P., A. El-Mowafy, and M. Wei, "Testing GPS Attitude System in Kinematic Mode," Proceedings of ION GPS-92, Albuquerque, NM, Sept. 16-18, 1992.

[18] Ward, L.M., "Spacecraft Attitude Estimation Using GPS: Methodology and Results," Ph.D. Dissertation Prospectus, University of Colorado, Dept. of Aerospace Engineering Sciences, August 12, 1994.

4. Spinning Satellite Attitude Determination Techniques *Charles P. Behre*

This section describes several techniques for the determination of the attitude of a spinning satellite using GPS. Because both spinning satellites and GPS receivers have the potential to provide high reliability at low cost, the combination of the two is quite promising. Furthermore, the kinematics of spinning satellites provide unique advantages for GPS-based attitude estimation. GPS antennas mounted on the satellite's rim are constantly undergoing large displacements, and phase difference measurements can be used to determine the oscillating displacement vector between the two antennas. Previously, Martin-Niera and Lucas [5] showed that by analyzing these measurements in the frequency domain, one can determine vehicle attitude, nutation angle, body nutation rate, and inertial nutation rate. The spin frequencies appear as spikes in the frequency domain and the attitude is related to the amplitude of the spikes. Alternative time domain techniques can be used to estimate the instantaneous angular velocity which is related to the principle spin frequencies. The spacecraft attitude can then be derived by averaging the vector perpendicular to the antenna displacement.

A comparison is made between the performance of these techniques when applied to a simulated spinning satellite. Analysis focuses on the effect of nutation angle magnitude on the accuracy of the different algorithms and their relative advantages and disadvantages. Simulation results indicated that frequency domain techniques perform quite well with large nutation angles; whereas a Kalman Filter approach is superior for small nutation angles.

4.1 Introduction

Low cost satellite missions such as the Student Nitric Oxide Explorer [1] are designed to spin about the spacecraft major axis for both attitude stabilization and instrument scanning of the Earth. This type of spacecraft typically does not have very stringent onboard attitude control requirements; however, both position and attitude knowledge to better than 1 km and 1 degree, respectively are needed for post mission analysis of the science data. GPS has the potential to provide this information cost effectively in terms of dollars, weight, and power.

The use of GPS for spacecraft attitude determination onboard an Earth pointing spacecraft has been already demonstrated on the USAF RADCAL satellite [2,3] and the Crista Spas missions [4]. In general, a minimum of two antenna baselines comprising three antennas are required for full attitude estimation. Phase difference measurements to two or more satellites form the basis for the attitude estimation algorithms.

The application of GPS specifically to spinning satellites was suggested by Martin-Neira and Lucas in 1992 [5]. They described an FFT based method for using a single GPS antenna baseline to determine spacecraft spin and nutation rates as well as nutation angles and orientation of the angular momentum vector. Their approach uses triple differenced phase measurements as the basic observable.

Attitude determination of a spinning vehicle with GPS is particularly attractive because of the inherent baseline motion. This regular motion permits direct three axis attitude estimation with a single baseline, i.e. two antennas or in some cases even a single GPS antenna. This may result in a reduction in onboard hardware or improved redundancy with existing hardware. Furthermore, the baseline motion permits highly accurate solutions to be obtained from time differenced observations, thus eliminating the need for ambiguity resolution and minimizing the effect of cycle slips.

This section discusses and compares several algorithms for estimation of the spinning spacecraft angular rates and orientation of the angular momentum vector based on GPS data. We begin with a description of the GPS observables to be used in section 4.2 plus a description of the satellite motion in section 4.3. Section 4.4 describes a simple method for determining the orientation of the spacecraft's angular momentum vector. In section 4.5, two frequency domain approaches are investigated - the FFT method and an alternative Auto-Regressive method (AR). Sections 4.6 and 4.7 present two time domain approaches - an averaging method and a Kalman Filtering approach to the same problem. Section 4.8 describes the computer simulation used to test the algorithms and the results obtained. The section concludes with a comparison of the various approaches, a description of an upcoming experiment to validate these results, and suggestions for future work.

4.2 Displacement Vectors

Time differenced GPS phase observations have been used in surveying to establish an initial estimate for long antenna baselines [7] and in attitude determination as a means for initial ambiguity resolution [9]. In general, they do not produce high accuracy estimates because the measurement noise is higher and the geometry is weaker than a single difference (between antennas) or double difference (between antennas and satellites) observable. The latter problem is not the case for a spinning satellite, where the rapid antenna motion produces a strong geometry for time differenced observations. The time difference observations are used to solve for what we will call antenna displacement vectors, which form the basis for the attitude solution methods described subsequently.

The basic equation for the $\Delta\phi$ measurement for one baseline and from one satellite is

$$\Delta\phi = \hat{e} \bullet \vec{r} - j + \beta + \upsilon \tag{4.1}$$

where $\hat{e}$ is the line of sight unit vector to the GPS satellite, $\vec{r}$ is the baseline vector, j is an integer ambiguity, β is a line bias, and υ is noise. The symbol Δ will subsequently be used to denote a difference between two antennas. By time differencing two $\Delta\phi$ measurements and assuming no cycle slips, an equation for the antenna displacement vector, $\vec{\delta r}$, at each measurement time, t_i, can be formed as

$$\delta\Delta\phi(t_i) = \hat{e}(t_i) \bullet \vec{\delta r}(t_i) + (\nu_{i+1} - \nu_i) \tag{4.2}$$

where the symbol δ will be used to denote time differences and

$$\delta\Delta\phi(t_i) \equiv \Delta\phi(t_{i+1}) - \Delta\phi(t_i) \tag{4.3}$$

Because of the effects of noise, it might be desirable to increase the size of the displacement vectors. Figure 1 shows two different sizes of displacement vectors. In equation (4.2) two consecutive $\Delta\phi$ measurements are differenced to compute $\vec{\delta r}_1$. Larger displacements, designated as $\vec{\delta r}_k$, can be computed by differencing two $\Delta\phi$ measurements taken more than one measurement interval apart as in equation (4.4)

$$\delta\Delta\phi_k(t_i) = \hat{e}(t_i) \bullet \vec{\delta r}_k(t_i) + (\nu_{i+k} - \nu_i) \tag{4.4}$$

where

$$\delta\Delta\phi_k(t_i) \equiv \Delta\phi(t_{i+k}) - \Delta\phi(t_i) \ , \tag{4.5}$$

k is a constant integer equal to the number of measurement intervals between two differenced $\Delta\phi$ values, and i is a changing index for each measurement time. Neglecting changes in the line of sight vector plus errors in the measurements, $\vec{\delta r}_k$ is exactly equal to the sum of single interval displacement vectors as in equation (4.6).

$$\vec{\delta r}_k(t_i) = \sum_{n=1}^{k-1} \vec{\delta r}_1(t_{i+n}) \tag{4.6}$$

It should be noted that while the time interval between antenna position is increased, the measurements are still accumulated at every sample time. Therefore, there is no loss in the amount of observational data.

To solve (4.4) for $\vec{\delta r}_k$, measurements from at least three GPS satellites must be available and the line of sight vectors must be approximately constant over the interval t_i to t_{i+k}. If we assume that the noise is uncorrelated and unbiased, then the least squares solution is

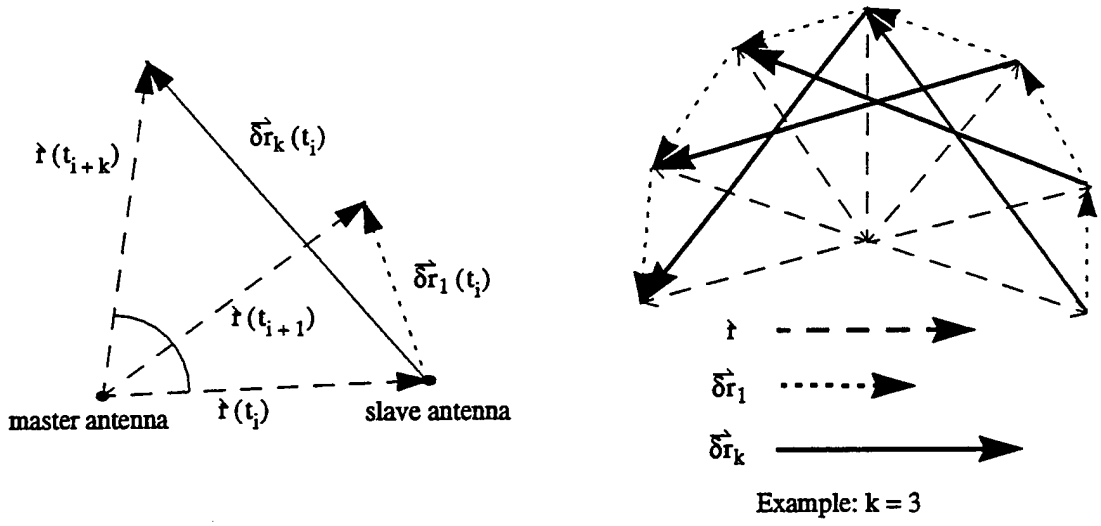

Figure 1. Antenna displacement vectors.

$$\vec{\delta r}_k(t_i) = (H^T H)^{-1} H^T \begin{bmatrix} \delta\Delta\phi^1(t_i) \\ \delta\Delta\phi^2(t_i) \\ \vdots \\ \delta\Delta\phi^M(t_i) \end{bmatrix} \tag{4.7}$$

where

$$H = \left[\hat{e}^1\ \hat{e}^2\ \ldots\ \hat{e}^M\right]^T, \tag{4.8}$$

the superscript refers to each satellite, and M is the number of satellites.

4.3 Satellite Kinematic Model

Figure 2 illustrates the antenna configuration on the spinning satellite and defines the key vectors and angular rates. For simplicity, the vehicle is assumed to be axisymetric about the z^B axis. The master antenna is located at the center with the master-slave baseline perpendicular to the axis of symmetry. The body x-axis is defined by the position of the slave antenna. I_s is defined to be the spin axis moment of inertia and I_t is the transverse moment of inertia. The angular velocities are defined in [8] as follows: ω is the inertial spin rate about the instantaneous rotation axis; ω_p is the body nutation rate; and ω_I is the inertial nutation rate. The nutation angle is θ. The relationships between ω, ω_p, ω_I, θ, and the inertias are

$$\omega_p = \frac{I_t - I_s}{I_s}\omega_I \cos\theta \tag{4.9}$$

and

$$\omega^2 = \omega_p^2 + \omega_I^2 + 2\omega_p\omega_I\cos\theta\ . \tag{4.10}$$

The body frame is fixed to the rotating satellite and is denoted with a superscript B. The angular momentum frame,

denoted by the superscript H, is defined with the z axis along the spacecraft's angular momentum vector. The orbit local frame is designated by the superscript L.

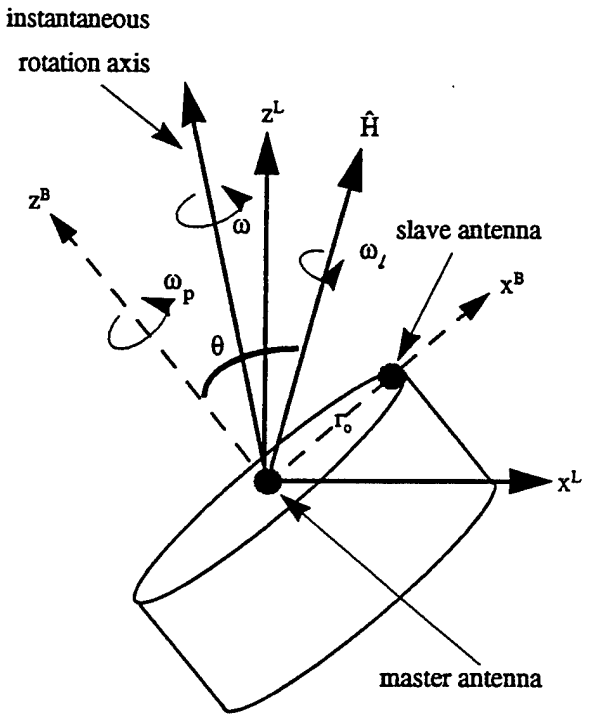

Figure 2. Kinematic model.

4.3.1 Antenna Motion

In the absence of external torques a GPS antenna on the rim of a spinning satellite will move according to the kinematic model described in equations (4.9) and (4.10). In the body fixed system, the antenna position remains constant. In the local system, however, the position is dependent on satellite rotations and the orientation of the angular momentum vector in this system.

The position of the antenna in these two coordinate systems can be related with two separate rotation matrices given by

$$r^L = {}^L_C{}^H_H C^B_B r^B \tag{4.11}$$

where

$$r^B = \begin{bmatrix} r_o \\ 0 \\ 0 \end{bmatrix}$$

is the position of the antenna in the body frame, and

$${}^H_C{}^B_B = \begin{bmatrix} c\psi c\phi - c\theta s\psi s\phi & -s\psi c\phi - c\theta c\psi s\phi & s\theta s\phi \\ c\psi s\phi + c\theta s\psi c\phi & -s\psi s\phi + c\theta c\psi c\phi & s\theta c\phi \\ \sin\theta \sin\psi & s\theta c\psi & c\theta \end{bmatrix} \tag{4.12}$$

is the rotation matrix from the body fixed system to the angular momentum system. The angles ψ and ϕ are time

dependent angles related to the kinematic frequencies by

$$\psi = \omega_p t + \psi_o \tag{4.13}$$

and

$$\phi = \omega_l t + \phi_o . \tag{4.14}$$

The matrix ${}^{L}C^{H}$ rotates from the angular momentum system to the local system. If equation (4.11) is differenced in time an expression relating the displacement vectors to the satellite kinematics can be formulated. For a constant orientation of a satellite's angular momentum vector, this relationship at time t_i is

$$\vec{\delta r}^{L}(t_i) = {}^{L}C^{H}\left[{}^{H}C^{B}(t_{i+k}) - {}^{H}C^{B}(t_i)\right]\begin{bmatrix} r_o \\ 0 \\ 0 \end{bmatrix}. \tag{4.15}$$

The displacement vectors in the local frame were computed from the GPS phase differences by equation (4.7). Equation (4.15) describes how these components are related to the spacecraft attitude. In particular, the ${}^{L}C^{H}$ matrix is a function of the orientation of the angular momentum vector, and ${}^{H}C^{B}$ is a function of the nutation angle, as well as the body and inertial nutation rates.

The following section discusses a simple method to estimate the elements of ${}^{L}C^{H}$ from the cross products of the $\vec{\delta r}(t_i)$ values. Section 4.5 describes a frequency domain technique that determines the frequencies in (4.15) as well as the nutation angle and ${}^{L}C^{H}$. Section 4.7 shows a time domain method to compute ω_p and θ.

4.4 Orientation of the Angular Momentum Axis from Displacement Vector Cross Products

Ideally, a spinning satellite is rotating perfectly about its rotation axis (i.e. no nutation) which will also be its angular momentum axis. A GPS antenna located on one face of the satellite will rotate in a plane perpendicular to this axis. The displacement vector of the moving antenna will be in this plane. Taking the cross products of two of these vectors will yield a vector with the same orientation as the angular momentum axis given by

$$\hat{H} = \frac{\vec{\delta r}(t_i) \times \vec{\delta r}(t_{i+k})}{\left|\vec{\delta r}(t_i) \times \vec{\delta r}(t_{i+k})\right|} \tag{4.16}$$

Because the GPS measurements are taken in the local frame, $\hat{H}$, will be computed in the local frame. As a result, $\hat{H}$, defines the orientation of the satellite in the local frame.

When nutation is introduced, the cross product of two successive displacement vectors is not the orientation of $\hat{H}$. However, as the satellite's instantaneous spin axis rotates about $\hat{H}$, the average of all the vectors formed from these cross products will tend towards the actual orientation $\hat{H}$. This is given by

$$\hat{H} = \frac{1}{N}\sum_{i=1}^{N} \frac{\vec{\delta r}(t_i) \times \vec{\delta r}(t_{i+k})}{\left|\vec{\delta r}(t_i) \times \vec{\delta r}(t_{i+k})\right|} \tag{4.17}$$

where N is the number of measurements.

4.5 Modal Analysis Techniques

From equations (4.12), (4.13), and (4.14) we see that the displacement vector is comprised of terms containing the sines and cosines of ψ and ϕ. From equation (4.15) it can be seen that only the first column of ${}^{H}C^{B}$ is required. Since the angle ψ rotates at ω_p and ϕ rotates at ω_l, the sine and cosine products will cause oscillations at $\omega_l \pm \omega_p$. The $\sin\psi$ term in the last row will cause an oscillation at ω_p. Thus, three frequencies can be determined from the displacement vector components. Two methods for extracting the desired frequencies are described in this section.

4.5.1 FFT Method

To determine the modal frequencies and modal amplitudes of a signal the following steps are applied:
1) Apply an FFT algorithm to the sampled signal data.
2) Compute the power spectral density (PSD) of the transformed data in step 1.
3) Identify the peaks of the PSD.
4) Determine the frequency at which each peak occurs.
5) Relate these frequencies back to a kinematic model.

Using only the PSD values, the frequencies found in step 4 are the most likely estimate (MLE) of each signal mode. Ideally, they are the exact frequencies of the modes. However, the sampling properties of the signal can lead to errors.

Ideally, the signal should be sampled so that the modal frequencies are integer multiples of the frequency bin. The frequency bin size is determined from dividing the sample frequency by the number of data points.

In reality, however, the peaks of the PSD occur in the frequency bins that are closest to the correct modes. The signal power of each mode is spread over a range of frequency bins surrounding the correct frequency. In order to determine a better estimate, the frequency center of the bins are computed by weighting them according to their power. Additionally, increasing the sample size increases the resolution of each bin.

Another problem that degrades the determination of the modal frequencies is noise in the signal. For the ideal sampling case, this is not a problem if the signal power is significantly larger than the noise level. The frequency of each mode still occurs exactly at one bin. For the non-ideal sampling case, there are some additional effects. When bin weighting is used, extra power due to noise contained in these surrounding bins causes the estimation of the frequency center to be less accurate.

One way to decrease the effect of noise is to use a window function on the data. Ideally, the most accurate FFT would be of an infinite length of data, however, in reality a finite set of data has to be used. Mathematically, this appears as an abrupt change from some sampled data value to an infinite number of zeros. This has the effect of amplifying the noise. If a window function is applied to the data, this abrupt change is smoothed and the effect of noise is decreased.

In the implementation of an FFT algorithm there are no assumptions about the structure of the signal. In other words, the FFT can be applied to any type of signal. There are other frequency estimation methods which can take advantage of the knowledge of the signal's structure. The next section discusses one of these methods called the auto regressive or AR method.

4.5.2 AR Method

In general, a discrete-time process can be well approximated by a time series or rational transfer function model [6]. If it is modeled as an AR process of order p, the sampled data can be represented by the recursive difference relation

$$x[n] = -\sum_{k=1}^{p} a[k]\, x[n-k] + u[n] \tag{4.18}$$

where the coefficients $a[k]$ are estimated from the sampled data. Taking the Z-transform of (4.18) yields the trans-

fer function

$$\frac{X(z)}{U(z)} = \frac{1}{P(z)} \tag{4.19}$$

where

$$z = \exp(j2\pi fn) \tag{4.20}$$

and

$$P(z) = 1 + \sum_{k=1}^{p} a[k]\, z^{-k}. \tag{4.21}$$

From the estimated a[k] in (4.18) the roots of P(z) are found from (4.21). The roots occur in complex conjugate pairs and lie on a unit circle at angles corresponding to the sinusoidal frequencies $\tilde{f}_k$, where

$\tilde{f}_k = \frac{f_k}{f_s}$ are the normalized sinusoidal frequencies

and

f_s is the sample frequency in Hertz.

This is illustrated in Figure 3. It should be noted that this technique directly estimates the frequencies $\tilde{f}_k$, therefore it

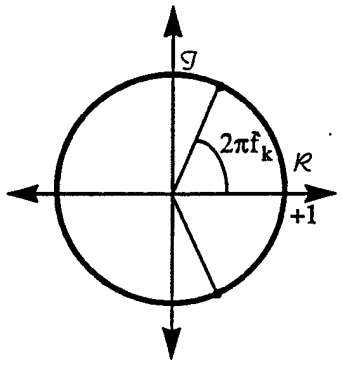

Figure 3. Relationship between signal frequency and transfer function poles.

does not depend on the modal frequencies being multiples of the frequency bins.

Ideally for the case where there is no noise and the signal is perfectly modeled by (4.21), the signal is assumed to be composed of exactly 2p sinusoids. This means that each pole of (4.19) lies exactly on the unit circle at the exact angle of $2\pi\tilde{f}_k$.

For the non-ideal case, however, there is noise and the signal can not be perfectly modeled by (4.21). To take into account the noise, a higher order model than 2p is used. This allows for the power contained in the noise to be spread among the non-modal frequencies. The poles of (4.19) corresponding to the modes now lie near the unit circle, while the poles corresponding to the noise lie farther away. The angles of the poles are only approximately equal to $2\pi\tilde{f}_k$. As the model order is increased, there are more frequencies available for the noise. As a result, the poles for the modal frequencies get closer to the unit circle and the angles get closer to $2\pi\tilde{f}_k$. If the model order is too high spurious frequencies might become dominant. This is illustrated in Figure 4.

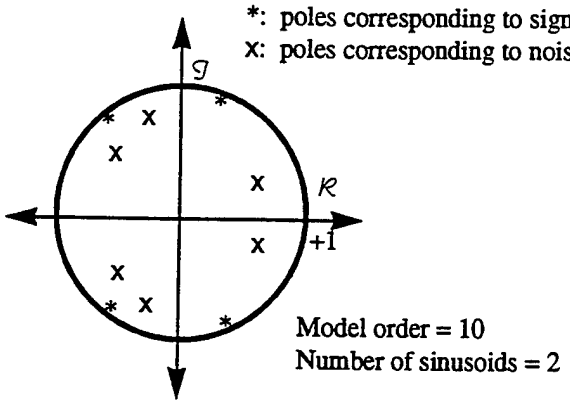

Figure 4. The Pole - Frequency relationship for a noisy sampled signal.

4.5.3 Application of Modal Analysis to Spinning Satellites

The modal analysis methods as described in the last section can be used to determine the frequencies associated with a spinning satellite and to determine its attitude. The components of the antenna displacement vectors oscillate according to the kinematic model illustrated in Figure 2. The frequency estimation techniques can be applied to the antenna displacements. The dominant frequencies as found from the FFT or AR methods correspond to the frequencies contained in the model. After the frequencies are computed, other techniques can be used to determine the elements of the attitude matrix. The next section describes the application of the frequency and amplitude estimation methods.

4.5.4 Application of Frequency Estimation Techniques to the Spinning Satellite Model

There are three frequencies contained in (4.15):

1) $f_d = f_l - f_p$,

where $f_l = \frac{\omega_l}{2\pi}$ and $f_p = \frac{\omega_p}{2\pi}$,

3) f_p,

and

4) $f_t = f_l + f_p$.

Applying an FFT algorithm to observations computed by (4.7) yields a PSD with spikes at these three frequencies. Applying the AR method to (4.7) yields three pairs of complex roots of (4.19). The positive angles on the unit circle are

$$\frac{2\pi f_d}{f_s}, \frac{2\pi f_p}{f_s}, \text{ and } \frac{2\pi f_t}{f_s}.$$

4.5.5 Attitude and Nutation Angle Estimation

The technique for attitude estimation involves first reformulating the right hand side of equation (4.15) into the product of a constant element matrix, an oscillatory one, and the constant r_o.

$$\vec{\delta r}(t_i) = AB(t_i)\, r_o \tag{4.22}$$

where A is 3 x 5 matrix given by

$$A = \begin{bmatrix} a_{11} & -a_{11}c\theta & a_{12} & a_{12}c\theta & a_{13}s\theta \\ a_{21} & -a_{21}c\theta & a_{22} & a_{22}c\theta & a_{23}s\theta \\ a_{31} & -a_{31}c\theta & a_{32} & a_{32}c\theta & a_{33}s\theta \end{bmatrix} \tag{4.23}$$

and a_{ij} are the nine elements of ${}^{L}C^{H}$. Matrix B is a 5 x 1 matrix composed of the sines and cosines of ψ and ϕ given by

$$B(t_i) = \begin{bmatrix} c\psi(t_{i+k})\, c\phi(t_{i+k}) - c\psi(t_i)\, c\phi(t_i) \\ s\psi(t_{i+k})\, s\phi(t_{i+k}) - s\psi(t_i)\, s\phi(t_i) \\ c\psi(t_{i+k})\, s\phi(t_{i+k}) - c\psi(t_i)\, s\phi(t_i) \\ s\psi(t_{i+k})\, c\phi(t_{i+k}) - s\psi(t_i)\, c\phi(t_i) \\ s\psi(t_{i+k}) - s\psi(t_i) \end{bmatrix} \tag{4.24}$$

where ψ and ϕ are found by equations (4.13) and (4.14) respectively.

The elements of A can be estimated using the following steps:

1) Collect a batch of data and apply (4.7) to get $\vec{\delta r}(t_i)$ at time i = 1, 2, 3, . . . N, where N is the number of measurement times;
2) Estimate the three frequencies using either the FFT or AR method;
3) Using these estimated frequencies accumulate the 5xN matrix

$$\beta = \left[B(t_1)\ B(t_2)\ \ldots\ B(t_N)\right]; \tag{4.25}$$

4) Form the 3xN matrix

$$\Lambda = \left[\vec{\delta r}(t_1)\ \vec{\delta r}(t_2)\ \ldots\ \vec{\delta r}(t_N)\right] \tag{4.26}$$

5) Solve for A by

$$A = \Lambda\beta^{T}(\beta\beta^{T})^{-1}. \tag{4.27}$$

4.6 Approximation of Instantaneous Angular Velocity

As an alternative to determining the angular rates based on frequency domain techniques, we can develop a model based on the approximation of the instantaneous angular velocity. Every two successive positions of a rotating antenna creates an angle with the spin axis that can be used for this approximation. This angle shown in Figure 5 can be computed by

$$\alpha = 2\text{asin}\left(\frac{\frac{1}{2}|\vec{\delta r}|}{r_o}\right) \tag{4.28}$$

where $r_o = |\vec{r}|$. If we define the mean angular rate ω^* by

$$\omega^* = \frac{\alpha(t_i)}{\Delta t} \tag{4.29}$$

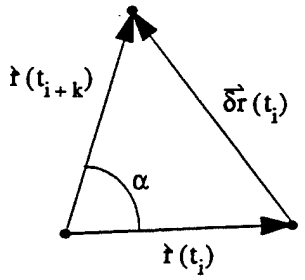

Figure 5. Angular displacement.

where $\Delta t = t_{i+k} - t_i$ and define the rate of change of the antenna position with respect to the local frame expressed in the local frame by

$$(\dot{\vec{r}})^L \equiv \frac{\vec{dr}}{dt}, \tag{4.30}$$

then as $\Delta t \rightarrow 0$ we can say

$$\omega^* \approx \frac{1}{r_o}\left|\frac{\vec{dr}}{dt}\right| . \tag{4.31}$$

In general

$$\dot{\vec{r}}^L = \dot{\vec{r}}^B + {}^B\omega^L \times r \tag{4.32}$$

and if (4.32) is expressed in the body frame then $\dot{\vec{r}}^B = 0$ and

$$(\dot{\vec{r}})^B = [\times {}^B\omega^L]\dot{r}^B . \tag{4.33}$$

Taking the magnitude of the right hand side of (4.33) and using (4.31) we get

$$\omega^* = \frac{1}{r_o}\left|\begin{bmatrix} 0 & -\omega_3 & \omega_2 \\ \omega_3 & 0 & -\omega_1 \\ -\omega_2 & \omega_1 & 0 \end{bmatrix}\dot{r}^B\right| \tag{4.34}$$

where ω_1, ω_2, and ω_3 are the angular rates about the body axis and

$$\omega = \sqrt{\omega_1^2(t_i) + \omega_2^2(t_i) + \omega_3^2} . \tag{4.35}$$

Since

$$\dot{r}^B = \begin{bmatrix} r_o \\ 0 \\ 0 \end{bmatrix},$$

the equation for ω^* can be reduced to

$$\omega^* = \sqrt{\omega_2^2 + \omega_3^2}\,. \tag{4.36}$$

The equations of motion for the spinning satellite written in terms of ω_1, ω_2, and ω_3 are

$$\dot{\omega}_1 = \left(1 - \frac{I_s}{I_t}\right)\omega_2\omega_3\,, \tag{4.37}$$

$$\dot{\omega}_2 = -\left(1 - \frac{I_s}{I_t}\right)\omega_2\omega_3\,, \tag{4.38}$$

and

$$\dot{\omega}_3 = 0\,. \tag{4.39}$$

The solution to this set of differential equations is

$$\omega_1(t_i) = \omega_T \cos\omega_p(t_i - t_0)\,, \tag{4.40}$$

$$\omega_2(t_i) = -\omega_T \sin\omega_p(t_i - t_0)\,, \tag{4.41}$$

and

$$\omega_3 = \frac{\omega_p}{\left(1 - \frac{I_s}{I_t}\right)} \tag{4.42}$$

where $\omega_T = \sqrt{\omega_1^2(t_i) + \omega_2^2(t_i)}$.

Looking at (4.36) and (4.41), it can be seen that ω^* oscillates according to ω_p. Its minimum value is ω_3 and its maximum value is ω. For a nutation angle of zero, equations (4.9), (4.10), and (4.42) can be combined to show that $\omega=\omega_3=\omega^*$. As a result, for small nutation angles, ω can be approximated by the average of the ω^* computed from the displacement vectors. Furthermore, if an accurate value of the satellite's inertia ratio is known, an estimate of ω_p and ω_l can also be found.

4.7 Nutation Angle Filter

The nutation angle filter is a Kalman filter that uses the GPS antenna displacement vectors to estimate the nutation angle θ, the angular rate of the antenna about the body z^B-axis, ω_p, and the initial phase about the z^B-axis, ψ_o. A graphical representation of these states is shown in Figure 6.

4.7.1 Equations of motion

In the absence of external torques and nutation damping, the rate of change for each of the states is zero. The case involving passive nutation damping has been examined, but for typical damping time constants of hours the rate of change can still be considered zero for short time spans.

4.7.2 Observation Equation

The observation for the nutation angle filter is derived by rotating the displacement vector into the angular moment frame, scaling it by the radius of the satellite, and taking the third component.

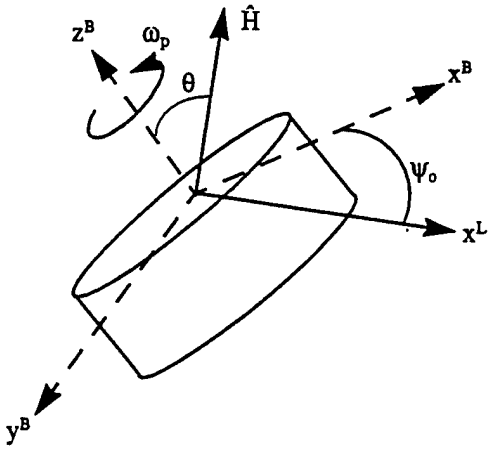

Figure 6. Filter states.

$$(\vec{\delta r}')^H = \begin{bmatrix} \delta x' \\ \delta y' \\ \delta z' \end{bmatrix}^H = \frac{{}^H C^L (\vec{\delta r})^L}{r_o} \tag{4.43}$$

Expanding the $\delta z'$ component of $\vec{\delta r}'$ yields

$$\delta z' = s\theta(t_{i+k})\, c\psi(t_{i+k}) - s\theta(t_i)\, c\psi(t_i) \tag{4.44}$$

where

$$\psi(t) = \omega_p(t)t + \psi_o . \tag{4.45}$$

4.8 Simulation

A computer simulation was set up to generate GPS measurements for a comparison by these various methods. The program simulated $\Delta\phi$ measurements from two antennas on a spinning satellite. Gaussian noise with a mean of zero and a standard deviation of 5 mm was added to each $\Delta\phi$ measurement. Two nutation angle cases were examined. Table 1 shows the parameters used for the simulation.

Table 1. Simulation parameters.

Satellite radius	0.381 m
Nominal spin rate (ω)	5 rpm
Inertia ratio $\left(\frac{I_s}{I_t}\right)$	1.3
Nutation angles	5 and 25 degrees
Batch lengths	30, 100, and 400 seconds
Sample frequency	2 Hz
Differencing Interval	5 seconds (i.e. k = 10)

4.8.1 Frequency Estimation

The body and inertial nutation rates were estimated using the FFT and AR frequency domain techniques, using the averaging of ω^*, and using the nutation filter. The nutation filter, however, was only used to estimate ω_p. The results for each nutation angle are shown in Tables 2 and 3. The estimated frequencies are given to four decimal places. This degree of precision is required in the next section for adequate attitude estimation when using the batch least squares

technique.

Table 2. Frequency estimation for $\theta = 25$ deg.

Method	30 second batch		100 second batch		400 second batch	
	ω_l (rad/s)	ω_p (rad/s)	ω_l (rad/s)	ω_p (rad/s)	ω_l (rad/s)	ω_p (rad/s)
True Value	0.6423	-0.1343	0.6423	-0.1343	0.6423	-0.1343
AR	0.6424	-0.1344	0.6422	-0.1343	0.6424	-0.1344
FFT	0.5821	-0.0748	0.6416	-0.1331	0.6424	-0.1340
Average ω^*	0.6088	-0.1405	0.6071	-0.1401	0.6073	-0.1403
Nutation filter		-0.1415		-0.1342		-0.1343

Table 3. Frequency estimation for $\theta = 5$ deg.

Method	30 second batch		100 second batch		400 second batch	
	ω_l (rad/s)	ω_p (rad/s)	ω_l (rad/s)	ω_p (rad/s)	ω_l (rad/s)	ω_p (rad/s)
True Value	0.6789	-0.1561	0.6789	-0.1561	0.6789	-0.1561
AR	0.6760	-0.1530	0.6779	-0.1550	0.6794	-0.1565
FFT	no solution	no solution	0.6473	-0.1226	0.6795	-0.1562
Average ω^*	0.6780	-0.1565	0.6748	-0.1557	0.6759	-0.1560
Nutation filter		-0.1488		-0.1605		-0.1556

The frequency domain techniques performed better with the large nutation angle. For the large angle case, the AR method performs very well with only a small batch size. The error is less 0.1% after 30 seconds. The FFT method, however, requires a larger batch size for comparable performance. The nutation angle filter also works well, but also requires more time to equal the performance of the AR method.

For smaller nutation angles, the accuracy of the frequency domain techniques gets worse. This is expected because the third term in the first column of (4.12), containing the ω_p frequency, approaches zero as the nutation angle goes to zero. Both the AR and FFT methods require a larger batch size to match the results shown for the large angle. A 100 second batch is needed before the AR errors are under one percent. The FFT does not produce meaningful results with a 30 second batch and it achieves errors less than one percent with the 400 second batch. The nutation filter, however, shows only a small drop in performance for the small angle case.

The approximation involved in computing the value of ω^* is worse for larger nutation angles. This shows up in the results in determining frequencies for large and small nutation. For small angles, the estimations are comparable to the other methods. For large angles, they are much worse. The 100 second batch produced errors around five percent for the 25 degree nutation angle, while the errors were less than one percent for the 5 degree angle. It should also be noted that this technique is dependent on an accurate knowledge of the satellite's inertia values.

4.8.2 Attitude Estimation

The orientation of the angular momentum axis was estimated using the batch least squares method in section 4.5.5 and using the averaging of the displacement vector cross products described in section 4.4. Tables 4 and 5 show results for each nutation angle. Figures 7 and 8 show a time history for the cross product method of estimation.

The batch least squares method shows its best performance for the larger nutation angle. Results improve with a larger batch size. This is most likely due to the increased accuracy of the frequency estimation as the batch size grows larger.

Table 4. Angular mom. axis estimation for $\theta = 25$ deg.

Method	$\hat{H}$ pointing error (deg)		
	30 s	100 s	400 s
Batch least squares	0.42	0.26	0.13
$\vec{dr}$ cross products	0.98	0.35	0.17

Table 5. Angular mom. axis estimation for $\theta = 5$ deg.

Method	$\hat{H}$ pointing error (deg)		
	30 s	100 s	400 s
Batch least squares	0.53	0.31	0.16
$\vec{dr}$ cross products	0.13	0.13	0.11

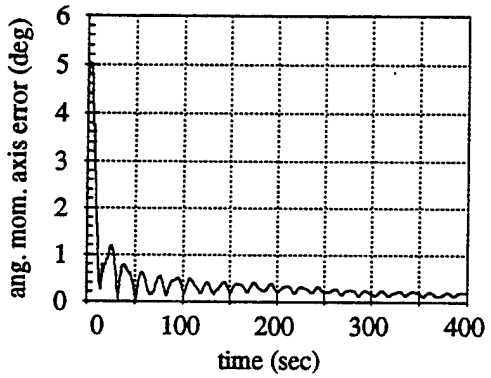

Figure 7. Cross product axis estimation for $\theta = 25$ deg.

The cross product method does better for small angles. As the nutation angle becomes larger, the approximation that equation (4.16) is correct gets worse. As more cross products are added to the average in equation (4.17), the estimate improves. For small angles the approximation improves very quickly. This is demonstrated in Figures 7 and 8. The frequency of the bumps in the graphs is approximately equal to $\frac{\omega_I - \omega_P}{2}$.

4.8.3 Nutation Angle Estimation

The nutation angle θ was estimated using the method of batch least squares and the nutation angle filter. Tables 6 and 7 show results for each nutation angle. Figures 9 and 10 show a time history of the nutation angle estimation from the nutation angle filter.

As with the angular momentum axis determination, the batch least squares technique for determining the nutation angle worked best with large angles. However, large batch sizes did not show an increase in accuracy. Several other cases with batch sizes between 30 and 400 seconds showed about a 10% fluctuation in the error. For small angles the batch size did make a significant difference. The small batch case failed to provide a meaningful result. The 100 second size batch still had a 3 degree error. Even with the largest batch the error was still 1.6 degrees.

The nutation filter, on the other hand, worked well with both nutation angles. In both cases the error was under

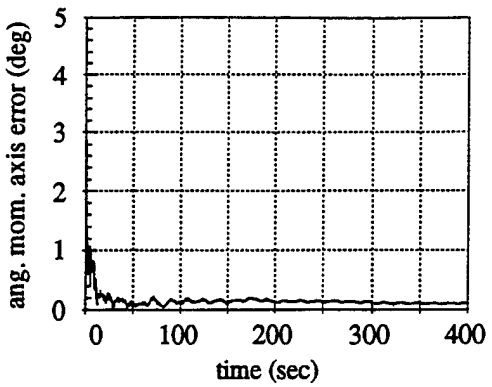

Figure 8. Cross product axis estimation for θ = 5 deg.

Table 6. Nutation angle estimation for θ = 25 deg.

Method	θ (deg)		
	30 s	100 s	400 s
True value	25.00	25.00	25.00
Batch least squares	27.94	25.43	27.48
Nutation filter	20.98	24.38	24.91

Table 7. Nutation angle estimation for θ = 5 deg.

Method	θ (deg)		
	30 s	100 s	400 s
True value	5.00	5.00	5.00
Batch least squares	no sol.	2.02	6.65
Nutation filter	4.23	4.79	5.04

ten percent in about 40 seconds and steadily improved afterwards.

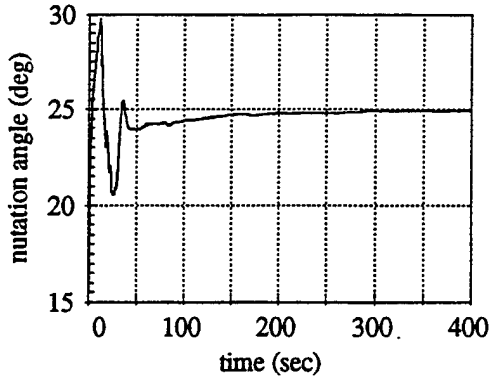

Figure 9. Nutation filter estimation for θ = 25 deg.

4.9 Conclusions

A comparison of several methods for GPS based attitude determination of a spinning satellite has been presented.

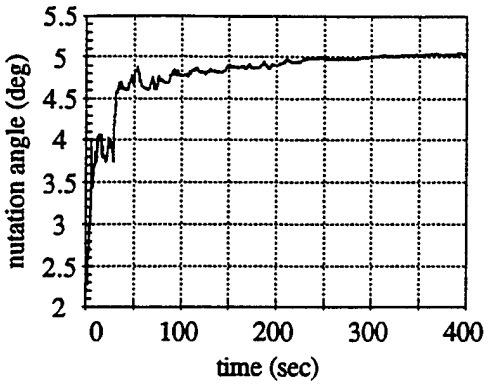

Figure 10. Nutation filter estimation for $\theta = 5$ deg.

For large nutation angles the frequency domain techniques, especially the AR method, offer a way to estimate the spin frequencies with a high degree of accuracy. The computationally simpler method of averaging ω^* is not that accurate. The accuracy of the nutation filter is comparable only after a long period of time.

For small nutation angles, on the other hand, the frequency domain techniques require a much greater batch size to achieve a certain level of accuracy. The averaging of ω^* works much better and quickly gets a high level of accuracy but it requires knowledge of the inertias. The nutation filter still requires a longer time than the AR method to achieve a certain level of accuracy.

For large nutation angles both the batch least squares and cross product methods have comparable accuracy in estimation of attitude. The batch least squares is better with small batch sizes. The cross product method, however, is much simpler and its accuracy quickly improves. For small angles, the cross product method is very accurate with only a small amount of data.

The nutation filter is the only one of the two methods to give a very accurate estimation of the nutation angle. For both small and large angles, the percentage error is about the same for a given length of time.

The performance of these methods appears more than adequate to meet the requirements of an inexpensive satellite mission. The SNOE satellite has a pointing requirement of ± 5 deg and spin rate requirement of ± 1 rpm [1]. This level of precision is well with the levels shown in this section. For the typical time scales of hours, the techniques have more than enough performance for an accurate estimation of the satellite's parameters. After only one minute of data collection and processing, the pointing error is below one degree and the angular rate errors are below one percent.

4.10 Future plans

To further assess the usefulness of these methods, experimental data is required. Future test plans include mounting a GPS receiver on a spinning platform. The platform will have the ability to simulate the kinematics of a spinning satellite for a range of frequencies and nutation angles. Another area for further investigation includes the development of a more robust method to determine the correct frequencies from the AR method. We hope to implement the proposed approaches on a future satellite mission. The ultimate goal is closed loop attitude control based on GPS data from an antenna on a spinning spacecraft.

References

[1] Barth, C. A., S.C. Solomon, D.W. Rusch, and T. N. Woods, "Student Nitric Oxide Explorer", Investigation and Technical Plan - Proposal to the Universities Space Research Association Student Explorer Demonstration Initiative, from the Laboratory for Atmospheric and Space Physics, University of Colorado, 1994.

[2] Ward, L.M. and P. Axelrad, "Spacecraft Attitude Estimation Using GPS: Methodology and Results for RADCAL," ION National Technical Meeting, Anaheim, CA, 813-825, January 1995.

[3] Lightsey, E.G., C.E. Cohen, W.A. Fees, B.W. Parkinson, "Analysis for Spacecraft Attitude Measurements Using Onboard GPS," AAS Guidance and Control Conference, Keystone, CO, Feb. 1994, pp. 521-532.

[4] Brock, J. K., R. Fuller, B. Kemper, D. Mleczko, J. Rodden, and A. Tadros, "GPS Attitude Determination and Navigation Flight Experiment," To Be Given at Proceedings of ION GPS-95, Palm Springs, California, Sept 12-15 1995.

[5] Martin-Niera, M. and R. Lucas, "GPS Attitude Determination of Spin Stabilized Satellites," Proceedings of ION GPS-92, Albuquerque, New Mexico, Sept 16-18, 1992.

[6] Kay, Steven M., *Modern Spectral Estimation Theory & Application*, Prentice Hall, 1988.

[7] Hofmann-Wellenhof, B., H. Lichtenegger, and J. Collins, *GPS Theory and Practice*, Springer-Verlag Wien, 1992.

[8] Wertz, James R., ed., *Spacecraft Attitude Determination and Control*, D. Reidel Publishing Company Library in Astrophysics and Space Science, 1978.

[9] Cohen, Clark E., *Attitude Determination Using GPS*, Phd. Dissertation, Department of Aeronautics and Astronautics, Standford University, Dec. 1992.

1.0 OVERVIEW

This report describes the research performed by the Colorado Center for Astrodynamics Research during the second half of FY'94-95 on spacecraft attitude determination using GPS. The work is a continuation of research described in the first and second technical reports for FY'93-94 [1,2] and the first technical report for FY'94-95 [3].

The overall project encompasses various methods for using GPS to determine the attitude of a spacecraft in near Earth orbit. The specific topics covered in this technical report are a combined Kalman filter for both attitude and baseline estimation, an adaptive estimation algorithm to be used for multipath mitigation, and experimental and simulation results for GPS on a ground based spinning platform.

The highlights of the technical advances made during the second half of FY'94-95 are as follows:

- Development of a Kalman filter for combined attitude, line bias, and baseline estimation.
- Evaluation of the combined filter on simulated and RADCAL data.
- Development of an algorithm combining an adaptive notch filter approach for frequency identification and adaptive least squares for amplitude and argument estimation for use in multipath mitigation.
- Evaluation of the adaptive estimation technique on simulated and experimental multipath data.
- Collection of GPS experimental data on a spinning platform at Maryland Point.
- Preliminary analysis of spin data demonstrating frequency domain techniques.

Section 2 describes the new combined filter methodology including motivation for its use. Results are presented for both simulated and RADCAL data and comparisons are made between the new formulation and results from the previously developed bootstrapping algorithms. The baseline estimation results from the two methods are quite comparable. The attitude-only filter works better than the combined filter when the baseline estimates are already known to better than a few millimeters. The combined filter has the potential to work well when the true baselines are varying due to vehicle flexure. Plans for future work in this area are provided.

Section 3 presents detailed algorithms for an infinite impulse response (IIR) adaptive notch filter (ANF) for frequency estimation and an adaptive least squares (ALS) algorithm for determination of signal amplitude and argument. These techniques are combined to form a robust estimator of signal-to-noise ratio (SNR) fluctuations due to multipath. The combined algorithm is demonstrated to be able to reproduce fluctuations in both simulated and experimental SNR data. The next step in this area is to map the constructed SNR profiles to phase difference corrections.

Section 4 describes an experiment conducted to investigate algorithms for determination of attitude of a spinning platform. A Trimble Vector receiver was mounted on a platform atop

the NRL spin table located at Maryland Point, and raw GPS phase differences were collected. This section provides preliminary results of the experiment including a frequency domain analysis of the data. Suggestions for future work are given.

[1] Axelrad, P., C.P. Behre, C.J. Comp, and L.M. Ward, "GPS Based Spacecraft Attitude Determination", FY'93-94 Technical Report I to the Naval Research Laboratory, May 16, 1994.

[2] Axelrad, P., B.C. Chesley, C.J. Comp, and L.M. Ward, "GPS Based Spacecraft Attitude Determination", FY'93-94 Technical Report II to the Naval Research Laboratory, October 16, 1994.

[3] Axelrad, P., C.P. Behre, C.J. Comp, and L.M. Ward, "GPS Based Spacecraft Attitude Determination", FY'94-95 Technical Report I to the Naval Research Laboratory, October 6, 1995.

2.0 GPS Based Attitude and Baseline Estimation

Lisa M. Ward

2.1 Introduction

A number of algorithms for GPS-based attitude determination have been developed, studied, and presented in the previous reports to NRL [1], [2], [3], and [4]. Until now, the emphasis has been on a bootstrapping method that begins with rough estimate of vehicle attitude and antenna locations and uses the algorithms sequentially to work up to a highly accurate solution. Presented here is an algorithm that combines some of these steps into one algorithm: the combined attitude-baseline filter.

The next section of this report reviews the original bootstrapping algorithms and describes the utility of the combined filter. Section 2.3 gives a complete discussion of the methodology for the combined attitude-baseline filter. Results from the new filter are presented in Section 2.4. And finally, conclusions and suggestions for future work are given in Section 2.5.

2.2 Review of Bootstrapping Process

Given a rough estimate of vehicle attitude and antenna locations, we have enough information to start the bootstrapping process. The first step is the attitude initialization algorithm which resolves integer ambiguities and improves the attitude estimate to with 10 degrees. This algorithm is a least squares batch process that uses a simplified dynamical model which assumes that the rotation of the vehicle is constant in the orbit local frame.

If the antenna locations in the vehicle frame are not accurately known (i.e. to within 3 mm), the next step in the bootstrapping process is the baseline estimation algorithm. This algorithm is a sequential filter that estimates the baselines in the orbit local frame. Then using the local baseline estimates, the local-to-body transformation is defined. The local baselines are converted to the body frame and averaged over time to obtain the best estimate.

After determining an initial attitude estimate and obtaining accurate baseline estimates, an extended Kalman filter is used for ongoing attitude determination. The attitude filter combines GPS measurements and dynamic information to accurately estimate the spacecraft attitude, angular velocity, disturbing torques, and line biases.

If the above two steps could be combined into one algorithm, this would simplify and streamline the bootstrapping method by simultaneously estimating he attitude and baseline states. In past studies we found that estimating attitude along with the three coordinates for each baseline does not provide enough observability to distinguish attitude errors from baseline errors. However, reducing the number of baseline parameters to estimate provides the necessary observability. The approach we employ here is to fix baselines in the body frame by estimating only six baseline parameters.

2.3 Combined Filter Methodology

In GPS based attitude determination, all knowledge of the body frame is completely derived from the baseline positions and their relationship with the body frame. Since the attitude

solution is simply the transformation between the body frame and some other frame of reference, accurate knowledge of of the baseline positions in the body frame is paramount.

If the baseline positions are not well known in the body frame, they need to be estimated. The baseline estimator presented in [3] is one way of accomplishing this. The disadvantage of using this type of baseline only estimator is that no attitude knowledge is produced. On the other hand, estimating the attitude along with all three coordinates of each baseline vector causes a number of other problems. First, by estimating all baseline coordinates we are, in effect, estimating the body frame itself. As the baseline estimates vary, so does the definition of the body frame. And without a clear definition of the body frame we don't really know what rotation the attitude represents. Second, the attitude and baseline errors are not distinguishable from one another (to the first order). This can cause the filter to make corrections to the wrong state which will eventually lead to filter divergence.

To avoid these problems we have developed a method of that fixes the definition of body frame and allows for a reduced set of baseline parameters to be estimated. The procedure is to define the body frame (B) using components of baseline 1 and baseline 2 (denoted $\mathbf{b}_1$ and $\mathbf{b}_2$, respectively) as follows: The $\mathbf{j}_B$ vector is aligned with the direction of baseline 2. The $\mathbf{i}_B$ vector is aligned with the $\mathbf{b}_1 \times \mathbf{b}_2$ direction. And finally, the $\mathbf{k}_B$ vector completes the orthogonal triad. Then estimate the baseline coordinates that have not been used in the definition of the body frame. To summarize:

1. Estimate only the $\mathbf{j}_B$ coordinate of baseline 2. The other coordinates are assumed to be zero. By doing this, we fix the direction of baseline 2 and estimate only its length.
2. Estimate the $\mathbf{j}_B$ and $\mathbf{k}_B$ coordinates of baseline 1. This fixes the baseline in the $\mathbf{j}_B - \mathbf{k}_B$ plane.
3. Estimate all coordinates of baseline 3.

Based on the attitude filter presented in [4], an extended Kalman filter is used to estimate the vehicle attitude with respect to some orbit local frame (L) and the 6 baseline parameters described above. The remainder of this section describes the state vector, the measurement prediction equation, and the measurement gradient matrix needed to form the Kalman filter.

In this particular formulation, the state vector is given by:

$$\mathbf{x} = \left[\begin{array}{ccc|ccc|ccc|ccc|ccc|ccc} \delta q_1 & \delta q_2 & \delta q_3 & \delta\omega_1 & \delta\omega_2 & \delta\omega_3 & \delta\tau_1 & \delta\tau_2 & \delta\tau_3 & \delta b_{1y} & \delta b_{1z} & \delta b_{2y} & \delta b_{3x} & \delta b_{3y} & \delta b_{3z} & \delta\beta_1 & \delta\beta_2 & \delta\beta \end{array} \right. \tag{2.1}$$

where δ represents a correction the state and where

$$\begin{aligned} \mathbf{q} &= \text{local-to-body quaternion,} \\ \omega &= \text{inertial angular velocity vector,} \\ \tau &= \text{disturbing torque vector,} \\ b &= \text{baseline coordinate,} \\ \beta &= \text{line bias.} \end{aligned}$$

The GPS observable for attitude determination is the fractional difference in carrier phase across a baseline. The equation for the predicted phase difference for baseline i observing satellite j is

$$\Delta\hat{\phi}_{ij} = \left(\mathbf{b}_i^B\right)^T \left({}^B\hat{\mathbf{C}}_0^L \, \mathbf{e}_j^L\right) + \hat{\beta}_i - \hat{k}_{ij}, \tag{2.2}$$

where

$\Delta\phi$ = phase difference,
$\mathbf{b}^B$ = the baseline vector in body coordinates,
$\mathbf{e}^L$ = line-of-sight vector to the GPS satellite in local coordinates,
β = line bias,
k = integer ambiguity,
${}^B\hat{\mathbf{C}}_0^L$ = *apriori* estimate of local-to-body transformation matrix.

In the above equation $\hat{k}_{ij}$ is calculated by

$$\hat{k}_{ij} = \text{int}\left[\left(\mathbf{b}_i^B\right)^T \left({}^B\hat{\mathbf{C}}_0^L\,\mathbf{e}_j^L\right) + \hat{\beta}_i - \Delta\phi_{ij}\right] \tag{2.3}$$

where the **int** rounds to the nearest integer.

The measurement gradient $\mathbf{H}_{ij}$ for baseline i and satellite j has several different components. The part of $\mathbf{H}_{ij}$ corresponding to the quaternion states is

$$\frac{\partial(\Delta\phi_{ij})}{\partial(\delta\mathbf{q})} = 2\left({}^B\hat{\mathbf{C}}_0^L\,\mathbf{e}_j^L\right)^T \mathbf{B}_i^{\times}, \tag{2.4}$$

where $\mathbf{B}_i^{\times}$ is the cross product matrix associated with baseline $\mathbf{b}_i^B$. The measurement gradient component corresponding to the line bias β_i is 1. For the baseline states, the gradient matrix is not as straightforward. If all three elements for the baseline vector are being estimated, as is the case with baseline 3, then the corresponding $\mathbf{H}_{ij}$ components are simply

$$\frac{\partial(\Delta\phi_{ij})}{\partial(\delta\mathbf{b}_3)} = \left({}^B\hat{\mathbf{C}}_0^L\,\mathbf{e}_j^L\right)^T = \left(\mathbf{e}_j^{\hat{B}}\right)^T \tag{2.5}$$

On the other hand, if only one or two elements are being estimated, then the corresponding elements of Equation 2.5 are extracted. All other components are zero. For example, if baseline 1 observes satellite j, then the full gradient matrix is given by

$$\mathbf{H}_{1j} = \left[\; 2\left({}^B\hat{\mathbf{C}}_0^L\,\mathbf{e}_j^L\right)^T \mathbf{B}_1^{\times} \;\middle|\; 0\;\; 0\;\; 0 \;\middle|\; 0\;\; 0\;\; 0 \;\middle|\; \mathbf{e}_{jy}^{\hat{B}}\;\; \mathbf{e}_{jz}^{\hat{B}}\;\; 0\;\; 0\;\; 0\;\; 0 \;\middle|\; 1\;\; 0\;\; 0 \;\right]. \tag{2.6}$$

Between measurement epochs, the quaternion and angular velocity states are advanced to the current measurement time by numerically integrating the nonlinear equations of motion for a gravity gradient stabilized satellite. The derivatives of the disturbing torque and line biases, are equal to zero. The error covariance matrix is propagated forward with the state transition matrix derived from the linearized dynamical equations. All of these equations can be found in the NRL Report [4].

A new approach is being investigated for propagating the process noise covariance. Process noise values are set for the baseline, line bias and torque states, and the state transition matrix is used to compute the full discrete process noise matrix. This technique is still in the development stages and will be discussed more fully in the next report. Table 2.1 contains the process noise covariance values used for the results shown below.

Table 2.1: Process Noise Covariance for Combined and Attitude Filters

State	Process Noise	Units
radial torque	1×10^{-16}	$(\text{N}\cdot\text{m})^2$
normal, transverse torque	1×10^{-14}	$(\text{N}\cdot\text{m})^2$
line bias	1×10^{-9}	$(\text{cy})^2$
baseline coordinate b_{3x}	1×10^{-10}	$(\text{cy})^2$
other baseline coordinates	3×10^{-11}	$(\text{cy})^2$

2.4 Results for Combined Filter

The results from the combined attitude-baseline filter are presented in this section which is organized as follows: A description of the test data which includes both simulated data and flight data from RADCAL is given first. Then the results, which are separated in two parts, one for attitude solutions and another for baseline solutions, are shown next.

2.4.1 Test Data

Simulated differential phase data was produced by modeling a gravity-gradient symmetric satellite with a GPS receiver on board. The orbit was circular with an inclination of 82 degrees at an altitude of 834 km. The yaw rate of the vehicle was 10^{-3} radians/second. The pitch and roll oscillations peaked at 12.3 and 6.7 degrees, respectively. The simulation run was 8 hours in length with a measurement interval of 30 seconds. White measurement noise with a standard deviation of 1 cm was added to each differential phase measurement.

The RADCAL satellite is also a gravity-gradient symmetric satellite with a Trimble TANS Quadrex modified for attitude determination on board. The orbit is near-circular with an inclination of 90 at an altitude of 815 km. The data shown below was collected on 9 June 94 (denoted Day 160) and 8 July 94 (denoted Day 189). The measurement interval for both data sets is 30 seconds.

2.4.2 Attitude Results

The attitude solutions derived from the simulated data are shown in Figure 2.1. For this test the baseline estimates were initialized with a 1 cm error in each coordinate. The errors in the attitude solutions along with covariance bounds are shown in Figure 2.2. Notice that it takes about 3 hours for the solutions to converge, but once converged, the errors stay centered on zero.

Compare this to the results from the attitude-only filter shown in Figure 2.3. Again the baselines were initialized with a 1 cm error in each coordinate. With this algorithm, however, the baselines are not simultaneously estimated, but are fixed to the initial value. The baseline error produces an oscillation in the roll and pitch estimates. The yaw angle is not strongly affected because the baselines are perpendicular to the yaw axis. If the baselines were not coplanar, the errors in the yaw angle would oscillate as well. Of course, if the baselines are known and properly initialized, the attitude only filter works fine.

One point of concern is that the solution errors using both versions of the filter appear correlated. We believe this is due to the new process noise implementation. It does not seem to be adding enough process noise in the quaternion or angular velocity states. In the

future we plan to verify the validity of this implementation and see if anything additional can be done to correct the problem.

The root-mean-square (RMS) of the attitude errors for each case are given in Table 2.2. Two RMS values are reported: one using the errors after the filter has converged (after 3 hours), denoted *converged*, and the other using the errors in the entire data span, denoted *all*. Without baseline errors, that attitude filter works best, producing roll and pitch errors at the 0.30 degree level, RMS. When baseline errors are introduced, the attitude filter produces roll and pitch errors that are 1.75 and 1.95 times larger, respectively, than the errors produced by the combined filter.

Table 2.2: RMS of Attitude Errors

Filter Type	Initial Baseline Error	Data Span	RMS of Errors (deg)		
			yaw	roll	pitch
combined	1 cm	all	0.274	0.450	0.418
combined	1 cm	converged	0.272	0.323	0.320
attitude	1 cm	all	0.277	0.562	0.679
attitude	1 cm	converged	0.275	0.563	0.624
attitude	0 cm	all	0.269	0.302	0.364
attitude	0 cm	converged	0.269	0.278	0.302

The combined filter was also tested using the RADCAL data. For Day 160 the baselines were initialized from the mechanical drawings. Figure 2.4 shows the attitude solutions. This plot agrees closely with the results produced by the attitude filter using the baselines estimated from the baseline filter. However, since there is no truth reference for RADCAL, it is difficult to quantify which method works better in this case.

For Day 189, however, initializing the baselines to the mechanical drawings did not produce good results. The line biases and baselines converged to the wrong answer causing spurious attitude results. Recall that in our current algorithm the integers are recalculated at each measurement with the assumption that the combined error in the *apriori* estimate is less than an integer. Since this algorithm allows so many degrees of freedom, a large measurement error could cause an incorrect integer calculation without forming a large residual. Eliminating the recalculation by setting the integers to a fixed value should correct this problem. When the baselines were initialized closer the right answer, the combined filter worked well.

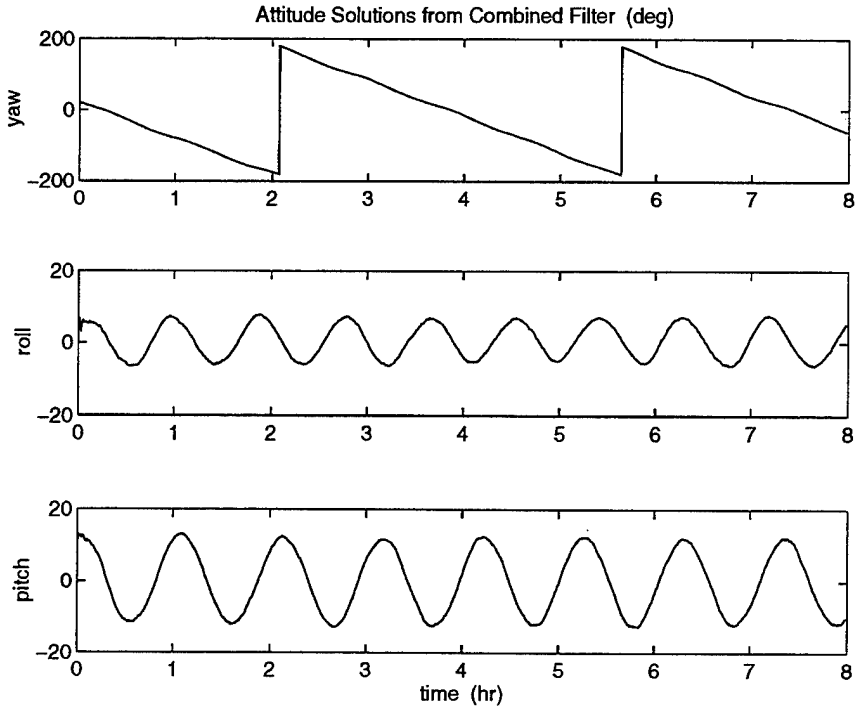

Figure 2.1: Attitude Solutions from Combined Filter for Simulated Data

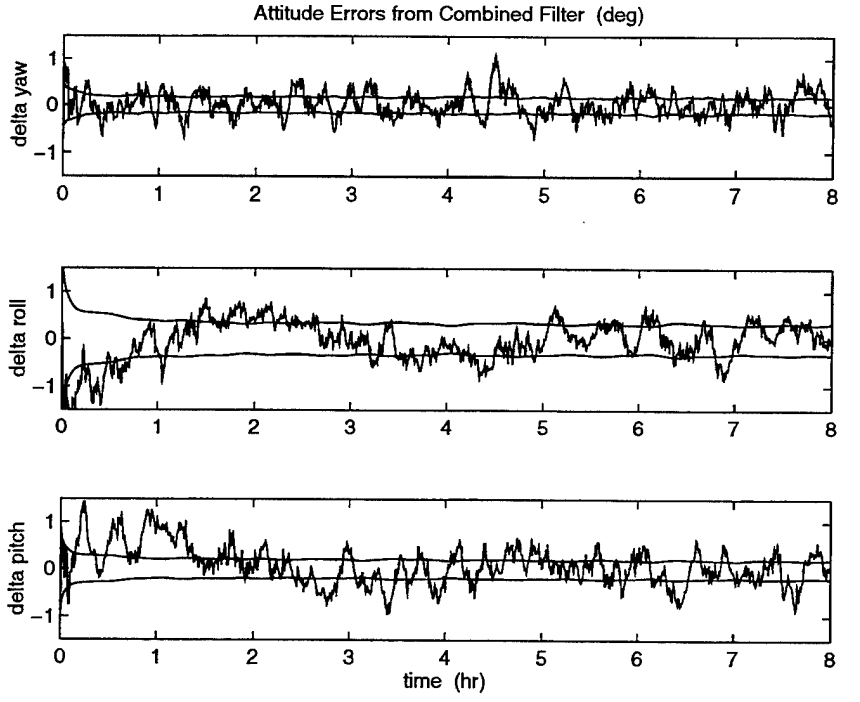

Figure 2.2: Attitude Errors from Combined Filter for Simulated Data

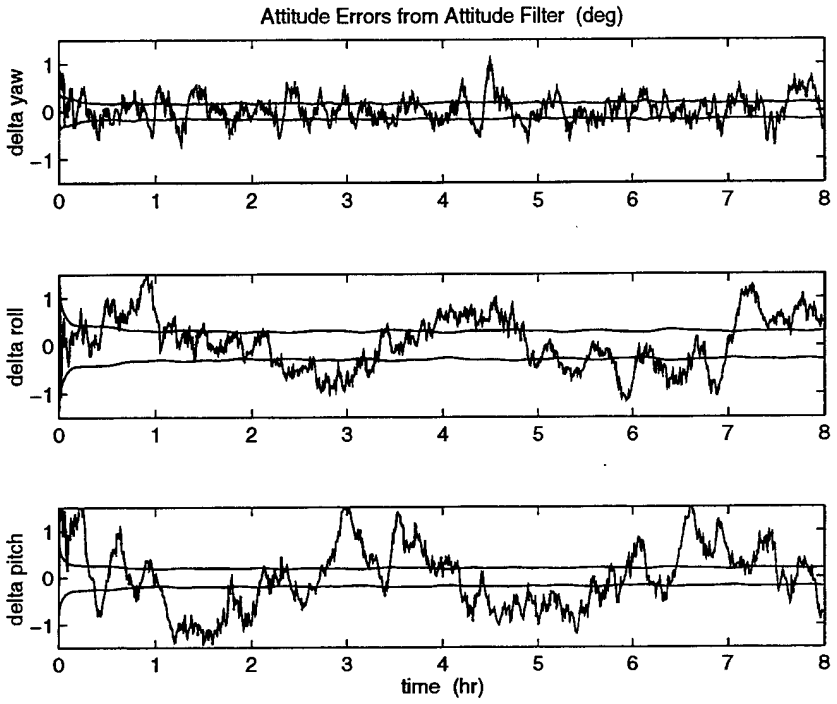

Figure 2.3: Attitude Errors from Attitude Filter for Simulated Data

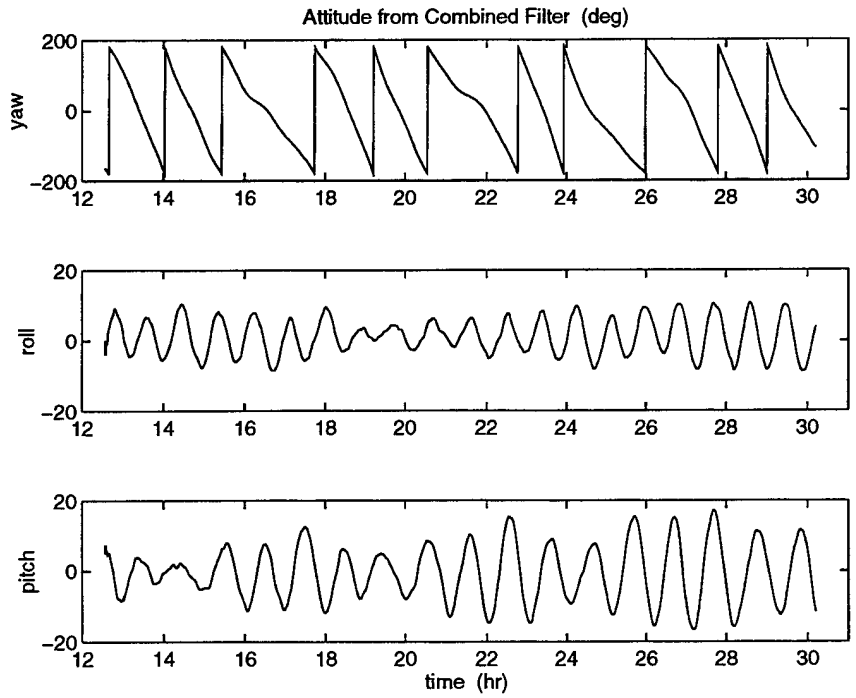

Figure 2.4: Attitude Solutions from Combined Filter for RADCAL Day 160

2.4.3 Baseline Results

Baseline errors from the combined filter using simulated data are shown in Figure 2.5. Plotted are the results for baseline 3. In the y and z components, the baseline errors are less than 1 mm after the filter has converged. However, the errors in x component are larger, up to 3 mm after convergence. Since the baselines lie mostly in the roll-pitch plane, this out-of-plane component is the most difficult to observe which accounts for the larger errors.

We also noted that, for the x component especially, the covariance bounds clamp down early on in the run and do not reflect how long it takes for the solutions to actually converge. In fact, the process noise for this coordinate was increased to spread out the covariance bounds, which should not be necessary. We suspect that there may be some coupling between the attitude and baseline errors that is not being accounted for. Perhaps the neglected second order terms in the measurement gradient matrix calculation are the source of this discrepancy.

Combined filter estimates for baseline 3 from RADCAL Day 160 are given in Figure 2.6. The estimates vary at about the 3 mm level and agree closely with the estimates for Day 189. While these variations seem reasonable, the covariance reported by the filter do not reflect fluctuations of this magnitude, but instead reflect fluctuations at the 0.5 mm level, 1-σ. Although this could be just a tuning error, it is more likely due to some type of dynamic mismodeling.

Despite these problems, the combined filter still works remarkable well. Table 2.3 contains a comparison of the baseline estimates from the combined filter and the baseline only filter. Results from both simulated and RADCAL data are compiled here. The true baselines used to generate the simulated data are also given. Note that the baseline estimates reported for combined filter are the final estimate, while those reported for the baseline only filter are averages over the converged portion of the data. Looking at the estimates from the simulated data, we see that all estimates, regardless of filter type, are within 0.4 mm of the true values.

For the RADCAL data, since we don't know the true baselines, we can only compare the results from different filter types and different days. Four out of the six coordinate estimates are consistently within 2.7 mm of one other. The difference between estimates for coordinates b_{3x} and b_{3y} is 5.8 mm and 5.9 mm, respectively. While we expect the out-of-plane coordinate to be larger, we do not expect the estimates for coordinate b_{3y} to vary that much. With closer inspection of Figure 2.6, we see that the estimate for b_{3y}, drops off at the end. Since the covariance bounds are not accurate, it is difficult to determine if this is filter divergence or simply an artifact of the data.

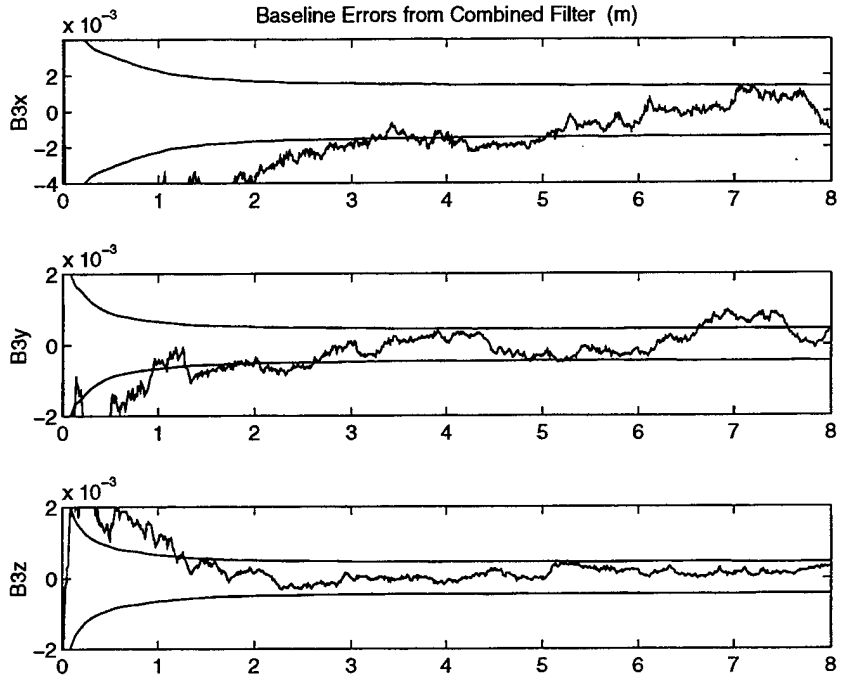

Figure 2.5: Baseline 3 Solutions from Combined Filter for Simulated Data

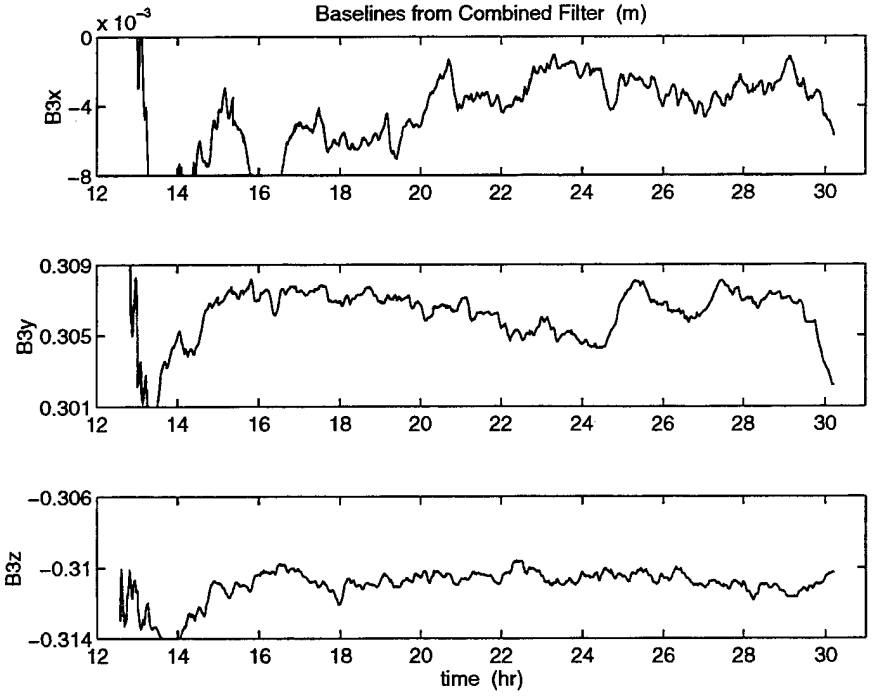

Figure 2.6: Baseline 3 Solutions from Combined Filter for RADCAL Day 160

Table 2.3: Baseline Estimates (m)

Filter Type	Data Type	b_{1y}	b_{1z}	b_{2y}	b_{3x}	b_{3y}	b_{3z}
True	Simulated	0.3044	0.3012	0.6088	0.0	0.3044	-.3012
Combined	Simulated	0.3046	0.3012	0.6094	-.0009	0.3048	-.3009
Baseline	Simulated	0.3046	0.3016	0.6092	-.0010	0.3046	-.3009
Combined	RADCAL 160	0.3030	0.3091	0.6135	-.0058	0.3022	-.3103
Baseline	RADCAL 160	0.3028	0.3083	0.6131	-.0044	0.3065	-.3095
Combined	RADCAL 189	0.3050	0.3079	0.6145	0.0000	0.3070	-.3112
Baseline	RADCAL 189	0.3044	0.3091	0.6158	-.0050	0.3081	-.3101

2.5 Conclusions and Future Work

While the combined attitude-baseline filter presented here shows some promise, there are still a number of issues to be address before further comments can be made about the performance of this algorithm. These issues include

1. Filter tuning. A straightforward method of tuning the filter needs to be developed. Current implementation of the process noise does not seem to be performing as hoped and needs to be reexamined.

2. Measurement mismodeling. The covariance bounds seem to clamp down before the solutions have actually converged, even with simulated data, where we know the dynamic model is correct. Including second order terms that have been neglected from the measurement gradient matrix needs to be investigated.

3. Dynamic mismodeling. The discrepancy observed in the covariance bounds for the RADCAL baseline estimates suggests some type of dynamic mismodeling which needs to be identified. Modeling the disturbance torques as a correlated process may help.

Even without the resolution of the above issues, we have come some conclusions about the utility of the combined filter as compared to the original bootstrapping method. If baselines are known, the attitude filter produces the best results. Clearly, the more knowledge we have about the baseline positions, the better the attitude estimate will be. Furthermore, since the attitude filter has fewer states to estimate, it can do better when there are not as many measurements, and less computational power is needed. If baselines are unknown but constant, either approach may work with the following considerations: The baseline filter may be best in a post-processing mode where lots of data can be used to average over. These baseline estimates can then be used in the attitude filter which will provide the best results now that the baselines are known. The combined filter may be best in a real-time mode where some attitude knowledge is needed from the start. Again, once baseline solutions are good enough, the attitude filter could be invoked to increase robustness. If baselines are flexible and changing over time, the combined filter approach is the only possibility. Both the attitude filter and the baseline filter work on the assumption that the baselines are constant. The combined filter is the only method that could actually track changes in the baselines.

With the resolution of the above issues, a number of additional tasks have been identified for future work that would increase the usefulness of the combined filter. Currently, the

combined filter actually estimates baseline coordinates in a body frame that is defined by the baseline positions. However, most missions require attitude knowledge with respect to another frame of reference. This frame is usually defined by either the mechanical drawings or the position of some other sensor. Therefore, it would be useful to develop a method of estimating the baselines in the mission defined body frame. Rather than estimating baseline coordinates, the state vector would have to be changed to estimate other baseline parameters such as length or direction.

In both the attitude and combined filters, the principal axes are assumed to be aligned with the body frame axes. While this is generally true for gravity-gradient symmetric spacecraft, it does not necessarily hold for other types of vehicles. To allow for a more general definition of the principal axes, the equations of motion would have to be expressed in terms of a full inertia matrix. This change will be necessary for before processing data from the CRISTA-SPAS satellite which is neither symmetric nor gravity-gradient stabilized.

All of the work with to date with the combined filter has involved only constant baselines. Since the most promising application of the combined filter is estimating attitude with flexible baselines, investigating this aspect will be key in determining the utility of this algorithm.

References

[1] Penina Axelrad, Bruce C. Chesley, and Lisa M. Ward. GPS Based Spacecraft Attitude Determination. Final Report for FY'92-93, Naval Research Laboratory, September 1993.

[2] Penina Axelrad, Charles P. Behre, Christopher J. Comp, and Lisa M. Ward. GPS Based Attitude Determination. FY'93-94 Technical Report I, Naval Research Laboratory, May 1994.

[3] Penina Axelrad, Bruce C. Chesley, Christopher J. Comp, and Lisa M. Ward. GPS Based Attitude Determination. FY'93-94 Technical Report II, Naval Research Laboratory, October 1994.

[4] Penina Axelrad, Charles P. Behre, Christopher J. Comp, and Lisa M. Ward. GPS Based Attitude Determination. FY'94-95 Technical Report I, Naval Research Laboratory, October 1995.

3 MULTIPATH MODELLING AND CORRECTION - *Christopher J. Comp*

3.1 INTRODUCTION AND OVERVIEW

High precision measurements of the GPS L-Band carrier phase have been used for a wide variety of surveying applications ranging from worldwide geodetic networks to kinematic survey on both land and sea. More recently, attitude determination systems based on the carrier phase observable have been developed and demonstrated on land [15], sea [10], air [5, 3], and in space [6, 17]. The key measurement in each of these systems is the difference in the received phase measured by two antennas to a single satellite, known as the differential phase. When two separate receivers are used to track the two antennas, as is the case in a survey application or in some attitude determination systems [15, 10, 3], the difference between differential phase measurements for two satellites (double difference) is used as the measurement, eliminating the effect of the different receiver clocks.

The limiting factor on performance in almost all attitude determination applications has been identified as multipath. Similarly, in some high precision surveying environments, multipath appears to be the dominant error source. Multipath is the corruption of the direct GPS signal by one or more signals reflected from the local surroundings. Figure 3.1 shows an example of differential phase residuals between two fixed antennas. The structured oscillations are characteristic of multipath interference. The residual data has the first order GPS satellite motion removed, leaving the multipath and receiver measurement noise. In this particular set of data, the multipath produced peak errors of 8 millimeters with low frequency components. Uncorrected, these measurement errors would produce attitude errors at the level of 8 milliradians (0.46 degrees) for a 1 meter antenna baseline length.

The primary goal of this research is to develop and implement a technique to correct for multipath in GPS carrier phase measurements. The technique should be successful in reducing multipath to the level of receiver measurement noise. The technique should also work in a variety of precise GPS applications involving both static and dynamic platforms, and also in a changing multipath environment. The research will emphasize multipath correction for attitude determination onboard near-earth spacecraft. Generality is desired to include commercially viable areas such as terrestrial attitude determination and differential surveying. A distant goal is to implement the technique in a near real-time operational mode.

The theoretical foundation of multipath with the GPS carrier signal has been studied, and was laid out in detail in the September, 1994 Technical Report [2]. Based on that knowledge, a procedure for estimating the multipath present in the phase measurement of the carrier signal was devised. The multipath correction approach overcomes many of the shortcomings of previously recommended techniques. It utilizes the ratio of the amplitude of the recovered carrier signal to the noise (SNR) and the known antenna gain pattern to create a multipath correction profile for the carrier phase measurements. Thus, a new correction profile is generated for each data set, eliminating the constraint that the environment remain unchanged.

The relationship between the direct GPS signal, one or more multipath signals, and the resulting composite signal which is reported by the receiver, was developed as in [7]. The relationship was then used to derive the phase error due to multipath, based on information obtained from the amplitude of the composite signal (*i.e.* the SNR). When the multipath signal strength relative to the direct signal is small, the expression for the phase error due to multipath is given by the

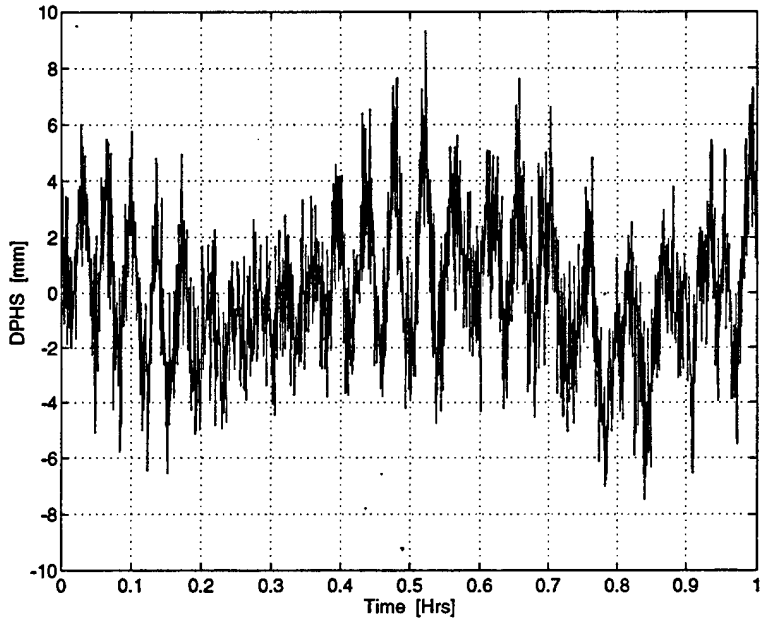

Figure 3.1: Differential phase data for a 1 meter patch antenna baseline. The data was collected May 24, 1994, with a Trimble Vector attitude receiver. The horizontal axis is time in minutes, the vertical axis is differential phase residual in millimeters.

following approximate formula:

$$\delta\phi \approx \frac{\sum_i \alpha_i A_o \sin(\omega_i t + \theta_i)}{A_o A_a + \sum_i \alpha_i A_o \cos(\omega_i t + \theta_i)} \tag{3.1}$$

where i is summed over all multipath signals present. The $\alpha_i A_o$ is the amplitude of the multipath fluctuations, ω_i is the frequency of the multipath, t is a time reference, θ_i is the phase offset of the multipath in the SNR, and A_c is the actual composite SNR.

The frequency, amplitude, and phase offset of the multipath are determined from the SNR data using spectral estimation techniques. Inserting the parameters into Equation 3.1 creates a profile of the multipath error in the phase data. This profile is subtracted from the phase data to eliminate the multipath error, leaving uncorrupted navigation information. Modeling and subsequent subtraction of multipath error that is identified directly from the phase data would be incorrect, due to the risk of removing fluctuations from actual vehicle dynamics.

The technique has proven successful for correcting multipath in differential phase measurements to near the receiver noise level, in limited trials. The technique was used in a post-processing mode on data from static terrestrial platforms. The data was either simulated using a model of a generic code-correlating receiver, or was collected by a Trimble Vector code-correlating attitude receiver during experiments. Also, simulations have been performed which analyze the effect of multipath on a dynamic orbiting spacecraft, in so doing the multipath characteristics are well understood. At this time, however, the correction technique has been used only with simulated and experimental static scenarios.

In order to reach the true potential of the technique, improved performance must be attained in the limited trials, and eventually an automated approach to experimental data from dynamic platforms should be realized. An important step in the direction of this goal is to develop a procedure to better estimate the spectral content of the multipath in the SNR data. The procedure must be capable of identifying parameters of non-stationary sinusoidal signals from varying amounts of data, and must also lend itself to automation.

Various candidate spectral estimators were identified in [1]. Of those, the short-time FFT, data-adaptive evolutionary periodogram, and FIR adaptive filters were examined on simulated dual-chirp and multipath data sets. It was determined that these methods were unsatisfactory for the following reasons. In traditional fashion, they estimate the entire spectrum of a given signal. Extensive interaction was required to search the spectrum and identify peaks associated with predominant frequencies. In other words, automation would be difficult. Furthermore, the frequency estimates were inaccurate, and no amplitude estimates were easily obtainable. In the case of multipath signals where the true frequencies were unknown, there was no way of checking the integrity of the frequency estimates.

The research conducted since the last progress report has concentrated on more advanced adaptive estimation mechanisms, namely the IIR adaptive filter and the adaptive least squares. These methods differ from the traditional spectral estimators discussed previously, because they inherently estimate the specific time-varying parameters of quasi-periodic signals. Using a fundamentally different approach to the same problem, the IIR adaptive filter is superior to the FIR types. It has the advantage that one filter weight per signal achieves the same performance of an FIR filter employing hundreds of weights. The IIR filter also reports the frequency estimates directly, eliminating the search for peaks in the spectrum. The adaptive least squares is another efficient and powerful routine that directly reports the amplitude and phase estimates in addition to the frequency. Both methods provide a conclusive way of checking the integrity of the estimated parameters.

The IIR adaptive filter and adaptive least squares methods have been tested extensively on simulated and experimental multipath signals. The frequencies were estimated with sufficient accuracy by the IIR adaptive notch filter technique. The adaptive least squares technique also provided the signal amplitude and phase offset estimates, but was discovered to be less robust. Although individually they performed well, when used together the result is a remarkably robust and accurate tool that estimates the amplitude, frequency, and phase offset of the multipath signals. This is accomplished at a low computational cost due to the small number of estimated parameters, and not needing to do a spectrum search.

Section 3.2 covers the adaptive spectral estimation discussion as a whole. It includes subsections 3.2.1 and 3.2.2 which explain the individual IIR adaptive filter and adaptive least squares approaches. Section 3.3 presents the results from using the techniques on multipath data. Section 3.4 discusses meaning of the results. Section 3.5 concludes the multipath portion of this report by outlining future research.

3.2 ADAPTIVE SPECTRAL PARAMETER ESTIMATION

Classical spectral estimation and parameter identification techniques approximated time-varying signals by utilizing stationary models, and assuming the slowly changing signal characteristics

remained locally stationary within specified time windows. The output was a spectral image representing an average of the changing signal through the processed time span. In so doing, the performance was limited. With adaptive methods, the spectral estimate is updated as each data record is processed. The traditional adaptive methods studied in [1] presented a spectral image that reflected the signal as it changed through time. However, search routines to identify the spectral peaks and compute the associated frequencies and amplitudes were cumbersome.

The adaptive spectral parameter estimation techniques described in this report differ from true spectral estimators. The amplitudes, frequencies, phase offsets of predominant pseudo-periodic constituents contained within a signal are estimated, as opposed to the entire spectrum. The outcome is better accuracy at lower computational cost. The adaptive estimation schemes fit in well with the multipath correction architecture. The spectral parameters of the multipath in the SNR measurements are tracked through time as each data record is processed. The parameters may then be inserted into Equation 3.1, which relates the multipath errors in the SNR to those in the phase measurements.

3.2.1 IIR ADAPTIVE FILTER

A digital filter takes discrete samples of an input signal, manipulates it in some specified manner, and outputs a desired signal. The input-output relationship is formally expressed as a transfer function:

$$H(z) = \frac{a_0 + a_1 z^{-1} + \cdots + a_n z^{-n}}{1 + b_1 z^{-1} + \cdots + b_n z^{-n}} \tag{3.2}$$

where the a_i's and b_i's are the filter coefficients, and z^{-1} is the z-transform of the unit-delay operator. $H(z)$ is derived from the z-transform of the standard difference equation, which describes the filter input-output in the time domain:

$$y(k) = \sum_{i=0}^{n} a_i u(k-i) - \sum_{i=1}^{n} b_i y(k-i) \tag{3.3}$$

where $u(k)$ is the input signal, $y(k)$ is the output signal, and k is the data record.

The output response of a filter is the frequency representation of the phase and magnitude of the complex transfer function, and indicates the affect of the filter on the input signal. For example, magnitudes of signal constituents at a specific frequency are attenuated by such an amount, or phases of constituents at the frequency are shifted by so many radians. Generally, the filter is defined by a number of frequency-domain requirements that specify a desired output response, such as pass-band, stop-band, transition-band, attenuation, and Nyquist frequency (half the sampling frequency). Figure 3.2 provides a pictorial explanation of these terms.

In practice, it is infeasible to implement an ideal digital filter. There are two types of filter approximations (refer once again to Figure 3.2): the Infinite-Impulse Response (IIR) and the Finite-Impulse Response (FIR). The IIR filter approximation solves for the poles and zeros of the transfer function that satisfies the given task. This type of filter is characterized by abrupt transition-bands in the magnitude output response for a low number of filter coefficients. Historically, the cost has been that even small and simple models can be highly unstable, ending up in complicated solutions for the coefficients. In the FIR filter approximation, the denominator terms (the b_i's) in Equation

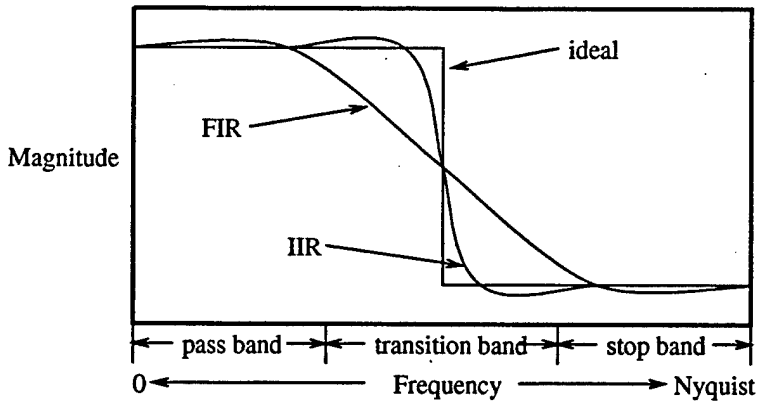

Figure 3.2: Example magnitude output response for ideal filter, and FIR and IIR approximations.

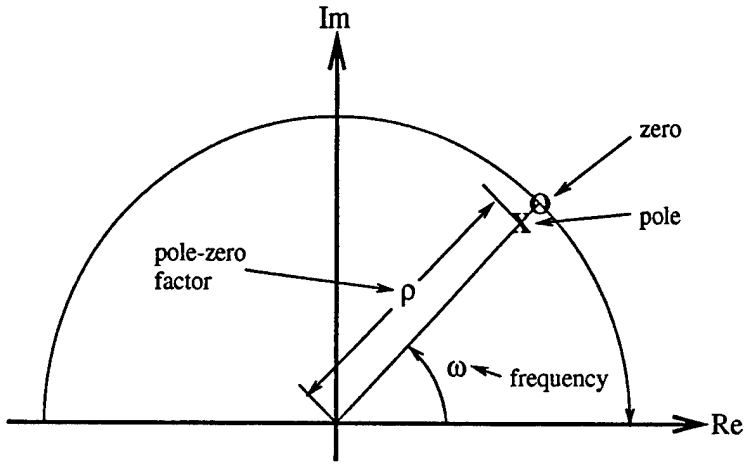

Figure 3.3: Location of zeros and poles with respect to the unit circle for the IIR adaptive notch filter.

3.2 are zero. It is more difficult to approximate the ideal filter when only the numerator coefficients are available. Hence, significantly more coefficients are needed to match the IIR performance. The order of the model is increased, however it is more stable, and solutions for the coefficients tend to be numerically simpler. Consult [14, 13] for more detailed information.

An IIR Adaptive Notch Filter (ANF) is used in this research. The initial motivation for such a filter was to remove quasi-periodic interference from noisy or non-periodic data [11]. A prime example would be a set of measurements corrupted by 60 Hz sinusoidal interference from a power signal. The frequencies of the sinusoidal signals are identified in the process of their removal. For this reason, the ANF eventually became recognized as an excellent tool for spectral parameter estimation.

An IIR ANF is capable of providing narrow notches using a low number of filter coefficients. Keeping in mind that the transfer function is a z-transform, the a_i's and b_i's are zeros and poles,

respectively. In this filter scheme, a notch is produced in the output magnitude response by placing the poles and zeros along the same line radiating out to the unit circle, as illustrated in Figure 3.3. The angular distance of the line from the real axis is equal to the frequency. For stability, the zeros are constrained to lie on the unit circle. The filter transfer function is given as (c.f. [11, 12, 4]):

$$H(z^{-1}) = \frac{1 + a_1 z^{-1} + \cdots + a_n z^{-n} + \cdots + a_1 z^{-2n+1} + z^{-2n}}{1 + \rho a_1 z^{-1} + \cdots + \rho^n a_n z^{-n} + \cdots + \rho^{2n-1} a_1 z^{-2n+1} + \rho^{2n} z^{-2n}} \tag{3.4}$$

where the $a_i's$ are the filter coefficients, and n is the number of desired notches (*i.e.* the number of frequencies to be estimated). The width of the notch, and hence the transition-band, is a function of the proximity of the pole to the zero, signified by the pole-zero contraction factor ρ. The factor must be in the range $0 < \rho < 1$ for a stable filter, $\rho = 1$ forms the ideal notch,

The mirror symmetry form of the numerator and denominator polynomials in Equation 3.4 is a necessary condition for the zeros to lie on the unit circle. The associated benefits make this particular type of ANF invaluable. Writing the transfer function as follows:

$$H(z^{-1}) = \frac{A(z^{-1})}{A(\rho z^{-1})} \tag{3.5}$$

the polynomial $A(z^{-1})$ may be written in either product or summation form:

$$A(z^{-1}) = \prod_{i=0}^{n} (1 + \alpha_i z^{-1} + z^{-2}) = \sum_{i=0}^{2n} a_i z^{-i}, \quad a_{n+m} = a_{n-m}, \quad m \leq n \tag{3.6}$$

with closed-form relationships between the a_i and α_i coefficients dependent on n. The actual number of filter coefficients is equal to the number of notches, and that number is a minimum. Other IIR notch filters require more than twice the number of coefficients. Also, the high degree of similarity between the numerator and denominator cause the input-output relationship to be close to linear, and therefore very stable. Due to the symmetry, the output phase response is nearly linear as well. Phase distortion arising from phase response nonlinearity is often a severe problem with IIR filters.

The most useful feature of the IIR ANF is that the frequencies of the sinusoidal signals are directly related to the α_i coefficients by [4]:

$$f_i = acos(-\frac{\alpha_i}{2}) \tag{3.7}$$

The value of the IIR ANF, in contrast to an FIR type, becomes very clear. The number of estimated frequencies is equal to the number of filter coefficients. The fact that this number is a minimum has a profound influence on accuracy and computational efficiency. If an FIR approach were to be used, the number of coefficients needed to generate the magnitude response with sufficient accuracy would be orders of magnitude greater. In addition, there is no direct relationship between the coefficients and the frequencies. In fact, the output response would have to be searched to locate the bottoms of the notches to find their corresponding frequencies. This procedure is both time consuming and inaccurate.

The adaptive procedure that determines the ANF coefficients will now be derived. The basic function of the ANF is to remove quasi-periodic interference from noisy or non-periodic signals. The filter output is then regarded as the error, which in the time-domain is:

$$\epsilon(k) = \frac{A(q^{-1})}{A(\rho q^{-1})} u(k) \tag{3.8}$$

where $A(q^{-1})$ is the time-domain representation of the z-transform polynomial in Equation 3.6, and q^{-1} is the unit-delay operator. The coefficients a_i are adjusted in the adaptive procedure to minimize the cost function:

$$V = \sum_{k=1}^{L} \epsilon^2(k) \tag{3.9}$$

which is the squared error summed over L data samples. Minimizing this cost function means that the error is equal to the filter output: $\epsilon(k) = y(k)$. The minimization, along with the polynomial symmetry, also guarantees that the zeros lie on the unit circle.

The coefficient adjustment is achieved with a recursive prediction error algorithm. In particular, the quadratic criterion in 3.9 is minimized via a stochastic Gauss-Newton search method [9]. Define the parameter vector to be the set of filter coefficients:

$$\theta = [a_1 \dots a_n]^T \tag{3.10}$$

and the regression vector:

$$\phi_i(k) = \begin{cases} -y(k-i) - y(k-2n+i) + \rho^i \epsilon(k-i) + \rho^{2n-i}\epsilon(k-2n+i), & 1 \le i \le n-1 \\ -y(k-n) + \rho^n \epsilon(k-n), & i = n \end{cases} \tag{3.11}$$

such that $\phi(k) = [\phi_1(k) \dots \phi_n(k)]^T$. The standard difference equation can then be written in terms of the error:

$$\epsilon(k) = u(k) + u(k-2n) - \rho^{2n}\epsilon(k-2n) - \phi^T\theta \tag{3.12}$$

The first order gradient of the error:

$$\psi(k) = [\psi_1(k) \dots \psi_n(k)]^T, \quad \psi_i(k) = -\frac{\partial \epsilon(k)}{\partial a_i} \tag{3.13}$$

is shown in [11] to be a filtered form of the regression vector:

$$\psi(k) = \frac{\phi(k)}{A(\rho q^{-1})} \tag{3.14}$$

In practice, the first order gradient is approximated by substituting filtered versions of the input and error signals, $u_F(k)$ and $\epsilon_F(k)$ respectively, into Equation 3.11. A useful expression for the second order gradient is:

$$P(k) = \frac{1}{\gamma}\left[P(k-1) - \frac{P(k-1)\psi(k)\psi^T(k)P(k-1)}{\psi^T(k)P(k-1)\psi(k) + \gamma}\right] \tag{3.15}$$

where γ is a convergence parameter that is updated via:

$$\gamma(k+1) = \gamma_o\gamma(k) + (1-\gamma_o)\gamma_\infty \tag{3.16}$$

If desired, the pole-zero contraction factor can be updated in the same way. Equation 3.15 is in reality equivalent to the inverse of the second order gradient, and was arrived upon using a matrix inversion approximation for recursive applications. Finally, the coefficient update is carried out with the formula:

$$\hat{\theta}(k) = \hat{\theta}(k-1) + P(k)\psi(k)\epsilon(k) \tag{3.17}$$

Equations 3.11, 3.12, 3.15, and 3.17, collectively make up the recursive algorithm. As input, the algorithm requires the following: sampling frequency, number of frequencies to estimate, convergence parameter and pole-zero contraction factor values, and the data sequence itself. No initial frequency estimates are needed.

The IIR ANF requires the use of a second order gradient search, such as the Gauss-Newton method, for two main reasons. The performance surface corresponding to the multi-variable function in Equation 3.9 may contain local minima, where a global minimum is sought. There are also potential nonlinear instabilities associated with IIR filters in general. When this algorithm is used to compute the minimum number of filter coefficients, accuracies are within an order of magnitude of the Cramer-Rao bound for large data sets. Moreover, an order of n^2 multiplications are needed, much less than for other ANF algorithms [11].

3.2.2 ADAPTIVE LEAST SQUARES

The adaptive least squares (ALS) technique begins by modelling the signal under analysis as multiple sinusoids embedded in noise:

$$y(k) = s(k) + \nu(k) = \sum_{i=1}^{n} A_i(k)\sin(k\omega_i(k) + \phi_i) + \nu(k) \tag{3.18}$$

where $A_i(k)$ is the amplitude, $\omega_i(k)$ is the frequency, and ϕ_i is the phase offset of the i^{th} sinusoid, and $\nu(k)$ is Gaussian noise, all for the discrete time index $k = 1, \ldots, L$. The signal $y(k)$ can be interpreted as noise corrupted measurements of the sinusoids $s(k)$. Define the state space model:

$$s(k) = J^T\theta(k) \tag{3.19}$$

where the state vector is given as:

$$\theta(k) = \begin{bmatrix} \theta_1(k) \\ \vdots \\ \theta_n(k) \end{bmatrix}, \quad \theta_i(k) = \begin{pmatrix} A_i(k)\sin(k\omega_i(k) + \phi_i) \\ A_i(k)\cos(k\omega_i(k) + \phi_i) \end{pmatrix} \tag{3.20}$$

and also $J^T = [1\ 0\ 1\ 0\ \ldots\ 1\ 0]$. Next define the state transition matrix:

$$F(k+1,k) = \begin{pmatrix} F_1(k) & & 0 \\ & \ddots & \\ 0 & & F_n(k) \end{pmatrix}, \quad F_i = \begin{pmatrix} \cos(\omega_i(k)) & \sin(\omega_i(k)) \\ -\sin(\omega_i(k)) & \cos(\omega_i(k)) \end{pmatrix} \tag{3.21}$$

such that the state may be propagated through one discrete time step:

$$\theta(k+1) \;=\; F(k+1,k)\theta(k) \tag{3.22}$$

The one-step ahead prediction of the sinusoidal portion of the signal $y(k)$ is then:

$$s(k) \;=\; J^T F(k,k-1)\theta(k-1) \tag{3.23}$$

In least squares fashion, a quadratic error cost function is employed:

$$V = \sum_{k=1}^{L} \lambda(k)^{j-k}[y(k) - s(k)]^2 = \sum_{k=1}^{L} \lambda(k)^{j-k}\left[y(k) - J^T F^{k-j}\theta(j)\right]^2 \tag{3.24}$$

which is equivalent to the square of the measurement noise, ν^2. The forgetting factor $\lambda(k)$ is introduced to discount old measurements, and is updated by:

$$\lambda(k) = \lambda o \lambda(k-1) + (1-\lambda o)\lambda_\infty \tag{3.25}$$

The following state estimate is reached by minimizing the above cost function:

$$\hat{\theta}(k) = F\hat{\theta}(k-1) + K(k)\left[y(k) - \hat{y}(k|k-1)\right] \tag{3.26}$$

where the gain $K(k)$ is given as:

$$K(k) = G(k)^{-1}J, \;\; G(k) = JJ^T + \lambda(k)F(k)G(k-1)F^T \tag{3.27}$$

and $\hat{y}(k|k-1)$ is a one-step ahead prediction of $y(k)$ using Equation 3.23.

Estimates of the amplitude, frequency, and phase offset are all derived from the state estimate. To be precise, the amplitude estimate of the i^{th} sinusoidal component is obtained by the relationship:

$$\hat{A}_i(k) = ||\theta_i(k)|| = \sqrt{\hat{\theta}_{is}^2(k) + \hat{\theta}_{ic}^2(k)} \tag{3.28}$$

where the is and ic subscripts respectively denote the *sin* and *cos* parts of the θ_i element of the state vector. The argument estimate of the sinusoidal component is determined by:

$$\hat{\eta}_i(k) \equiv \hat{\omega}_i(k)k + \hat{\phi}_i = \arctan\left(\frac{\hat{\theta}_{is}(k)}{\hat{\theta}_{ic}(k)}\right) \tag{3.29}$$

The difference between two consecutive argument estimates is equivalent to the frequency averaged over the time differential:

$$\hat{\delta\eta}_i(k) = \hat{\eta}_i(k) - \hat{\eta}_i(k-1) = \bar{\omega}_i(k) \tag{3.30}$$

The frequency estimate is then assembled using the recursion formula:

$$\hat{\omega}_i(k) = \mu(k)\hat{\omega}_i(k-1) + (1-\mu(k))\hat{\delta\eta}_i(k) \tag{3.31}$$

where $\mu(k)$ is a convergence factor incorporated to smooth the frequency estimates. It is also updated in the same manner as $\lambda(k)$. The phase offset estimate is deduced from using the argument and frequency estimates and: $\hat{\phi}_i = \hat{\eta}_i(k) - \hat{\omega}_i(k)k$.

Equations 3.25 through 3.31 collectively make up the ALS algorithm. The state transition matrix $F(k)$ is calculated using $\hat{\omega}_i(k-1)$, the frequency estimate from the previous record. As input, the algorithm requires the following: sampling frequency, the number of signals to estimate parameters for, forgetting factor values, and the data sequence. No initial parameter estimates are needed.

The ALS approach described here is simple yet quite powerful. Similar to the IIR ANF, the estimates approach the Cramer-Rao bound for accuracy. Among all spectral methods investigated, this one is the best suited for the multipath correction technique. The primary reason being that the amplitude and argument of the time-varying signals are directly available, and they easily fit into the formula relating the SNR to the phase multipath (Equation 3.1). Under the multipath correction setting, the frequency estimate is used only to propagate the state (*i.e.* to compute F), and to compute the gain K. The phase offset estimate need not be performed.

3.3 SPECTRAL PARAMETER ESTIMATION RESULTS

Individually, the IIR ANF and ALS approaches have their respective strengths and weaknesses. In practice, the IIR ANF has shown to produce excellent frequency estimates. The performance has been very robust as the algorithm has proven successful under varying circumstances, such as sampling rate and number of frequencies estimated. The main problem is difficulties in estimating the amplitude and phase offset. On the other hand, the ALS routine estimates the amplitude and phase offsets as well as the frequencies. It unfortunately suffers under adverse conditions where the IIR filter excels.

An algorithm combining the IIR ANF and ALS methods was devised based on suggestions in [12]. In essence, the frequencies are first estimated by the ANF. They are subsequently used as truth in the ALS to propagate the state and compute the gain. Based on practical experience, this tends to make the amplitude and argument estimation in the ALS more robust. The combined ANF-ALS algorithm outperforms the individual ones in all areas. For that reason, the ANF results will be presented, followed by ALS results based on the ANF frequency estimates. The dual-chirp signal, which was a familiar sight in the last report, will not be used here. Due to the excellent performance of the routines, we will move directly to simulated and experimental multipath signals.

Figures 3.4 and 3.5 contain plots pertaining to the spectral parameter estimation for the simulated multipath data. The data is the identical set described previously in [1]. Recall that there exists a low and high frequency multipath signal (*i.e.* $n = 2$), which are produced by reflectors located 1 and 10 meters away, respectively. The relative amplitudes of the multipath produced by the near and far reflectors are respectively 0.1 and 0.05. The data was generated at 1.5 second intervals, and was decimated by a factor of 10 for the analysis, giving an effective sampling rate of $f_s = 0.0667Hz$ (15 second intervals). The convergence parameter was a constant $\gamma = 0.9$ and the pole-zero contraction factor was held at $\rho = 0.5$ for the ANF. The forgetting factors were kept constant at $\lambda = \mu = 0.9$ for the ALS.

Figure 3.4 exhibits the IIR ANF simulated data results. The top plot shows the frequency estimates as they evolve through time. The middle plot depicts the magnitude output response of the filter versus frequency. The bottom plot displays the input and output signals of the filter. At about 30 minutes into the sequence the frequency estimates converge to the correct values, and continue to track them as they change over time. At the point of convergence, the filter begins to successfully remove the sinusoidal constituents. This event is observed by comparing the input and output signals.

Figure 3.5 presents the ALS simulated results. The top plot again shows the frequency estimates that were determined with the ANF. The middle plot shows the amplitude estimates as they evolve over time. The bottom plot displays the original multipath signal, and the signal reconstructed from the estimated spectral parameters. The ALS amplitude estimation needs more time to converge (35 minutes) than does the ANF frequency estimation. The argument estimation follows the same trend, but is not shown here. The reconstructed signal provides a nearly identical match for the original signal once the estimates have converged.

Figures 3.6 and 3.7 contain plots from the spectral parameter estimation for the experimental multipath data. The data was obtained from the reflective multipath injection experiment first detailed in [2]. This particular set of data was collected May 25, 1994, on the Engineering Center roof using the Trimble TANS Vector receiver, and GPS PRN 27. The average sampling interval was

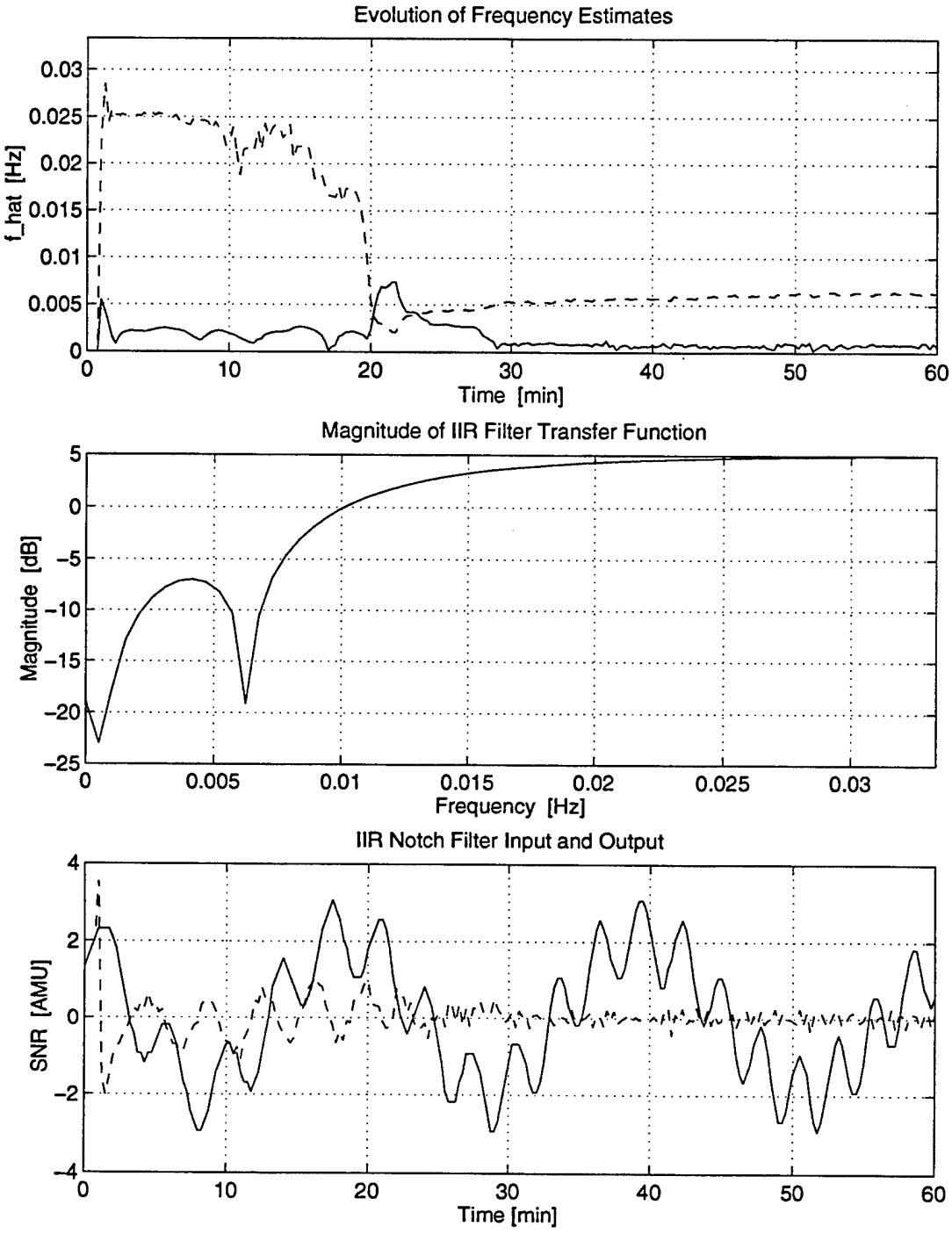

Figure 3.4: IIR adaptive notch filter results for simulated multipath data. Top plot: evolution of low (solid) and high (dashed) frequency estimates; Middle plot: magnitude output response at final time record; Bottom plot: input (solid) and output (dashed) of notch filter.

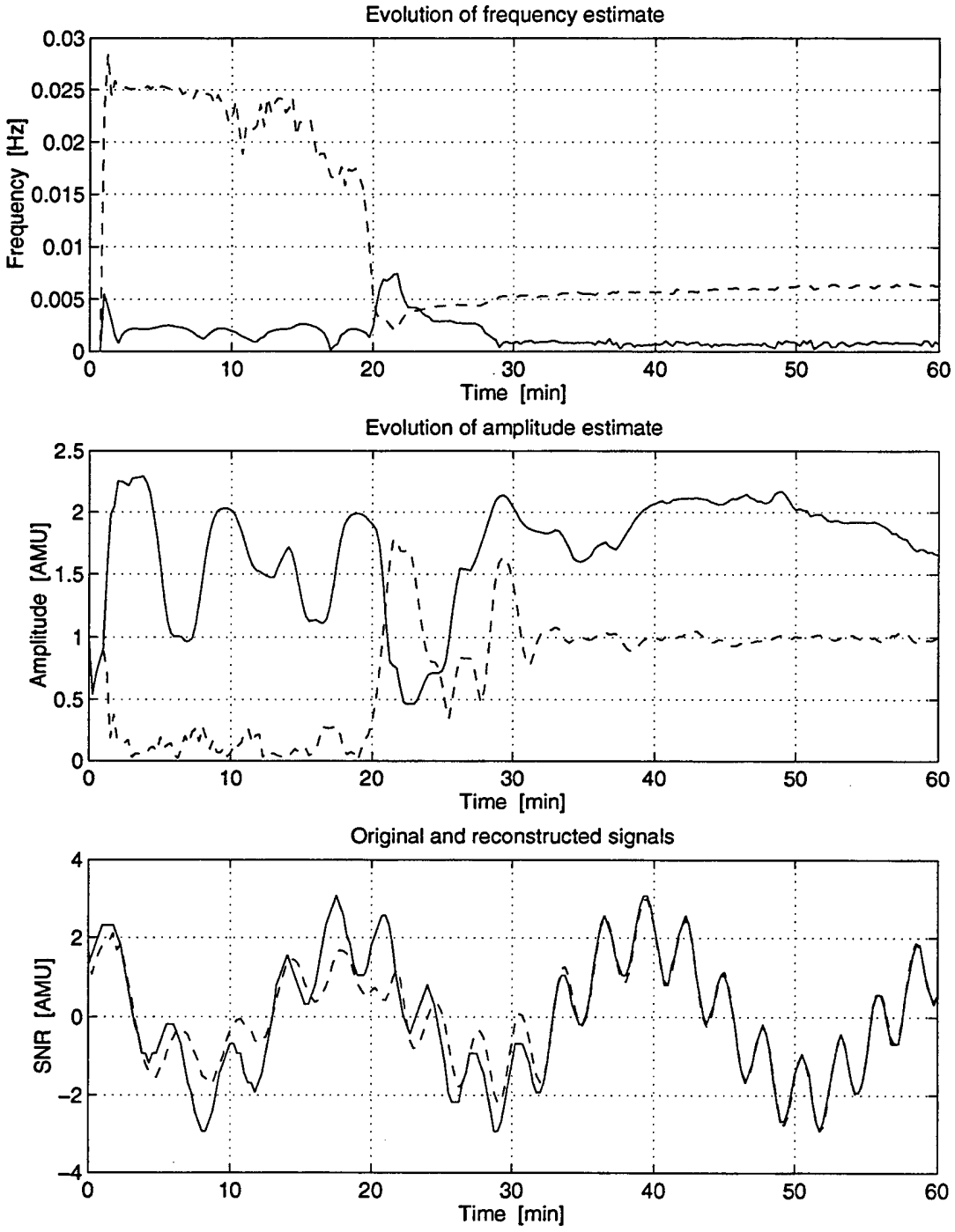

Figure 3.5: Adaptive least squares results for simulated multipath data. Top plot: evolution of low (solid) and high (dashed) frequency estimates from ANF; Middle plot: evolution of corresponding amplitude estimates from ALS; Bottom plot: original signal (solid) and signal reconstructed from spectral parameters (dashed).

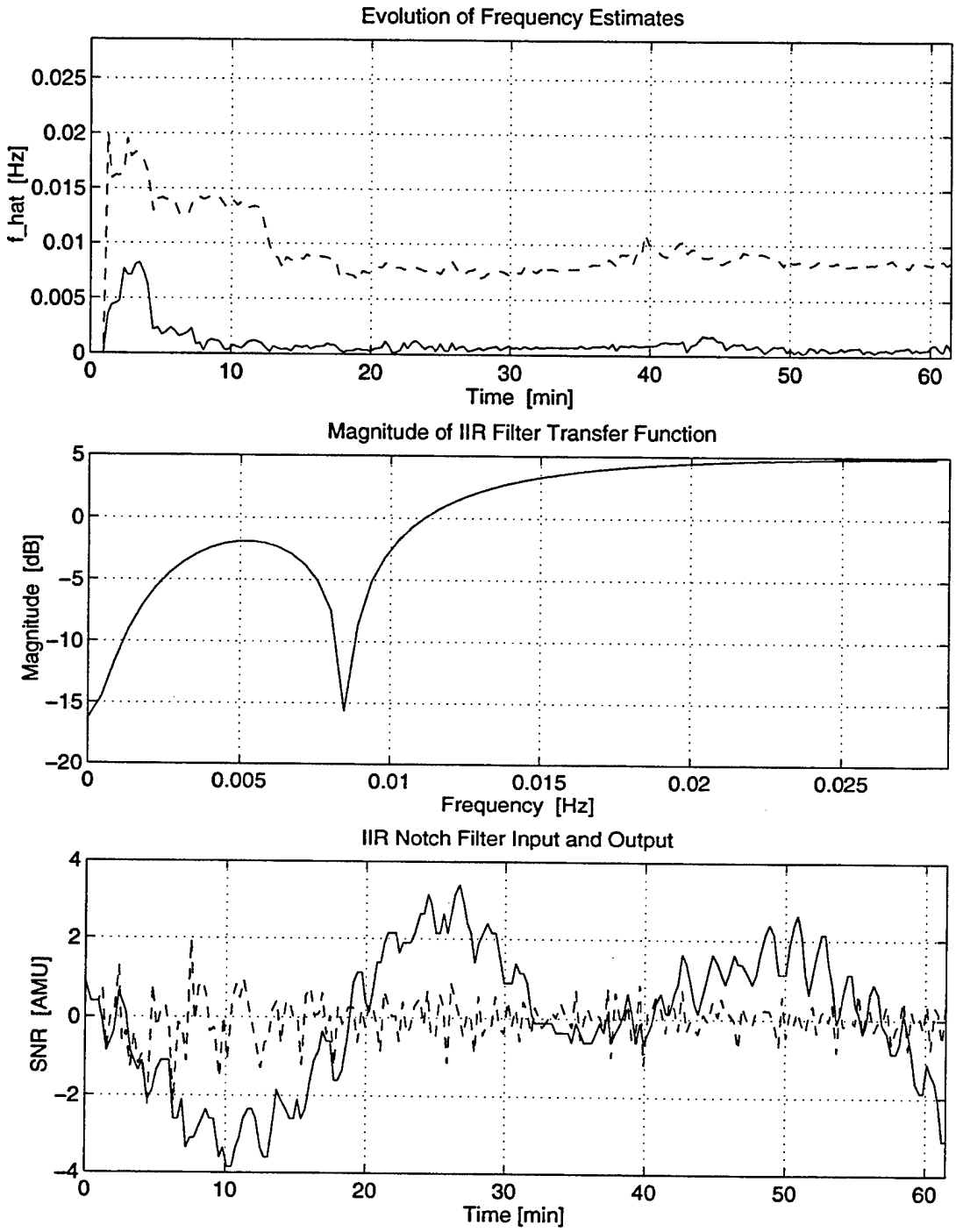

Figure 3.6: IIR adaptive notch filter results for experimental multipath data. Top plot: evolution of low (solid) and high (dashed) frequency estimates; Middle plot: magnitude output response at final time record; Bottom plot: input (solid) and output (dashed) of notch filter.

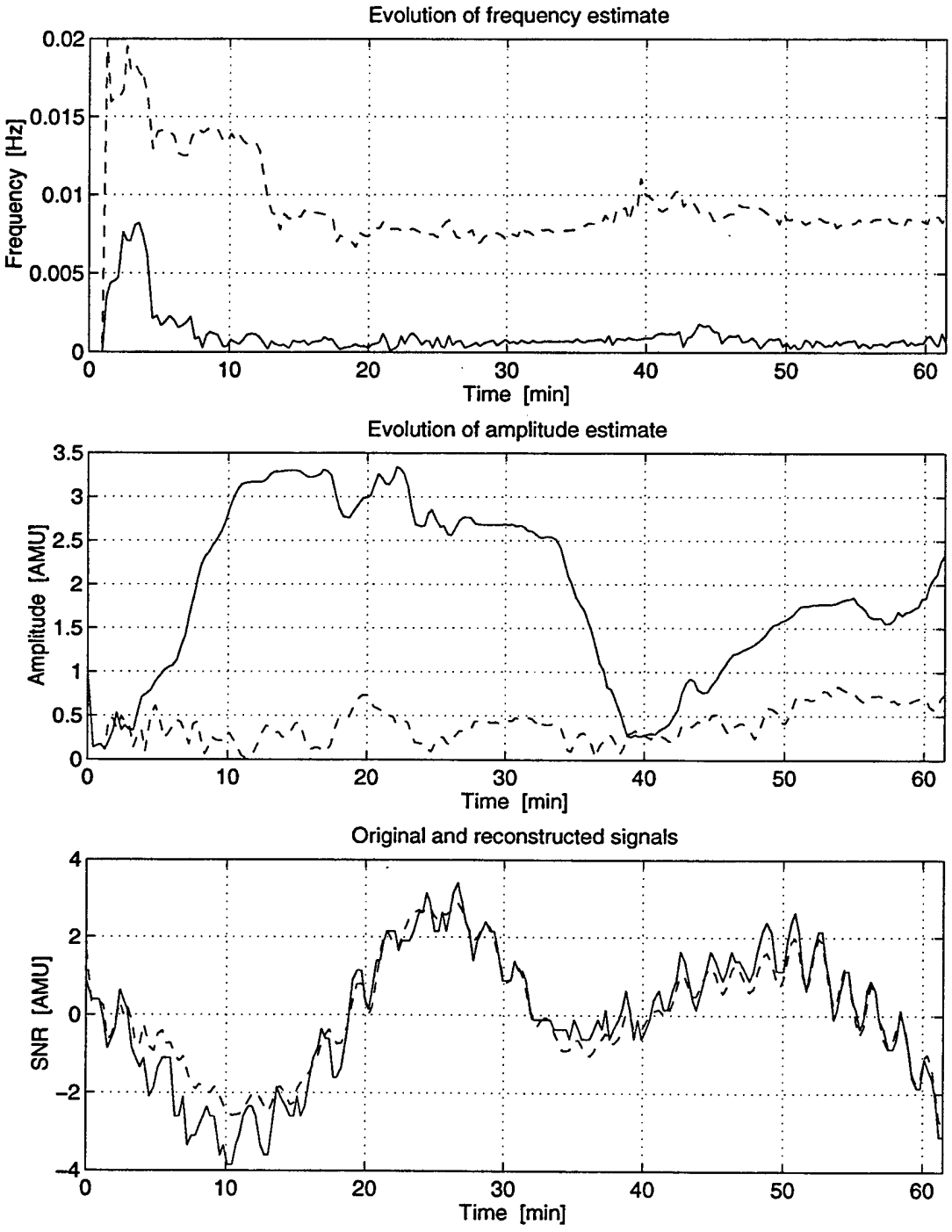

Figure 3.7: Adaptive least squares results for experimental multipath data. Top plot: evolution of low (solid) and high (dashed) frequency estimates from ANF; Middle plot: evolution of corresponding amplitude estimates from ALS; Bottom plot: original signal (solid) and signal reconstructed from spectral parameters (dashed).

1.75 seconds, but was decimated by a factor of 10 for the analysis, yielding an effective sampling rate of $f_s = 0.057$ Hz (17.5 second intervals). It is known from previous analysis that two distinct multipath constituents were present ($n = 2$). The γ, ρ, λ, μ, values were the same as those used for the simulated data.

Figure 3.6 exhibits the IIR ANF experimental data results. Again, the top plot shows the frequency estimates as they evolve through time. The middle plot depicts the magnitude output response of the filter versus frequency. The bottom plot displays the input and output signals of the filter. At about 20 minutes into the sequence the frequency estimates converge to the correct values, and continue to track them as they change over time. At the point of convergence, the filter begins to successfully remove the sinusoidal constituents. This event is observed by comparing the input and output signals. Note that the filter output for the experimental data is greater than that for the simulated data.

Figure 3.7 presents the ALS simulated results. Once again, the top plot shows the frequency estimates that were determined with the ANF. The middle plot shows the amplitude estimates as they evolve over time. The bottom plot displays the original multipath signal, and the signal reconstructed from the estimated spectral parameters. In this case, the ALS amplitude estimation needs about 50 minutes to converge. The post-convergence reconstructed signal provides a reasonable match to the original signal for the remaining duration of the data.

3.4 DISCUSSION OF RESULTS

The input variables for the ANF and ALS algorithms were chosen based on suggestions in [11, 12, 16, 8], and also on experience from analyzing a variety of data sets. The tradeoff of the convergence/forgetting factors is fast convergence for low values versus less noisy estimates for values close to unity. A good compromise was accomplished by setting the convergence parameter in the ANF (γ) and the forgetting factors in the ALS (λ, μ) to 0.9. They were kept constant for best performance with the nonstationary signals. A pole-zero contraction factor in the ANF (ρ) that is close to unity produces narrow notches, thereby removing less wide-band signal with the sinusoidal constituents, and providing more accurate frequency estimates. A lower value would allow the filter notches to better track nonstationary frequencies. Tracking capability was deemed a more valuable attribute, and 0.5 was the selected value. It is important to recognize that once these variables were decided upon, they remained the same regardless of the input data sequence. This makes a statement of the overall stability of the combined routines. The input variables that were changed for different input data sequences were the sampling frequency and the number of sinusoidal constituents whose spectral parameters are to be estimated.

If the ANF is estimating the correct frequencies, the sinusoids present in the input signal no longer exist in the output. Moreover, the amount of sinusoidal content in the output signifies the degree of success in estimating the frequencies. The magnitude output response, which is computed by taking the magnitude of the filter transfer function, depicts the notches placed at the estimated frequencies. Correspondingly, the filter output shows the removal of the associated sinusoidal constituents. This provides a check of the ANF frequency estimates.

In a similar vein, if the ALS is estimating the correct amplitudes and arguments, the reconstructed signal matches the original signal. The closeness of the match signifies the degree of success of the spectral parameter estimation as a whole. The amplitude and argument estimation

performed by the ALS needs more time to converge than does the ANF frequency estimation, which is indicative of the sensitivity of the ALS.

The potential capabilities of the combined ANF-ALS routine was demonstrated in the reconstructed signal for the simulated data. The performance with the experimental data is not quite as good, due to the complex nature of the actual multipath process. Only the spectral parameter estimation of the multipath in the SNR measurements, and the reconstruction thereof, has been presented so far. Whether or not the level of performance will be satisfactory within the multipath correction scheme remains to be seen, but favorable results are anticipated.

3.5 SUMMARY AND FUTURE WORK

A highly effective technique for the correction of multipath errors in GPS phase data, based on SNR measurements, was described and demonstrated in [2]. The technique, applied to data sets collected on static baselines in severe multipath environments, reduced the differential phase errors to near receiver noise levels.

The IIR adaptive notch filter and the adaptive least squares, when used together, provide a remarkably robust tool for estimation the time-varying spectral parameters of the multipath signals. The IIR ANF first estimates the frequencies, which are then used as a truth reference to estimate the amplitudes and arguments with the ALS. No initial estimates are required, and the results may be easily verified. The spectral parameters were successfully estimated for simulated and experimental multipath data sets. The amplitude and argument estimates should be easily inserted into the multipath correction formula (Equation 3.1).

The next area of research will be to operate the multipath correction technique using the combined ANF-ALS spectral parameter estimation. This shall be conducted on simulated and experimental static data, in a post-mission mode as before. Upon success with the static data, the next and final step will be to apply the technique to dynamic data, again in a post-mission mode. The first step in the dynamic procedure is to compute an initial time history of the vehicle attitude. This information serves as the basis for computing the correct antenna gain to be removed from each amplitude observation, and for removing the expected phase difference from the phase observables to permit the constituent sign determination. Post-mission accuracy refinement is a valuable tool for analysis of spacecraft data, and airborne altimetry or photogrammetry.

References

[1] Axelrad, P., C.P. Behre, C.J. Comp, and L.M. Ward, "GPS Based Attitude Determination," NRL FY'94-95 Technical Report I, October 6, 1995.

[2] Axelrad, P., C.P. Behre, C.J. Comp, and L.M. Ward, "GPS Based Attitude Determination," NRL FY'93-94 Technical Report II, October 14, 1994.

[3] Cannon, M.E., and M. Haverland, "Experiments of GPS Attitude Determination Within A Helicopter Pod," Proceedings of ION GPS-93, Salt Lake City, UT, Sept. 22-24, 1993.

[4] Chicharo, J.F., "High Resolution Spectral Estimation Using a Specially Constrained Adaptive Notch Filter," International Journal of Electronics, Vol. 72, No. 1, pp. 57-66, 1992.

[5] Cohen, C.E., B.W. Parkinson, "Aircraft Applications of GPS-Based Attitude Determination," Proceedings of ION GPS-92, Albuquerque, NM, Sept. 16-18, 1992.

[6] Cohen, C.E., E.G. Lightsey, B.W. Parkinson, and W.A. Fees, "Space Flight Tests of Attitude Determination Using GPS: Preliminary Results," Preprint of paper presented at ION GPS-93, Salt Lake City, UT, Sept. 22-24, 1993.

[7] Comp, C.J., "Carrier Phase Multipath Characterization and Mitigation For High Precision GPS Applications," Ph.D. Dissertation Prospectus, University of Colorado, Dept. of Aerospace Engineering Sciences, January 16, 1995.

[8] Händel, P. and P. Tichavský, "Adaptive Estimation for Periodic Signal Enhancement and Tracking," International Journal of Adaptive Control and Signal Processing, Vol. 8, 1994.

[9] Ljung, L. and T. Söderström, *Theory and Practice of Recursive Identification*, The MIT Press, Cambridge, MA, 1985.

[10] Lu, G., M.E. Cannon, and G. Lachapelle, "Attitude Determination in a Survey Launch Using Multi-Antenna GPS Technologies," Proceedings of ION National Technical Meeting, San Francisco, CA, Jan. 20-22, 1993.

[11] Nehorai, A., "A Minimal Parameter Adaptive Notch Filter With Constrained Poles and Zeros," IEEE Transactions on Acoustics, Speech, and Signal Processing, Vol. ASSP-33, No. 4, pp. 983-996, Aug., 1985.

[12] Nehorai, A. and B. Porat, "Adaptive Comb Filtering for Harmonic Signal Enhancement," IEEE Transactions on Acoustics, Speech, and Signal Processing, Vol. ASSP-34, No. 5, pp. 1124-1138, Oct., 1986.

[13] Oppenheim, A.V. and R.W. Schafer, *Discrete-Time Signal Processing*, Prentice-Hall, Englewood Cliffs, NJ, 1989.

[14] Roberts, R.A. and C.T. Mullis, *Digital Signal Processing*, Addison-Wesley, Reading, MA, 1987.

[15] Schwarz, K.P., A. El-Mowafy, and M. Wei, "Testing GPS Attitude System in Kinematic Mode," Proceedings of ION GPS-92, Albuquerque, NM, Sept. 16-18, 1992.

[16] Tichavsky, P. and P. Handel, "Efficient Tracking of Multiple Sinusoids With Slowly Varying Parameters," Proceedings of 1993 IEEE International Conference on Acoustics, Speech, and Signal Processing, Vol. III, 1993.

[17] Ward, L.M., "Spacecraft Attitude Estimation Using GPS: Methodology and Results," Ph.D. Dissertation Prospectus, University of Colorado, Dept. of Aerospace Engineering Sciences, August 12, 1994.

4. Spinning Satellite Attitude Determination Techniques *Charles P. Behre*

Previously, attitude determination techniques were applied to a computer simulation of GPS measurements from a spinning satellite. In October, 1995 a series of tests were conducted at the NRL Maryland Point facility using hardware to mimic this data. A Trimble TANS Vector receiver was mounted on a structure representing a typical small satellite. Using equipment with the ability to perform automated rotations, motion of the structure was implemented that simulated, as closely as possible, the kinematics of a spinning satellite. As the structure rotated, GPS data was collected.

Section 4.1 talks about the purpose of the tests. Sections 4.2 and 4.3 give a detailed description of the capabilities of the equipment and their relationship to the motion of an actual spinning satellite. Sections 4.4 and 4.5 describe how the tests were conducted. Sections 4.6 through 4.8 present an examination of the data. Section 4.9 concludes with plans for future data analysis.

4.1 Experiment Objectives

The primary goal of the tests conducted using the NRL spinning table equipment was to simulate the collection of measurements from a GPS receiver mounted on a spinning satellite. The measurements were analyzed to validate spinning vehicle attitude determination techniques. A secondary goal was to collect GPS measurements in a dynamic situation for multipath analysis. The tests were conducted using a TANS Vector receiver with four antennas mounted on the top corners of a structure with the dimensions of a typical small satellite.

The equations of motion for a spinning satellite are well understood, based on the relationship between the angular momentum, the moments of inertia, and externally applied torques. From Euler's equations characteristics such as the satellite angular rates and nutation angle can be computed. On the surface of the Earth, however, the effects of gravity and friction do not allow a structure to spin as it would in space. By using a motorized spin platform a structure can be forced to move according to Euler's equations. The intent was to use the NRL spin table to accomplish this task.

By mounting a GPS receiver and antennas on this structure, as shown in Figure 1, data was collected that mimicked, as closely as possible, the collection of data on an actual spinning satellite. The data was then reduced to verify various techniques for attitude determination. While no ground based test can equal the exact conditions found in space, they can be an improvement over pure computer simulation of data and be used to correct simulation errors. The successful demonstration of the techniques on experimental data can lead to more confidence in applying them to more expensive tests on a space based platform.

4.2 Experimental Apparatus

The complete test apparatus consists of two pieces of equipment with a combined total of three rotation axes as shown in the diagram in Figure 1. The first piece is the TRT-7 two axis tilter. In the local level coordinate frame, the first axis is oriented along an east-west direction. The second axis is aligned perpendicular to the first and rotates about it. When the first rotation angle is zero the second axis lies in the north-south direction. The maximum tilting angle about both axes is approximately ±45 degrees. The second piece of equipment is the BDS-5 spinner. It provides a constant angular rate about a third axis. This axis rotates according to the tilt angles of the TRT-7. It is mounted so that when the first two rotation angles are zero its orientation is in the up-down direction. The GPS antennas are mounted on the top plane of the satellite structure perpendicular to this axis.

The TRT-7 is programmable through an LCD display, a numeric keypad, and a few other function buttons. The angle of each tilt axis can be commanded to specific values in a series of steps. These steps can then be looped through for a periodic motion profile. The BDS-5 can be set to a constant rotation rate through a PC interface. A picture of the actual hardware is shown in Figure 2.

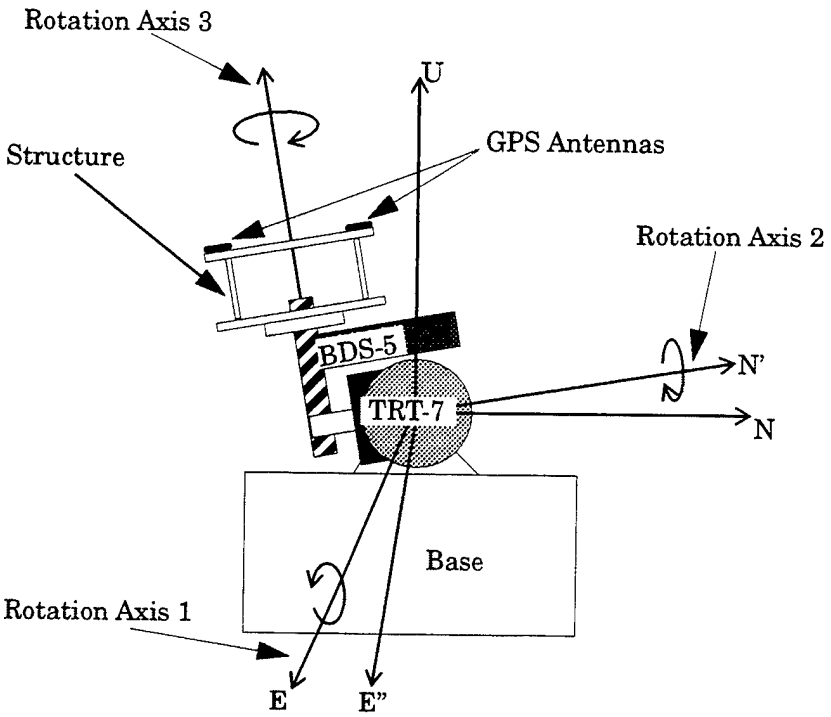

Figure 4.1. Equipment Diagram

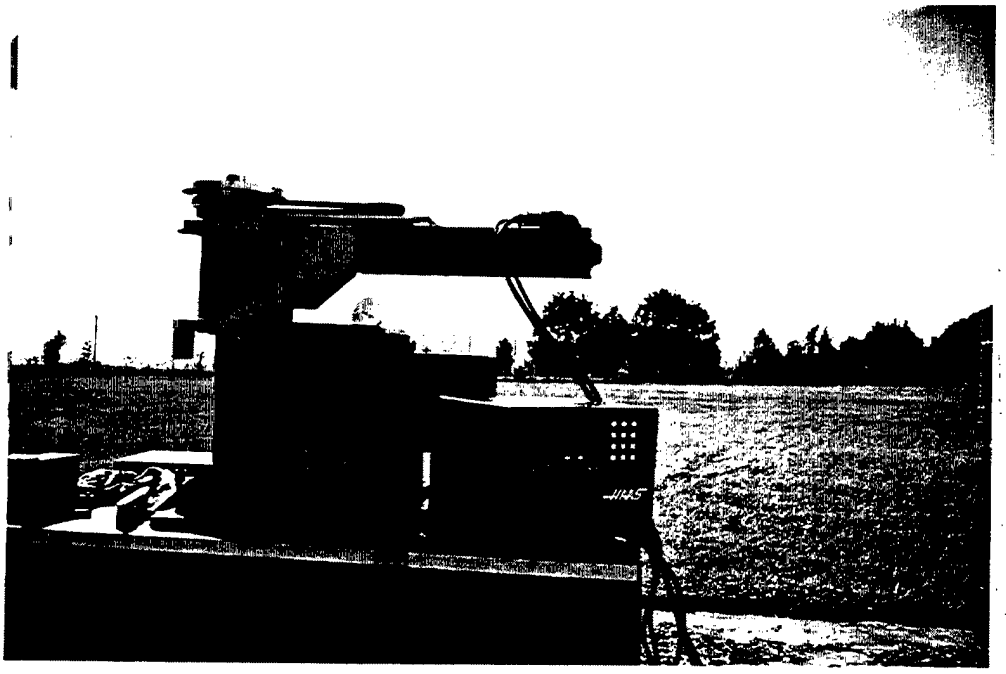

Figure 4.2. The TRT-7 and BDS-5 combination.

4.3 Theoretical Equations of Motion

The rotations derived by the Euler's equations for an axially symmetric spinning satellite show a 3-1-3 sequence. In other words, the position of the antenna is rotated from a locally fixed reference frame (L) to a body fixed (B) by a 3-1-3 series of time dependent rotations. The three Euler angles are ϕ, ψ, and γ, where

$$\phi = \omega_l t + \phi_o , \tag{4.1}$$

ω_l is the angular rate about the angular momentum axis,

$$\psi = \omega_p t + \psi_o , \tag{4.2}$$

ω_p is the angular rate about the spacecraft spin axis,
and θ is the nutation angle. The total rotation matrix is defined by

$${}^{B}C^{L}(\phi, \theta, \psi) = R_3(\psi)\, R_1(\theta)\, R_3(\phi) . \tag{4.3}$$

The satellite structure in the experimental setup has to be moved according to the rotations defined by the TRT-7 and the BDS-5. For this case the local system is defined by the orientation of the TRT-7's tilt axis when the plane of the structure is level to the ground. The body system is defined by the spin axis of the structure and the position of one of the GPS antennas as shown in Figure 3. In the body frame the position of the GPS antenna is always on the x^B-axis.

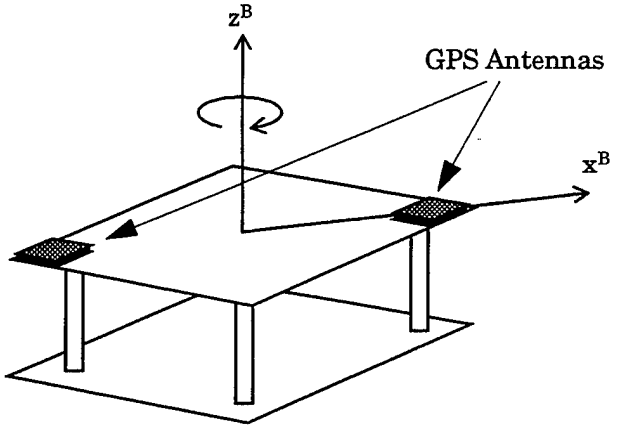

Figure 4.3. Body frame definition.

If the east direction is called the 1 axis, the north direction the 2 axis, and the up direction the 3 axis, then the series of rotations used to move the GPS antenna is a 1-2-3 sequence. If we define the three rotation angles as β, α, and γ, respectively, then the total rotation matrix is

$${}^{L}C^{B}(\beta, \alpha, \gamma) = R_3(\gamma)\, R_2(\alpha)\, R_1(\beta) . \tag{4.4}$$

In order to simulate the correct movement of a GPS antenna mounted on a spinning satellite with motion governed by the Euler angles ϕ, θ, and ψ, the angles β, α, and γ, must be varied in time as a function of them. These relations are computed by using the equality

$$^{B}C^{L}(\beta, \alpha, \gamma) = {}^{B}C^{L}(\phi, \theta, \psi) \ . \tag{4.5}$$

The resulting equations for α, β, and γ, are a function of the sums and products of the sinusoids of ϕ, θ, and ψ. These equations are very involved. However, for small nutation angles they are approximated by

$$\beta(t) \approx \theta \sin(\phi(t)) \ , \tag{4.6}$$

$$\alpha(t) \approx \theta \cos(\phi(t)) \ , \tag{4.7}$$

and

$$\gamma(t) \approx \phi(t) + \psi(t) \ , \tag{4.8}$$

where ϕ and ψ are computed by (4.1) and (4.2) respectively.

4.4 Experimental Equations of Motion

In order to correctly move the structure the two tilt angles of the TRT-7 must change according to equations (4.6) and (4.7). The angular rate of the BDS-5 must correspond to the derivative of (4.8). The implementation of these equations into the motion of the spin table, however, revealed a major limitation of the test equipment. The programming capabilities of the TRT-7 only allowed simple motion profiles such as linear changes in the title angle. Furthermore, the magnitude of the angular rates about the 1 and 2 axes had to be the same for each program step. As a result the desired sinusoids for α and β could not be implemented (Equations (4.6) and (4.7) show that α and β are 90 degrees out of phase, therefore, the $\left|\frac{d\alpha}{dt}\right|$ is a maximum when $\left|\frac{d\beta}{dt}\right|$ is a minimum).

The solution to this problem was to approximate the sinusoids in (4.6) and (4.7) with triangle waves. The resulting function for α is shown in Figure 4.

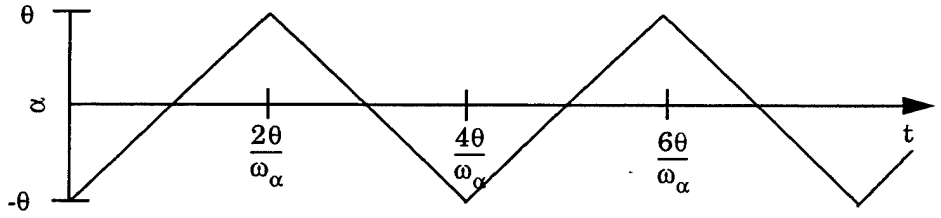

Figure 4.4. TRT-7 tipping profile.

where

$$\omega_{\alpha} = \frac{2\theta}{\pi}\omega_{l} \tag{4.9}$$

is the absolute rate of change of α.

Two problems occurred due to running this profile on the TRT-7. The first was that there was a noticeable delay when the TRT-7 had to reverse its direction after reaching the maximum angle*. The second problem was that the TRT-7's motor did not have sufficient torque to perform the triangle wave tipping about the east-west axis with the combined weight of the structure, GPS equipment,

*. The reversal delay was found to be due to a braking parameter in the program that caused the TRT-7 to slow down gradually (about 0.5 seconds) instead of instantaneously. The braking parameter was removed for subsequent tests. Note that this was not a recommended option in the equipment operators manual.

and BDS-5. Looking at Figure 1 it can be seen that there was a large weight imbalance about this axis. As a result, only tipping about the north-south axis was used. Most likely, the combination of the equipment weight and the desire for continuous triangle wave motion exceeded the performance limitations of the TRT-7.

Another problem occurred with the BDS-5. The BDS-5 motor was used to drive a gear and belt system that rotated the satellite structure. As a result, the programmed speed of the BDS-5 was not the actual angular rate of the structure. Furthermore, there was no other independent method to obtain the true spin rate. The solution to this problem was to time several rotation with a stop watch and then estimate the actual spin rate. This was repeated for several different rates. The values were then averaged to determine a conversion between programmed speed and actual speed.

4.5 Experiments

A Trimble TANS Vector receiver was mounted on the inside of the satellite structure and four antennas were mounted on the top corners. A diagram of the structure is shown in Figure 5. A picture of the actual structure mounted to the spin table is shown in Figure 6. Two types of structure motions were implemented. The first was a no nutation spin. After leveling the structure, it was tipped to fixed angles about both the east and north axes using the TRT-7. Next, the structure was spun about the third axis using the BDS-5. Several combinations of tilt angles and spin speeds were used. Figure 7 gives two views of the structure after it has been tilted. The second type of test consisted of using the triangle tipping profile described in the previous section. In each of the tests the structure was first leveled and then tipped at ±5 degrees about the north axis while spun about the third axis. Several tipping rates and spin speeds were used. In both types of tests, antenna phase difference, $\Delta\varphi$, and line of sight data was collected from the GPS receiver.

Appendix A gives a diary of the testing and shows a table of the experiments that were conducted.

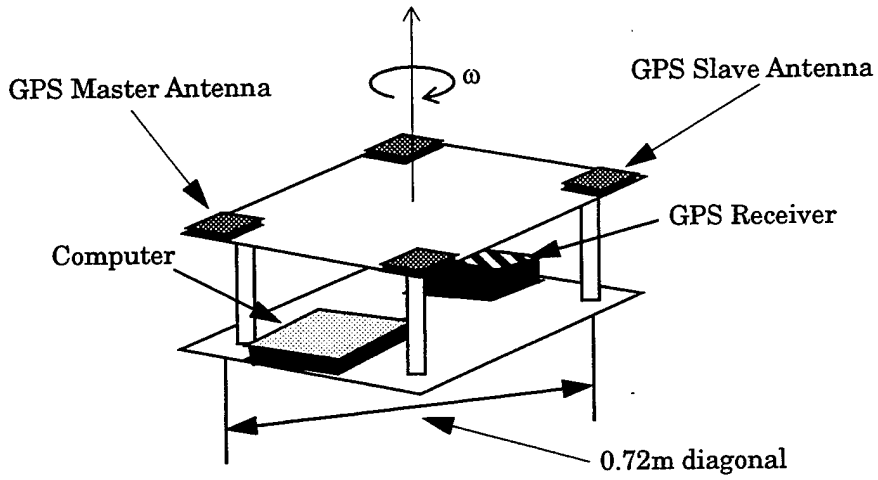

Figure 4.5. GPS data collection arrangement.

4.6 Results

The initial information that is determined is the displacement vector, $\vec{\delta r}$, of the GPS slave antenna relative to the structure's center, i.e. the change in its position in the ENU frame as the structure is moved. This value is computed from the $\Delta\varphi$ measurement between the master and diagonally opposite antenna by

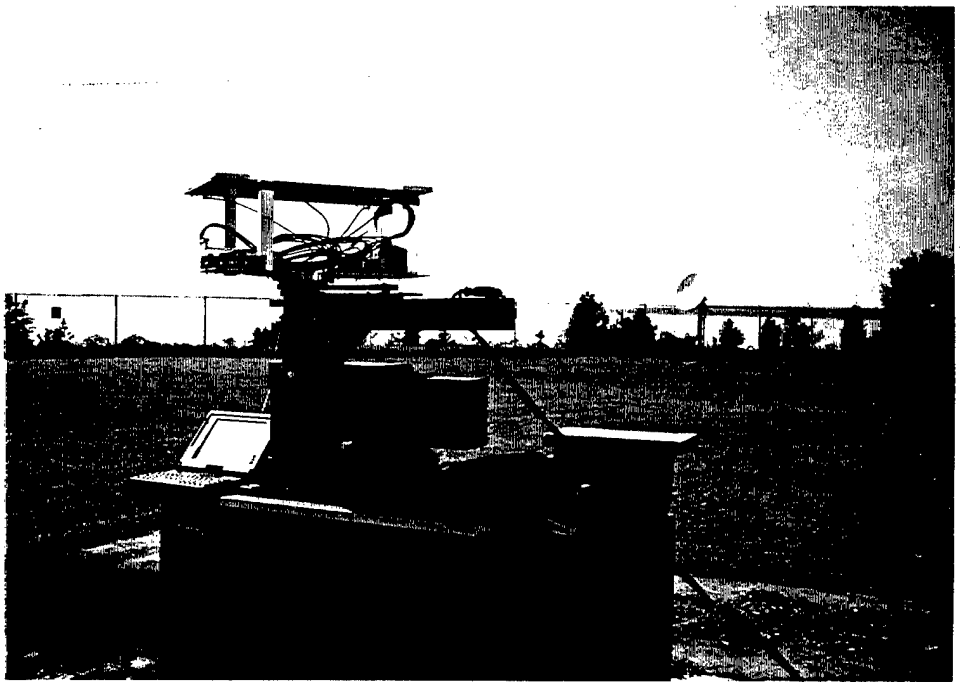

Figure 4.6. Satellite structure mounted on the spin table.

$$\vec{\delta r}(t_i) = \frac{1}{2}(H^T H)^{-1} H^T \begin{bmatrix} \delta\Delta\varphi^1(t_i) \\ \delta\Delta\varphi^2(t_i) \\ \vdots \\ \delta\Delta\varphi^M(t_i) \end{bmatrix}, \tag{4.10}$$

where H is the standard measurement connection matrix composed of the line of sight vectors to satellites 1 through M and $\delta\Delta\varphi$ is the time difference between two $\Delta\varphi$ measurements of the same satellite. The factor of 1/2 is used because the two antennas are on opposite sides of the structure's diagonal as opposed to one antenna being in the center.

Figure 8 shows an FFT of the δx component of the displacement vector when there is no tipping. In this case the spin frequency, ω, is 0.0852 Hz. While the dominant frequency spike is clearly located at the expected value of ω there are also noticeable spikes at 1.5ω, 2ω, and 3ω. In fact computing the

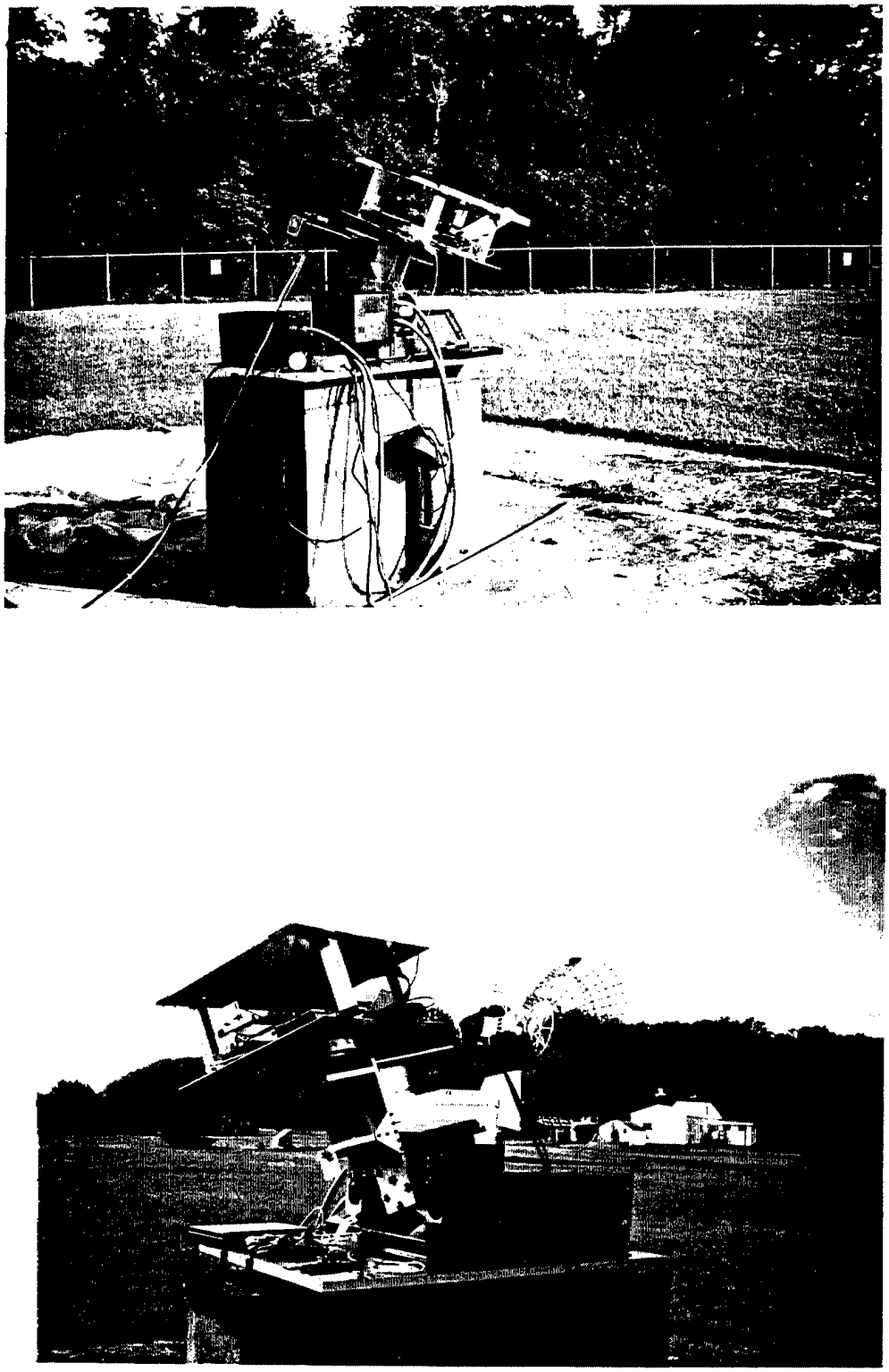

Figure 4.7. Two views of the tilted structure.

frequencies using the AR method shows significant frequencies at even more multiples of ω. The plots for δy and δz are very similar.

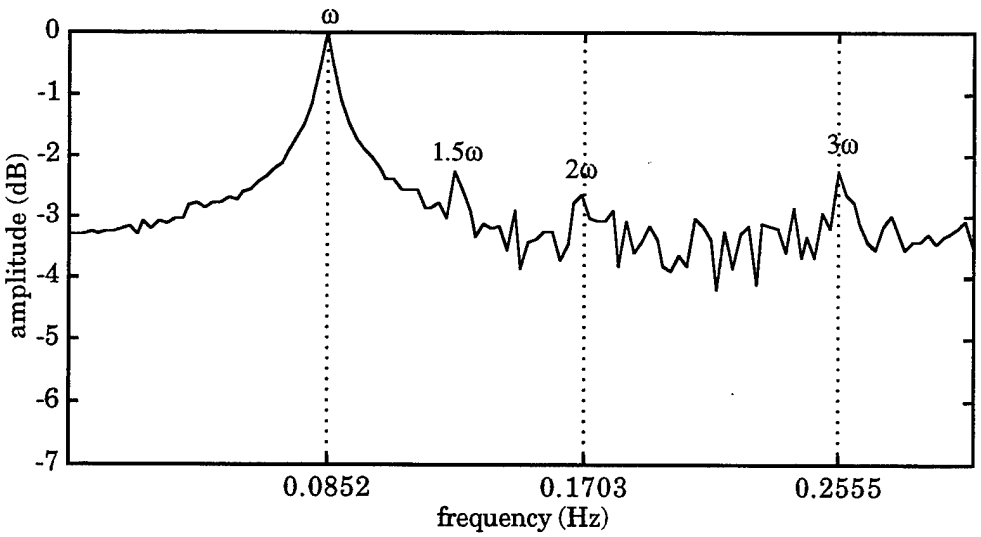

Figure 4.8. FFT of δx component of $\vec{\delta r}$.

Figure 9 shows an FFT of both the δx and δz component of the displacement vector when there is tipping. The tipping rate, ω_α, is 0.095 Hz. The most prominent spikes for the δx plot are located at ω, 1.5ω, and 3ω. The dominant frequencies in the δz plot are ω, $\omega+\omega_\alpha$, $\omega_\alpha-\omega$, $3\omega_\alpha-\omega$, and 3ω.

4.7 Frequency Analysis

In (4.10) the values of $\delta\Delta\varphi$ are scalars and the line of sight vectors are resolved in the local ENU frame. As a result, the reference frame of the displacement vectors is also ENU. To determine the equations relating the body frame displacement of the GPS antenna to its displacement in ENU coordinates, two sets of rotations must be performed. The first set involves fixed rotations of the angular momentum axis. If the orientation of the untilted angular momentum axis is defined to be $[0\ 0\ 1]^T$, then its tilted orientation can be computed by

$$\hat{H} = R_N(\eta)\, R_E(\sigma) \begin{bmatrix} 0 \\ 0 \\ 1 \end{bmatrix}, \tag{4.11}$$

where σ and η are fixed rotations about the east and north axes respectively. The second set consists of the β, α, and ψ rotation angles as previously described. In the no tipping case, $\hat{H}$ is the vector about which the structure is spinning and is equal to the vector z^B rotated into the local system. For the tip-

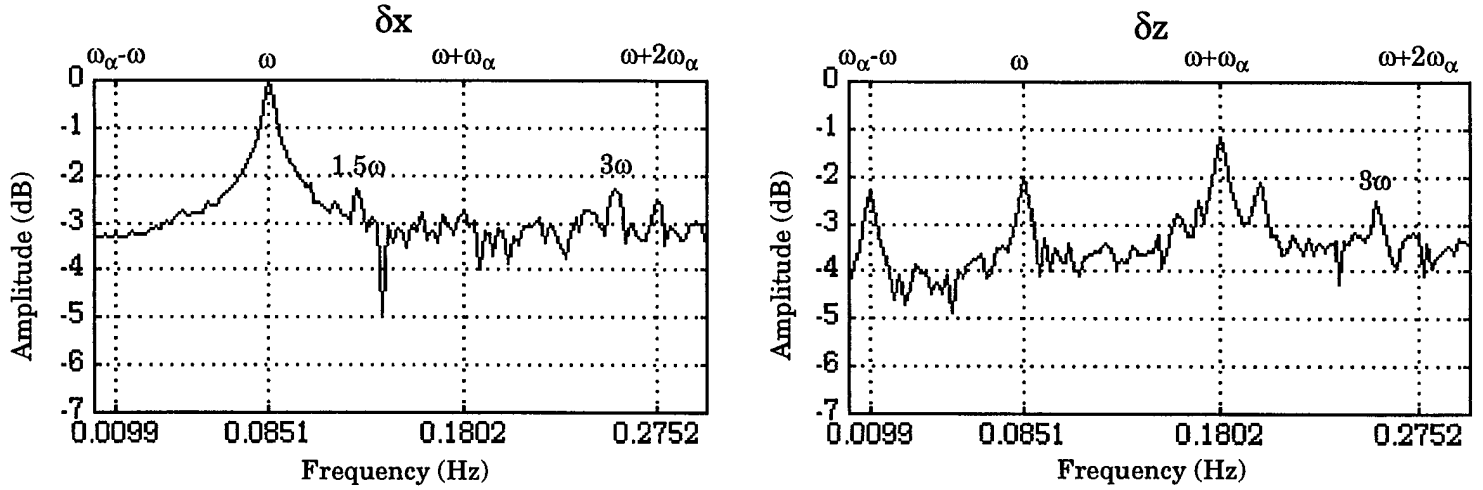

Figure 4.9. FFT of δx and δz from experimental data tipping profile.

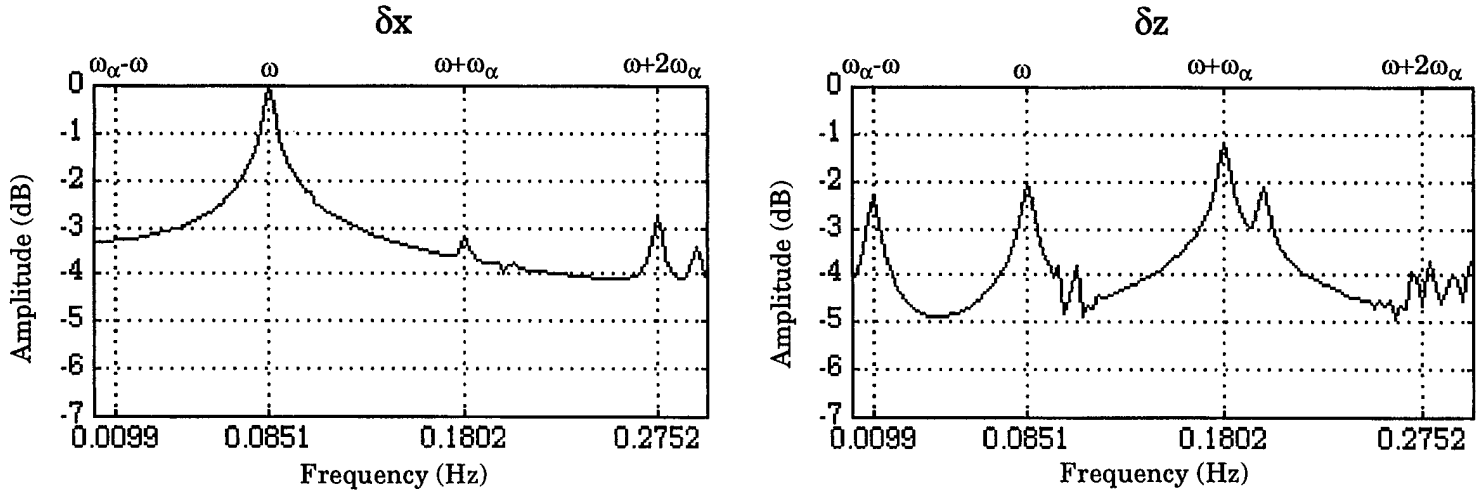

Figure 4.10. FFT of δx and δz from simulated data tipping profile.

ping case, $\hat{H}$ is the vector about which z^B is oscillating in the local frame. This is represented in Figure 11. This oscillation is governed by the value of α. In each of the tests the angle β is zero.

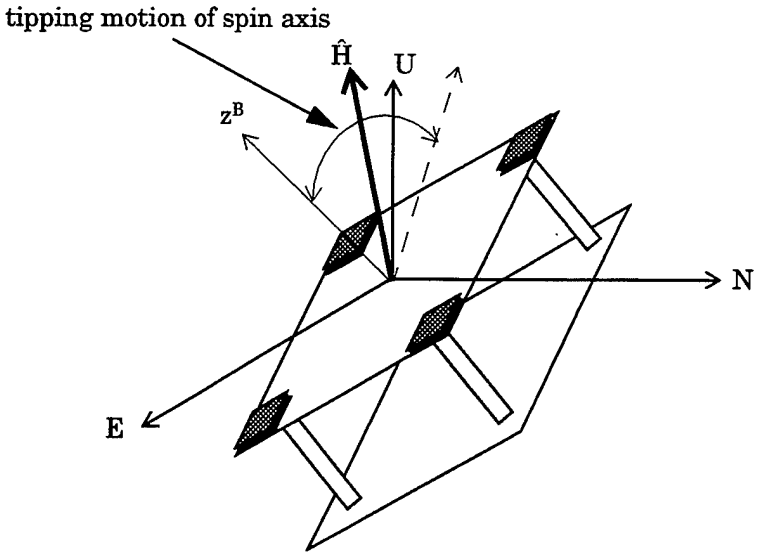

Figure 4.11. Orientation of angular momentum vector

The resulting equations for the antenna position in the local coordinate system are

$$\begin{aligned} x^L &= \{c\gamma c\alpha c\eta - c\gamma s\alpha c\sigma s\eta + s\gamma s\sigma s\eta\}\, x^B \\ y^L &= \{c\gamma s\alpha s\sigma + s\gamma c\sigma\}\, x^B \\ z^L &= \{-c\gamma c\alpha s\eta - c\gamma s\alpha c\sigma c\eta + s\gamma s\sigma c\eta\}\, x^B \end{aligned} \qquad (4.12)$$

where

$$\gamma(t) = \omega t + \gamma_o, \qquad (4.13)$$

ω is the angular rate produced by the BDS-5, and α is the angle produced by the TRT-7. The displacement vectors can be computed by time differencing (4.12). If $\alpha(t)=0$ for all t (i.e. $\omega_\alpha=0$) then the only frequency contained in $\vec{\delta r}$ is ω. If tipping is introduced, then $\omega_\alpha \neq 0$ and other frequencies appear.

If a(t) is varied sinusoidally, we would observe the product of two sinusoids producing frequencies at $\omega_1 \pm \omega_2$, where ω_1 and ω_2 are the two sinusoidal frequencies. In the case of the tipper motor, the function $\alpha(t)$ in (4.12) is a triangle wave. The triangle wave has frequencies at $k\omega_\alpha$ for k=1,2,3,... . Taking the cosine of $\alpha(t)$ produces only the even multiples, while taking the sine of $\alpha(t)$ generates the odd frequencies. As a result, the frequencies contained in (4.10) are

$$\begin{aligned} dx^L &: \omega \pm k\omega_\alpha \\ dy^L &: \omega \text{ and } \omega \pm (2k+1)\,\omega_\alpha \quad k=0,1,2,\ldots \\ dz^L &: \omega \pm k\omega_\alpha \end{aligned} \qquad (4.14)$$

The magnitude of σ and η determine the amplitude of the FFT frequency spikes. If these two angles are small (i.e. a slight tilt of $\hat{H}$), then the $\sin(\sigma)$ and $\sin(\eta)$ terms are also small and the $\cos(\sigma)$ and $\cos(\eta)$ terms are close to one. As a result the $\sin(\alpha)$ term in δx is multiplied by a small value pro-

ducing a small amplitude at odd multiples of ω_α. The cos(α) in δz is also multiplied by a small value producing a small amplitude at even multiples of ω_α. Furthermore, the amplitude decreases as the value of k gets bigger.

The test parameters that produced the data for Figure 9 use values of σ and η very close to zero. As shown in this figure, the predicted spike at $\omega+\omega_\alpha$ for the δx plot is almost completely lost in the noise, there is no noticeable spike at $\omega_\alpha-\omega$ (the absolute value of $\omega-\omega_\alpha$), while the spike at $\omega+2\omega_\alpha$ is slightly more pronounced. In the δz plot there are obvious frequencies at $\omega+\omega_\alpha$, $\omega_\alpha-\omega$, and $3\omega_\alpha-\omega$ as predicted while the frequency at $\omega+2\omega_\alpha$ is in the noise. In both plots, there are noticeable spikes at 3ω. These multiples of ω which are even more prominent in Figure 8 are not predicted by the theoretical equations of motion. Presently, there is no explanation for their existence.

4.8 Simulation

Using the frequencies determined through either the FFT of the experimental data, simulated data can be generated to verify the equations in (4.12) and to estimate the values of σ, η, and θ, the amplitude of α. The simplest way to accomplish this is to vary these values until the standard deviation of the error between the experimental and simulated data is a minimum. Also, the initial phases of α and γ must be adjusted to correspond with the segment of experimental data being used. Figure 12 shows a comparison between the δx and δz components of experimental and simulated data in the time domain.

Figure 10 shows an FFT of the simulated data in the frequency domain. As compared with Figure 9, the frequencies found in (4.12) agree with those found in the experimental data. With out the presence of noise, the $\omega+\omega_\alpha$ spike shows up in the δx plot. The frequencies at $|\omega\pm2\omega_\alpha|$ are now evident in the δz plot. It should be noted, however, that in the simulated data there are no frequency spikes corresponding to multiples of ω_α.

4.9 Future Work

The previous sections describe the experimental setup, the initial results, and the theory behind the results. No quantitative comparison or estimation of accuracy is given for the numbers. Furthermore, only two different tests runs are examined. The first is a no tipping case with very little tilt of the angular momentum axis. The second is a tipping case.

The next step is to examine in detail the estimates of ω, ω_α, σ, η, and θ by analyzing the results of all of the no tipping and tipping tests. Preliminary analysis shows a slight disagreement between the estimates of these parameters and their programmed values.

The estimates of ω and ω_α are found using both the FFT and AR methods. The estimates for σ, η, and θ, however, are determined by a crude trial and error method. Their values are manually varied along with the initial phases of α and γ until the standard deviation of the estimation error is as close to zero as possible. The next goal is to construct a filter based on the theoretical equations in (4.12) which will be used to sequentially estimate these parameters.

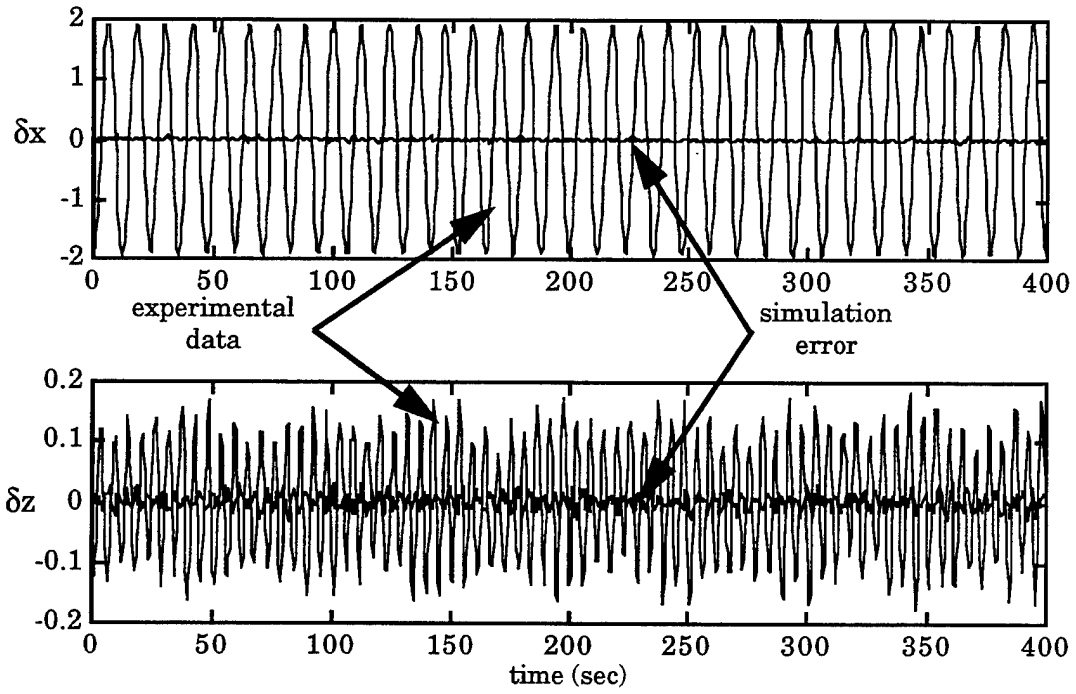

Figure 4.12. Comparison between experimental and simulated data in the time domain.

Appendix A: Diary and Table of Tests

10/2/95, NRL Maryland Point Test Facility, Charles Behre and Alan Hope

The first day of experiments consisted of mounting and testing the satellite structure on the spindle and familiarization with the TRT-7 and BDS-5 controls.

The first set of tests were used to determine the conversion ratio between the BDS-5 rate commands and the actual spindle rates. The BDS-5 was commanded at several angular rate values. At each of these values, a stop watch was used to time a set number of revolutions of the structure. These values were later averaged to determine the best approximation for the conversion factor.

To determine a conversion between the GPS measurements reference frame and the local level frame static attitude tests were determined. First, the structure was leveled, then the vector between the master antenna and slave number two was aligned with the TRT-7's 1-axis. The TRT-7 was mounted so that the 1-axis was aligned east to west in the local frame. Finally, position and attitude data were recorded for about 15 minutes. This procedure was repeated several time more.

10/3/95, NRL Maryland Point Test Facility, Charles Behre and Alan Hope

Programming the TRT-7 revealed some major problems. The programming capabilities of the TRT-7 were not very sophisticated. To program a sinusoidal tipping profile, a series of discreet angle values plus a series of angular rates would have to be inputted. Furthermore, the two axes could only be commanded at the same absolute rate. This means that the desired sinusoids for α and β could not be implemented (α and β are 90 degrees out of phase, therefore, the $\left|\frac{d\alpha}{dt}\right|$ is a maximum when $\left|\frac{d\beta}{dt}\right|$ is a minimum). The best approximation to these sinusoids that could be programed was a triangle wave. The angles would have a maximum value equal to the desired nutation angle and would have a rate derived from ω_l. The second problem was a pause between the execution of each step in the program. It was determined that this was due to a motor brake parameters which had to be set to zero. Upon setting the values to zero, the pause appeared to be eliminated.

In the first set of tests the structure was spun about the 3-axis at various speeds while the TRT-7 was commanded to tilt about the 2-axis at different rates and at several values of the nutation angle. Next the TRT-7 was commanded to tip about the 1-axis. This revealed another problem. An error message of 'high load' appeared on the TRT-7 display. This caused the TRT-7 to discontinue moving. The resulting data has to be examined to determine when the motion stopped.

10/4 - 10/5/95, NRL Maryland Point Test Facility, Charles Behre and Bill Betts

It was raining on both of these days. Some more spin rate calibrations were performed. The TRT-7 was programed to execute a simultaneous tipping about the 1 and 2-axes. The profiles were two triangle waves 90 degrees out of phase. Insufficient good weather was available for any further data collection.

10/6/95, NRL Maryland Point Test Facility, Charles Behre and Bill Betts

In the first set of planned tests the structure was commanded to move under the simultaneous tipping profiles. The results, however, were more 'high load' errors. Reducing the tipping rate and magnitude was tried as a solution to this problem, but this was not successful. I believe that the TRT-7 could not execute the instantaneous change in tipping direction required under the triangle wave profile. This would require the motors to rapidly change their spin direction. This rapid deceleration

and acceleration requirement probably exceeded design limitations, especially with the weight of the BDS-5, satellite structure and equipment. As a result, the simultaneous tipping experiments were stopped.

In next set of tests the structure was tipped to various orientations and no nutation spin tests were performed (i.e. the TRT-7 was not moving). At these positions several spin rates were used and GPS measurements were collected.

Finally, the structure was removed from the test stand and a reflector plate was mounted for multipath tests. These tests were performed on the following day.

10/7/95, NRL Maryland Point Test Facility, Charles Behre and Bill Betts

The first multipath test involved tipping the satellite back and forth at a very slow rate. The weight of the reflector once again caused 'high load' errors. Even with the brake parameters re-installed in the TRT-7 programs, the errors appeared. This test was cancelled. The next test was a 90 minute collection of static measurements. The final test consisted of rotating the structure at 24 degrees per minute. Data was also collected for 90 minutes.

Following this last test, the structure was removed from the structure and packed up for shipping.

Table 1. Test Descriptions.

Name	Date	Type	Spin Frequency (Hz)	Tip Frequency (Hz)	$\hat{H}$ Orientation
S11	10/2/95	Static	NA	NA	0 deg E, 0 deg N
R11	10/2/95	Flat rotation	0.0852	NA	0 deg E, 0 deg N
S12	10/2/95	Static	NA	NA	0 deg E, 0 deg N
S21	10/3/95	Static	NA	NA	0 deg E, 0 deg N
R21	10/3/95	Flat rotation	0.0852	NA	-10 deg E, -10 deg N
N21	10/3/95	Tipping 5 deg about N axis + rotating	0.0852	0.1	0 deg E, 0 deg N
N22	10/3/95	Tipping 5 deg about N axis + rotating	0.0852	0.05	0 deg E, 0 deg N
N23	10/3/95	Tipping 5 deg about N axis + rotating	0.0639	0.05	0 deg E, 0 deg N
N24	10/3/95	Tipping 5 deg about N axis + rotating	0.1277	0.05	0 deg E, 0 deg N
N25	10/3/95	Tipping 5 deg about N axis + rotating	0.0639	0.025	0 deg E, 0 deg N

Table 1. Test Descriptions.

Name	Date	Type	Spin Frequency (Hz)	Tip Frequency (Hz)	$\hat{H}$ Orientation
N26	10/3/95	Tipping 5 deg about E axis + rotating*	0.0639	0.025	0 deg E, 0 deg N
N27	10/3/95	Tipping 5 deg about E axis + rotating*	0.0852	0.05	0 deg E, 0 deg N
R51	10/6/95	Tipping about E and N axes + rotating*	0.0833	0.025	0 deg E, 0 deg N
R52	10/6/95	Tipping about E and N axes + rotating*	0.05	0.0125	0 deg E, 0 deg N
R53	10/6/95	Flat rotation	0.1167	NA	-10 deg E, -10 deg N
R54	10/6/95	Flat rotation	0.1667	NA	-10 deg E, -15 deg N
R55	10/6/95	Flat rotation	0.05	NA	-10 deg E, -15 deg N
C61	10/7/95	Multipath	No spin	NA	0 deg E, 0 deg N
C62	10/7/95	Multipath	0.0011	NA	0 deg E, 0 deg N

* Tests were stopped and are invalid because of equipment failure.